Title
Development and Applications of New Chemical Tools for Studying the Cell Biology of Metals

Author
Dodani, Sheel

Publication Date
2013

Peer reviewed|Thesis/dissertation

Development and Applications of New Chemical Tools for Studying the Cell Biology of Metals

By

Sheel Chandra Dodani

A dissertation submitted in partial satisfaction of the

requirements for the degree of

Doctor of Philosophy

in

Chemistry

in the

Graduate Division

of the

University of California, Berkeley

Committee in charge:

Professor Christopher J. Chang, Chair
Professor Michelle C.Y. Chang
Professor Christopher Vulpe

Spring 2013

Development and Application of New Chemical Tools for Studying the Cell Biology of Metals

by Sheel Chandra Dodani

Abstract

Development and Applications of New Chemical Tools for Studying the Cell Biology of Metals

by

Sheel Chandra Dodani

Doctor of Philosophy in Chemistry

University of California, Berkeley

Professor Christopher J. Chang, Chair

Cells have evolved intricate mechanisms that coordinate the activity of transporters, chaperones, and small-molecule ligands to control the spatial and temporal positioning of metal ions. Alkali and alkaline earth metal ions are known to play essential roles in cellular signaling and charge balance whereas transition metals are typically found in the active sites of enzymes to carry out organic transformations. In order to carry out these functions the cell maintains static and labile metal ion pools. These pools can be characterized by bulk molecular biology and bioinorganic techniques on fixed samples in combination with fluorescent indicators that afford the ability to track metal ions in real-time through molecular imaging. In this regard, cellular calcium has been well characterized in variety of biological contexts, but methods to monitor biologically relevant transition metal ions in real-time have not been well established. This dissertation describes the synthesis, characterization, and applications of new fluorescent sensors for Ni^{2+} and Cu^{+}, as well as approaches to discover new roles of biological copper in cell signaling. Nickelsensor-1 is a new water-soluble, turn-on fluorescent sensor that is capable of selectively responding to Ni^{2+} in aqueous solution and in living cells. Coppersensor-3 and X-ray fluorescence microscopy reveal that neuronal cells mobilize significant pools of copper from their cell bodies to peripheral processes in a calcium dependent fashion upon depolarization with KCl. Mitochondrial Coppersensor-1 (Mito-CS1) is a bifunctional reporter that combines a Cu^{+}-responsive fluorescent platform with a mitochondrial-targeting triphenylphosphonium moiety for the reversible detection of endogenous, exchangeable mitochondrial Cu^{+} pools. Mito-CS1 in conjunction with ICP metal analyses, show that both the exchangeable Cu^{+} and total mitochondrial copper pools are only mildly perturbed in fibroblasts with mutant *SCO1* and *SCO2* mitochondrial copper chaperones. Molecular imaging of neural calcium transients reveals that that endogenous copper is used to tune inhibitory and excitatory inputs during neural circuit development through the dynamic functions of CTR1. Finally, methods for high-throughput RNAi screening and immunofluorescence have been optimized to understand how the kinome regulates the copper mediated mobilization of ATP7A in mammalian cells.

For my parents.

Table of Contents

Acknowledgements

My Ph.D. has been a time filled with scientific pursuits and self-discovery, and here I express my gratitude for all the amazing people who have accompanied me on this journey. First and foremost, I would like to thank my dissertation advisor Professor Chris Chang for his support, guidance, and patience during my graduate work. He has always encouraged me to push the envelope and take scientific risks as we are limited only by our own curiosity and not our failures. This has become a standard to which I hold myself both scientifically and personally. I could not have made it to the finish line without the mentorship, scientific expertise, and camaraderie of the Chang lab members. In particular I would like to acknowledge: Bryan Dickinson, Dylan Domaille, Sami Farhi, Lakshmi Krishnamoorthy, Alex Lippert, Evan Miller, Christine Nam, Carl Onak, Emily Que, and May Srikun.

For Chapter 1 of this dissertation, portions of the work were published in *Journal of the American Chemical Society* **2009**, *131*, 18020—18021 were performed in collaboration with Qiwen He who designed a portion of the synthetic route for the binding domain. For Chapter 2 of this dissertation, portions of this work were published in the *Proceedings of the National Academy of Science, U.S.A.* **2011**, *108*, 5980—5985 and were performed in collaboration with the following people: Dylan W. Domaille designed the synthetic route and characterized the spectroscopy of CS3 and prepared some of the X-ray fluorescence samples and performed some of the X-ray fluorescence imaging experiments, Christine I. Nam prepared the neuronal cultures and performed all of the neuron imaging experiments with CS3, Evan W. Miller performed some of the X-ray fluorescence imaging experiments, and Lydia Finney and Stefan Vogt fitted the data for the X-ray fluorescence experiments. For Chapter 3 of this dissertation, portions of the work were published in *Journal of the American Chemical Society* **2011**, *133*, 8606—8616 and were performed in collaboration with the following people: Scot C. Leary isolated primary liver tissues and derived immortalized fibroblasts from patient samples, prepared whole cell/mitochondrial samples for and completed the inductively coupled plasma optical emission spectrometry experiments, measured COX activity, and determined the purity of isolated mitochondria and Lydia Finney and Stefan Vogt fitted the data for the X-ray fluorescence experiments. Portions of the work presented in Chapter 4 of this dissertation were performed in collaboration with the following people: Christine I. Nam prepared the rat neuronal cultures and with Dylan W. Domaille performed the calcium imaging of the dissociated rat hippocampal cultures, Christine I. Nam prepared the mouse neuronal cultures and performed the calcium imaging of the WT and CTR1$^{-/-}$ dissociated mouse hippocampal cultures, and Alana Firl isolated the retina, performed some of the calcium imaging experiments, generated the MATLAB algorithms, and performed some of the data analysis. Portions of the work presented in Chapter 5 of this dissertation were performed in collaboration with Lakshmi Krishnamoorthy. Portions of the work presented in Appendix 2 of this dissertation were performed in collaboration with the following people: Bryan C. Dickinson maintained neural stem cells and continued this study with Lakshmi Krishnamoorthy and Lydia Finney and Stefan Vogt fitted the data for the X-ray fluorescence experiments. Portions of the work presented in Appendix 3 of this dissertation were performed in collaboration with the following people: Lydia Finney and Stefan Vogt fitted the data for the X-ray fluorescence experiments

Next, I would have never discovered my passion for science if it were not for my undergraduate experience at UT Dallas in Professor John Sibert's lab under the mentorship of Phillip Forhsee. Their enthusiasm for scientific discovery and teaching was absolutely

contagious and served as a motivation for me to pursue my graduate work. Finally, I am blessed to have the love and support of my parents who encouraged me to embark on this journey even though I was going to be away from home for the first time. On the days when I was ready to give up because graduate school was just too hard or when I added too much soap to the washer, my parents were my cheerleaders on the other end of the phone. Thank goodness for unlimited minutes! As I close this chapter of my life and embark on a new journey, the experiences and people that I have met during my Ph.D. at Berkeley will always be dear to my heart.

Chapter 1:
A Turn-On Fluorescent Sensor for Detecting Nickel in Living Cells

Abstract

We present the synthesis and properties of Nickelsensor-1 (NS1), a new water-soluble, turn-on fluorescent sensor that is capable of selectively responding to Ni^{2+} in aqueous solution and in living cells. NS1 combines a BODIPY chromophore and a mixed N/O/S receptor to provide good selectivity for Ni^{2+} over a range of biologically abundant metal ions in aqueous solution. In addition to these characteristics, confocal microscopy experiments further show that NS1 can be delivered into living cells and report changes in intracellular Ni^{2+} levels in a respiratory cell model.

Introduction

Nickel is an essential metal nutrient for supporting life, but loss of nickel homeostasis is harmful to prokaryotic and eukaryotic organisms alike.[1] Elegant studies continue to elucidate mechanisms for Ni^{2+} uptake, regulation, and efflux,[2—10] as well as to define the redox and non-redox roles of nickel biochemistry in microbial and plant systems.[11—17] However, the contributions of nickel homeostasis to mammalian health and disease remain largely unexplored.[18] In this context, excess nickel accumulation can aberrantly affect respiratory and immune systems, but mechanisms of nickel imbalance are insufficiently understood.[19,20]

To help elucidate the roles of nickel in living systems, we are developing Ni^{2+}-selective fluorescent indicators as part of a larger program aimed at studying metals in biology by molecular imaging.[21,22] Such chemical tools, in principle, can be used to monitor exchangeable nickel pools with spatial and temporal resolution and provide a complement to standard bulk techniques for measuring total nickel content such as atomic absorption or inductively coupled plasma mass spectrometry. A major chemical challenge to this end is designing systems with Ni^{2+}-specific responses over other biologically relevant metal ions in water. Examples of Ni^{2+}-responsive fluorescent probes remain rare; Ni^{2+}-selective peptide,[23,24] protein,[25] polymer,[26,27] and small-molecule based sensors[28-30] have been reported but have not been utilized for cellular imaging, whereas the commercial Zn^{2+} sensor Newport Green DCF also responds to Ni^{2+} and Ti^{3+} and has been used to detect their accumulation in cells.[31—34] In this report, we present the synthesis and properties of Nickelsensor-1 (NS1, **5**), a new turn-on fluorescent sensor for the selective detection of Ni^{2+} in water and in biological samples. NS1 features visible wavelength spectral profiles and a ca. 25-fold fluorescence increase upon Ni^{2+} binding. Confocal microscopy experiments show that this indicator can reliably monitor changes in Ni^{2+} levels within living mammalian cells.

Results and Discussion

Our design for NS1 combines a BODIPY dye reporter with a mixed N/O/S receptor to satisfy the Ni^{2+} cation (Scheme 1-1). Addition of ditosylate **1** to Cs_2CO_3 and methyl thiogylcolate affords diester **2** in 41% yield. Vilsmeier formylation of **2** using $POCl_3$/DMF followed by basic workup furnishes aldehyde **3** in 60% yield. BODIPY **4** is obtained in a one-pot, three-step procedure via condensation of **3** with 2,4-dimethylpyrrole, followed by DDQ oxidation and boron insertion with BF_3•OEt_2 (38% overall yield for three steps). Ester hydrolysis of **4** under basic conditions gives NS1 (**5**) in 71% yield.

Spectroscopic evaluation of NS1 was performed in 20 mM HEPES buffered to pH 7.1. The optical features of the probe are characteristic of the BODIPY platform. Apo NS1 displays one visible region absorption band centered at 495 nm (ε = 5.8 x 10^4 M^{-1} cm^{-1}) and an emission maximum at 507 nm (Φ = 0.002). Addition of 50 equiv of Ni^{2+} triggers a ca. 25-fold fluorescence turn-on (Φ = 0.055, Figure 1-1) with no shifts in absorption (λ_{abs} = 495 nm, ε = 5.5 x 10^4 M^{-1} cm^{-1}) or emission maxima (λ_{em} = 507 nm) compared to the apo probe. The turn-on response is reversible; treatment of Ni^{2+}-loaded NS1 with the divalent metal ion chelator TPEN restores NS1 fluorescence back to baseline levels. A Hill plot indicates a simple binding process with no cooperativity (Figure 1-2a), and the apparent Kd for Ni^{2+} binding to NS1 is 193 ± 5 μM (Figure 1-2b).

NS1 exhibits a selective turn-on fluorescence response to Ni^{2+} in water. Responses of 2 μM NS1 to the presence of various biologically relevant metal ions are shown in Figure 1-3. The fluorescence profiles of apo or Ni^{2+}-bound NS1 are unchanged in the presence of 1 mM Na^+, K^+, Mg^{2+}, and Ca^{2+}, indicating excellent selectivities for Ni^{2+} over these alkali and alkaline earth cations. Moreover, a series of 3d divalent metal cations, including 100 μM Mn^{2+}, Fe^{2+}, Co^{2+}, and Zn^{2+}, do not trigger NS1 fluorescence enhancements or interfere with the Ni^{2+} response. The addition of excess Zn^{2+} can displace Ni^{2+} from the bound NS1 with an apparent K_d 1640 μM (Figure 1-4). Furthermore of the first-row divalent transition metal ions, Cu^{2+} at 100 μM can mute the turn-on Ni^{2+} response of NS1, but lower Cu^{2+} levels (2 μM) minimize this interference. As expected, Cu^{2+} binds the sensor due to Irving-Williams series considerations and can displace Ni^{2+} from the Ni^{2+}-bound complex with an apparent K_d 0.58 μM, but the paramagnetic d^9 ion quenches the fluorescence, suggesting that the fluorescence increase for Ni^{2+} is due to a diamagnetic d^8 state (Figure 1-5). We also examined the response of NS1 to various heavy metal ions. As seen in Figure 1-6, the addition of Hg^{2+} results in a fluorescence enhancement.

We next established the ability of NS1 to track Ni^{2+} levels in living cells using a model for respiratory nickel exposure. Live-cell confocal microscopy imaging experiments utilized the acetoxymethyl ester form of NS1 (NS1-AM) to enhance membrane permeability. Live human lung carcinoma A549 cells loaded with a 1:1 (v/v) mixture of NS1-AM and F-127 Pluronic acid (10 μM) for 35 min at 37 °C show weak intracellular fluorescence (Figure 1-7a). A549 cells supplemented with 1 mM $NiCl_2$ in the growth medium for 18 h at 37 °C and then staining with NS1-AM under the same loading conditions results in an increase in observed intracellular fluorescence intensity (Figure 1-7b); previous experiments establish that this exposure level of nickel is not lethal to lung carcinoma cells, whereas 2-10 mM Ni^{2+} causes widespread cell death.[35] Treatment of cells loaded with NS1-AM and Ni^{2+} with the divalent metal chelator TPEN (1 mM) for 1 min at 25 °C reverses the observed fluorescence increases (Figure 1-7c). Finally, Hoechst-33342 staining confirms that the cells are viable throughout the imaging studies (Figure 1-7d). Quantification of the intracellular fluorescence intensity is shown in Figure 1-7e. These data establish that NS1 can respond to changes in intracellular Ni^{2+} levels within living cells.

Concluding Remarks

In closing, we have described the synthesis, spectroscopy, and application of NS1, a new fluorescent sensor for Ni^{2+} in biological samples. NS1 is a unique Ni^{2+}-responsive small-molecule indicator that features visible excitation and emission profiles and a selective turn-on response to Ni^{2+} compared to other biological metal ions. Confocal microscopy experiments

show that NS1 can be used for detecting changes in Ni^{2+} levels within living cells. Future plans will focus on improving the optical brightness and binding affinities of this first-generation probe as well as applying NS1 and related chemical tools to probe the cell biology of nickel.

Experimental Section

Synthetic Materials and Methods. All reactions were carried out under a dry nitrogen atmosphere. Silica gel P60 (SiliCycle) was used for column chromatography. Analytical thin layer chromatography was performed using SiliCycle 60 F254 silica gel (precoated sheets, 0.25 mm thick). Compound 1 was prepared according to previously reported procedures.[36—38] *N*-phenyldiethanolamine and *p*-toluenesulfonyl chloride were purchased from Acros Organics (Morris Plains, NJ) and were used as received. All other chemicals were purchased from Sigma-Aldrich (St. Louis, MO) and were used as received. Pluronic F-127 and Hoechst-33342 were purchased from Invitrogen (Carlsbad, CA). ^{1}H and ^{13}C NMR spectra were collected in $CDCl_3$ or CD_3OD (Cambridge Isotope Laboratories, Cambridge, MA) at 25 °C on a Bruker AVB-400 spectrometer at the College of Chemistry NMR Facility at the University of California, Berkeley. All chemical shifts are reported in the standard notation of parts per million using the peak of residual proton signals of $CDCl_3$ as an internal reference. Low-resolution mass spectral analyses were carried out using a 6130 quadrupole LC/MS 1200 Series (Aglient Technologies, Santa Clara, CA). High-resolution mass spectral analyses were carried out at the College of Chemistry Mass Spectrometry Facility at the University of California, Berkeley.

Dimethyl 2,2'-(2,2'-(phenylazanediyl)bis(ethane-2,1-diyl)bis(sulfanediyl))diacetate (2). A solution of **1** (5.03 g, 10.3 mmol) in anhydrous DMF (60 mL) was added dropwise over 1 h to a mixture of methyl thioglycolate (2.0 mL, 22.4 mmol) and Cs_2CO_3 (7.34 g, 22.5 mmol) in anhydrous DMF (40 mL) at 60 °C. The reaction mixture continued to stir for 2 d. The reaction was filtered, and the salts were washed with DMF (50 mL). Water (200 mL) and brine (50 mL) were added to the filtrate, and the reaction was extracted with EtOAc (1 x 200 mL). The organic phase was washed with water (2 x 150 mL) and brine (2 x 50 mL), dried over Na_2SO_4, filtered, and concentrated to dryness. The crude reaction mixture was purified by flash column chromatography (silica gel, CH_2Cl_2 to 1% MeOH in CH_2Cl_2) to furnish **2** as a yellow oil (1.51 g, 41%). ^{1}H NMR (400 MHz, $CDCl_3$): δ 2.88 (t, 4H, J = 7.6 Hz), 3.32 (s, 4H), 3.61 (t, 4H, J = 7.6 Hz), 3.78 (s, 6H), 6.73-6.78 (m, 3H), 7.25-7.30 (m, 2H). ^{13}C NMR (100 MHz, $CDCl_3$): δ 29.7, 33.4, 50.8, 52.5, 112.0, 116.9, 129.6, 146.6, 170.8. LRESI-MS calculated for [MH^+] 358.1, found 358.1.

Dimethyl 2,2'-(2,2'-(4-formylphenylazanediyl)bis(ethane-2,1-diyl)bis(sulfanediyl)) diacetate (3). $POCl_3$ (0.75 mL, 8.0 mmol) was added dropwise to a stirring solution of **2** (1.45 g, 4.5 mmol) in anhydrous DMF (10 mL) at 0 °C. The reaction mixture was allowed to warm to room temperature and stirred overnight. The crude mustard yellow reaction mixture was poured into water (150 mL), cooled to 0 °C, and the pH was adjusted to pH 7-8 with solid K_2CO_3. The reaction mixture was stirred at room temperature for 10 min and extracted with CH_2Cl_2 (3 x 100 mL). The organic extracts were combined, dried over Na_2SO_4, filtered, and concentrated to dryness. The crude reaction mixture was purified by flash column chromatography two times (1st column: silica, CH_2Cl_2; 2nd column: silica, $CHCl_3$) to provide **3** as a yellow oil (0.929 g, 60%). ^{1}H NMR (400 MHz, $CDCl_3$): δ 2.72 (t, 4H, J = 7.4 Hz), 3.16 (s, 4H), 3.52 (t, 4H, J = 7.4 Hz), 3.58 (s, 6H), 6.60 (d, 2H, J = 8.8 Hz), 7.56 (d, 2H, J = 8.4 Hz), 9.55 (s, 1H). ^{13}C NMR (100

MHz, $CDCl_3$): δ 28.9, 32.8, 50.2, 52.1, 53.4, 110.3, 110.7, 125.4, 131.8, 151.0, 170.3, 189.6. LRESI-MS calculated for [MH^+] 386.1, found 386.1.

10-(4-(Bis(2-(2-methoxy-2-oxoethylthio)ethyl)amino)phenyl)-5,5-difluoro-1,3,7,9-tetramethyl-5H-dipyrrolo[1,2-c:1',2'-f][1,3,2]diazaborinin-4-ium-5-uide (4). Five drops of TFA were added dropwise to a vigorously stirring solution of **3** (449 mg, 1.17 mmol) and 2,4-dimethylpyrrole (245 mg, 2.58 mmol) in anhydrous CH_2Cl_2 (150 mL). The resulting red solution was stirred at room temperature in the dark for 90 min. DDQ (293 mg, 1.29 mmol) was then added in one portion and reaction was stirred for an additional hour. DIEA (3.0 mL, 17.2 mmol) was then added dropwise to this mixture over a period of 10 min, and the resulting orange-brown solution was allowed to stir for an additional 20 min. BF_3•OEt_2 (3.0 mL, 23.7 mmol) was then added dropwise over a period of 5 min, and the resulting purple solution was allowed to stir overnight. A second BODIPY condensation reaction of the same scale was performed (450 mg, 1.17 mmol of **3**) in parallel and both reaction mixtures were combined for a single workup procedure. The combined reactions were stirred with water (100 mL) for 10 min, and then water (50 mL) and brine (50 mL) were added. The resulting slurry was allowed to sit for 30 min, during which time the mixture separated into two phases. The aqueous layer was decanted, and the organic phase was washed with water (2 x 100 mL). The aqueous layers were then re-extracted with CH_2Cl_2 (3 x 100 mL), and the combined organic layers were washed with water (1 x 100 mL), dried over Na_2SO_4, filtered, and concentrated to dryness. The crude purple residue was purified by flash column chromatography (silica, 1% EtOAc in CH_2Cl_2) to afford **4** as an orange solid with a green luster (535 mg, 38%). ^{1}H NMR (400 MHz, 10% CD_3OD in $CDCl_3$): δ 1.42 (s, 6H), 2.47 (s, 6H), 2.83 (t, 4H, J = 7.4 Hz), 3.24 (s, 4H), 3.58 (t, 4H, J = 7.4 Hz), 3.69 (s, 6H), 5.91 (s, 2H), 6.71 (d, 2H, J = 8.4 Hz), 6.98 (d, 2H, J = 8.8 Hz). ^{13}C NMR (100 MHz, $CDCl_3$): δ 14.4, 14.6, 29.3, 32.2, 50.6, 52.4, 112.0, 120.8, 122.5, 129.1, 131.9, 142.6, 143.0,147.0, 154.6, 170.6. LRESI-MS calculated for [MH^+] 604.2, found 604.3.

Nickelsensor-1 (NS1, 5). LiOH (85 mg, 3.54 mmol) was added to a solution of diester **4** (515 mg, 0.89 mmol) in anhydrous THF (5 mL) and anhydrous MeOH (7 mL). The resulting red-orange solution continued to stir overnight. The reaction mixture was concentrated to dryness, and the remaining residue was dissolved in water (75 mL) and $CHCl_3$ (50 mL). The pH of the aqueous layer was adjusted to pH 5-6 by 0.5 M HCl and extracted with $CHCl_3$ (2 x 50 mL). The combined organics were washed with water (75 mL), dried over Na_2SO_4, filtered, concentrated to dryness, and purified by flash column chromatography (silica, 3% MeOH in CH_2Cl_2) to furnish NS1 as an orange solid (362 mg, 71%). ^{1}H NMR (400 MHz, $CDCl_3$): δ 1.40 (s, 6H), 2.45 (s, 6H), 2.81 (t, 4H, J = 7.6 Hz), 3.21 (s, 4H), 3.57 (t, 4H, J = 7.6 Hz), 5.90 (s, 2H), 6.70 (d, 2H, J = 8.4 Hz), 6.98 (d, 2H, J = 8.4 Hz). ^{13}C NMR (100 MHz, $CDCl_3$): δ 14.4, 14.6, 29.4, 33.6, 50.7, 112.1, 120.9, 122.6, 129.2, 132.1, 142.9, 143.3, 147.2, 154.8, 172.8. HRESI-MS calculated for [MH^+] 576.1968, found 576.1990.

Nickelsensor-1-acetoxymethyl ester (NS1-AM, 6). Bromomethyl acetate (110 mg, 0.72 mmol) in anhydrous DMF (1 mL) was added dropwise to a solution of NS1 (101 mg, 0.18 mmol) and DIEA (185 mg, 1.43 mmol) in anhydrous DMF (2 mL). The reaction mixture was allowed to stir overnight. Water (10 mL) was added to the reaction mixture and extracted with EtOAc (3 x 10 mL). The combined organics were washed with water (5 x 20 mL), dried over Na_2SO_4, filtered, concentrated to dryness, and purified by flash column chromatography (silica, 1.5% EtOAc in CH_2Cl_2) to furnish NS1-AM as a red-orange oil (99 mg, 78% yield). ^{1}H NMR (400 MHz, $CDCl_3$): δ 1.45 (s, 6H), 2.09 (s, 6H), 2.51 (s, 6H), 2.87 (t, 4H, J = 7.4 Hz), 3.30 (t, 4H, J = 7.4

Hz), 3.30 (s, 4H), 3.61 (t, 4H, J = 7.6 Hz), 5.76 (s, 2H), 5.95 (s, 2H), 6.74 (d, 2H, J = 8.4 Hz), 7.04 (d, 2H, J = 8.8 Hz). ^{13}C NMR (100 MHz, $CDCl_3$): δ 14.6, 14.7, 20.7, 29.5, 33.2, 50.7, 79.7, 112.2, 121.0, 123.0, 129.3, 132.1, 142.7, 143.1, 147.1, 154.9, 169.1, 169.5. HRESI-MS calculated for [MH^+] 720.2391, found 720.2400.

Spectroscopic Materials and Methods. Millipore water was used to prepare all aqueous solutions. All spectroscopic measurements were performed in aqueous 20 mM HEPES, pH 7.1. Absorption spectra were recorded on a Varian Cary 50 spectrophotometer (Walnut Creek, CA) and fluorescence spectra were recorded using a Photon Technology International Quanta Master 4 L-format scanning spectrofluorometer (Lawrenceville, NJ) equipped with an LPS-220B 75-W xenon lamp and power supply, A-1010B lamp housing with integrated igniter, switchable 814 photon-counting/analog multiplier detection unit, and MD5020 motor driver. Samples for absorption and emission measurements were contained in 1-cm x 1-cm quartz cuvettes (1.4-mL volume, Starna, Atascadero, CA). Fluorescence quantum yields were determined by reference to fluorescein in 0.1 M NaOH (Φ = 0.95).[39] Excitation was provided at 488 nm, and collected emission was integrated from 498 to 700 nm. The apparent dissociation constant (K_d) was determined from a plot of normalized fluorescence response versus [Ni^{2+}]. The data were fitted to the following equation: $F = (F_{max}[Ni^{2+}] + F_{min}K_d)/(K_d + [Ni^{2+}])$, where F is the observed fluorescence, F_{max} is the fluorescence for the Ni^{2+}:NS1 complex, and F_{min} is the fluorescence for the free NS1 dye. The Hill coefficient was determined from the slope of the linear least squares fit of $\log[(F_{min}-F_1)/(F_1-F_{max})]$ vs. $\log[Ni^{2+}]$.[40] Ni^{2+} was delivered in the form of $NiCl_2$ x $2H_2O$ from an aqueous stock solution (1, 5, 10, 25, 100, 500 mM). All other metal ions tested for metal ion selectivity studies with the exception of Pb^{2+} and Fe^{2+} were from their chloride salts as aqueous solutions. Pb^{2+} was delivered in the form of aqueous $Pb(NO_3)_2$. Ammonium iron(II) sulfate hexahydrate was used as a source of Fe^{2+}. This salt was dissolved in degassed water, and then aliquots of the stock Fe^{2+} solution were added to a degassed aqueous solution of NS1. The solution was degassed once again before the addition of Ni^{2+}.

Preparation and Staining of Cell Cultures. Cells were grown in the Tissue Culture Facility at the University of California, Berkeley with expert technical assistance from Ann Fischer and Michelle Yasukawa. A549 cells were cultured in Dulbecco's Modified Eagle Medium (DMEM, Invitrogen, Carlsbad, CA) supplemented with 10% Fetal Bovine Serum (FBS, Invitrogen, Carlsbad, CA) and glutamine (2 mM). Two days before imaging, cells were passed and plated on 12-mm glass coverslips coated with poly-L-lysine (50 mg/mL, Sigma, St. Louis, MO). For all experiments, solutions of dyes (from 5 mM stocks in DMSO) were made in HBSS without calcium chloride, magnesium chloride, magnesium sulfate, sodium bicarbonate, or phenol red (HBSS, pH 7.1, Invitrogen, Carlsbad, CA). For nickel treatment, A549 cells were cultured as described above. One day prior to imaging, 1 mM $NiCl_2$ was added to cells from a 0.1 M aqueous stock solution. Cells were then incubated at 37 °C, 5% CO_2. After 18 hours, the media was exchanged for HBSS with 10 μM dye and incubated for 35 min followed by imaging in fresh HBSS.

Fluorescence Imaging Experiments. Confocal fluorescence images were acquired at the Molecular Imaging Center at the University of California, Berkeley. Imaging experiments were performed with a Zeiss LSM510 META/NLO Axioplan 2 laser-scanning microscope and a 40x water-immersion objective lens. Excitation of NS1-loaded cells at 488 nm was carried out with an argon ion laser (37% laser power), and emission was collected in a window from 494 nm—634 nm using a META detection system. Excitation of Hoechst-33342 was carried out using a

MaiTai two-photon laser at 780-nm pulses (36% laser power, mode-locked Ti:sapphire laser, Tsunami Spectra Physics) and emission was collected between 452—538 nm. A 1:1 (v/v) mixture of NS1-AM and Pluronic F-127 (10 μM) and Hoechst-33342 (5 μM) was incubated with live cell samples for 35 min at 37 °C, 5% CO_2. Addition of TPEN (1 mM from a 0.1 M stock in DMSO) was performed directly on the microscope stage. Image analysis was performed in ImageJ.

Schemes and Figures

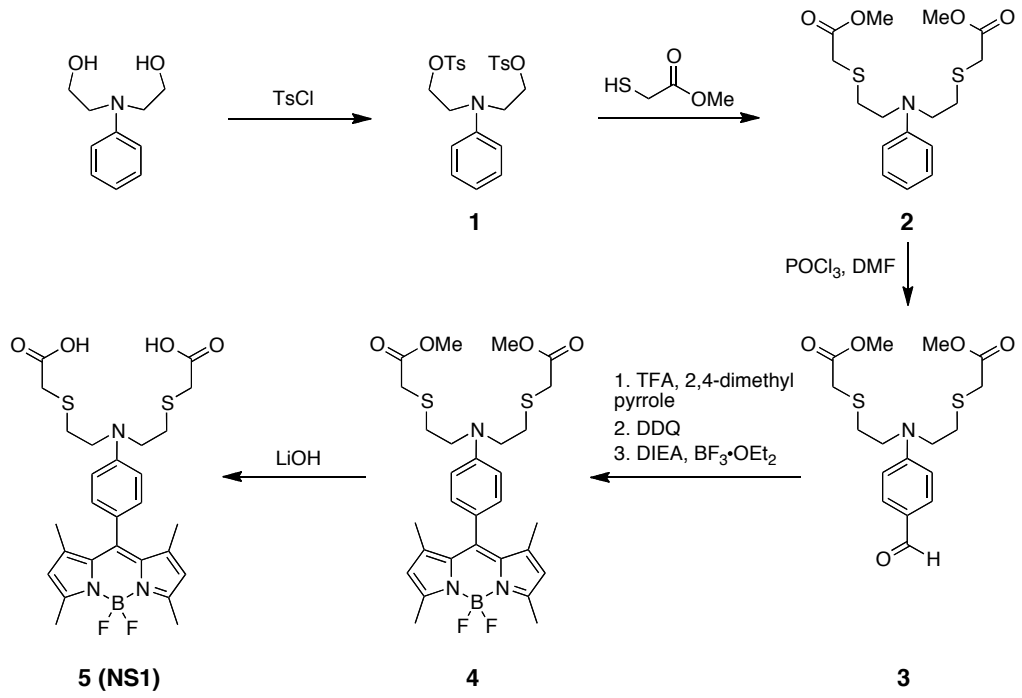

Scheme 1-1. Synthesis of Nickelsesnsor-1 (NS1).

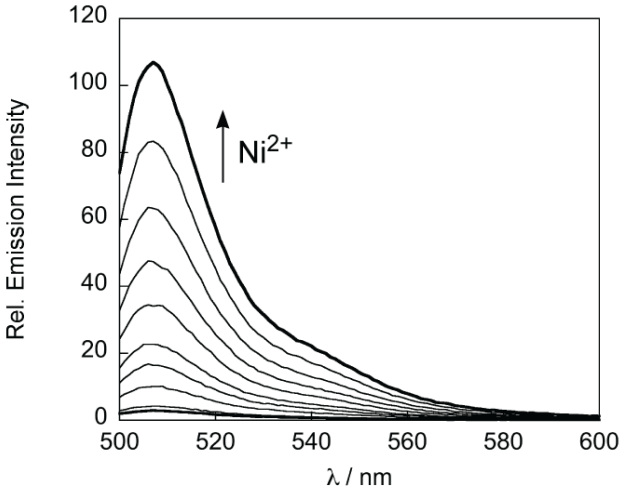

Figure 1-1. Fluorescence response of 2 μM NS1 to Ni^{2+}. Spectra shown are for Ni^{2+} concentrations of 0, 2, 5, 10, 15, 25, 35, 50, 75, 100 μM. Spectra were acquired in 20 mM HEPES, pH 7.1, with 488 nm excitation.

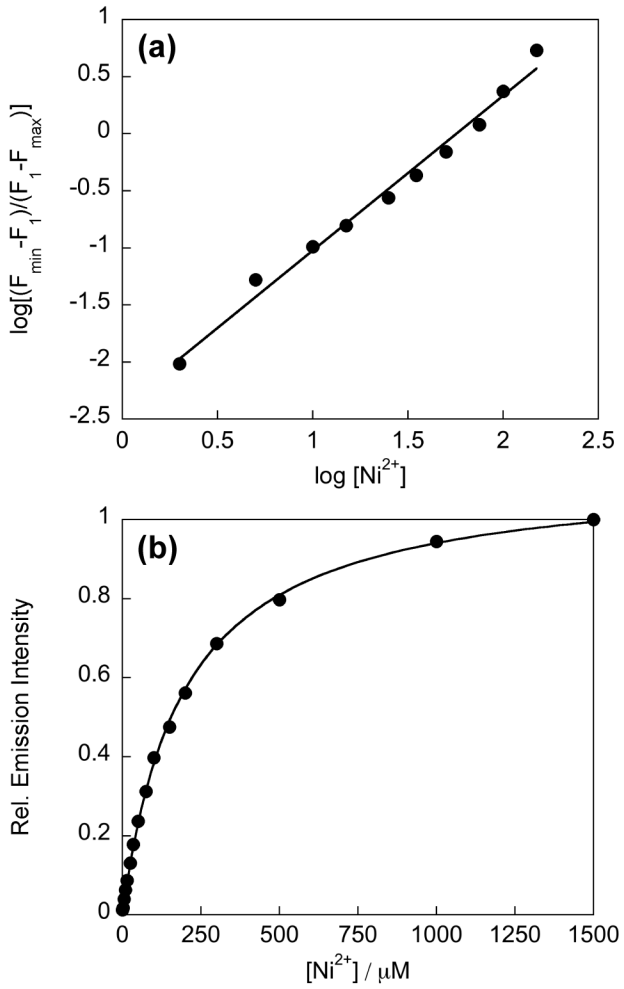

Figure 1-2. (a) Hill plot of the normalized fluorescence responses of 2 μM NS1 to various [Ni^{2+}]. The data points shown are for added Ni^{2+} concentrations of 2, 5, 10, 15, 25, 35, 50, 75, 100, 150 μM, with a slope of 1.36 ± 0.06. Spectra were acquired in 20 mM HEPES, pH 7.1. Excitation was provided at 488 nm and the collected emission was integrated over 498—700 nm. (b) Normalized fluorescence responses of 2 μM NS1 to Ni^{2+} solutions for K_d value determination. Excitation was provided at 488 nm and the collected emission was integrated over 498—700 nm. Spectra were acquired in HEPES, pH 7.1. The data points shown are for Ni^{2+} added at 0, 2, 5, 10, 15, 25, 35, 50, 75, 100, 150, 200, 300, 500, 1000, and 1500 μM. The apparent K_d value is 193 ± 3 μM.

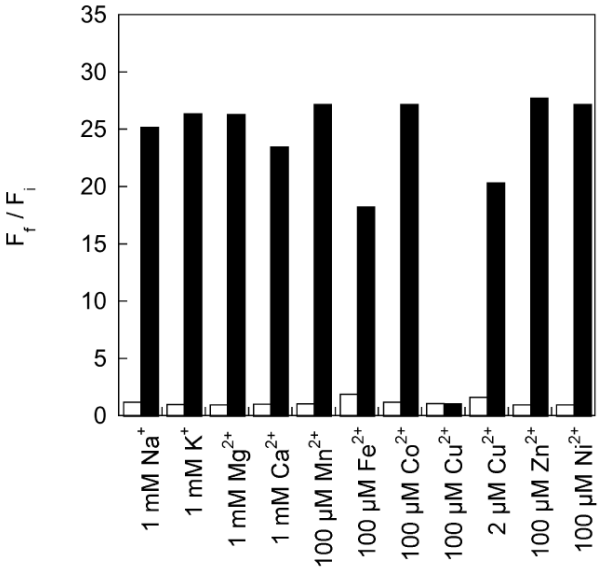

Figure 1-3. Fluorescence responses of 2 μM NS1 to various metal ions. Bars represent the final (F_f) over the initial (F_i) integrated emission. Spectra were acquired in HEPES, pH 7.1. White bars represent the addition of the competing metal ion to a 2 μM solution of NS1. Black bars represent addition of 100 μM Ni^{2+} to the solution. Excitation was provided at 488 nm, with emission integrated over 498—700 nm.

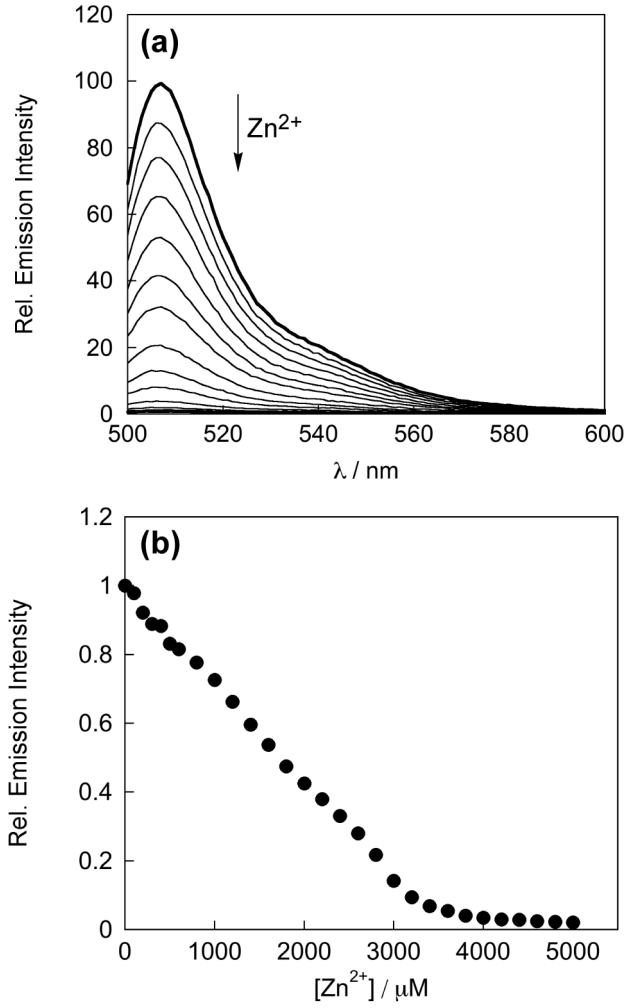

Figure 1-4. (a) Fluorescence response of 2 μM NS1 with 100 μM Ni^{2+} to Zn^{2+}. Spectra are shown for Zn^{2+} concentrations of 0, 400, 800, 1200, 1600, 2000, 2400, 2800, 3000, 3200, 3600, 4000, 4400, and 5000 μM Zn^{2+}. Spectra were acquired in 20 mM HEPES, pH 7.1. Excitation was provided at 488 nm and the collected emission was integrated over 498—700 nm. (b) Normalized fluorescence responses of 2 μM NS1 with 100 μM Ni^{2+} to Zn^{2+} for relative K_d value determination. Excitation was provided at 488 nm and the collected emission was integrated over 498—700 nm. Spectra were acquired in 20 mM HEPES, pH 7.1. The data points shown are for Zn^{2+} added at 0, 100, 200, 300, 400, 500, 600, 800, 1000, 1200, 1400, 1600, 1800, 2000, 2200, 2400, 2600, 2800, 3000, 3200, 3400, 3600, 3800, 4000, 4200, 4400, 4600, 4800, and 5000 μM. The apparent K_d value is 1640 μM.

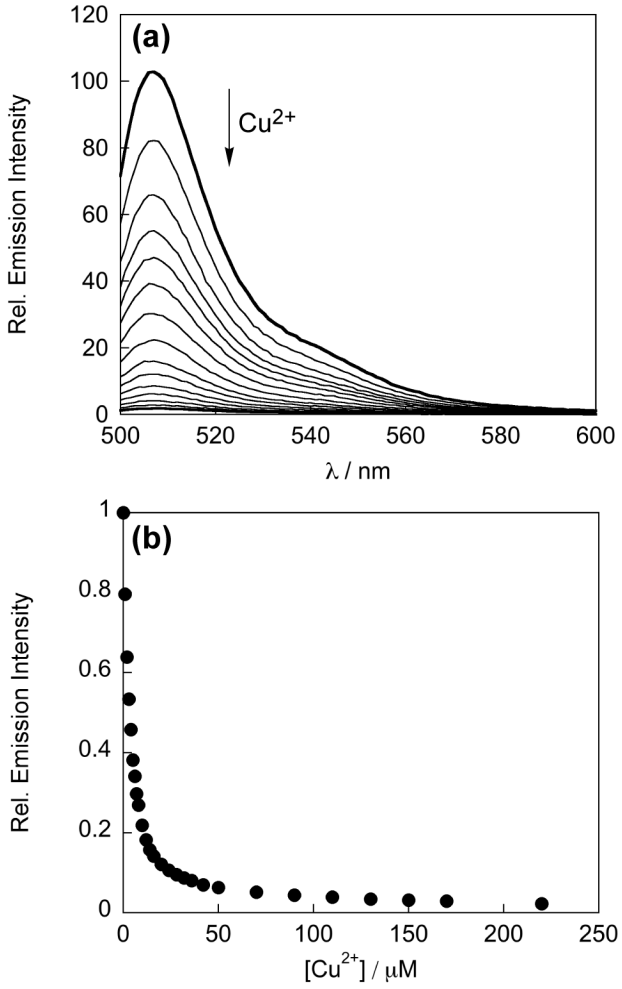

Figure 1-5. Fluorescence response of 2 μM NS1 with 100 μM Ni^{2+} to Cu^{2+}. Spectra are shown for Cu^{2+} concentrations of 0, 1, 2, 3, 4, 5, 7, 10, 14, 20, 32, 50, 90, 150, 220 μM. Spectra were acquired in 20 mM HEPES, pH 7.1. Excitation was provided at 488 nm and the collected emission was integrated over 498—700 nm. (b) Normalized fluorescence responses of 2 μM NS1 with 100 μM Ni^{2+} to Cu^{2+} for relative K_d value determination. Excitation was provided at 488 nm and the collected emission was integrated over 498—700 nm. Spectra were acquired in 20 mM HEPES, pH 7.1. The data points shown are for Cu^{2+} added at 0, 1, 2, 3, 5, 6, 7, 8, 10, 12, 14, 16, 20, 24, 28, 32, 36, 42, 50, 70, 90, 110, 130, 150, 170 and 220 μM. The apparent K_d value is 0.58 μM.

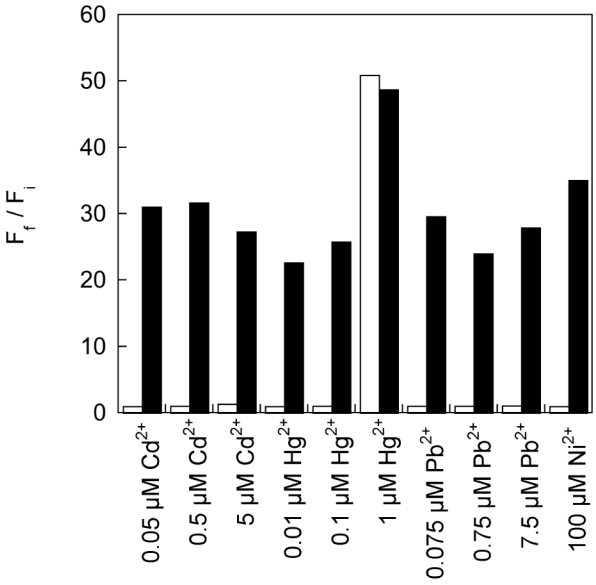

Figure 1-6. Fluorescence responses of 2 μM NS1 to various heavy metal ions. Bars represent the final integrated fluorescence response (F_f) over the initial integrated emission (F_i). Spectra were acquired in 20 mM HEPES, pH 7.1. White bars represent the addition of the maximum allowable EPA level, 10 times the maximum allowable EPA level, and 100 times the maximum allowable EPA level of the competing heavy metal ion to a 2 μM solution of NS1. Black bars represent the addition of 100 μM Ni^{2+} to the solution. Excitation was provided at 488 nm, and the emission was integrated over 498—700 nm.

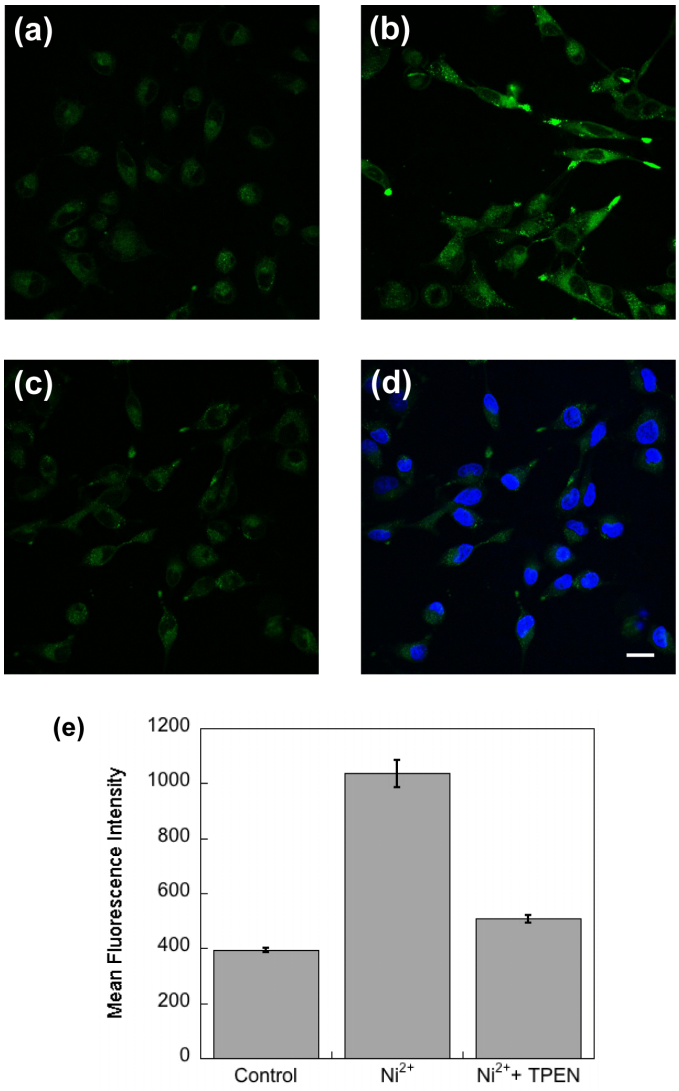

Figure 1-7. Live-cell imaging of intracellular Ni^{2+} levels by confocal microscopy. (a) Control A549 cells incubated with a 1:1 mixture of 10 μM NS1-AM and F-127 Pluronic acid for 35 min at 37 °C. (b) Cells supplemented with 1 mM $NiCl_2$ in the growth medium for 18 h at 37 °C and stained with 10 μM NS1-AM and F-127 Pluronic acid for 35 min at 37 °C. (c) NS1-loaded, 1 mM Ni^{2+}-supplemented cells treated with 1 mM of the divalent metal chelator TPEN for 1 min at 25 °C. (d) NS1-loaded, 1 mM Ni^{2+}-supplemented cells treated with 1 mM TPEN, stained with 5 μM Hoechst-33342 to show cell viability. Scale bar equals 20 μm. (e) Plot of the mean fluorescence intensity of (a)—(c). These data represent the mean fluorescence intensity of at least three fields of cells plotted with standard error.

References

1. Sigel, A.; Sigel, H.; Sigel, R. K. O., Eds. *Nickel and Its Surprising Impact in Nature*; John Wiley & Sons Ltd.: England, 2007; Vol. 2.
2. Chivers, P. T.; Sauer, R. T. *Protein Sci.* **1999**, *8*, 2494—2500.
3. Dosanjh, N. S.; Michel, S. L. *Curr. Opin. Chem. Biol.* **2006**, *10*, 123—130.
4. Giedroc, D. P.; Arunkumar, A. I. *Dalton Trans.* **2007**, 3107—3120.
5. Hausinger, R. P.; Zamble, D. B. In *Molecular Microbiology of Heavy Metals* (Nies, D. H.; Silver, S., Eds.); Springer: Heidelberg, Germany, 2007, 287—320.
6. Wang, S. C.; Dias, A. V.; Zamble, D. B. *Dalton Trans.* **2009**, 2459—2466.
7. Carrington, P. E.; Chivers, P. T.; Al-Mjeni, F.; Sauer, R. T.; Maroney, M. J. *Nat. Struct. Biol.* **2003**, *10*, 126—130.
8. Schreiter, E. R.; Sintchak, M. D.; Guo, Y.; Chivers, P. T.; Sauer, R. T.; Drennan, C. L. *Nat. Struct. Biol.* **2003**, *10*, 794—799.
9. Phillips, C. M.; Schreiter, E. R.; Guo, Y.; Wang, S. C.; Zamble, D. B.; Drennan, C. L. *Biochemistry* **2008**, *47*, 1938—1946.
10. Iwig, J. S.; Leitch, S.; Herbst, R. W.; Maroney, M. J.; Chivers, P. T. *J. Am. Chem. Soc.* **2008**, *130*, 7592—7606.
11. Maroney, M. J. *Curr. Opin. Chem. Biol.* **1999**, *3*, 188—199.
12. Drennan, C. L.; Doukov, T. I.; Ragsdale, S. W. *J. Biol. Inorg. Chem.* **2004**, *9*, 511—515.
13. Evans, D. J. *Coord. Chem. Rev.* **2005**, *249*, 1582—1595.
14. Fontecilla-Camps, J. C.; Volbeda, A.; Cavazza, C.; Nicolet, Y. *Chem. Rev.* **2007**, *107*, 4273—4303.
15. Lindahl, P. A. *Angew. Chem., Int. Ed. Engl.* **2008**, *47*, 4054—4056.
16. Ragsdale, S. W. *J. Biol. Chem.* **2009**, *284*, 18571—18575.
17. Xia, W.; Li, H.; Sze, K. H.; Sun, H. *J. Am. Chem. Soc.* **2009**, *131*, 10031—10040.
18. Goodman, J. E.; Prueitt, R. L.; Dodge, D. G.; Thakali, S. *Crit. Rev. Toxicol.* **2009**, *39*, 365—417.
19. Costa, M.; Davidson, T. L.; Chen, H.; Ke, Q.; Zhang, P.; Yan, Y.; Huang, C.; Kluz, T. *Mutat. Res.* **2005**, *592*, 79—88.
20. Nemec, A. A.; Leikauf, G. D.; Pitt, B. R.; Wasserloos, K. J.; Barchowsky, A. *Am. J. Respir. Cell Mol. Biol.* **2009**, *41*, 69—75.
21. Domaille, D. W.; Que, E. L.; Chang, C. J. *Nat. Chem. Biol.* **2008**, *4*, 168—175.
22. Que, E. L.; Domaille, D. W.; Chang, C. J. *Chem. Rev.* **2008**, *108*, 1517—1549.
23. Torrado, A.; Walkup, G. K.; Imperiali, B. *J. Am. Chem. Soc.* **1998**, *120*, 609—610.
24. Pearce, D. A.; Walkup, G. K.; Imperiali, B. *Bioorg. Med. Chem. Lett.* **1998**, *8*, 1963—1968.
25. Salins, L. L.; Goldsmith, E. S.; Ensor, C. M.; Daunert, S. *Anal. Bioanal. Chem.* **2002**, *372*, 174—180.
26. Wang, B. Y.; Hu, Y. L.; Su, Z. X. *React. Funct. Polym.* **2008**, *68*, 1137—1143.
27. Wang, B. Y.; Liu, X. Y.; Hu, Y. L.; Su, Z. X. *Polym. Int.* **2009**, *58*, 703—709.
28. Fabbrizzi, L. L., M.; Pallavicini, P.; Perotti, A.; Taglietti, A.; Sacchi, D. *Chem. Eur. J.* **1996**, *2*, 75—82.
29. Bolletta, F.; Costa, I.; Fabbrizzi, L.; Licchelli, M.; Montalti, M.; Pallavicini, P.; Prodi, L.; Zaccheroni, N. *J. Chem. Soc., Dalton Trans.* **1999**, 1381—1385.
30. Jiang, L. J.; Luo, Q. H.; Wang, Z. L.; Liu, D. J.; Zhang, Z.; Hu, H. W. *Polyhedron* **2001**, *20*, 2807—2812.

31. Ke, Q.; Davidson, T.; Kluz, T.; Oller, A.; Costa, M. *Toxicol. Appl. Pharmacol.* **2007**, *219*, 18—23.
32. Thierse, H. J.; Helm, S.; Pink, M.; Weltzien, H. U. *J. Immunol. Methods* **2007**, *328*, 14—20.
33. Zhao, J.; Bertoglio, B. A.; Devinney, M. J., Jr.; Dineley, K. E.; Kay, A. R. *Anal. Biochem.* **2009**, *384*, 34—41.
34. Cadosch, D.; Meagher, J.; Gautschi, O. P.; Filgueira, L. *J. Neurosci. Methods* **2009**, *178*, 182—187.
35. Chen, H.; Costa, M. *Exp. Biol. Med.* **2006**, *231*, 1474—1480.
36. dos Santos, D. F.; Argentini, M.; Weinreich, R.; Hansen, H. J. *Helv. Chim. Acta.* **2000**, *83*, 2926—2938.
37. Yoon, S.; Albers, A. E.; Wong, A. P.; Chang, C. J. *J. Am. Chem. Soc.* **2005**, *127*, 16030—16031.
38. Yoon, S.; Miller, E. W.; He, Q.; Do, P. H.; Chang, C. J. *Angew. Chem., Int. Ed. Engl.* **2007**, *46*, 6658—6661.
39. Brannon, J. H.; Magde, D. *J. Phys. Chem.* **1978**, *82*, 705—709.
40. Hill, A. V. *J. Physiol.* **1910**, *40*, 389—403.

Chapter 2:

Calcium Dependent Copper Redistributions in Neuronal Cells Revealed by a Fluorescent Copper Sensor and X-ray Fluorescence Microscopy

Abstract

Dynamic fluxes of s-block metals like potassium, sodium, and calcium are of broad importance in cell signaling. In contrast, the concept of mobile transition metals triggered by cell activation remains insufficiently explored, in large part because metals like copper and iron are typically studied as static cellular nutrients and there are a lack of direct, selective methods for monitoring their distributions in living cells. To help meet this need we now report Coppersensor-3 (CS3), a bright new small-molecule fluorescent probe that offers the unique capability to image labile copper pools in living cells at endogenous, basal levels. We use this new chemical tool in conjunction with synchotron-based microprobe X-ray fluorescence microscopy (XRFM) to discover that neuronal cells move significant pools of copper from their cell bodies to peripheral processes upon their activation. Moreover, further CS3 and XRFM imaging experiments show that these dynamic copper redistributions are dependent on calcium release, establishing a link between mobile copper and major cell signaling pathways. By providing the first small-molecule fluorophore that is selective and sensitive enough to image labile copper pools in living cells under basal conditions, CS3 opens new opportunities for discovering and elucidating functions of copper in living systems.

Introduction

Metals are essential components of all living cells and in many cases cells trigger and utilize dynamic metal movements for signaling purposes. Such processes are well established for alkali and alkaline earth metals like potassium, sodium, and calcium (1-3) but not for transition metals like copper and iron, which are traditionally studied for their roles as static cofactors in enzymes (4, 5, 6). We have initiated a program aimed at exploring the concept of mobile transition metals and their contributions to cell physiology and pathology, and in this context, brain neurons offer an attractive model for this purpose owing to their widespread use of potassium and sodium ion channels and calcium release for signaling events (7), as well as a high requirement for copper and iron to meet their steep oxidative demand (8-12). Indeed, the brain needs much higher levels of copper compared to other parts of the body under normal physiological conditions (9, 12), but at the same time mishandling of neuronal copper stores and subsequent oxidative stress and damage events are connected to a variety of neurodegenerative ailments, including Menkes and Wilson's diseases (13, 14), Alzheimer's disease (15-17), familial amyotrophic lateral sclerosis (fALS) (18, 19), and prion-mediated encephalopathies (20, 21). Previous work hints at the importance of exchangeable copper in neurophysiology, including observations of ^{64}Cu efflux from stimulated neurons (22, 23), export of Cu from isolated synaptosomes (24), and elevated susceptibility of neurons to excitotoxic insult with copper chelation (25), but none of these reports show direct, live-cell monitoring of spatial copper distributions during various stages of neural activity.

Along these lines, molecular imaging with copper-responsive fluorescent sensors offers a potentially powerful methodology for interrogating its cell biology by allowing the specific tracking of copper pools in living cells with spatial and temporal resolution (12, 26-32). In this regard, analogous tools have revolutionized the study of calcium in a variety of biological settings (1) and hold promise for interrogating other cellular metals (26). However, fluorescence-based sensing of Cu^{+}, the oxidation state stabilized in reducing cytosolic environments, presents several additional challenges that make it more difficult to detect compared to other abundant

metal ions in cells (e.g. Na^+, K^+, Ca^{2+}, Mg^{2+}, Zn^{2+}). The most prominent of these challenges include (i) redox specificity over Cu^{2+}, the other major oxidation state for biological copper, (ii) the propensity for Cu^+ in water to disproportionate to Cu^{2+} and Cu metal, and (iii) the ability of Cu^+ to quench fluorescence by electron and/or energy transfer. Indeed, of the growing number of reported strategies for fluorescence copper detection (12, 26), only three synthetic sensors, CTAP-1 (29), CS1 (30, 31), and RCS1 (32), and two protein-based sensors (33, 34) have been validated for live-cell imaging with Cu^+. Moreover, the relatively low quantum efficiencies of the first-generation synthetic reagents ($\Phi \leq 0.14$ in Cu^+-bound forms) have limited their use to date for cellular imaging under conditions of prolonged copper overload or depletion.

Here we present the synthesis, properties, and applications of Coppersensor-3 (CS3) (Figure 2-1), a bright new fluorescent sensor that now offers the unique ability to detect labile copper pools at basal, endogenous levels in living cells. This BODIPY-based probe features high selectivity over competing cellular metal ions, including redox differentiation between Cu^+ and Cu^{2+}, visible wavelength excitation and emission profiles, and a 75-fold fluorescence turn-on response with high quantum efficiency ($\Phi = 0.40$) for Cu^+ detection. By using this new chemical tool in conjunction with synchotron-based microprobe X-ray fluorescence microscopy (microXFM) in a combined imaging study, an approach that has been successfully employed for monitoring resting copper distributions in mammalian cells (29), we have discovered that neuronal cells trigger a marked translocation of copper pools from their cell bodies to extended outer processes when activated by depolarization. Moreover, additional CS3 and microXFM studies show that these dynamic copper movements are dependent on the release of calcium, establishing a link between mobile copper and major cell signaling pathways. The combined advances in optical brightness and turn-on response for CS3 afford a host of new opportunities for studying the cell biology of copper by providing the ability to visualize labile copper pools in living cells under basal and stimulated conditions.

Results and Discussion

The design, synthesis, and spectroscopic evaluation of CS3 are presented in Dylan W. Domaille's dissertation and in our publication (35). Here, owing the thioether groups in the sensor, I present a panel of trace soft heavy metal ions for selectivity studies, including Hg^{2+}, Ag^+, Tl^+, and Pb^{2+} (6) (Figure 2-2). Of these heavy metal ions, CS3 does show some turn-on response to Ag^+ at high, non-physiological levels, but the addition of Cu^+ reveals that Cu^+ can displace Ag^+ from the sensor. The large fluorescent turn-on response of CS3 to Cu^+, in conjunction with its high selectivity in the presence of interfering ions, suggests that this novel tool is a promising reagent for imaging basal levels of exchangeable Cu^+ pools in living cells.

The two previously reported turn-on small-molecule fluorescent probes for live-cell Cu^+ detection, CTAP-1 and CS1, are capable of detecting changes in labile intracellular copper levels, but their relatively low quantum efficiencies limits their use to visualizing differences under situations of acute or prolonged copper overload (29, 30). We reasoned that CS3, with its improved brightness and turn-on response to Cu^+, would provide the new ability to report pools of intracellular, exchangeable Cu^+ at basal levels. We therefore sought to test whether this new chemical tool could image labile copper stores under both basal and copper-depleted conditions. To this end we depleted cells of their endogenous copper stores by culturing them in media containing the membrane-impermeable chelator bathocuproine disulfonate (BCS). This treatment

has been shown to mildly decrease copper levels within mammalian cells without compromising their viability (36). Accordingly, human embryonic kidney (HEK 293T) cells were grown either in normal media or in media containing 200 μM BCS for 20 h to make them copper depleted, stained with 2 μM CS3 for 10 min, and subsequently imaged by confocal microscopy (Figure 2-3). Cells grown in normal control media exhibit markedly higher fluorescence signals compared to cells grown in the presence of BCS (Figure 2-3A, 2-3B), indicating that CS3 can respond to changes in basal, endogenous levels of exchangeable Cu^+ as well as sense differences between copper-depleted and copper-normal conditions. To provide further support that BCS targets copper selectively, we treated HEK 293T cells with BCS and then stained them with the Zn^{2+}-responsive dye FluoZin-3 AM. We find that the zinc levels as measured by the zinc probe are not statistically different in the BCS treated cells relative to the control (Figure 2-5). In addition, we treated HEK 293T cells with BCS and imaged total metal pools by X-ray fluorescence microscopy (XRFM). We find that copper levels are significantly decreased in BCS treated cells relative to control cells, whereas phosphorus and zinc show the opposite trend (Figure 2-6).

We also examined whether CS3 could report more acute changes in exchangeable intracellular copper pools by treating cells with 100 μM of the competing cell-permeable Cu^+-chelator tris((ethylthio)ethylamine) (TEMEA) and CS3 for 10 min. (Figure 2-3C). The observed fluorescence signal was muted upon introduction of this competing copper ligand, indicating that CS3 responds reversibly to Cu^+ and can sense dynamic variations in kinetically labile Cu^+ pools in living mammalian cells. In addition, nuclear staining with Hoechst 33342 affirms that the viability of HEK 293T cells is not affected by CS3 staining or the manipulation of cellular copper status

With data showing that CS3 is capable of reporting dynamic changes in endogenous intracellular Cu^+ stores by molecular imaging and that this probe is sensitive enough to visualize labile pools under basal conditions, we then sought to use this new chemical tool to probe copper homeostasis in brain neurons. To this end, live hippocampal dissociated cultured neurons stained with 2 μM CS3 show a diffuse fluorescent signal pattern, localized mainly in the soma (Figure 2-7A). To evaluate the spatial distributions of labile Cu^+ pools in these neuronal cells under basal conditions, we measured the emission intensity ratio of dendritic copper to somatic copper regions (D_{Cu}:S_{Cu}). Quantification of the dendritic and somatic fluorescence intensity signals provides a D_{Cu}:S_{Cu} ratio signal of 0.24 ± 0.04 in these resting neurons.

We then moved on to characterize the distribution of labile copper pools in activated neuronal cells. Interestingly, we observed that neurons treated with 50 mM KCl for 2 min to induce their depolarization and stained with 2 μM CS3 show a marked redistribution of labile copper pools from their somatic cell bodies to peripheral processes, quantified by a patent increase in D_{Cu}:S_{Cu} ratio to 0.35 ± 0.04 (Figure 2-7E). These imaging data, which provide the first direct evidence that the spatial distributions of copper change upon neuronal activation, suggest that the redistribution of labile copper pools might be a result of a rise in dendritic levels and/or a decrease in somatic levels.

To study mobile copper in neuronal cells using an independent technique as well as verify our CS3-based molecular imaging results, we performed X-ray fluorescence microscopy (XRFM) experiments at the Advanced Photon Source of the Argonne National Laboratory. XRFM affords, without any added reagents, a direct method for measuring total copper and other element distributions by their synchotron-induced X-ray fluorescence signatures (29, 37-40). In particular, the instrument at the 2-ID-E beamline at the Advanced Photon Source of the Argonne

National Laboratory boasts a spatial resolution of 200 nm, which makes it appropriate for examining the subcellular elemental distributions of single cells (41). We emphasize that the XRFM method measures total element content on fixed samples, thus providing a complementary approach to live-cell imaging of labile metal pools using fluorescent sensors. Moreover, the combination of small-molecule fluorescence imaging and XRFM has been exploited previously to provide a coherent picture of copper homeostasis in resting mammalian cells, setting the stage for studies of copper homeostasis in dynamic and stimulated situations in the present study (26, 27).

For the XRFM experiments, we utilized the same types of hippocampal neurons employed for the live-cell CS3 imaging studies but cultured on silicon nitride windows. These neuronal cell cultures were incubated either in buffer for 2 min as a baseline control or in buffer supplemented with 50 mM KCl to trigger their depolarization. The cells were then promptly fixed with paraformaldehyde and examined by XRFM (Figure 2-7). The elemental maps of total copper, zinc and phosphorus pools are shown for baseline control neurons treated with buffer prior to fixation (Figure 2-7B, 2-7C, 2-7D). Phosphorus and zinc signals are concentrated in the nuclear region, whereas copper maintains a perinuclear distribution pattern located primarily in the somatic cell body, consistent with the results obtained from the live-cell CS3 imaging studies. Also in line with the CS3 imaging data, neurons depolarized with 50 mM KCl show a significant change in cellular copper signal that is more diffuse in the depolarized brain cells compared to resting ones (Figure 2-7F, 2-7G, 2-7H), with copper pools displaying a marked redistribution from the cell body to peripheral processes. In contrast to the copper channel, similar elemental distributions of phosphorus and zinc are observed in the KCl-depolarized neurons compared to their unstimulated counterparts, revealing the relative mobility of copper pools in this model under these conditions. Quantification of the dendritic:somatic copper ratio from XRFM data collected from multiple APS beam runs over four years shows a statistically significant increase in KCl-stimulated neurons (0.84 ± 0.04) compared to basal, untreated neurons (0.54 ± 0.07) (Figure 2-7J). Taken together, the CS3 and XRFM imaging experiments provide two independent methods that have allowed us to discover and establish that brain neurons trigger movements of intracellular copper pools upon their activation, causing a significant redistribution of neuronal copper stores from their somatic cell bodies to peripheral processes.

We next used CS3-based molecular imaging and XFRM to probe the effects of intracellular calcium release, a primary consequence of depolarization-induced neural activity, on the observed cellular copper movements. Multiple and distinct types of treatments to alter calcium release, including direct metal chelation or inhibition of cellular calcium entry channels or intracellular receptors, support a relationship between mobile copper and calcium signaling in this model.

First, intracellular calcium rises in neurons were blocked by treatment with the established intracellular Ca^{2+} chelator BAPTA, delivered in its membrane-permeable acetoxymethyl form BAPTA-AM; this prochelator undergoes rapid hydrolysis by intracellular esterases to produce BAPTA (42). As shown in Figure 2-8, Ca^{2+} chelation prevents KCl-induced redistribution of neuronal copper pools, as the observed D_{Cu}:S_{Cu} ratio in BAPTA-AM-treated, KCl-depolarized neurons is similar to unstimulated samples as measured by CS imaging. The collective data provide evidence that transient elevation of intracellular calcium levels is required

upstream of depolarization-induced copper translocation and provide a link between mobile copper and calcium, a major modulator of cell signaling pathways.

We then performed XRFM experiments to independently establish that calcium signaling is required to trigger activity-dependent copper movements in these neuronal cell models. Neurons were pre-treated with BAPTA-AM and either mock treated with BAPTA-containing buffer for 2 min or with buffer containing 50 mM KCl and 10 μM BAPTA. Notably, the XRFM images directly show that the levels and distributions of cellular copper are not perturbed by BAPTA treatment. Moreover, XRFM analysis of these cells indicated no significant differences in copper distributions between cells that had been treated with only buffer (Figure 2-8B, 2-8C, 2-8D) or cells that had been depolarized (Figure 2-8F, 2-8G, 2-8H). These results, in conjunction with the CS3-imaging of live neurons, reinforce the link between calcium signaling and mobile copper pools in brain cell systems.

In further support of the aforementioned experiments, we then proceeded to alter calcium signaling pathways using reagents that are not metal chelators. First, we added dantrolene, a well-established drug that decreases intracellular calcium levels by binding to the ryanodine receptor (43, 44). As shown in Figure 2-9, dantrolene also blocks KCl-induced redistribution of neuronal copper pools, as the observed D_{Cu}:S_{Cu} ratio in dantrolene-treated, KCl-depolarized neurons is similar to unstimulated samples as monitored by CS imaging. Next, we added nifedipine, a classic dihydropyridine calcium channel blocker that inhibits transmembrane flux of extracellular calcium ions (44). Unlike the dantrolene and BAPTA treatments, nifedipine at this dose does not diminish the KCl-induced mobilization of labile copper pools to the same extent. Finally, the combined application of both dantrolene and nifedipine also abolishes the depolarization-triggered soma-to-dendrite movements of neuronal copper. By showing that interfering with calcium entry or intracellular receptor pathways can also block depolarization-induced movements of neuronal copper, these additional lines of evidence provide further support for a link between mobile copper and calcium signaling.

Concluding Remarks

Dynamic metal fluxes triggered by physiological stimulation are well established for alkali and alkaline earth metals like potassium, sodium, and calcium in a wide range of cell types but are insufficiently explored for transition metals. In this work, we utilize a new fluorescent sensor and XRFM imaging to directly show that movements of copper pools are triggered by cell activation in a neuronal model, suggesting that this transition metal nutrient can also participate as a dynamic component for essential physiological functions. Indeed, cellular copper uptake and release is kinetically rapid (45) and growing evidence highlights the importance of orchestrating transient copper accumulation, compartmentalization, and efflux events within subcellular compartments at a molecular level (13, 28, 46-51). The brain's high copper demand, along with growing connections between copper misregulation and neurodegenerative diseases, point to the particular importance of understanding copper homeostasis in this unique biological system.

In this report, we have presented CS3, a new fluorescent sensor where improvements in turn-on response and quantum efficiency give this probe a unique ability to monitor labile copper pools in living cells at basal and copper-depleted conditions. We have used this new chemical probe in conjunction with XRFM in a combined imaging study to discover that neuronal cells move significant pools of copper from their somatic cell bodies to extended outer processes

when activated by depolarization. Moreover, additional CS3 and XRFM imaging experiments establish that the observed copper redistributions are dependent on calcium release, showing that mobile copper is linked to a major hub of cell signaling pathways and presages a wide range of possibilities for exploring copper and calcium crosstalk.

The ability to directly monitor mobile pools of copper during different stages of neuronal cell activity highlights the combined use of live-cell molecular imaging for visualizing exchangeable copper pools along with XRFM to characterize total copper content as a synergistic approach to study metal homeostasis in a native cellular context. Our findings, taken together with previous reports showing accumulation of mitochondria to neuronal filopodia and dendritic spines upon repeated depolarization (52), reversible trafficking of the P-type ATPase ATP7A from the perinuclear trans-Golgi to neuronal processes by NMDA receptor activation (23), and axonal localization of ATP7A potentially involved in process guidance (53, 54) point to the intriguing possibility that subcellular compartmentalization and transient reorganization of copper stores is essential to tuning dynamic neuronal activity. Furthermore, the requirement for calcium release to trigger copper movements provides an entry for connecting copper to canonical signal transduction pathways. We are actively pursuing an understanding of mobile copper as a potential new metal signal in the context of neuronal activity and other fundamental physiological processes.

Experimental Section

Synthetic Materials and Methods. The synthetic materials and methods for CS3 are described in Dylan W. Domaille's dissertation and in our publication (35). Tris((ethylthio)ethyl)amine (TEMEA) was synthesized according to literature procedures (30, 55). Hoechst 33342, Fluo-Zin3-AM, and Pluronic F-127 were purchased from Invitrogen. All other chemicals were purchased from Sigma-Aldrich and used as received.

Spectroscopic Materials and Methods. The spectroscopic materials and methods for CS3 are described in Dylan W. Domaille's dissertation and in our publication (35). Millipore water was used to prepare all aqueous solutions. Heavy metal ion selectivity was performed in 20 mM HEPES buffer, pH 7. Copper (Cu^+) was delivered in the form of $[Cu(MeCN)_4][PF_6]$ from an acetonitrile stock solution (2 mM). Heavy metals were delivered in the form of $HgSO_4$, $AgSO_4$, $PbCl_2$, Tl_2SO_4 from an aqueous stock solution (2 mM). Excitation of 4 μM CS3 (2 mM DMSO stock) was provided at 530 nm and collected emission was integrated from 540 to 700 nm. Fluorescence spectra were recorded using a Photon Technology International Quanta Master 4 L-format scan spectrofluorometer equipped with an LPS-220B 75-W xenon lamp and power supply, A-1010B lamp housing with integrated igniter, switchable 814 photocounting/analog photomultiplier detection unit, and MD5020 motor driver. Samples for absorption and emission measurements were contained in 1-cm x 1-cm path length quartz cuvettes (1.4-mL or 3.5-mL volume, Starna).

Cell Culture. HEK 293Tcells were cultured in Dulbecco's modified Eagle medium (DMEM, Invitrogen) supplemented with 10% fetal bovine serum (Invitrogen) and glutamine (2 mM). Three days before imaging, cells were passed and plated in 4-well chambered coverglass slides coated with poly-L-lysine (50 μg⁄mL, Sigma). Dissociated embryonic rat hippocampal neurons (DIV 12–20) were plated at 200,000 cells mL^{-1} on 12-mm poly-L-lysine-coated coverslips in

serum-containing medium. All animal care and experimental protocols were approved by the Animal Care and Use Committee at the University of California, Berkeley.

Live-Cell Imaging. Confocal fluorescence imaging was performed with a Zeiss LSM 710 laser-scanning microscope, a 40x water-immersion objective lens, and at 37 °C with 5% CO_2 for the HEK 293T cells. Confocal fluorescence imaging was performed with a Zeiss LSM 510 NLO Axiovert 200 laser-scanning microscope and a 40x or 63x water-immersion objective lens for the rat hippocampal neurons. HEK 293T cells were treated with a water vehicle or BCS and a DMSO vehicle or TEMEA for chelator experiments. HEK 293T cells were loaded with CS3 (2 μM, 10 min) and Hoechst 33342 (5 μM, 10 min) in DMEM at 37 °C, washed and imaged in fresh DMEM, and excited at 543 nm with a HeNe laser for CS3 and excited at 405 nm with a diode laser for Hoechst 33342. For experiments with FluoZin-3, HEK 293T cells were stained with FluoZin-3 (2 μM, 10 min) and Pluronic F-127 (vol/vol) and Hoechst 33342 (5 μM, 10 min) in DMEM at 37 °C, washed and imaged in fresh DMEM, and excited at 488 with an Ar laser. The median fluorescence intensity of each field of cells was measured in ImageJ, the mean was calculated, and a two-tailed Student's t-test was used to establish statistical significance. Rat hippocampal neurons (DIV 14–20) were incubated in either extracellular solution (ECS) buffer (23) or ECS buffer containing 50 mM KCl for 2 min. The solution was aspirated and washed with ECS containing MgCl2, and incubated with CS3 (2 μM, 10 min) In studies of neurons with calcium chelation, neurons were incubated with 10 μM BAPTA-AM for 30 min in media at 37 °C. The media was aspirated, and ECS buffer containing 10 μM BAPTA-AM or ECS buffer with 10 μM BAPTA-AM with 50 mM KCl was added. The neurons were allowed to sit in this solution for 2 min, at which point the buffer was removed and ECS with $MgCl_2$ added and the cells were incubated with CS3 (2 μM, 10 min). Neurons were imaged identically to HEK cells, except z stacks were acquired with a 1-μm slice thickness. Images of neurons were subjected to a blinded quantification with ImageJ, wherein the fluorescence intensity in a user-defined dendrite and soma region was measured to determine the dendrite: soma CS3-ratio. Neuron studies with dantrolene and nifedipine treatments were carried out using DIV 12 cells. Coverslips containing neurons were washed once with ECS and then incubated with 30 μM dantrolene (30 mM stock in DMSO) and/or 100 μM nifedipine (100 mM stock in DMSO) for 10 min in ECS buffer at 37 °C. For KCl-treated cells, the KCl concentration was adjusted to 90 mM, and the cells were incubated for 2 min at 37 °C. After their respective treatments, all coverslips were washed with ECS (three times) and stained with CS3 (2 μM, 10 min) at room temperature. Neurons were subsequently washed with ECS containing $MgCl_2$ (three times) and imaged.

X-Ray Fluorescence Microscopy (XRFM) Samples. HEK 293T cells and rat hippocampal neurons were plated on poly-L-lysine coated silicon nitride windows (2 × 2 mm; thickness 500 nm) manufactured by Silson. After the treatments indicated in the text, cells were fixed in 4% paraformaldehyde (PFA) in PBS for 10 min. Residual PBS was removed by several washes in 20 mM PIPES, pH 7.2⁄200 mM sucrose followed by air drying. X-ray imaging was carried out with the scanning X-ray microprobe at beamline 2-ID-E at the Advanced Photon Source (Argonne National Laboratory) as previously describe (56).

Schemes and Figures

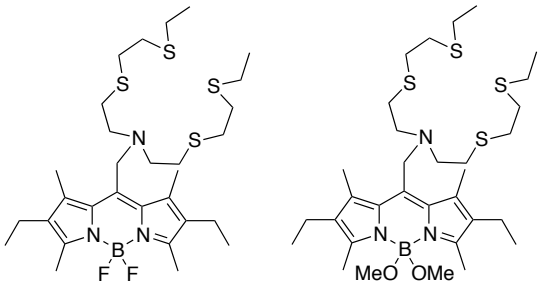

Figure 2-1. Structures of Coppersensor-1 (CS1) and Coppersensor-3 (CS3).

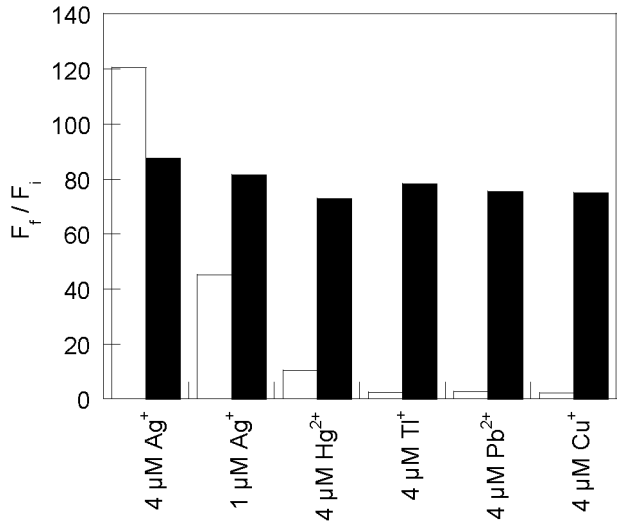

Figure 2-2. Fluorescence responses of CS3 to various heavy metal ions. Bars represent the final integrated fluorescence response (F_f) over the initial integrate emission (F_i). White bars represent the addition of the competing metal ion to a 4 µM solution of CS3. Black bar represent the subsequent addition of 4 µM Cu^+ to the solution. Excitation was provided at 530 nm, and the collected emission was integrated over 540—700 nm.

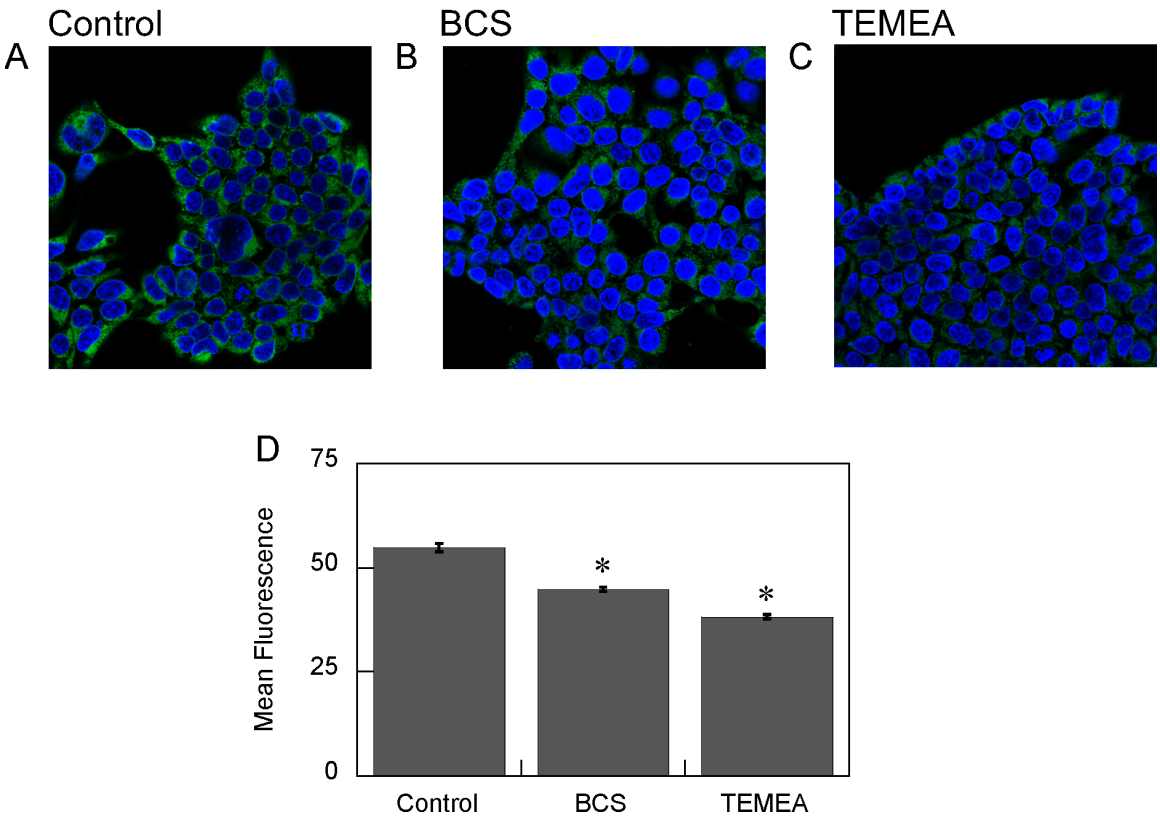

Figure 2-3. Molecular imaging of endogenous basal Cu in HEK 293T cells with CS3. (a) Control HEK 293T cells, (b) HEK 293T cells supplemented with 200 μM BCS in the growth medium for 20 h at 37 °C, and (c) HEK 293T cells treated with 100 μM TEMEA for 10 min were stained with 2 μM CS3, 5 μM Hoechst 33342, and DMSO vehicle for TEMEA for 10 min at 37 °C in DMEM. (d) Graph showing the quantification of mean fluorescence intensity of each condition normalized to the control condition (n = 5 fields of cells per condition). Error bars represent the SEM. Asterisk (*) indicates $P < 0.01$ compared to control cells.

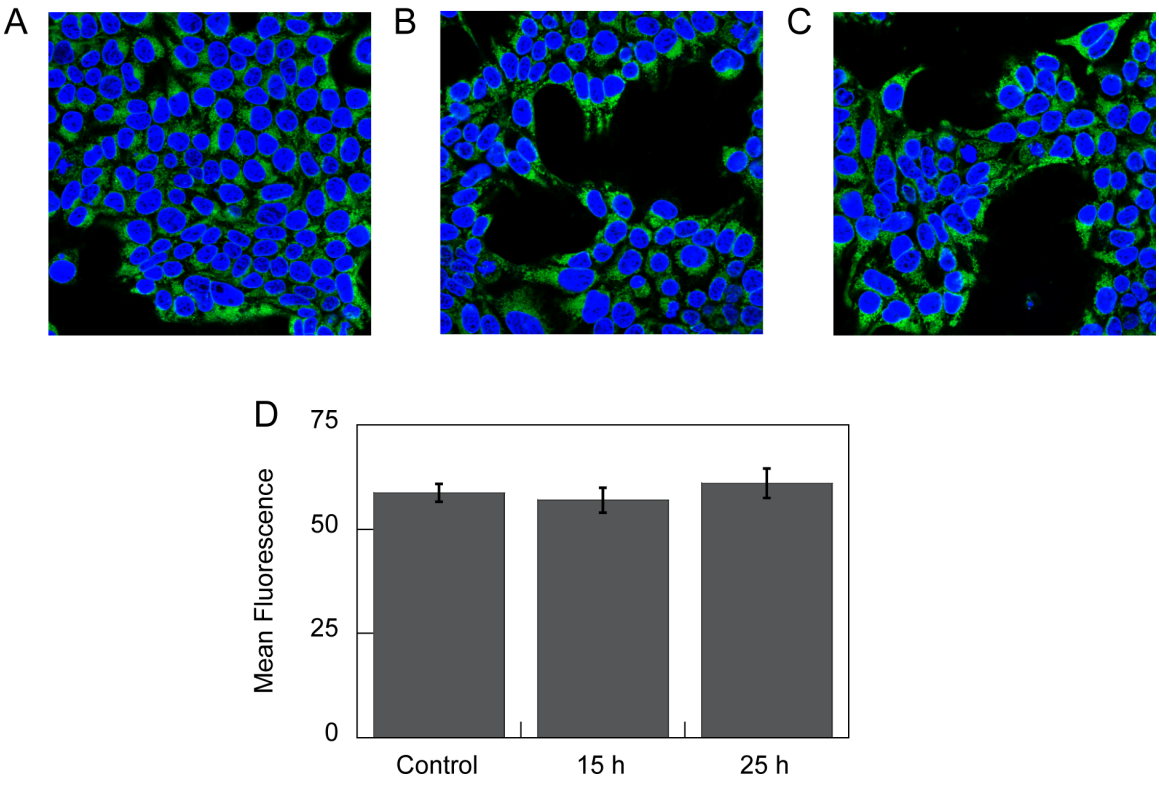

Figure 2-4. Molecular imaging of vehicle alone treated HEK 293T cells with CS3. (a) Control HEK 293T cells, (b) HEK 293T cells supplemented with 2 µL of water vehicle in the growth medium for 15 h at 37 ºC, and (c) HEK 293T cells supplemented with 2 µL of water vehicle in the growth medium for 25 h at 37 ºC were stained with 2 µM CS3 and 5 µM Hoechst 33342 for 10 min at 37 ºC in DMEM. (d) Graph showing the quantification of the mean fluorescence intensity of each conditions (n = 4 fields of cells per condition). Error bars represent the SEM.

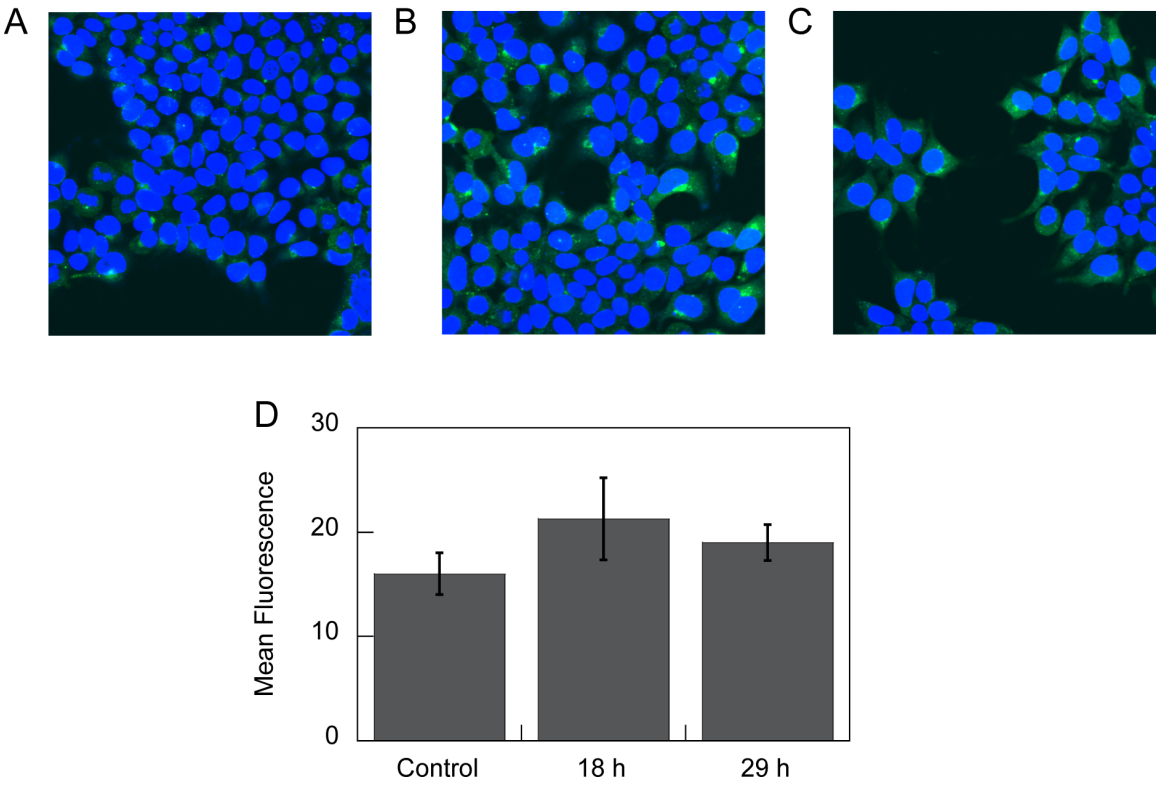

Figure 2-5. Molecular imaging of endogenous basal Zn in HEK 293T cells with FluoZin-3 AM. (a) Control HEK 293T cells, (b) HEK 293T cells supplemented with 200 μM BCS in the growth medium for 18 h at 37 ºC, and (c) HEK 293T cells supplemented with 200 μM BCS in the growth medium for 29 h at 37 ºC were stained with 2 μM FluoZin-3 AM and Pluronic F-127 (vol/vol) and 5 μM Hoechst 33342 for 30 min at 37 ºC in DMEM. (d) Graph showing the quantification of the mean fluorescence intensity of each conditions (n = 3 fields of cells per condition). Error bars represent the SEM.

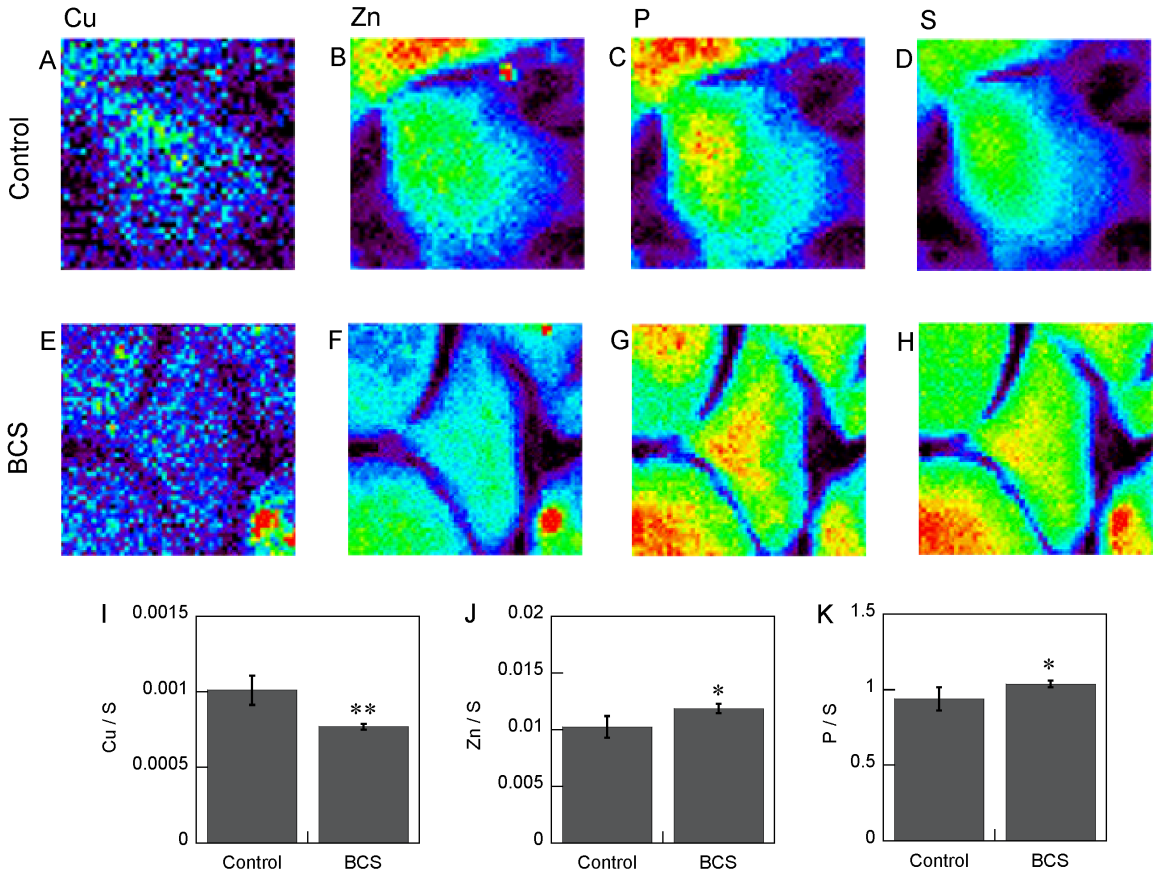

Figure 2-6. Molecular imaging of P, Cu, and Zn distributions in control HEK 293T cells and HEK 293T cells treated with 200 μM BCS in the growth medium for 40 h t 37 ºC with XRFM. (a—d) Untreated HEK 293T cells were fixed with 4% PFA and imaged by XRFM. Images shown are for (a) Cu, (b) Zn, (c) P, and (d) S channels. (e—h) BCS-treated HEK 293T cells were fixed with 4% PFA and imaged by XRFM. Images shown are for (e) Cu, (f) Zn, (g) P, and (h) S channels. Quantification of the mean of the median fluorescence intensity of each condition (n = 8 cells per condition). (i) Cu (μg/cm^2) normalized to S (μg cm^2), (j) Zn (μg/cm^2) normalized to S (μg/cm^2), and (k) P (μg/cm^2) normalized to S (μg/cm^2). Error bars represent the SEM. Asterisk (*) indicates $P < 0.05$ compared to control cells, and double asterisk (**) indicates $P < 0.01$.

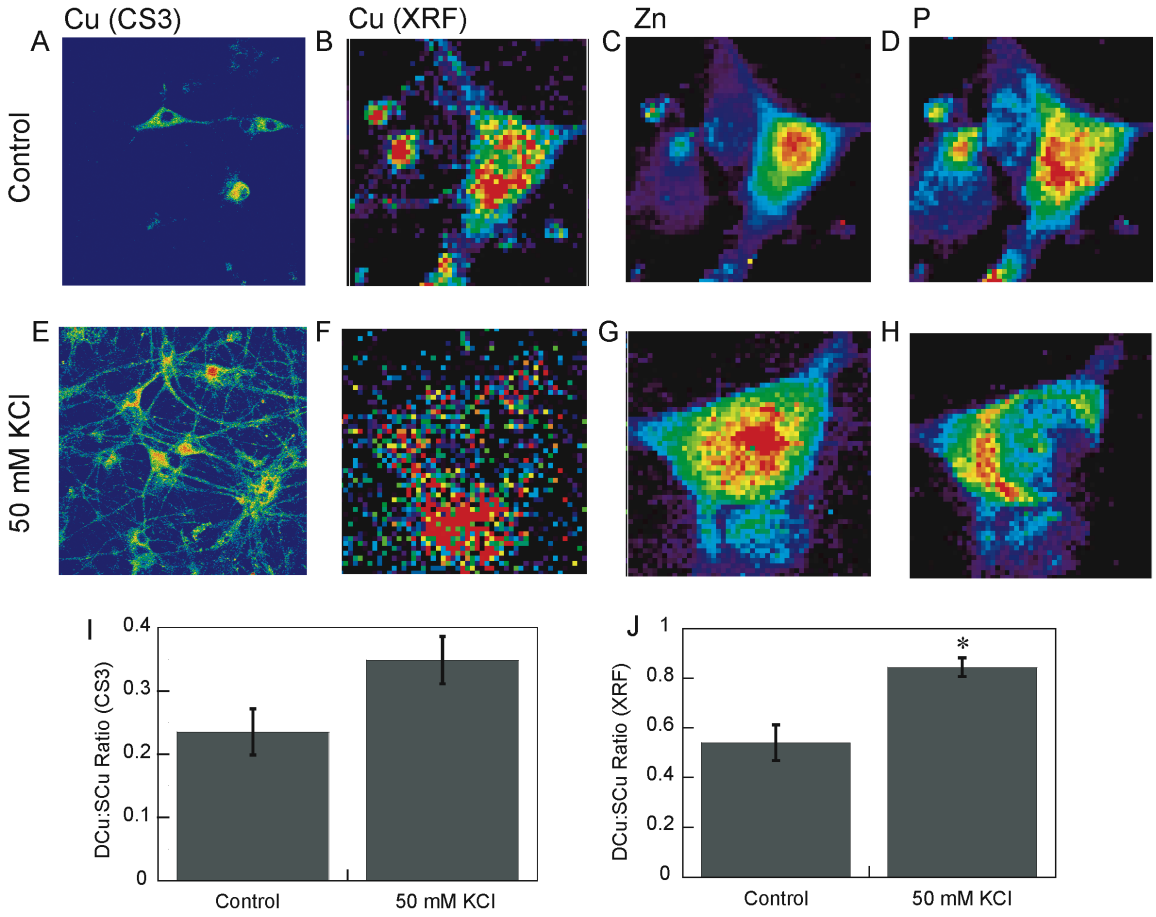

Figure 2-7. (a) Rat hippocampal neurons treated with ECS buffer for 2 min and then stained with 2 μM CS3 for 10 min. (b—d) Rat hippocampal neurons treated with ECS buffer for 2 min and then fixed with 4% PFA and imaged by XRFM. Images shown are for (b) Cu, (c) Zn, and (d) P channels. (e) Live primary rat hippocampal neurons treated with 50 mM KCl in ECS buffer for 2 min and then stained with 2 μM CS3 for 10 min. (f—h) Rat hippocampal neurons treated with 50 mM KCl in ECS buffer for 2 min and then fixed with 4% PFA and imaged by XRFM. Images shown are for (f) Cu, (g) Zn and (h) P channels. (i) Graph showing the blinded quantification of CS3-derived dendrite:soma fluorescence ratios for control (n = X) and depolarized (n = 18) neurons. Error bars represent SEM. (J) Graph showing the XRF dendrite:soma fluorescence ratios for resting and depolarized treated neurons. Error bars represent SEM.

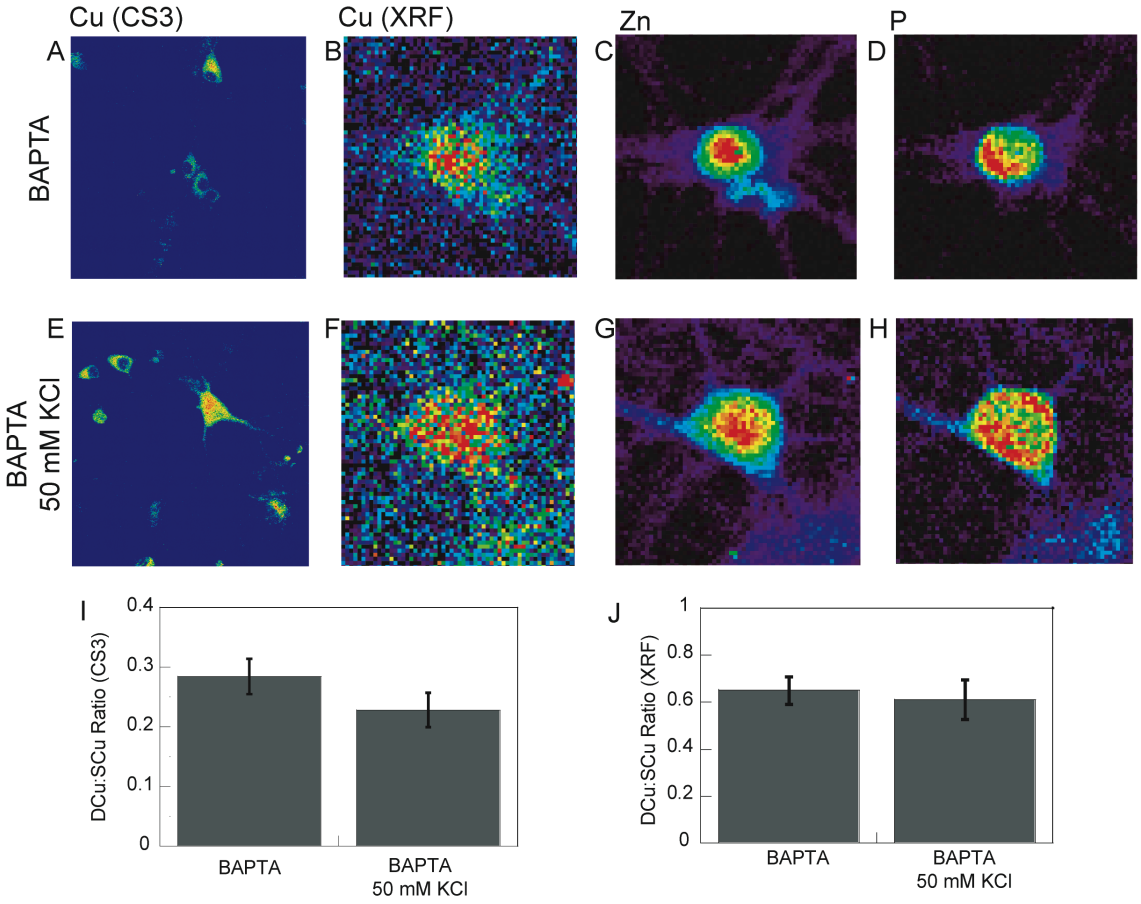

Figure 2-8. (a) Rat hippocampal neurons treated with ECS buffer for 2 min with 10 μM BAPTA-AM and then stained with 2 μM CS3 for 10 min. (b—d) Rat hippocampal neurons treated with ECS buffer with 10 μM BAPTA-AM for 2 min and then fixed with 4% PFA and imaged by XRFM. Images shown are for (b) Cu, (c) Zn, and (d) P channels. (e) Live primary rat hippocampal neurons treated with 50 mM KCl in ECS buffer with 10 μM BAPTA-AM for 2 min and then stained with 2 μM CS3 for 10 min. (f—h) Rat hippocampal neurons treated with 50 mM KCl in ECS buffer with 10 μM BAPTA-AM for 2 min and then fixed with 4% PFA and imaged by XRFM. Images shown are for (f) Cu, (g) Zn and (h) P channels. (i) Graph showing the blinded quantification of CS3-derived dendrite:soma fluorescence ratios for BAPTA-AM–treated (n = 22) and BAPTA-AM/KCl–treated (n = 16) neurons. Error bars represent SEM. (J) Graph showing the XRF dendrite:soma fluorescence ratios for resting and depolarized BAPTA-AM–treated neurons. Error bars represent SEM.

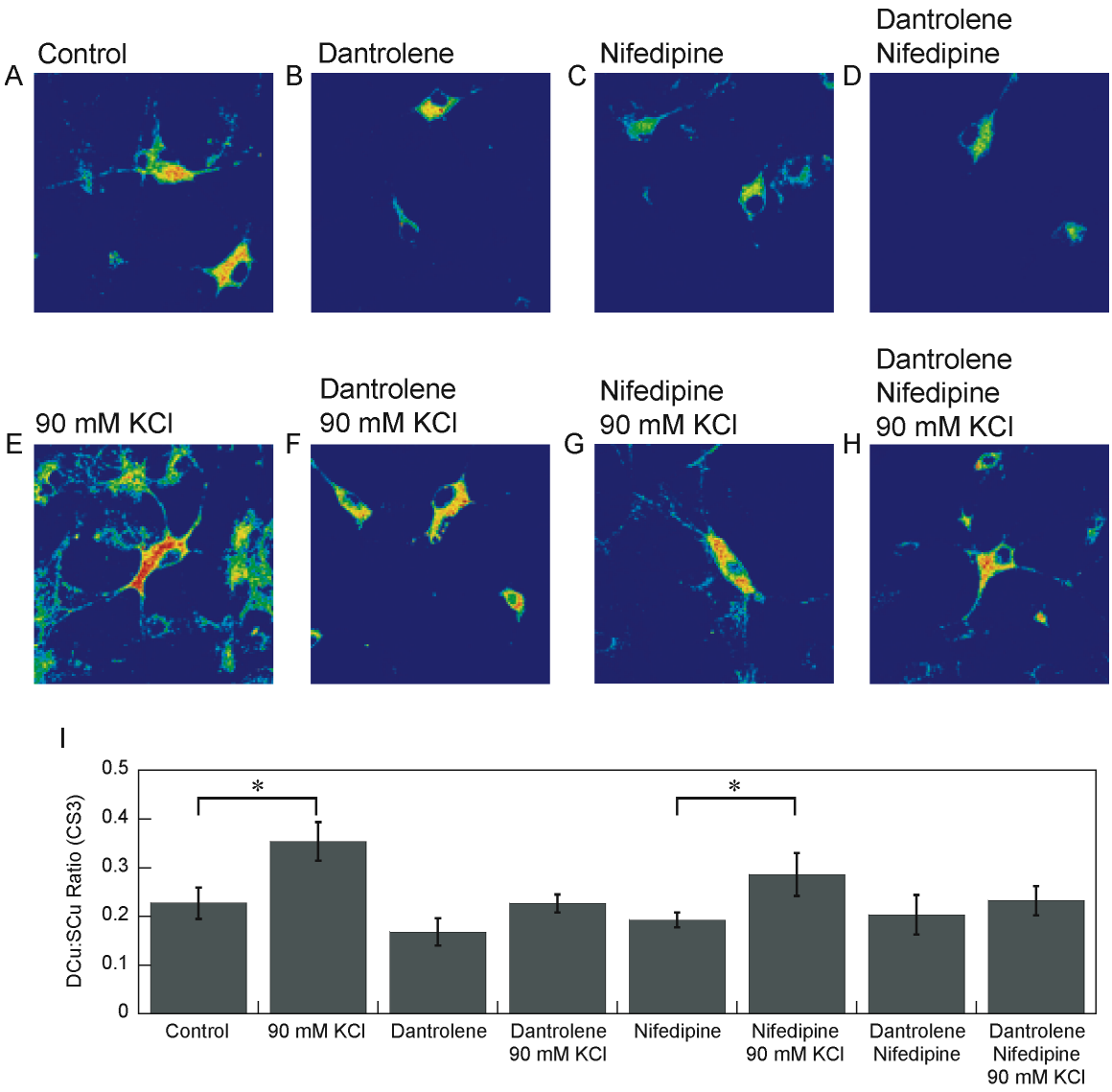

Figure 2-9. Molecular imaging of Cu distributions in resting, depolarized, and inhibitor-treated rat hippocampal neurons with CS3. (a) Live primary rat hippocampal neurons treated with ECS buffer for 10 min, (b) treated with ECS buffer with 30 μM dantrolene for 10 min, (c) treated with ECS buffer with 100 μM nifedipine for 10 min, (d) treated with ECS buffer with 30 μM dantrolene and 100 μM nifedipine for 10 min, (e) treated with 90 mM KCl in ECS buffer for 2 min, (f) treated with 30 μM dantrolene in ECS buffer for 10 min and then 90 mM KCl in ECS buffer for 2 min, (g) treated with 100 μM nifedipine in ECS buffer for 10 min and then 90 mM KCl in ECS buffer for 2 min, and (h) treated with 30 μM nifedipine and 100 μM dantrolene in ECS buffer for 10 min and then 90 mM KCl in ECS buffer for 2 min and then stained with 2 μM CS3 for 10 min. (i) Graph showing the blinded quantification of CS3-derived dendrite:soma fluorescence ratios for resting, depolarized, and inhibitor-treated neurons ($n \geq 11$). Error bars represent the SEM. Asterisk (*) indicates $P < 0.05$.

References

1. Tsien RW, Tsien RY (1990) Calcium channels, stores, and oscillations. *Annu Rev Cell Biol* 6:715-760.
2. Debanne D (2004) Information processing in the axon. *Nat Rev Neurosci* 5:304-316.
3. Clapham DE (2007) Calcium signaling. *Cell* 131:1047-1058.
4. Lippard SJ, Berg JM (1994) *Principles of Bioinorganic Chemistry* (University Science Books, Mill Valley).
5. Gray HB, Stiefel EI, Valentine JS, Bertini I (2007) *Biological Inorganic Chemistry* (University Science Books, Mill Valley).
6. Cvetkovic, A, et al. (2010) Microbial metalloproteomes are largely uncharacterized. *Nature* 466:645-648.
7. Berridge MJ, Bootman MD, Lipp P (1998) Calcium - a life and death signal. *Nature* 395:645-648.
8. Atwood CS, Huang X, Moir RD, Tanzi RE, et al. (1999) *Metal Ions in Biological Systems: Interrelations Betwen Free Radicals and Metal Ions in Life Processes* (CRC, New York).
9. Bush AI (2000) Metals and neuroscience. *Curr Opin Chem Biol* 4:184-191.
10. Burdette SC, Lippard SJ (2003) Bioinorganic Chemistry Special Feature: Meeting of the minds: Metalloneurochemistry. *Proc Natl Acad Sci USA* 100:3605-3610.
11. Prohaska JR, Gybina AA (2004) Intracellular copper transport in mammals. *J Nutr* 134:1003-1006.
12. Que EL, Domaille DW, Chang CJ (2008) Metals in neurobiology: Probing their chemistry and biology with molecular imaging. *Chem Rev* 108:1517-1549.
13. Camakaris J, Voskoboinik I, Mercer JF (1999) Molecular mechanisms of copper homeostasis. *Biochem Biophys Res Commun* 261:225-232.
14. Bertini I, Rosato A (2008) Menkes disease. *Cell Mol Life Sci* 65:89-91.
15. Barnham KJ, Masters CL, Bush AI (2004) Neurodegenerative diseases and oxidative stress. *Nat. Rev. Drug. Discov.* 3:205-214.
16. Gaggelli E, Kozlowski H, Valensin D, Valensin G (2006) Copper homeostasis and neurodegenerative disorders (Alzheimer's, prion, and Parkinson's diseases and amyotrophic lateral sclerosis). *Chem Rev* 106:1995-2044.
17. Lutsenko S, Gupta A, Burkhead JL, Zuzel V (2008) Cellular multitasking: The dual role of human Cu-ATPases in cofactor delivery and intracellular copper balance. *Arch Biochem Biophys* 476:22-32.
18. Beckman JS, Estevez AG, Crow JP, Barbeito L (2001) Superoxide dismutase and the death of motoneurons in ALS. *Trends Neurosci* 24:S15-S20.
19. Valentine JS, Hart PJ (2003) Bioinorganic Chemistry Special Feature: Misfolded CuZnSOD and amyotrophic lateral sclerosis. *Proc Natl Acad Sci USA* 100:3617-3622.
20. Brown DR, Kozlowski H (2004) Biological inorganic and bioinorganic chemistry of neurodegeneration based on prion and Alzheimer diseases. *Dalton Trans* 1907-1917.
21. Millhauser GL (2004) Copper binding in the prion protein. *Acc Chem Res* 37:79-85.
22. Hartter DE, Barnea A (1988) Evidence for release of copper in the brain: Depolarization-induced release of newly taken up copper. *Synapse* 2:412-415.
23. Schlief ML, Craig AM, Gitlin JD (2005) NMDA receptor activation mediates copper homeostasis in hippocampal neurons. *J Neurosci* 25:239-246.
24. Hopt A, Korte S, Fink H, Panne U, et al. (2003) Methods for studying synaptosomal copper release. *J Neurosci Methods* 128:159-172.

25. Schlief ML, West T, Craig AM, Holtzman DM, et al. (2006) Role of the Menkes copper-transporting ATPase in NMDA receptor-mediated neuronal toxicity. *Proc Natl Acad Sci USA* 103:14919-14924.
26. Domaille DW, Que EL, Chang CJ (2008) Synthetic fluorescent sensors for studying the cell biology of metals. *Nat Chem Biol* 4:168-175.
27. McRae R, Bagchi P, Sumalekshmy S, Fahrni CJ (2009) In situ imaging of metals in cells and tissues. *Chem Rev* 109:4780-4827.
28. Haas KL, Franz KJ (2009) Application of metal coordination chemistry to explore and manipulate cell biology. *Chem Rev* 109:4921-4960.
29. Yang LC, McRae R, Henary MM, Patel R, et al. (2005) Imaging of the intracellular topography of copper with a fluorescent sensor and by synchrotron x-ray fluorescence microscopy. *Proc Natl Acad Sci USA* 102:11179-11184.
30. Zeng L, Miller EW, Pralle A, Isacoff EY, et al. (2006) A selective turn-on fluorescent sensor for imaging copper in living cells. *J Am Chem Soc* 128:10-11.
31. Miller EW, Zeng L, Domaille DW, Chang CJ (2006) Preparation and use of Coppersensor-1, a synthetic fluorophore for live-cell copper imaging. *Nature Protocols* 1:824-827.
32. Domaille DW, Zeng L, Chang CJ (2010) Visualizing ascorbate-triggered release of labile copper within living cells using a ratiometric fluorescent sensor. *J Am Chem Soc* 132:1194-1195.
33. Wegner SV, Arslan H, Sunbul M, Yin J, et al. (2010) Dynamic copper(I) imaging in mammalian cells with a genetically encoded fluorescent copper(I) sensor. *J Am Chem Soc* 132:2567-2569.
34. Wegner SV, Sun F, Hernandez N, He C. (2011) The tightly regulated copper window in yeast. *Chem Commun* 47:2571-2573.
35. Dodani SC, Domaille DW, Nam CI, Miller EW, et al. (2011) Calcium-dependent copper redistributions in neuronal cells revealed by a fluorescent copper sensor and X-ray fluorescence microscopy. *Proc Natl Acad Sci USA* 108: 5980-5985.
36. Hamza I, Prohaska J, Gitlin JD (2003) Essential role for Atox1 in the copper-mediated intracellular trafficking of the Menkes ATPase. *Proc Natl Acad Sci USA* 100:1215-1220.
37. Glesne D, Vogt S, Maser J, Legnini D, et al. (2006) Regulatory properties and cellular redistribution of zinc during macrophage differentiation of human leukemia cells. *J Struct Biol* 155:2-11.
38. Finney L, Mandava S, Ursos L, Zhang W, et al. (2007) X-ray fluorescence microscopy reveals large-scale relocalization and extracellular translocation of cellular copper during angiogenesis. *Proc Natl Acad Sci USA* 104:2247-2252.
39. Fahrni CJ (2007) Biological applications of X-ray fluorescence microscopy: exploring the subcellular topography and speciation of transition metals. *Curr Opin Chem Biol* 11:121-127.
40. Finney L, Chishti Y, Khare T, Giometti C, et al. (2010) Imaging metals in proteins by combining electrophoresis with rapid X-ray fluorescence mapping. *ACS Chem Biol* 5:577-587.
41. Twining BS, Baines SB, Fisher NS, Maser Jr, et al. (2003) Quantifying trace elements in individual aquatic protist cells with a synchrotron X-ray fluorescence microprobe. *Anal Chem* 75:3806-3816.
42. Tsien RY (1980) A non-disruptive technique for loading calcium buffers and indicators into cells. *Nature* 290:527-528.

43. Balkowiec A, Katz DM. (2002) Cellular mechanisms regulating activity-dependent release of native brain-derived neurotrophic factor from hippocampal neurons. *J Neurosci* 22:10399-10407.
44. Hayashi T, Kagaya A, Takebayashi M, Oyamada T, et al. (1997) Effect of dantrolene on KCl- or NMDA-induced intracellular Ca^{2+} changes and spontaneous Ca^{2+} oscillation in cultured rat frontal cortical neurons. *J Neural Transm* 104:811-824.
45. Herd SM, Camakaris J, Christofferson R, Wookey P, et al. (1987) Uptake and efflux of copper-64 in Menkes'-disease and normal continuous lymphoid cell lines. *Biochem J* 247:341-347.
46. O'Halloran TV, Culotta VC (2000) Metallochaperones, an intracellular shuttle service for metal ions. *J Biol Chem* 275:25057-25060.
47. Rosenzweig AC, O'Halloran TV (2000) Structure and chemistry of the copper chaperone proteins. *Curr Opin Chem Biol* 4:140-147.
48. Cobine PA, Pierrel F, Winge DR (2006) Copper trafficking to the mitochondrion and assembly of copper metalloenzymes. *BBA-Cell Biol Res* 1763:759-772.
49. Kim B-E, Nevitt T, Thiele DJ (2008) Mechanisms for copper acquisition, distribution and regulation. *Nat Chem Biol* 4:176-185.
50. Davis AV, O'Halloran TV (2008) A place for thioether chemistry in cellular copper ion recognition and trafficking. *Nat Chem Biol* 4:148-151.
51. Ma Z, Jacobsen FE, Giedroc DP (2009) Coordination chemistry of bacterial metal transport and sensing. *Chem Rev* 109:4644-4681.
52. Li Z, Okamoto K-I, Hayashi Y, Sheng M (2004) The importance of dendritic mitochondria in the morphogenesis and plasticity of spines and synapses. *Cell* 119:873-887.
53. El Meskini R, Cline LB, Eipper BA, Ronnett GV (2005) The developmentally regulated expression of Menkes protein ATP7A suggests a role in axon extension and synaptogenesis. *Dev Neurosci-Basel* 27:333-348.
54. El Meskini R, Crabtree KL, Cline LB, Mains RE, et al. (2007) ATP7A (Menkes protein) functions in axonal targeting and synaptogenesis. *Mol Cell Neurosci* 34:409-421.
55. Cooper TH, Mayer MJ, Leung KH, Ochrymowycz LA, Rorabacher DB (1992) Kinetic and thermodynamic measurements on branched amino polythiaether ligands: a family of complexing agents analogous to EDTA and NTA exhibiting enhanced selectivity for copper(II). *Inorg Chem* 31:3796-3804.
56. Finney L, Mandava S, Ursos L, Zhang W, et al. (2007) X-ray fluorescence microscopy reveals large-scale relocalization and extracellular translocation of cellular copper during angiogenesis. *Proc Natl Acad Sci USA* 104:2247-2252.

Chapter 3:

A Targetable Fluorescent Sensor Reveals that Copper-Deficient *SCO1* and *SCO2* Patient Cells Prioritize Mitochondrial Copper Homeostasis

Abstract

We present the design, synthesis, spectroscopy, and biological applications of Mitochondrial Coppersensor-1 (Mito-CS1), a new type of targetable fluorescent sensor for imaging exchangeable mitochondrial copper pools in living cells. Mito-CS1 is a bifunctional reporter that combines a Cu^+-responsive fluorescent platform with a mitochondrial-targeting triphenylphosphonium moiety for localizing the probe to this organelle. Molecular imaging with Mito-CS1 establishes that this new chemical tool can detect changes in labile mitochondrial Cu^+ in a model HEK 293T cell line as well as in human fibroblasts. Moreover, we utilized Mito-CS1 in a combined imaging and biochemical study in fibroblasts derived from patients with mutations in the two synthesis of cytochrome *c* oxidase 1 and 2 proteins (SCO1 and SCO2), each of which is required for assembly and metallation of functionally active cytochrome *c* oxidase (COX). Interestingly, we observe that although defects in these mitochondrial metallochaperones lead to a global copper deficiency at the whole cell level, total copper and exchangeable mitochondrial Cu^+ pools in *SCO1* and *SCO2* patient fibroblasts are largely unaltered relative to wild type controls. Our findings reveal that the cell maintains copper homeostasis in mitochondria even in situations of copper deficiency and mitochondrial metallochaperone malfunction, illustrating the importance of regulating copper stores in this energy-producing organelle.

Introduction

Copper is a required element for life, and regulating its uptake, efflux, and compartmentalization at the cellular level is vital for maintaining normal physiology.[1—3] As such, cells have evolved intricate mechanisms that coordinate the activity of transporters, chaperones, and small-molecule ligands to dynamically control the distribution of copper within discrete subcellular spaces.[4—24] In this context, mitochondria are important reservoirs for cellular copper owing to the essential role of this metal ion as a cofactor for the respiratory enzyme cytochrome *c* oxidase (COX), which reduces oxygen to water in the terminal step of aerobic respiration.[25—30] In addition to the copper present in COX, mitochondria utilize this metal ion as a cofactor for superoxide dismutase (SOD1) contained within the mitochondrial intermembrane space (IMS), and a matrix-localized pool of copper is relocalized to the IMS to metallate both of these enzymes.[31] Assembly of active COX in mitochondria requires a host of proteins, including the two synthesis of cytochrome *c* oxidase genes (*SCO1* and *SCO2*) that collectively mediate a series of metal- and redox-dependent events crucial for COX metallation and holoenzyme maturation.[32—44] Mutations in either of the SCO chaperones result in severe, tissue-specific clinical phenotypes that are caused by both a failure to mature functionally active COX for aerobic respiration, and an inability to appropriately regulate cellular copper homeostasis.[36,45—59]

Because regulating mitochondrial copper homeostasis is critical to maintaining central oxygen metabolism in the cell, new chemical tools that allow direct, real-time visualization of exchangeable mitochondrial copper pools in living samples are potentially powerful reagents with which to directly investigate the spatiotemporal distribution of this redox-active metal in both healthy and diseased states. Towards this end, we have initiated a broad-based program to create fluorescent and MRI agents for monitoring labile copper stores in living systems.[60—68] Previous work from our laboratory on fluorescent sensors for live-cell copper imaging include intensity and ratiometric probes Coppersensor-1 (CS1)[60,61], Coppersensor-3 (CS3)[68], and Ratio-Coppersensor-1 (RCS1)[67], that are capable of selectively tracking labile cellular Cu^+ stores with

metal and/or redox stimulation. However, these first-generation sensors and other elegant examples of small molecule or protein-based copper sensors[69—71] are not preferentially directed to mitochondria or other organelles, which offers an opportunity to devise new probes that can be targeted to discrete subcellular compartments for imaging local changes in the abundance/availability of exchangeable Cu^+.

In this report we present the design, synthesis, spectroscopy, and biological applications of Mitochondrial Coppersensor-1 (Mito-CS1), a new type of fluorophore for imaging dynamic mitochondrial copper stores in living cells with metal ion and spatial specificity (Scheme 3-1). Mito-CS1 can reversibly detect endogenous, exchangeable mitochondrial Cu^+ pools in a model HEK 293T cell line as well as in cultured human fibroblasts. Moreover, we apply Mito-CS1 in a combined molecular imaging and biochemical study to investigate mitochondrial copper homeostasis in fibroblasts derived from patients with *SCO1* and *SCO2* mutations. Interestingly, the data establish that although loss of function mutations in *SCO1* and *SCO2* cause a severe, global copper deficiency at the whole cell level, both the exchangeable Cu^+ and total mitochondrial copper pools are only mildly perturbed in *SCO1* and *SCO2* patient fibroblasts compared to wildtype congeners. Our results show that the cell maintains the homeostatic regulation of copper within mitochondria, even when faced with a globally severe state of copper deficiency, and underscore the primary importance of this redox-active metal in central metabolism and cellular energy homeostasis.[72]

Results and Discussion

Design and Synthesis of a Targetable Coppersensor Platform and Preparation of Mito-CS1. In order to monitor labile mitochondrial copper pools in living cells by real-time fluorescence imaging, we designed a bifunctional BODIPY dye that contains both a fluorescence-responsive Cu^+-binding domain and a mitochondrial-targeting moiety. For the latter, we exploited phosphonium head groups that have been pioneered by Murphy[73—76] and subsequently utilized by ourselves[77,78] and others[79—84] to selectively direct attached cargo to mitochondria via their proton gradients. In addition, we designed a synthetic pathway that builds up to one key intermediate, Carboxy-CS1, that combines a BODIPY chromophore, a thioether-rich receptor for selective recognition and binding of Cu^+, and a carboxylic acid synthetic handle (Scheme 1, compound **9)** for facile introduction of a triphenylphosphonium tag or any other desired targeting functionality. We note that modification of the BODIPY chromophore to incorporate additional functionalities has been explored in the literature.[85,86]

Scheme 3-1 outlines the synthesis of Mito-CS1. Briefly, alkylation of aldehyde **1** with methyl bromoacetate furnishes the methyl ester **2** in 58% yield. Condensation of **2** with excess pyrrole and catalytic trifluoroacetic acid affords dipyrromethane **3** in 19% yield. Subsequent chlorination followed by oxidation with *p*-chloranil gives the dichloro dipyrromethene **4** in 44% yield over two steps; because isolation of the putative dichloro dipyrromethane intermediate is low yielding, we found that a halogenation/oxidation protocol was more synthetically tractable. Boron insertion with BF_3•OEt_2 generates the dichloro BODIPY **5** in 75% yield. Nucleophilic displacement with sodium methoxide yields **6**, which is then coupled to the azatetrathia receptor **7** to generate **8** in 56% yield. Ester hydrolysis of **8** under basic conditions yields Carboxy-CS1 **9**. Peptide coupling of **9** and the mitochondrial-targeted tag **10** with HATU delivers Mito-CS1 (**11**) in 48% yield. We note that these mild and robust coupling conditions allow for the potential

introduction of other functional tags onto Carboxy-CS1, including ones that can be used to direct fluorescent copper sensors to other organelles and other subcellular targets and that the synthetic pathway towards Mito-CS1 generates a versatile set of precursor materials (compounds **3**, **4**, **5**, and **6**).

Spectroscopic Properties of Mito-CS1. The spectroscopic properties of Mito-CS1 were evaluated in aqueous media buffered to physiological pH (PBS, pH 7.4). Apo Mito-CS1 features one prominent optical band at 555 nm ($\varepsilon = 2.8 \times 10^4$ M^{-1} cm^{-1}) with a shoulder at 520 nm and a corresponding emission maximum at 569 nm with weak fluorescence ($\Phi = 0.009$). Upon addition of Cu^+, the absorption spectrum of Cu^+-bound Mito-CS1 displays a single major visible absorption band at 550 nm ($\varepsilon = 2.6 \times 10^4$ M^{-1} cm^{-1}). The fluorescence intensity of Mito-CS1 increases by ca. 10-fold ($\Phi = 0.05$, Figure 3-1a) with a slight blue shift of the emission maximum to 558 nm with 1 equivalent of Cu^+ added (Figure 1a, inset), similar in photochemical properties to the previously reported turn-on fluorescent sensor CS1[60] (Cu^+-bound $\Phi = 0.13$, 10-fold turn-on response) but with the added functionality of a targeting phosphonium moiety. Binding analysis using the method of continuous variations (Job's plot) indicates a 1:1 Cu^+:dye complex is responsible for the observed fluorescence enhancement (Figure 3-1b). These results demonstrate that Mito-CS1 can dynamically respond to changes in Cu^+ levels in aqueous media. The apparent K_d for the Mito-CS1:Cu^+ complex is $7.2(3) \times 10^{-12}$ M in PBS buffer at pH 7.4 (Figure 3-2a). Even in the presence of a lipophilic phosphonium cation, Mito-CS1 maintains its high selectivity for Cu^+ over other biologically relevant metal ions (Figure 3-2b). The fluorescence response of apo or Cu^+-bound Mito-CS1 is not affected by the presence of physiologically relevant concentrations of Ca^{2+}, Mg^{2+}, and Zn^{2+}. Moreover, other bioavailable divalent metal ions (Mn^{2+}, Fe^{2+}, Co^{2+}, Ni^{2+}, Cu^{2+}) do not induce a change in the emission intensity of the apo probe and do not interfere with the Cu^+ response. Finally, Mito-CS1 is selective for Cu^+ over Cu^{2+}, showing that this probe has metal and redox specificity.

Fluorescence Detection of a Labile Mitochondrial Cu^+ Pool in HEK 293T Cells Using Mito-CS1. With spectroscopic data establishing that Mito-CS1 can selectively respond to Cu^+ in aqueous solution, we turned our attention to evaluate Mito-CS1 in live-cell imaging assays using HEK 293T as a model cell line. First, we tested Mito-CS1 for its ability to localize to mitochondria. Accordingly, HEK 293T cells stained with 500 nM Mito-CS1 for 15 min at 37 °C show measurable levels of fluorescence in discrete subcellular locations as determined by confocal microscopy (Figure 3-3a). Co-staining experiments with MitoTracker Deep Red, a commercially available mitochondrial tracker (Figure 3-3b), BODIPY FL C_5-ceramide, a marker for the trans-Golgi (Figure 3-3c), and LysoTracker Green DND-26, a lysosomal marker (Figure 3-3f), establish that the observed fluorescence from Mito-CS1 is localized to mitochondria in these live cells. Furthermore, nuclear staining with Hoechst 33342 indicates that the cells are viable throughout the imaging experiments (Figure 3-3d, Figure 3-3g).

We next tested whether Mito-CS1 was sensitive enough to detect basal levels of labile mitochondrial Cu^+ and whether it could respond to increases and/or decreases in the size of this pool. First, HEK 293T cells were cultured in growth media only or growth media supplemented with 300 μM $CuCl_2$ for 18 h to globally elevate intracellular copper stores and subsequently imaged by confocal microscopy (Figure 3-4a, 3-4b). As visualized by Mito-CS1, we observe that exchangeable mitochondrial Cu^+ levels rise by 34% with copper supplementation relative to control, indicating that Mito-CS1 can detect expansions in the mitochondrial Cu^+ pool (Figure 3-4d).[31] To evaluate whether Mito-CS1 can also report on decreases in exchangeable mitochondrial

Cu^+ levels, HEK 293T cells were cultured in growth media only or growth media supplemented with 100 μM of the membrane-impermeable Cu^+ chelator bathocuproine disulfonate (BCS) for 18 h to globally deplete intracellular copper stores,[87] and each set of cells were then stained with Mito-CS1 and imaged by confocal microscopy. Upon addition of BCS, labile mitochondrial Cu^+ levels decrease by 36% relative to basal Cu^+ levels (Figure 3-4a, 3-4c), showing that Mito-CS1 can image basal levels of mitochondrial Cu^+ and detect depletions in this pool. In addition, nuclear staining with Hoechst 33342 confirms that the viability of HEK 293T cells is unaffected by the manipulation of cellular copper status (Figure 3-4a, 3-4b, 3-4c).

Finally, as an additional set of controls to corroborate that Mito-CS1 is detecting copper-dependent events, we performed analogous imaging studies with Rhodamine 123, a well established fluorescent marker for assaying mitochondrial membrane potential [88,89], under basal, copper-supplemented, and copper-depleted conditions. As described above, endogenous copper pools of HEK 293T cells were elevated with supplementation or depleted with chelation and then stained with 100 nM Rhodamine 123 (Figure 3-4e, 3-4f, 3-4g). The membrane potential as measured by Rhodamine 123 does not show statistically significant changes with either 300 μM $CuCl_2$ or 100 μM BCS treatment relative to control HEK 293T cells (Figure 3-4h), providing further evidence that Mito-CS1 is sensing changes in labile mitochondrial copper pools rather than reporting on mitochondrial membrane potential.

Mito-CS1 Imaging and ICP-OES Experiments Reveal that Mitochondrial Cu^+ Pools in *SCO1* and *SCO2* Patient Fibroblasts Are Comparable to Wild type Counterparts. In our first application of Mito-CS1 as an analytical tool, we investigated whether the labile and total mitochondrial copper pools are affected by mutations in *SCO1* and *SCO2*, which are known to cause a severe copper deficiency at the cellular level in affected tissues and cell types.[36] We first evaluated the ability of Mito-CS1 to localize to mitochondria in human fibroblasts. As seen with HEK 293T cells, confocal microscopy of control fibroblasts stained with 5 mM Mito-CS1 for 15 min at 37 °C shows measurable levels of fluorescence in discrete subcellular locations (Figure 3-5a). Co-staining experiments with MitoTracker Deep Red, a commercially available mitochondrial tracker (Figure 3-5b), BODIPY FL C_5-ceramide, a marker for the trans-Golgi (Figure 3-5c), and LysoTracker Green DND-26, a lysosomal maker (Figure 3-5f), establish that the observed fluorescence from Mito-CS1 is localized to mitochondria of these cells. Furthermore, nuclear staining with Hoechst 33342 indicates that the cells are viable throughout the imaging experiments (Figure 3-5d, Figure 3-5g).

Analogous to the HEK 293T cells, we next tested how changes in global copper status affect the exchangeable mitochondrial copper pool in control fibroblasts. Control fibroblasts were grown in media supplemented with 300 μM and 500 μM $CuCl_2$ for 18 h and then stained with 5 μM Mito-CS1 for 15 min at 37 °C. The labile mitochondrial Cu^+ pool as visualized by Mito-CS1 is significantly expanded upon co-culture of fibroblasts with 500 μM $CuCl_2$ (Figure 3-6a, 3-6b, 3-6c). Staining with Rhodamine 123 does not show a statistically significant difference in the membrane potential between untreated and copper-supplemented fibroblasts (Figure 3-6d, 3-6e, 3-6f). Control fibroblasts treated with 100 μM BCS for 12 h and then stained with 5 mM Mito-CS1 for 15 min at 37 °C show a 45% decrease in mitochondrially-localized fluorescence intensity compared to their untreated counterparts (Figure 3-7a, 3-7b, 3-7c). The observed decrease in fluorescence intensity of Mito-CS1 in BCS-treated fibroblasts demonstrates that these cells possess a dynamic mitochondrial Cu^+ pool that is affected by changes in global copper status. In a set of parallel control experiments, Rhodamine 123 staining of control

fibroblasts grown in normal media or media with 100 μM BCS for 12 h reveals no differences in membrane potential (Figure 3-7d, 3-7e, 3-7f) and nuclear staining with Hoescht 33342 shows that the cells are viable throughout the BCS treatment and imaging experiments (Figure 3-7a, 3-7b, 3-7c, 3-7d). COX activity is mildly reduced with 100 μM BCS treatment for 24 h (Figure 3-7g) but not sufficiently to affect the membrane potential (Figure 3-7e). Taken together, the data further establish that Mito-CS1 directly detects and responds to changes in endogenous mitochondrial Cu^+ levels in cultured human fibroblasts.

After establishing that Mito-CS1 can monitor the labile mitochondrial Cu^+ pool in control fibroblasts and sense dynamic changes in its size with alterations in copper status, we used this new chemical tool to characterize mitochondrial Cu^+ homeostasis in fibroblasts derived from patients with mutations in *SCO1* and *SCO2*. We also included fibroblasts derived from a patient with mutations in the copper exporter protein ATP7A in our analyses, for loss of ATP7A function in this cell type results in significant increases in total cellular copper content.[90,91] Control, *SCO1*, *SCO2*, and *ATP7A* patient fibroblasts were cultured for 48 h in growth medium, stained with 5 μM Mito-CS1 in DMEM, and imaged live by scanning confocal microscopy. Consistent with our findings using control fibroblasts, mutations in *ATP7A*, *SCO1* and *SCO2* do not affect the mitochondrial localization of Mito-CS1 or overall cell viability (Figure 3-8a, 3-8b, 3-8c, 3-8d). Interestingly, quantification of the Mito-CS1 fluorescence intensities reveals that the size of the labile mitochondrial Cu^+ pool is comparable in control, *SCO1* and *SCO2* patient fibroblasts, while it is significantly expanded in *ATP7A* patient fibroblasts (Figure 3-8e). We next used ICP-OES to measure total Cu at the whole cell and mitochondrial levels of organization in all four genetic backgrounds (Figure 3-8f). As expected, total cellular copper content is elevated in *ATP7A* patient fibroblasts and decreased in *SCO1* and *SCO2* patient fibroblasts when compared to control fibroblasts. In contrast, the total mitochondrial copper pool is only modestly altered in the patient backgrounds (Figure 3-8g), illustrating that this organelle more tightly controls its total and labile copper pools relative to the whole cell. We also examined total metal pools in the fibroblasts by X-ray fluorescence microscopy (XRFM). The fibroblasts were stained with MitoTracker Deep Red to mark mitochondria, BODIPY FL C_5-ceramide to mark the Golgi, and Control-CS1 (Scheme 3-1, compound **12**) to map labile copper and imaged live prior to fixation and processing for XRFM. It is important to note that Control-CS1 has similar spectroscopic properties as Mito-CS1 but does not exclusively localize to mitochondria. The goal was to spatially correlate the labile copper pool from the live-cell imaging with the total copper pool from the XRFM metal maps. However, the resolution of the XRFM images was too low to distinguish discrete cellular compartments and compare to the live-cell imaging experiments (Figure 3-9). Visual assessment of the XRFM images reveals that the *ATP7A* patient fibroblasts have more copper and the *SCO1* patient fibroblasts have less copper when compared to the wild type controls on the whole cell level. Because the majority of mitochondrial copper is housed in the matrix and previous studies with competitor proteins, *in vitro* titrations and targeted chelators[31,69] argue that this pool is exchangeable, Mito-CS1 is likely visualizing this store within living cells. We performed two sets of additional control experiments to further support that Mito-CS1 is specifically reporting on a Cu^+-sensitive phenomenon in these patient fibroblasts. First, we used Rhodamine 123 staining to demonstrate that the mitochondrial membrane potential is maintained in both *SCO1* and *SCO2* patient backgrounds relative to the control (Figure 3-10a, 3-10b, 3-10c, 3-10d, 3-10e) Second, we measured COX activity in fibroblasts from all four genetic backgrounds (Figure 3-10f) to confirm the presence of a severe COX deficiency in fibroblasts lacking functional SCO1 or

SCO2. The collective data show that the observed changes in Mito-CS1 fluorescence are copper-dependent and are not an indirect consequence or non-specific phenomenon of differences across the cell lines in COX activity and/or membrane potential.

Finally, to support that the data obtained from *SCO1* and *SCO2* patient fibroblasts are representative of the observed *in vivo* phenotypes, we measured total copper content in crude mitochondria isolated from control, *SCO1* and *SCO2* patient livers by ICP-OES (Figure 3-11). As in cultured fibroblasts, the data show that the mitochondrial copper pool is not significantly altered in liver as a result of mutations in *SCO1* or *SCO2* (Figure 3-11a). While there was considerable variability in mitochondrial copper content across control liver samples, this observation can be explained by differences in total hepatocyte copper content (Figure 3-11b). Comparable copper levels in crude and highly purified mitochondria isolated from HEK 293T cells further suggest that the variation in mitochondrial copper levels observed across control liver samples is not simply a consequence of the isolation procedure (Figure 3-11a). Therefore, consistent with previously reported results[36] these data further suggest that fibroblasts are a competent disease model in terms of copper misregulation. Taken together, the combination of Mito-CS1 imaging and ICP-OES measurements patently shows that the mitochondrial copper store is a tightly regulated metal ion pool, as we observe little to no perturbation in the labile mitochondrial Cu^{+} and total mitochondrial copper pools in *ATP7A*, *SCO1*, and *SCO2* patient fibroblasts compared to control congeners.

Concluding Remarks

In this report, we have described the synthesis, properties, and biological applications of Mito-CS1, a new targetable fluorescent probe that can selectively detect labile Cu^{+} in mitochondria of living cells. Mito-CS1 is a unique Cu^{+}-specific small-molecule fluorescent indicator that features visible excitation and emission profiles, a turn-on response, and selectivity for Cu^{+} over other abundant mitochondrial metal ions, including Fe^{2+}, Cu^{2+}, and Zn^{2+}. Confocal microscopy experiments with a model HEK 293T cell line and human fibroblasts establish that Mito-CS1 is chemically and spatially specific within living cells for mitochondrial Cu^{+}. Furthermore, we used Mito-CS1 in conjunction with biochemical and ICP metal analyses to monitor mitochondrial copper pools in SCO and ATP7A patient fibroblasts, cell lines that exhibit profound alterations in total cellular copper levels that mirror those observed in affected patient tissues *in vivo*. Interestingly, these experiments show that the mutations in question do not dramatically alter labile mitochondrial Cu^{+} or total mitochondrial Cu pools relative to control cells, suggesting that cells maintain homeostatic control over mitochondria regulating copper homeostasis within a narrow window, to protect the main oxygen-consuming and energy-producing organelle relative to other areas of the cell. We anticipate that the Mito-CS1 reagent will find utility for future interrogations of how discrete copper handling pathways are organized into dynamic networks at the cell and systems levels of organization. In addition to applying Mito-CS1 for studies of mitochondrial copper biology, we are exploiting the modular probe scaffold to create new multifunctional probes for detecting Cu^{+} and other biologically relevant analytes in discrete subcellular locales.

Experimental Section

Synthetic Materials and Methods. All reactions were carried out under a dry nitrogen atmosphere with flame-dried glassware. Silica gel P60 (SiliCycle) was used for column chromatography. Analytical thin layer chromatography was performed using SiliCycle 60 F254 silica gel (precoated sheets, 0.25 mm thick). Compound 1[92], compound 10[93], and Rhodamine 123[94] were synthesized according to modified literature procedures. Compound 7[60,61] was prepared according to previously reported procedures. HATU was purchased from ChemPep Incorporated (Wellington, FL). MitoTracker Deep Red, BODIPY FL C_5-ceramide, LystoTracker DND-26, and Hoechst 33342 were purchased from Invitrogen (Carlsbad, CA). All other chemicals were purchased from Sigma-Aldrich (St. Louis, MO) and were used as received. ^{1}H and ^{13}C NMR spectra were collected in $CDCl_3$, CD_3OD, and $(CD_3)_2SO$ (Cambridge Isotope Laboratories, Cambridge, MA) at 25 °C on a Bruker AVB-400 spectrometer at the College of Chemistry NMR Facility at the University of California, Berkeley. All chemical shifts are reported in the standard notation of parts per million using the peak of residual proton signals of $CDCl_3$ as an internal reference. Low-resolution mass spectral analyses were carried out using a 6130 quadrupole LC/MS 1200 Series (Aglient Technologies, Santa Clara, CA). High-resolution mass spectral analyses were carried out at the College of Chemistry Mass Spectrometry Facility at the University of California, Berkeley.

4-Hydroxy-2,6-dimethylbenzaldehyde (1). Compound **1** was prepared according to a previously reported procedure with the following modifications: $CHCl_3$ was passed over alumina and then added dropwise over 30 min to the reaction mixture. Characterization was consistent with that previously reported in the literature.[92]

Methyl 2-(4-formyl-3,5-dimethylphenoxy)acetate (2). Methyl 2-bromoacetate (3.8 mL, 40 mmol) in anhydrous MeCN (60 mL) was added dropwise to a suspension of compound **1** (5.0 g, 33.3 mmol) and K_2CO_3 (9.19 g, 66.6 mmol) in MeCN (50 mL) at 60 °C. The resulting solution was heated at 60 °C for two days. The reaction mixture was cooled to room temperature and concentrated *in vacuo*. The crude reaction mixture was partitioned between water (100 mL) and EtOAc (3 x 100 mL). The organics were combined, dried over Na_2SO_4, filtered, and dried *in vacuo*. Diethyl ether (50 mL) was added to the crude solid and the resulting solid was collected via vacuum filtration and washed with diethyl ether (50 mL) to furnish compound **2** as an off-white solid (4.31 g, 58%). The reaction was repeated to generate more material for the subsequent reactions. ^{1}H NMR (400 MHz, $CDCl_3$): δ 2.59 (6H, s), 3.81 (3H, s), 6.58 (2H, s), 10.46 (1H, s). ^{13}C NMR (100 MHz, $CDCl_3$): δ 21.1, 52.5, 64.8, 115.3, 126.9, 144.6, 160.7, 168.8, 191.7. LRESI-MS calculated for [MH^+] 223.1, found 223.1.

Methyl 2-(4-(di(1*H*-pyrrol-2-yl)methyl)-3,5-dimethylphenoxy)acetate (3). A solution of **2** (6.38 g, 28.7 mmol) in freshly distilled pyrrole (50.0 mL, 721 mmol) was wrapped in foil to protect it from light and purged with a stream of N_2 for five minutes. TFA (240 μL, 5.4 mmol) was then added dropwise, and the solution was stirred at room temperature for 1 h. After 1 h, TEA (1.0 mL, 7.2 mmol) was added and the reaction mixture continued to stir for 15 min. The reaction mixture was poured into toluene (150 mL) and washed with brine (2 x 100 mL). The organics were combined, dried over Na_2SO_4, filtered, concentrated to dryness and purified by flash chromatography two times (1st column: silica $CHCl_3$ to 0.1% MeOH in $CHCl_3$, 2nd column: silica, 0.5% EtOAc in CH_2Cl_2) to give a crude solid. Diethyl ether was added (3 x 20 mL),

decanted, and the solid was collected via vacuum filtration and washed with diethyl ether (40 mL) to yield **3** as an off-white solid (1.81 g, 19%). ^{1}H NMR (400 MHz, $CDCl_3$): δ 2.08 (6H, s), 3.83 (3H, s), 4.62 (2H, s), 5.89 (1H, s), 5.99 (2H, br), 6.18 (2H, q, J = 2.8 Hz), 6.60 (2H, s), 6.67 (2H, br m), 7.97 (2H, s). ^{13}C NMR (100 MHz, $CDCl_3$): δ 21.0, 38.1, 52.3, 65.1, 106.6, 108.7, 115.4, 116.3, 131.1, 131.2, 139.5, 156.3, 169.6. LRESI-MS calculated for [MH^+] 339.2, found 339.2.

(*Z*)-Methyl 2-(4-((5-chloro-1*H*-pyrrol-2-yl)(5-chloro-2*H*-pyrrol-2-ylidene)methyl)-3,5-dimethylphenoxy)acetate (4). A solution of **3** (1.76 g, 5.2 mmol) in anhydrous THF (67 mL) was wrapped in foil to protect it from light and cooled to -78 °C. *N*-Chlorosuccinimide (1.53 g, 11.5 mmol) in anhydrous THF (20 mL) was wrapped in foil to protect it from light and was added dropwise in two portions via an addition funnel over the course of 15 min. The reaction was stirred for an additional 2 h at -78 °C, capped, and then placed in the freezer (-20 °C) overnight. The crude reaction mixture was poured into water (100 mL) at 0 °C and then extracted with CH_2Cl_2 (3 x 100 mL). The organics were combined, dried over Na_2SO_4, filtered, concentrated to dryness, and purified by flash chromatography (1st column: silica, 5% hexanes in CH_2Cl_2 to 5% MeOH in CH_2Cl_2, 2nd column: silica, 20% hexanes in CH_2Cl_2 to CH_2Cl_2) to provide the dichloro dipyrromethane as a crude red solid. This was carried onto the next step without further purification. *p*-Chloranil (1.30 g, 5.3 mmol) was added to a solution of the crude intermediate (1.05 g, 2.6 mmol) in CH_2Cl_2 (25 mL) and the reaction mixture continued to stir overnight at room temperature. The red-orange reaction mixture was concentrated to dryness and the residue was purified by flash chromatography (silica, 20% hexanes in CH_2Cl_2) afforded **5** as a dark orange solid (924 mg, 44% over two steps). ^{1}H NMR (400 MHz, $CDCl_3$): δ 2.08 (6H, s), 3.84 (3H, s), 4.67 (2H, s), 6.18 (2H, d, J = 4 Hz), 6.31 (2H, d, J = 4.4 Hz), 6.64 (2H, s). ^{13}C NMR (100 MHz, $CDCl_3$): δ 20.3, 52.4, 65.2, 113.3, 117.2, 128.1, 128.7, 138.2, 138.6, 138.9, 141.5, 157.6, 169.5. LRESI-MS calculated for [MH^+] 405.1, found 405.1.

3,7-Dichloro-5,5-difluoro-10-(4-(2-methoxy-2-oxoethoxy)-2,6-dimethylphenyl)-5*H*-dipyrrolo[1,2-*c*:2',1'-*f*][1,3,2]diazaborinin-4-ium-5-uide (5). Distilled DIEA (1.78 mL, 10.2 mmol) was added dropwise to a solution of **4** (924 mg, 2.3 mmol) in anhydrous CH_2Cl_2 (25 mL) and the resulting solution was allowed to stir for an additional 20 min. BF_3•OEt_2 (2.6 mL, 20.5 mmol) was then added dropwise over a period of 5 min, and the resulting solution was allowed to stir overnight. The reaction mixture was quenched with water (100 mL) and then extracted with CH_2Cl_2 (3 x 25 mL). The organics were combined, dried over Na_2SO_4, filtered, and dried *in vacuo*. Purification by flash chromatography (silica, 10% hexanes in CH_2Cl_2) gave **5** as a red-orange solid with a green luster (771 mg, 75%). ^{1}H NMR (400 MHz, $CDCl_3$): δ 2.06 (6H, s), 3.80 (3H, s), 4.65 (2H, s), 6.34 (2H, d, J = 4 Hz), 6.58 (2H, d, J = 4.4 Hz), 6.65 (2H, s). ^{13}C NMR (100 MHz, $CDCl_3$): δ 20.2, 52.3, 64.9, 113.6, 119.0, 123.3, 130.3, 134.2, 138.5, 143.1, 144.8, 158.2, 169.1. LRESI-MS calculated for [MH^+] 453.1, found 453.0.

3-Chloro-5,5-difluoro-7-methoxy-10-(4-(2-methoxy-2-oxoethoxy)-2,6-dimethylphenyl)-5*H*-dipyrrolo[1,2-*c*:2',1'-*f*][1,3,2]diazaborinin-4-ium-5-uide (6). A solution of **5** (771 mg, 17 mmol) in anhydrous THF (40 mL) was cooled to 0 °C and 25 wt% sodium methoxide (398 mg, 18.4 mmol) in anhydrous MeOH (90 mL) was added dropwise in two portions over 2.5 h. The reaction mixture was maintained at 0 °C for 4 h until the reaction was complete by TLC analysis. The solvent was removed *in vacuo*, and the resulting solid was partitioned between water (50 mL) and CH_2Cl_2 (3 x 50 mL). The organics were combined, dried over Na_2SO_4, filtered, and dried *in vacuo*. Purification by flash chromatography (silica, CH_2Cl_2) delivered **6** as a red-orange

solid (640 mg, 84%). ^{1}H NMR (400 MHz, $CDCl_3$): δ 2.08 (6H, s), 3.83 (3H, s), 4.13 (3H, s), 4.65 (2H, s), 6.10 (1H, d, *J* = 4.8 Hz), 6.20 (1H, d, *J* = 4.0 Hz), 6.31 (1H, d, *J* = 4 Hz), 6.65 (2H, s), 6.70 (1H, d, *J* = 4.4 Hz). ^{13}C NMR (100 MHz, $CDCl_3$): δ 20.3, 52.4, 59.3, 65.1, 104.9, 113.5, 115.5, 124.8, 125.2, 130.7, 132.4, 133.9, 137.0, 139.0, 139.2, 158.0, 169.3, 169.6. LRESI-MS calculated for [MH^+] 449.1, found 449.1.

3-(Bis(2-((2-(ethylthio)ethyl)thio)ethyl)amino)-5,5-difluoro-7-methoxy-10-(4-(2-methoxy-2-oxoethoxy)-2,6-dimethylphenyl)-5*H*-dipyrrolo[1,2-*c*:2',1'-*f*][1,3,2]diazaborinin-4-ium-5-uide (8). Anhydrous MeCN (10 mL) was added to **6** (185 mg, 413 μmol) and **7** (575 mg, 1.8 mmol). The reaction mixture was purged with a stream of N_2 for five minutes and continued to stir at 45 °C in the dark for 72 h. The reaction mixture was concentrated to dryness. Purification by column chromatography (silica, 0.5% toluene in CH_2Cl_2 to 0.25% MeOH in CH_2Cl_2 to 0.5% MeOH in CH_2Cl_2) provided **8** as a red oil (168 mg, 56%). ^{1}H NMR (400 MHz, $CDCl_3$): d 1.20 (6H, t, *J* = 7.4 Hz), 2.05 (6H, s), 2.53 (4H, q, *J* = 7.4 Hz), 2.70—2.74 (4H, m), 2.77—2.81 (4H, m), 2.86 (4H, t, *J* = 7.2 Hz), 3.79 (3H, s), 3.89 (4H, t, *J* = 7.4 Hz), 3.93 (3H, s), 4.62 (2H, s), 5.60 (1H, d, *J* = 4 Hz), 5.94 (1H, d, *J* = 4.8 Hz), 6.09 (1H, d, *J* = 3.6 Hz), 6.41 (1H, d, *J* = 4.8 Hz), 6.60 (2H, s). ^{13}C NMR (100 MHz, $CDCl_3$): d 14.8, 20.2, 25.6, 30.1, 31.8, 32.2, 52.3, 53.3, 58.0, 65.0, 94.9, 110.0, 113.1, 121.7, 125.5, 126.8, 131.5, 133.0, 139.3, 157.3, 159.7, 161.6, 169.4. LRESI-MS calculated for [MH^+] 726.3, found 726.3.

3-(Bis(2-((2-(ethylthio)ethyl)thio)ethyl)amino)-10-(4-(carboxymethoxy)-2,6 dimethylphenyl)-5,5-difluoro-7-methoxy-5*H*-dipyrrolo[1,2-*c*:2',1'-*f*][1,3,2]diazaborinin-4-ium-5-uide (Carboxy-CS1 9). Powdered LiOH (20 mg, 833 μmol) was added to a solution of **8** (168 mg, 231 μmol) in anhydrous MeOH (3 mL) and anhydrous THF (3 mL) and the reaction mixture continued to stir overnight at room temperature. The reaction mixture was concentrated *in vacuo*, dissolved in water (15 mL), and the pH was adjusted to pH 1—2 with 0.5 M HCl. The reaction mixture was extracted with $CHCl_3$ (2 x 25 mL), the organics were combined, dried over Na_2SO_4, filtered, and dried *in vacuo*. Purification by column chromatography (silica, 1.5% MeOH in CH_2Cl_2 yielded **9** as a red oil (98 mg, 60%). ^{1}H NMR (400 MHz, $CDCl_3$): δ 1.24 (6H, t, *J* = 7.2 Hz), 2.10 (6H, s), 2.57 (4H, q, *J* = 7.2 Hz), 2.73—2.78 (4H, m), 2.81—2.85 (4H, m), 2.89 (4H, t, *J* = 7.2 Hz, *J* = 7.6 Hz), 3.93 (4H, t, *J* = 7.4 Hz), 3.97 (3H, s), 4.71 (2H, s), 5.64 (1H, d, *J* = 4.4 Hz), 5.96 (1H, d, *J* = 4.8 Hz), 6.13 (1H, d, *J* = 4 Hz), 6.45 (1H, d, *J* = 4.8 Hz), 6.66 (2H, s). ^{13}C NMR (100 MHz, $CDCl_3$): δ 14.8, 20.3, 26.0, 30.3, 31.7, 31.9, 32.2, 32.5, 53.3, 58.1, 64.7, 95.0, 110.1, 113.2, 121.8, 125.6, 127.2, 131.4, 131.6, 133.0, 139.6, 157.0, 159.8, 161.7, 173.6. LRESI-MS calculated for [MH^+] 712.2, found 712.2.

(2-Aminoethyl)triphenylphosphonium bromide (10). Compound **10** was prepared according to a previously reported procedure with the following modifications: the crude solid was triturated with diethyl ether as reported but it was not further recrystallized from ethanol/diethyl ether as reported. The characterization data were consistent with results previously reported in the literature.[93]

Mitochondrial Coppersensor-1 (Mito-CS1, 11). Compound **9** (98 mg, 137 μmol) and HATU (59 mg, 155 μmol) were dissolved in anhydrous CH_2Cl_2 (6 mL) and purged with a stream of N_2 for five minutes. After 20 min, **10** (59 mg, 153 μmol) was added in one portion and the reaction mixture continued to stir for 20 min. Distilled DIEA was added after 20 min and the reaction stirred at room temperature overnight. The reaction mixture was concentrated *in vacuo* and purified by column chromatography (1st column: silica, 0.25% EtOAc and 0.25% MeOH in

CH_2Cl_2, 2nd column: silica, 0.5% EtOAc and 0. 5% MeOH in CH_2Cl_2, 3rd column: silica, 0.25% EtOAc and 0.25% MeOH in CH_2Cl_2 to 1% MeOH in CH_2Cl_2) to furnish **11** as a red semi-solid (67 mg, 48%). ^{1}H NMR (400 MHz, $CDCl_3$): δ 1.23 (6H, t, J = 7.2 Hz, J = 7.6 Hz), 2.07 (6H, s), 2.56 (4H, q, J = 7.4 Hz), 2.72—2.76 (4H, m), 2.80—2.84 (4H, m), 2.88 (4H, t, J = 7.4 Hz), 3.52 (2H, p, J = 7.2 Hz), 3.74 (2H, p, J = 6.4 Hz, J = 7.2 Hz), 3.91 (4H, t, J = 7.4 Hz), 3.95 (3H, s), 4.34 (2H, s), 5.62 (1H, d, J = 4 Hz), 5.95 (1H, d, J = 4.8 Hz), 6.11 (1H, d, 4 Hz), 6.45 (1H, d, J = 4.8 Hz), 6.71 (2H, s), 7.67—7.83 (15H, m). ^{13}C NMR (100 MHz, $CDCl_3$): δ 14.8, 20.2, 26.0, 30.3, 31.9, 32.4, 33.3, 53.3, 58.0, 66.6 95.0, 110.1, 113.4, 117.1, 117.9, 121.9, 125.7, 126.9, 130.7, 130.8, 133.4, 133.5, 135.5, 139.3, 156.9, 159.7, 169.5. HRESI-MS calculated for [M^+] 999.3576, found 999.3585.

Control-CS1 (12). Compound **9** (74.8 mg, 105 μmol) and HATU (44 mg, 116 μmol) were dissolved in anhydrous CH_2Cl_2 (7 mL) and purged with a stream of N_2 for five minutes. After 1 hr, 2 M solution of diethylamine (200 μL, 400 μmol) was added in one portion and the reaction mixture continued to stir for 20 min. Distilled DIEA (200 μL, 1.1 μmol) was added after 20 min and the reaction stirred at room temperature overnight. The reaction mixture was concentrated *in vacuo* and purified by column chromatography (1st column: silica, 0.5% MeOH in CH_2Cl_2) followed by preparatory TLC (1.5% MeOH in CH_2Cl_2, silicato furnish **12** as a red oil (46 mg, 59%). ^{1}H NMR (400 MHz, $CDCl_3$): δ 1.18—1.26 (9H, m), 2.61 (6H, s), 2.56 (4H, q, J = 7.6 Hz), 2.73—2.77 (4H, m), 2.80—2.84 (4H, m), 2.89 (4H, t, J = 7.6 Hz), 3.41 (2H, p, J = 6.8 Hz, J = 7.2 Hz), 3.92 (4H, t, J = 7.6 Hz), 3.97 (3H, s), 4.49 (2H, s), 5.64 (1H, d, J = 4 Hz), 5.96 (1H, d, J = 4.8 Hz), 6.11 (1H, d, J = 4 Hz), 6.43 (1H, d, J = 4.8 Hz), 6.60 (1H, br s), 6.65 (2H, s). ^{13}C NMR (100 MHz, $CDCl_3$): δ 14.8, 20.3, 26.0, 32.3, 31.9, 32.2, 34.0, 53.3, 58.1, 67.3, 95.0, 110.2, 113.3, 118.0, 121.7, 125.6, 127.3, 131.3, 133.0, 139.7, 156.8, 159.8, 161.7, 168.0. HRESI-MS calculated for [MH^+] 739.2821, found 739.2836.

Rhodamine 123. Rhodamine 123 was prepared according to a previously reported procedure with the following modifications: the crude solid was triturated with chloroform and the resulting solid was collected via vacuum filtration and washed with chloroform. Characterization was consistent with that previously reported in the literature.[94]

Spectroscopic Materials and Methods. Millipore water was used to prepare all aqueous solutions. All spectroscopic measurements were performed in phosphate buffered saline (1X PBS, pH 7.4, Invitrogen, Carlsbad, CA). Absorption spectra were recorded on a Varian Cary 50 spectrophotometer (Walnut Creek, CA) and fluorescence spectra were recorded using a Photon Technology International Quanta Master 4 L-format scanning spectrofluorometer (Lawrenceville, NJ) equipped with an LPS-220B 75-W xenon lamp and power supply, A-1010B lamp housing with integrated igniter, switchable 814 photon-counting/analog multiplier detection unit, and MD5020 motor driver. Samples for absorption and emission measurements were contained in 1-cm x 1-cm path length quartz cuvettes (1.4-mL volume, Starna, Atascadero, CA). Fluorescence quantum yields were determined by reference to rhodamine 101 inner salt in methanol (Φ = 1.0).[95] The binding affinity of Cu^+ to Mito-CS1 was measured using thiourea as a competitive ligand to provide a buffered Cu^+ solution. Stability constants for thiourea binding were taken from the literature $\beta_{12} = 2.0 \times 10^{12}$, $\beta_{13} = 2.0 \times 10^{14}$, $\beta_{14} = 3.4 \times 10^{15}$.[96] Thiourea was delivered from an aqueous stock solution (200 mM, 500 mM). Cu^+ was delivered in the form of $[Cu(MeCN)_4[PF_6]]$ from an acetonitrile stock solution (1 mM, 5 mM). Excitation was provided at 540 nm and collected emission was integrated from 550 to 700 nm after 1 min or 2 min after the addition of dye or metal analyte. The apparent dissociation constant (K_d) was determined

using the following equation: $(F - F_{min})/(F_{max} - F_{min}) = [Cu^+]/(K_d + [Cu^+])$, where F is the observed fluorescence, F_{max} is the fluorescence for the Cu^+:Mito-CS1 complex, F_{min} is the fluorescence for free Mito-CS1, and $[Cu^+]$ is the 'free' Cu^+ available for complexation, which was calculated using the stability constants for thiourea and standard competition equilibrium expressions. All other metal ions tested for metal ion selectivity studies with the exception of Fe^{2+} were from their chloride salts as aqueous solutions. Ammonium iron(II) sulfate hexahydrate was used as a source of Fe^{2+} and the salt was dissolved in degassed water.

Preparation of Cell Cultures. Cells were grown in the Tissue Culture Facility at the University of California, Berkeley with expert technical assistance from Ann Fischer and Michelle Yasukawa. HEK 293T cells were cultured in Dulbecco's Modified Eagle Medium (DMEM, Invitrogen, Carlsbad, CA) containing high glucose and without phenol red supplemented with GlutaMAX (Invitrogen, Carlsbad, CA) and 10% Fetal Bovine Serum (FBS, Hyclone, Logan, UT). Two days before imaging, cells were passed and plated on 12-mm glass coverslips coated with poly-L-lysine (50 mg/mL, Sigma, St. Louis, MO). Control (MCH58), *ATP7A* (WG1005), *SCO1* (Line C), and *SCO2* (Bloesel) fibroblasts were cultured in Dulbecco's Modified Eagle Medium (DMEM, Invitrogen, Carlsbad, CA) containing high glucose and without phenol red supplemented with GlutaMAX (Invitrogen, Carlsbad, CA), 1 mM sodium pyruvate, and 10% Fetal Bovine Serum (FBS, Hyclone, Logan, UT). Two days before imaging, cells were passed and plated on 12-mm glass coverslips or 4-well chambered coverglass slides.

Cell Staining. For all experiments, solutions of Mito-CS1 (from 1 mM or 5 mM stocks in DMSO), CS3 (from 1 mM stocks in DMSO), Rhodamine 123 (from 50 μM stocks in DMSO), MitoTracker Deep Red (from a 50 μM stocks in DMSO), BODIPY FL C5-ceramide-BSA complex (from 1 mM stocks in water), and Hoechst 33342 (from a 5 mM stock in DMSO) were made in Dulbecco's Phosphate Buffered Saline with calcium chloride and magnesium chloride (DPBS, Invitrogen, Carlsbad, CA) or Dulbecco's Modified Eagle Medium without phenol red (DMEM, Invitrogen, Carlsbad, CA). For colocalization experiments control HEK 293T cells were incubated with 500 nM Mito-CS1, 2.25 μM BODIPY FL C5-ceramide-BSA complex, 50 nM Mitotracker Deep Red, and 5 μM Hoechst 33342 for 15 min at 37 °C, 5% CO_2 in DPBS. Coverslips were then transferred to fresh DPBS for imaging. A similar procedure was followed for imaging with 500 nM Lysotracker Green DND-26. For copper and BCS treatments, 300 mM $CuCl_2$ or 100 μM BCS was added to the cells from a 0.1 mM aqueous stock solution one day prior to imaging. Cells were then incubated at 37 °C, 5% CO_2. After 18 hours, the media was exchanged for DPBS with 500 nM Mito-CS1 or 100 nM Rhodamine 123 and Hoechst 33342 and incubated for 15 min at 37 °C, 5% CO_2. Coverslips were then transferred to fresh DPBS for imaging. For colocalization experiments control fibroblasts were incubated with 5 μM Mito-CS1, 2.25 μM BODIPY FL C5-ceramide-BSA complex, and 5 μM Hoechst 33342 for 15 min at 37 °C, 5% CO_2 in DPBS. A similar procedure was followed for imaging with 250 nM Lysotracker Green DND-26 in DMEM. Coverslips were then transferred to fresh DPBS for imaging. MitoTracker Deep Red (50 nM in DPBS) was added on stage and then imaged. For BCS treatment, 100 μM BCS was added to the cells from a 0.1 mM aqueous stock solution one day prior to imaging. After 12 hours, the media was exchanged for DMEM with 5 μM Mito-CS1 or 100 nM Rhodamine 123 and 5 μM Hoechst 3342 and incubated for 15 min at 37 °C, 5% CO_2. Coverslips were then transferred to fresh DPBS for imaging. Similar procedures were followed for imaging changes in mitochondrial Cu^+ in the wild type, *ATP7A*, *SCO1*, and *SCO2* fibroblasts. For copper treatment, 300 μM or 500 μM $CuCl_2$ was added to the cells from a 0.1 mM aqueous

stock solution one day prior to imaging. After 18 hours, the media in the chambered coverglass slides was exchanged for DMEM with 5 μM Mito-CS1 or 100 nM Rhodamine 123 and 5 μM Hoechst 3342 and incubated for 15 min at 37 °C, 5% CO_2, washed with fresh DPBS, and imaged in fresh DPBS. Control and *ATP7A* patient fibroblasts were stained with 2 μM CS3 and incubated for 10 min at 37 °C, 5% CO_2 in DPBS, washed with fresh DPBS, and imaged in fresh DPBS.

Fluorescence Imaging Experiments. Confocal fluorescence images were acquired at the Molecular Imaging Center at the University of California, Berkeley. Imaging experiments were performed with a Zeiss LSM510 META NLO Axioplan 2 laser-scanning microscope, a Zeiss 510NL META AxioIMAGER laser-scanning microscope, and a Zeiss LSM 710 laser-scanning microscope with a 40x or 63x water-immersion objective lens. Excitation of Mito-CS1 or CS3 loaded cells at 543 nm was carried out with a HeNe laser, and emission was collected using a META detector between 554—650 nm. For the XRF samples described below excitation of Control-CS1 loaded cells was carried out at 543 nm with a HeNe laser, and emission was collected using a META detector between 553—651 nm. Excitation of Lysotracker Green DND-26 at 488 nm was carried out with an Ar laser, and emission was collected using a META detector between 501—533 nm. Excitation of BODIPY FL C5-ceramide-BSA complex at 488 nm was carried out with an Ar laser, and emission was collected using a META detector between 498—511 nm. Excitation of Rhodamine 123 at 488 nm was carried out with an Ar laser, and emission was collected using a META detector between 501—576 nm. Excitation of MitoTracker Deep Red at 633 nm was carried out with a HeNe laser, and emission was collected using a META detector between 640—704 nm. Excitation of Hoechst 33342 was carried out using a MaiTai two photon laser at 780-nm pulses or a 405 nm diode laser and emission was collected between 469—522 nm with Rhodamine 123 and 447—533 nm for all other dyes. ImageJ from the National Institutes of Health was used for analysis of the images. Specifically, the threshold for a field of cells was adjusted to select the pixels and was kept consistent in a given experiment. The selected pixels were analyzed for the median value. The mean of the median value for n fields of cells with standard error is reported and statistical analyses were performed with a two-tailed Student's *t*-test in Microsoft Excel.

X-Ray Fluorescence Microscopy (XRFM) Samples. Fibroblasts were plated on poly-L-lysine coated silicon nitride windows (2 × 2 mm; 250 nm or 500 nm thickness) manufactured by Silson and stained with 5 μM Control-CS1, 2.25 μM BODIPY FL C5-ceramide-BSA complex, and 50 nM Mitotracker Deep Red for 15 min 37 °C, 5% CO_2 in DMEM. The fibroblasts were then imaged live in in DPBS and then fixed in 4% paraformaldehyde (PFA) in PBS for 10 min. Residual PBS was removed by several washes in 20 mM PIPES, pH 7.2⁄200 mM sucrose followed by air drying. X-ray fluorescence imaging was carried out with the scanning X-ray microprobe at beamline 2-ID-E at the Advanced Photon Source (Argonne National Laboratory) using a 20 cm zone plate with 1-micron step size and 1 sec dwell time as previously described.[97]

ICP-OES analysis.[36] Mitochondria and whole cells were digested in 40% nitric acid by boiling for 1 hr in capped, acid-washed tubes; samples were then diluted in ultra-pure, metal-free water; and analyzed by ICP-OES (PerkinElmer, Optima 3100XL). Acid-washed blanks were used as controls. Concentrations were determined from a standard curve constructed with serial dilutions of commercially available mixed metal standards (Optima). Error bars cannot be added to the data points for mitochondria isolated from *SCO1* and *SCO2* patient liver, owing to the scarcity of the material; the total tissue sample only consists of milligram quantities originating from a

metabolic autopsy, thus precluding additional, large-scale analyses. Furthermore, we did not have access to liver samples from deceased *ATP7A* patients. To minimize any potential effects associated with experimental variability, mitochondria were isolated on the same day using identical buffers and reagents from each patient sample. Each sample was then split into two aliquots, and total mitochondrial copper content quantified in duplicate by ICP-OES in the same run.

Miscellaneous Procedures. COX and citrate synthase activities were measured in HEK 293T and fibroblast cell extracts as described elsewhere.[32,98] Protein concentration was measured by the Bradford method.[99]

Schemes and Figures

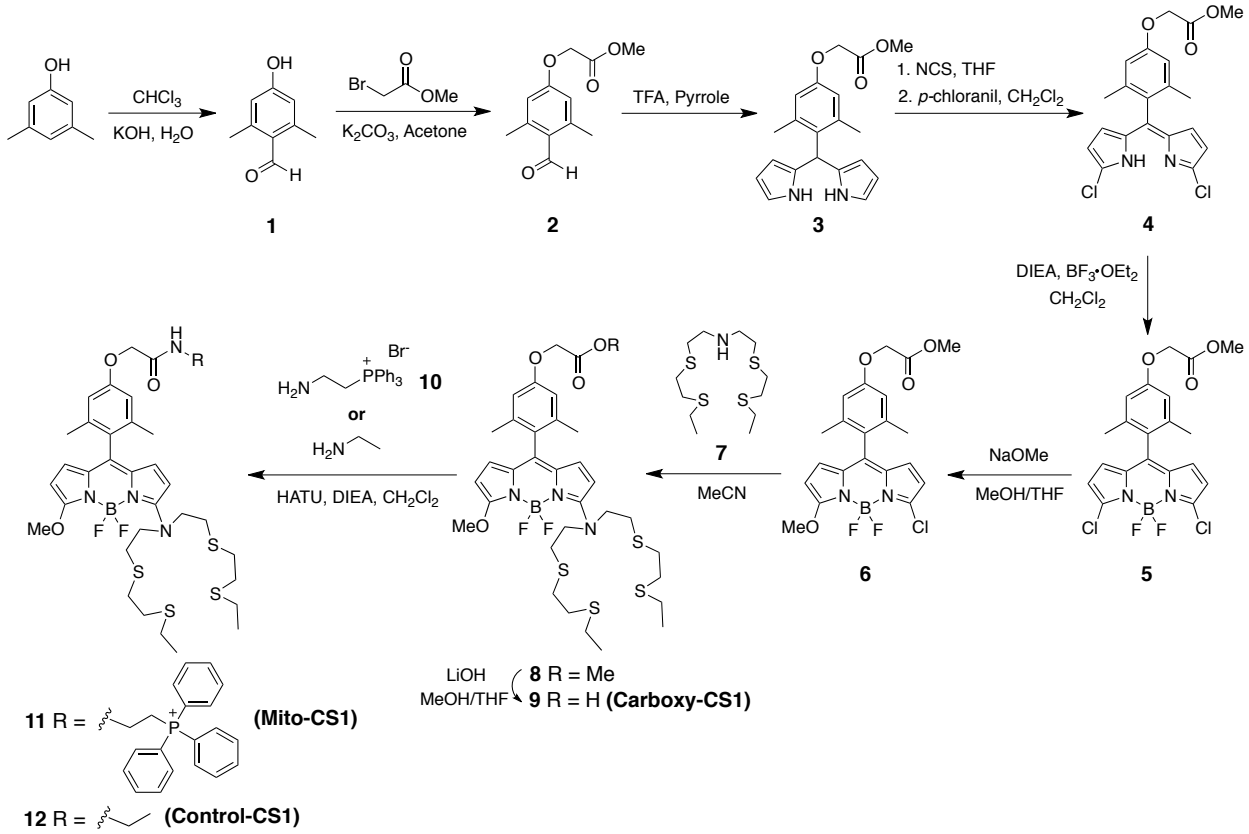

Scheme 3-1. Synthesis of Mitochondrial Coppersensor-1 (Mito-CS1).

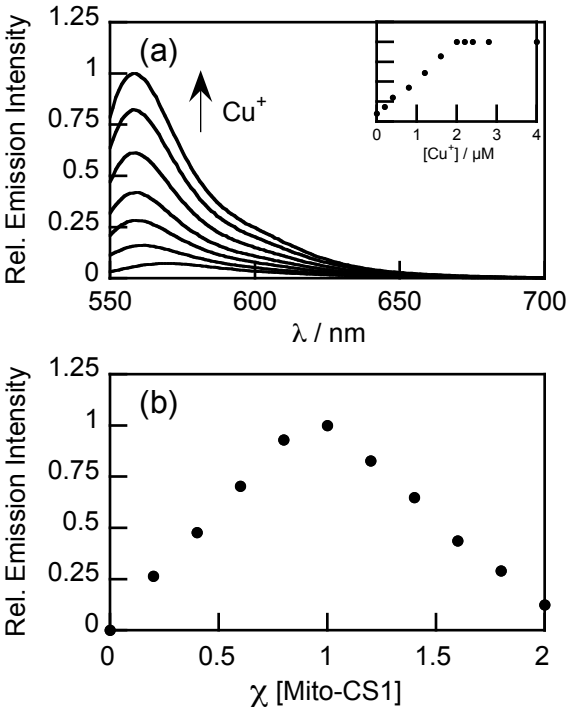

Figure 3-1. Mito-CS1 responds to Cu^+ in an aqueous solution with 1:1 binding. (a) Fluorescence response of 2 μM Mito-CS1 to Cu^+. Spectra shown are for Cu^+ concentrations of 0, 0.2, 0.4, 0.8, 1.2, 1.6, 2.0, 2.2, 2.4, 2.8, and 4 μM. Spectra were acquired in PBS, pH 7.4, with 540 nm excitation. Inset, normalized fluorescence response (y-axis) of 2 μM Mito-CS1 to Cu^+. Spectra were acquired in PBS, pH 7.4. Excitation was provided at 540 nm and the integrated emission was collected from 550—700 nm. (b) Normalized Job's plot of Mito-CS1 and Cu^+. The total concentration of Mito-CS1 and Cu^+ were kept constant at 2 μM. Spectra were acquired in PBS, pH 7.4. Excitation was provided at 540 nm and emission intensity was measured at 558 nm.

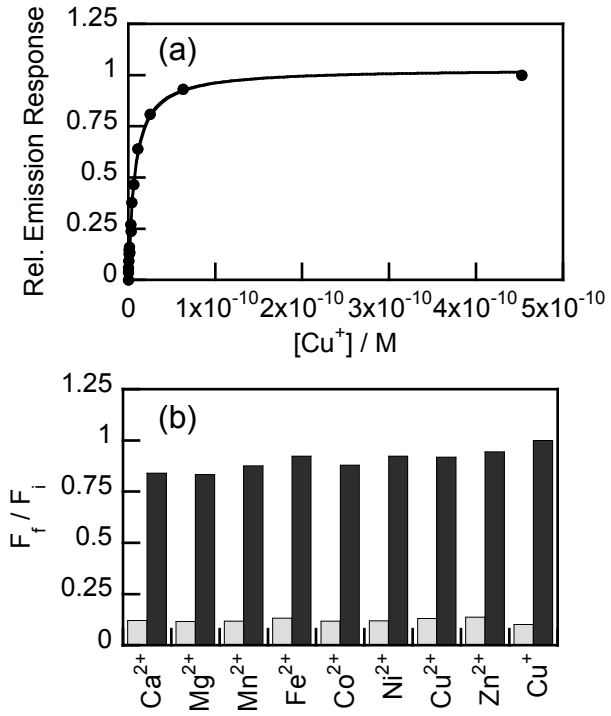

Figure 3-2. Mito-CS1 can respond to a dynamic range of Cu^+ concentrations and is selective for Cu^+ over other biologically relevant metal ions. (a) Normalized fluorescence responses of 2 μM Mito-CS1 to thiourea buffered Cu^+ solutions for K_d value determination. Spectra were acquired in PBS, pH 7.4. Excitation was provided at 540 nm and the collected emission was integrated over 550—700 nm. The points shown are for free Cu^+ buffered at 0.10, 0.21, 0.45, 0.72, 0.91, 1.3, 1.4, 2.6, 3.0, 3.8, 6.1, 10.9, 25.1, 63.1, 452.5 pM, respectively. The observed K_d value is 7.2(3) x 10^{-12} M. (b) Fluorescence responses of 2 μM Mito-CS1 to various metal ions. Bars represent the final (F_f) over the initial (F_i) integrated emission. Gray bars represent the addition of the competing metal ion (2 mM for Ca^{2+} and Mg^{2+}, 500 μM for Zn^{2+}, and 50 μM for all other cations) to a 2 μM solution of Mito-CS1. Black bars represent the addition of 2 mM Cu^+ to the solution. Spectra were acquired in PBS, pH 7.4. Excitation was provided at 540 nm, with emission integrated over 550—700 nm.

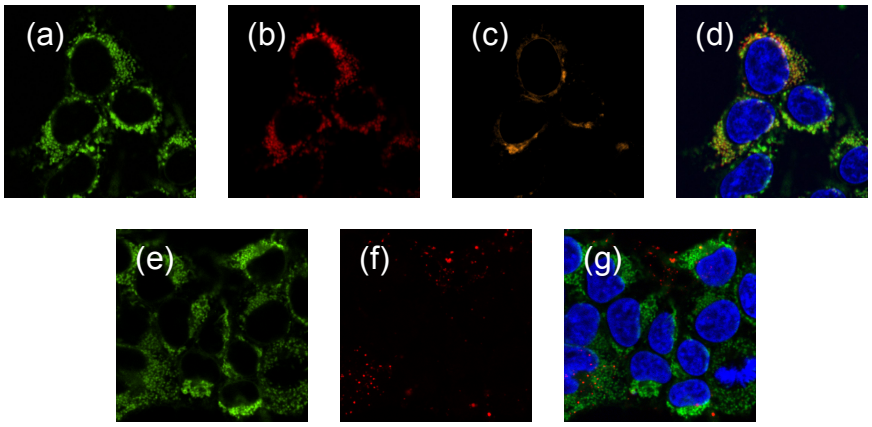

Figure 3-3. Mito-CS1 colocalizes to mitochondria in live HEK 293T cells. HEK cells were stained with (a) 500 nM Mito-CS1, (b) 50 nM MitoTracker Deep Red, and (c) 2.25 μM BODIPY FL C5-ceramide-BSA complex and 5 μM Hoechst 33342 for 15 min at 37 °C in DPBS. (d) Overlay of (a) and (b) with Hoechst 33342. Live-cell molecular imaging shows that Mito-CS1 does not colocalize to lysosomes in live HEK 293T cells. HEK 293T cells were stained with (e) 500 nM Mito-CS1, (f) 500 nM Lysotracker Green DND-26, and 5 μM Hoechst 33342 for 15 min at 37 °C in DPBS. (g) Overlay of (e) and (f) with Hoechst 33342.

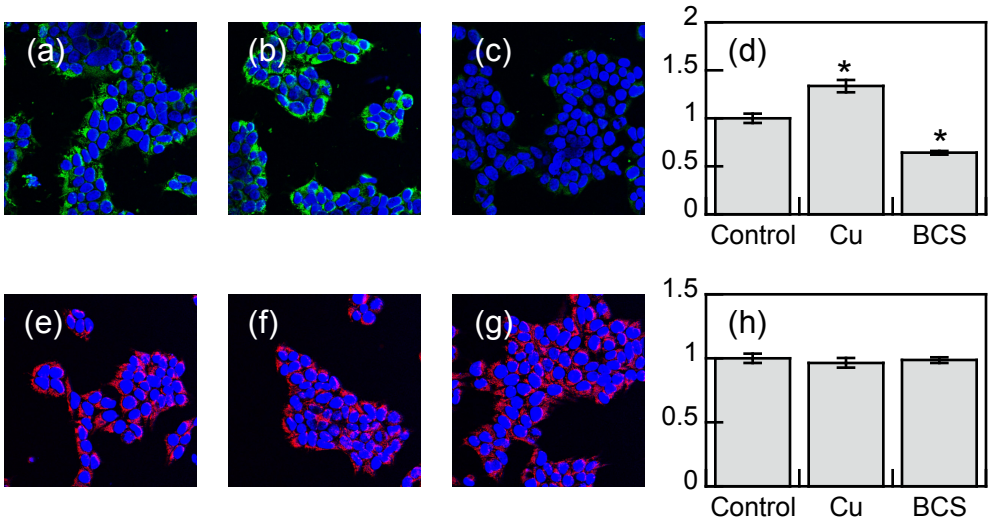

Figure 3-4. Live-cell molecular imaging with Mito-CS1 and Rhodamine 123 reveals a labile mitochondrial Cu^{+} pool in HEK 293T Cells. (a) Control HEK cells, (b) HEK cells supplemented with 300 μM $CuCl_2$ in the growth medium for 18 h at 37 °C, and (c) HEK cells supplemented with 100 μM BCS in the growth medium for 18 h at 37 °C were stained with 500 nM Mito-CS1 and 5 μM Hoechst 33342 for 15 min at 37 °C in DPBS. (d) Plot of the mean fluorescence intensity of (a)—(c). Data were normalized to the control and statistical analyses were performed with a two-tailed Student's *t*-test (n = 4 fields of cells) relative to the control. **P* < 0.01 and error bars are ± s.e.m. (e) Control HEK cells, (f) HEK cells supplemented with 300 μM $CuCl_2$ in the growth medium for 18 h at 37 °C, and (g) HEK cells supplemented with 100 μM BCS in the growth medium for 18 h at 37 °C were stained with 100 nM Rhodamine 123 and 5 μM Hoechst 33342 for 15 min at 37 °C in DPBS. (h) Plot of the mean fluorescence intensity of (e)—(g). Data were normalized to the control, statistical analyses were performed with a two-tailed Student's *t*-test (n = 4 fields of cells) relative to the control, and error bars are ± s.e.m.

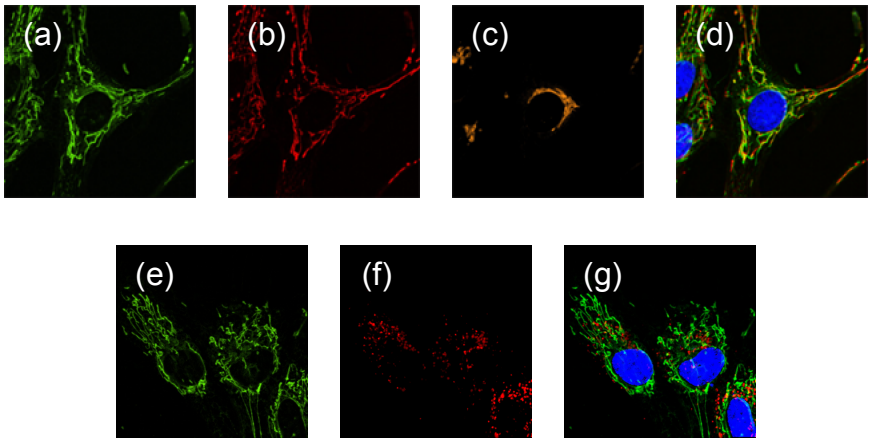

Figure 3-5. Live-cell molecular imaging shows that Mito-CS1 colocalizes to mitochondria in a control cell line derived from human fibroblasts. Control fibroblasts were stained with (a) 5 μM Mito-CS1, (b) 50 nM MitoTracker Deep Red, (c) 2.25 μM BODIPY FL C5-ceramide-BSA complex and 5 μM Hoechst 33342 for 15 min at 37 °C in DPBS. (d) Overlay of (a) and (b) with Hoechst 33342. Control fibroblasts were stained with (e) 5 μM Mito-CS1, (f) 250 nM Lysotracker Green DND-26 and 5 μM Hoechst 33342 for 15 min at 37 °C in DMEM. (g) Overlay of (e) and (f) with Hoechst 33342.

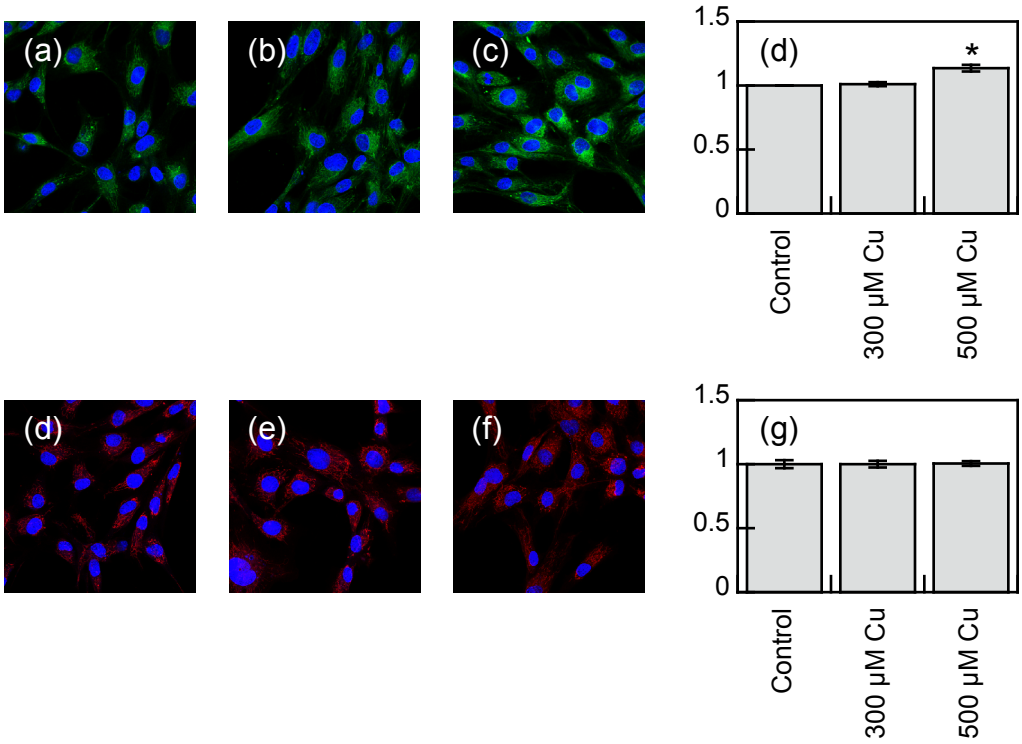

Figure 3-6. Live-cell molecular imaging with Mito-CS1 and Rhodamine 123 in an untreated and copper-supplemented control cell line derived from human fibroblasts. (a) Control fibroblasts, (b) control fibroblasts supplemented with 300 μM $CuCl_2$, and (c) 500 μM $CuCl_2$ in the growth medium for 18 h at 37 °C were stained with 5 μM Mito-CS1 and 5 μM Hoechst 33342 for 15 min at 37 °C in DMEM. (d) Plot of the mean fluorescence intensity of (a)—(c). Data were normalized to the control, statistical analyses were performed with a two tailed Student's *t*-test (n ≥ 4 fields of cells). **P* < 0.01 and error bars are ± s.e.m. (d) Control fibroblasts, (e) control fibroblasts supplemented with 300 μM $CuCl_2$, and (f) 500 μM $CuCl_2$ in the growth medium for 18 h at 37 °C were stained with 100 nM Rhodamine 123 and 5 μM Hoechst 33342 for 15 min at 37 °C in DMEM. (f) Plot of the mean fluorescence intensity of (d)—(f). Data were normalized to the control, statistical analyses were performed with a two tailed Student's *t*-test (n ≥ 4 fields of cells), and error bars are ± s.e.m.

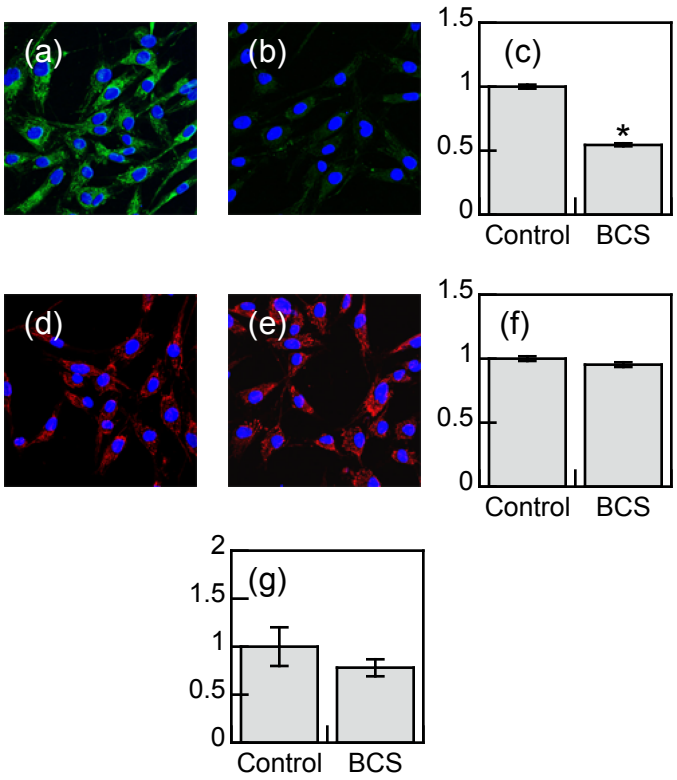

Figure 3-7. Live-cell molecular imaging with Mito-CS1 and Rhodamine 123, biochemical approaches, and elemental analyses reveal that there is a dynamic mitochondrial Cu^{+} pool in a control cell line derived from human fibroblasts. (a) Control fibroblasts, (b) control fibroblasts supplemented with 100 μM BCS in the growth medium for 12 h at 37 °C were stained with 5 μM Mito-CS1 and 5 μM Hoechst 33342 for 15 min at 37 °C in DMEM. (c) Plot of the mean fluorescence intensity of (a) and (b). Data were normalized to the control and statistical analyses were performed with a two-tailed Student's *t*-test (n = 5 fields of cells). **P* < 0. 01 and error bars are ± s.e.m. (d) Control fibroblasts, (e) control fibroblasts supplemented with 100 mM BCS in the growth medium for 12 h at 37 °C were stained with 100 nM Rhodamine 123 and 5 μM Hoechst 33342 for 15 min at 37 °C in DMEM. (f) Plot of the mean fluorescence intensity of (d) and (e). Data were normalized to the control, statistical analyses were performed with a two-tailed Student's *t*-test (n = 5 fields of cells), and error bars are ± s.e.m. (g) COX activity[32,98] was measured in control fibroblasts and control fibroblasts supplemented with 100 μM BCS in the growth medium for 24 h. Data were normalized to the control, statistical analyses were performed with a two-tailed Student's *t*-test (n = 3), and error bars are ± s.e.m.

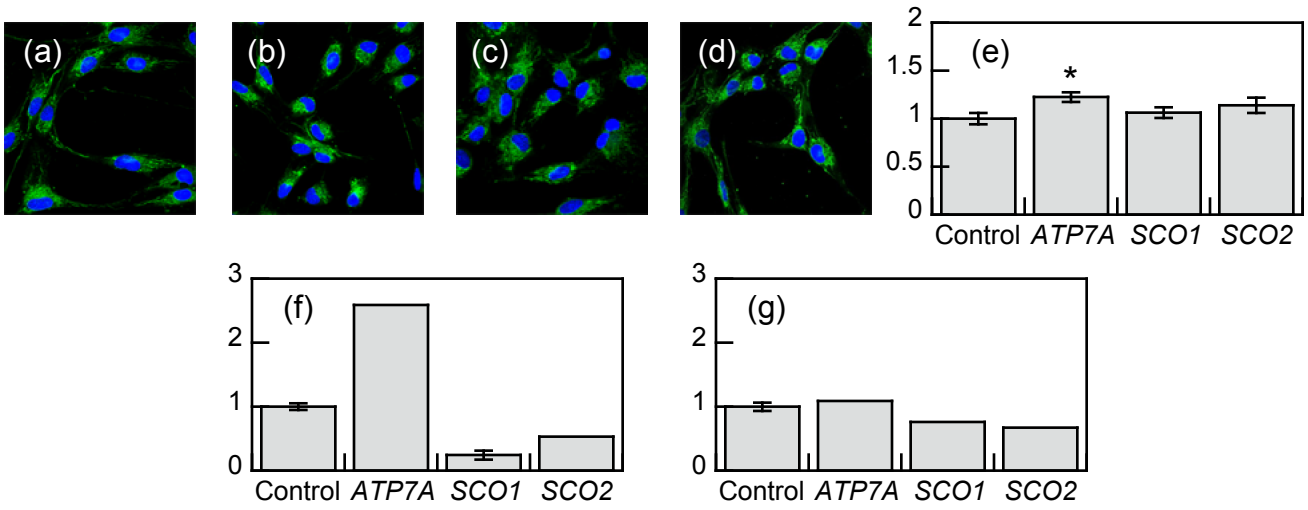

Figure 3-8. Live-cell molecular imaging with Mito-CS1, biochemical approaches, and bulk metal ion analyses confirm that mutations in *SCO1* and *SCO2* do not significantly perturb the mitochondrial copper homeostasis. (a) Control fibroblasts, (b) *ATP7A* patient fibroblasts, (c) *SCO1* patient fibroblasts, and (d) *SCO2* patient fibroblasts were stained with 5 μM Mito-CS1 and 5 mM Hoechst 33342 for 15 min at 37 °C in DMEM. (e) Plot of the mean fluorescence intensity of (a)—(d). Data were normalized to the control and statistical analyses were performed with a two-tailed Student's *t*-test (n ≥ 4 fields of cells) relative to the control. **P* < 0.05, and error bars are ± s.e.m. (f) Total copper levels were measured in control (n = 7), *ATP7A*, *SCO1* (n = 6) and *SCO2* patient fibroblasts and (g) mitochondrial copper levels were measured in control (n = 4), *ATP7A*, *SCO1* and *SCO2* patient fibroblasts by ICP-OES and are expressed as a fraction of the control using a previously described procedure.[36]

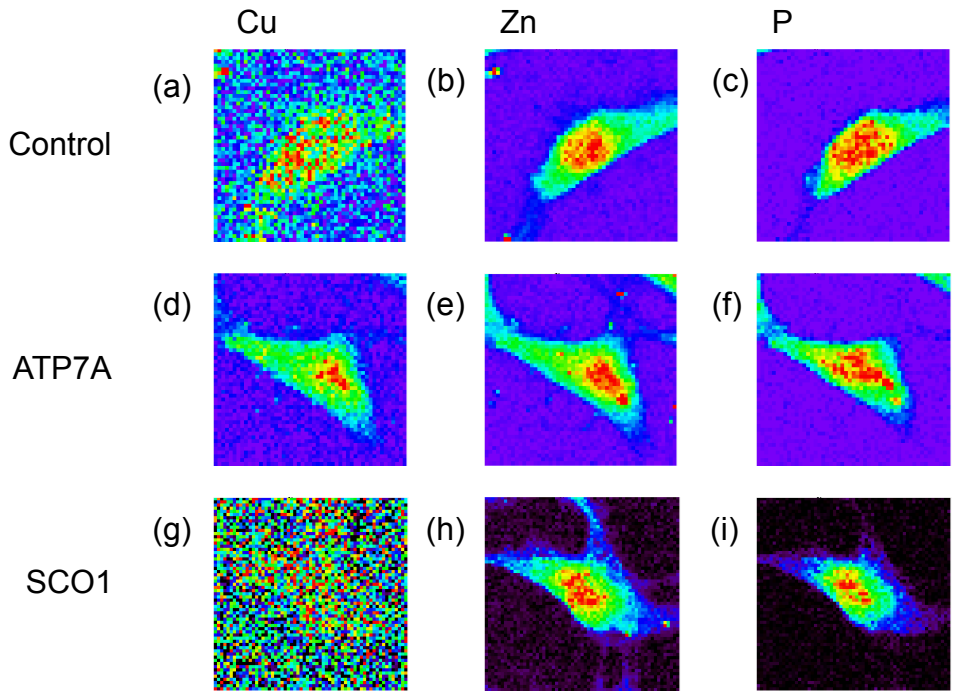

Figure 3-9. Representative XRFM metal maps from control (n = 9 cells), *ATP7A* (n = 8 cells), and *SCO1* (n = 8 cells) patient fibroblasts. Images shown are for (a, d, g) Cu, (b, e, h) Zn, and (c, f, i) P channels.

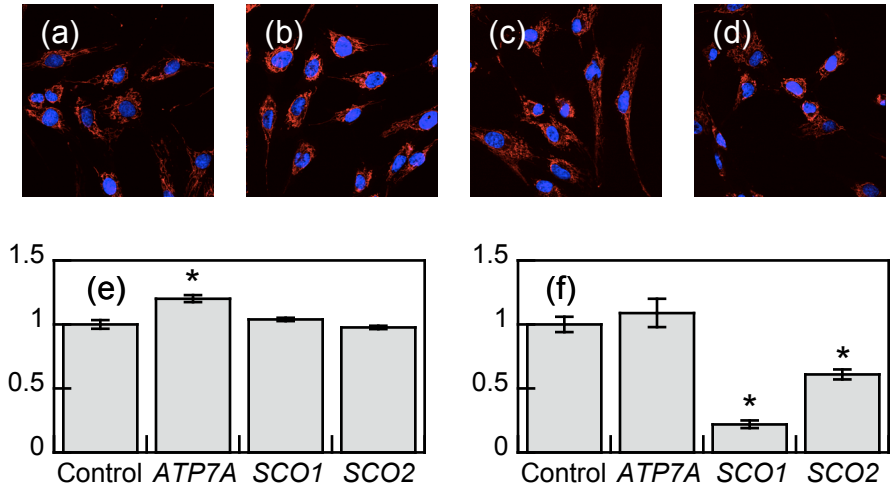

Figure 3-10. Live-cell molecular imaging with Rhodamine 123 and biochemical approaches reveal that the membrane potential is preserved in COX-deficient fibroblasts derived from SCO1 and SCO2 patients. (a) Control, (b) ATP7A, (c) SCO1, and (d) SCO2 patient fibroblasts were stained with 50 nM Rhodamine 123 and 5 μM Hoechst 33342 for 15 min at 37 °C in DMEM. (e) Plot of the mean fluorescence intensity of (a)—(d). Data were normalized to the control and statistical analyses were performed with a two-tailed Student's t-test ($n \geq 4$ fields of cells) relative to the control. $^{*}P < 0.01$ and error bars are ± s.e.m. (f) COX activity was measured in control, ATP7A, SCO1 and SCO2 fibroblasts using a previously described procedure.[32,98] Data were normalized to the control and statistical analyses were performed with a two-tailed Student's t-test ($n = 3$) relative to the control. $^{*}P < 0.01$ and error bars are ± s.e.m.

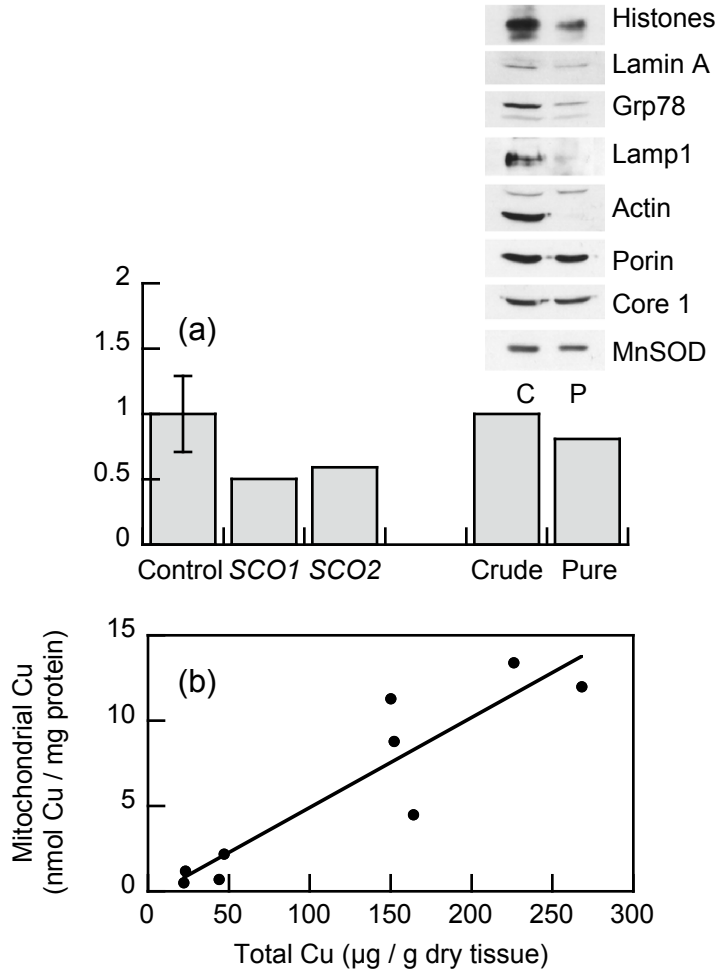

Figure 3-11. Biochemical approaches and elemental analyses confirm that mutations in *SCO1* and *SCO2* do not significantly perturb the mitochondrial copper pool. (a) ICP-OES measurements of copper content of crude mitochondria isolated from control (n = 9), *SCO1* and *SCO2* patient liver and crude and pure (nycodenz-floated) mitochondria from HEK 293T cells. Inset, immunoblot analysis of the abundance of various maker proteins in crude (C) and pure (P) mitochondria isolated from HEK 293T cells; nucleus (Histones, Lamin A), endoplasmic recticulum (Grp78), peroxisome (Lamp1), cytoskeleton (Actin) and mitochondria (Porin, Core1, SOD2). (b) Scatter plot of total copper versus mitochondrial copper in control livers (n = 9) (Linear regression: $y = 0.0526x - 0.3331$, $R^2 = 0.8293$).

References

1. Gray, H. B.; Stiefel, E. I.; Valentine, J. S.; Bertini, I. *Biological Inorganic Chemistry: Structure and Reactivity*, 1st ed.; University Science Books: California, **2006**.
2. Turski, M. L.; Thiele, D. J. *J. Biol. Chem.* **2009**, *284*, 717—721.
3. Banci, L.; Bertini, I.; Ciofi-Baffoni, S.; Kozyreva, T.; Zovo, K.; Paulmaa, P. *Nature*. **2010**, *465*, 645—648.
4. Camakaris, J.; Voskoboinik, I.; Mercer, J. F. *Biochem. Biophys. Res. Commun.* **1999**, *261*, 225—232.
5. Rosenzweig, A. C.; O'Halloran, T. V. *Curr. Opin. Chem. Biol.* **2000**, *4*, 140—147.
6. O'Halloran, T. V.; Culotta, V. C. *J. Biol. Chem.* **2000**, *275*, 25057—25060.
7. Lee, J.; Marjorette, M. O.; Nose, Y.; Thiele, D. J. *J. Biol. Chem.* **2002**, *277*, 4380—4387.
8. Rees, E. M.; Lee, J.; Thiele, D. J. *J. Biol. Chem.* **2004**, *279*, 54221—54229.
9. Fontaine, S. L.; Mercer, J. F. B. *Arch. Biochem. Biophys.* **2007**, *463*, 149—167.
10. Davis, A. V.; O'Halloran, T. V. *Nat. Chem. Biol.* **2008**, *4*, 148—151.
11. Kim, B. -E.; Nevitt, T.; Thiele, D. J. *Nat. Chem. Biol.* **2008**, *4*, 176—185.
12. Prohaska, J. R. *Am. J. Clin. Nutr.* **2008**, *88*, 826S—829S.
13. Kaplan, J. H.; Lutsenko, S. *J. Biol. Chem.* **2009**, *284*, 25461—25465.
14. Ma, Z; Jacobsen, F. E.; Giedroc, D. P. *Chem. Rev.* **2009**, *109*, 4644—4681.
15. Boal, A. K.; Rosenweig, A. C. *Chem. Rev.* **2009**, *109*, 4760—4779.
16. Hass, K. L.; Franz, K. J. *Chem. Rev.* **2009**, *109*, 4921—4960.
17. White, C.; Lee. J.; Kambe, T.; Fritsche, K.; Petris. M. J. *J. Biol. Chem.* **2009**, *284*, 33949—33956.
18. Barry, A. N.; Shinde, U.; Lutsenko, S. *J. Biol. Inorg. Chem.* **2010**, *15*, 47—59.
19. McRae, R.; Lai, B.; Fahrni, C. J. *J. Biol. Inorg. Chem.* **2010**, *15*, 99—105.
20. Bertini, I.; Cavallaro, G.; McGreevy, K. S. *Coord. Chem. Rev.* **2010**, *254*, 506—524.
21. Banci, L.; Bertini I.; McGreevy, K. S.; Rosato, A. *Nat. Prod. Rep.* **2010**, *27*, 695—710.
22. Robinson, N. J.; Winge, D. R. *Annu. Rev. Biochem.* **2010**, *79*, 537—562.
23. Banci, L.; Bertini, I.; Cantini, F.; Ciofi-Baffoni, S. *Cell. Mol. Life Sci.* **2010**, *67*, 2563—2589.
24. Rubino, J. T.; Riggs-Gelasco, P.; Franz, K. J. *J. Biol. Inorg. Chem.* **2010**, *15*, 1033—1049.
25. Cobine, P. A.; Pierrel, F.; Winge, D. R. *Biochim. Biophys. Acta*. **2006**, *1763*, 759—772.
26. Pierrel, F.; Cobine, P. A.; Winge, D. R. *Biometals*. **2007**, *20*, 675—682.
27. Horn, D.; Barrientos, A. *IUBMB Life*. **2008**, *60*, 421—429.
28. Abriata, L. A.; Banci, L.; Bertini, I.; Ciofi-Baffoni, S.; Gkazonis, P.; Spyroulias, G. A.; Vila, A. J.; Wang, S. *Nat. Chem. Biol.* **2008**, *4*, 599—601.
29. Leary, S. C.; Winge, D. R.; Cobine, P. A. *Biochim. Biophys. Acta*. **2009**, *1793*, 146—153.
30. Atkinson, A.; Winge, D. R. *Chem. Rev.* **2009**, *109*, 4708—4721.
31. Cobine, P. A.; Pierrel, F.; Bestwick, M. L.; Winge, D. R. *J. Biol. Chem.* **2006**, *281*, 36552—36559.
32. Leary, S. C.; Kaufman, B. A.; Pellecchia, G.; Guercin, G.; Mattman, A.; Jaksch, M.; Shoubridge, E. A. *Hum. Mol. Genet*. **2004**, *13*, 1839—1848.
33. Williams, J. C.; Sue, C.; Banting, G. S.; Yang, H.; Glerum, D. M.; Hendrickson, W. A.; Schon, E. A. *J. Biol. Chem*. **2005**, *280*, 15202—15211.
34. Horng, Y. –C.; Leary, S. C.; Cobine, P. A.; Young, F. B. J.; George, G. N.; Shoubridge, E. A.; Winge, D. R. *J. Biol. Chem.* **2005**, 280, 34113—34122.
35. Matoba, S.; Kang, J. –G.; Patino, W. D.; Wragg, A.; Boehm, M.; Gavrilova, O., Hurley, P. J.; Bunz, F.; Hwang, P. M. *Science*. **2006**, *312*, 1650—1653.

36. Leary, S. C.; Cobine, P. A.; Kaufman, B. A.; Guercin, G.; Mattman, A.; Palaty, J.; Lockitch, G.; Winge, D. R.; Rustin, P.; Horvath, R.; Shoubridge, E. A. *Cell Metabolism*. **2007**, *5*, 9—20.
37. Banci, L.; Bertini, I.; Cavallaro, G.; Rosato, A. *J. Proteome Res.* **2007**, *6*, 1568—1579.
38. Banci, L.; Bertini, I.; Ciofi-Baffoni, S.; Hadjiloi, T.; Martinelli, M.; Palumaa, P. *Proc. Natl. Acad. Sci. U.S.A*. **2008**, *105*, 6803—6808.
39. Rigby, K.; Cobine, P. A.; Khalimonchuk, O.; Winge, D. R. *J. Biol. Chem.* **2008**, *283*, 15015—15022.
40. Leary, S. C.; Sasarman, F.; Nishimura, T.; Shoubridge, E. A. *Hum. Mol. Genet*. **2009**, *18*, 2230—2240.
41. Sung, H. J.; Ma, W.; Wang, P. –y.; Hynes, J.; O'Riordan, T. C.; Combs, C. A.; McCoy, J. P. Jr.; Bunz, F.; Kang, J. –G.; Hwang, P. M. *Nat. Commun.* **2010**, *1*, 1—8.
42. Stiburek, L.; Zeman, J.; *Biochim. Biophys. Acta*. **2010**, *1797*, 1149—1158.
43. Leary, S. C. *Antioxid. Redox Signal.* **2010**, *13*, 1403—1416.
44. Banci, L.; Bertini, I.; Ciofi-Baffoni, S.; Kozyreva, T.; Mori, M.; Wang, S. *J. Biol. Inorg. Chem.* **2011**, *16*, 391—403.
45. Papadopoulou, L. C.; Sue, C. M.; Davidson, M. M.; Tanji, K.; Nishino, I.; Sadlock, J. E.; Krishna, S.; Walker, W.; Selby, J.; Glerum, D.M., et al. *Nat. Genet.* **1999**, *23*, 333—337.
46. Jaksch, M.; Ogilvie, I.; Yao, J.; Hortenhaus, G.; Bresser, H. G.; Gerbitz, K. D.; Shoubridge, E. A. *Hum. Mol. Genet.* **2000**, *9*, 795—801.
47. Horvath, R.; Lochmüller, Stucka, R.; Yao, J.; Shoubridge, E. A.; Kim, S. –H.; Gerbitz, K. –D.; Jaksch, M. *Biochem. Biophys. Res. Commun.* **2000**, *276*, 530—533.
48. Valnot, I.; Osmond, S.; Gigarel, N.; Mehaye, B.; Amiel, J.; Cormeir-Daire, V.; Munnich, A.; Bonnefont, J. P.; Rustin, P.; Rotig, A. *Am. J. Hum. Genet.* **2000**, 67, 1104—1109.
49. Jaksch, M.; Horvath, R.; Horn, N.; Auer, D. P.; Macmillan, C.; Peters, J.; Gerbitz, K. D.; Kraegeloh-Mann, I.; Muntau, A.; Karcagi, V.; Kalmanchey, R.; Lochmuller, H.; Shouebridge, E. A.; Freisinger, P. *Neurology*. **2001**, *57*, 1440—1446.
50. Jaksch, M.; Paret, C.; Stucka, R.; Horn, N.; Müller-Höcker, J.; Horvath, R.; Trepesch, N.m; Stecker, G.; Fresinger, P.; Thirion, C.; Müller, J.; Lunkwitz, R.; Rödel, G.; Shoubridge, E. A.; Lochmüller, H. *Hum. Mol. Genet*. **2001**, *10*, 3025—3035.
51. Salviati, L.; Hernandez-Rosa, E.; Walker, W. F.; Sacconi S.; Dimauro, S.; Schon, E. A.; Davidson, M. M. *Biochem. J.* **2002**, *363*, 321—327.
52. Hamza, I.; Giltin, J. D. *J. Bioenerg. and Biomembr*. **2002**, *34*, 381—388.
53. Foltopoulou, P. F.; Zachariadis, G. A.; Politou, A. S.; Tsiftsoglou, A. S. Papadopoulou, L. C. *Mol. Genet. Metab.* **2004**, *81*, 225—236.
54. Stiburek, L.; Vesela, K.; Hansikova, H.; Pecina, P.; Tesarova, M.; Cerna, L.; Houstek, J.; Zeman, J. *Biochem. J.* **2005**, *392*, 625—632.
55. Cobine, P. A.; Pierrel, F.; Leary, S. C.; Sasarman, F.; Horng, Y.; Shoubridge, E. A.; Winge, D. R. *J. Biol. Chem.* **2006**, *281*, 12270—12276.
56. Leary, S. C.; Mattman, A.; Wai, T.; Koehn, D. C.; Clarke, L. A.; Chan, S.; Lomax, B.; Eydoux, P.; Vallance, H. D.; Shoubridge, E. A. *Mol. Genet. Metab.* **2006**, *89*, 129—133.
57. Banci, L.; Bertinin, I.; Ciofi-Baffoni, S.; Leontari. I.; Martinelli, M.; Palumaa, P.; Sillard, R.; Wang, S. *Proc. Natl. Acad. Sci. U.S.A.*, **2007**, *104*, 15—20.
58. Stiburek, L., Vesela, K.; Hansikova, H.; Hulkova, H.; Zeman, J. *Am. J. Physiol. Cell Physiol.* **2009**, *296*, C1218—C1226.

59. Yang, H.; Brosel, S.; Acin-Perez, R.; Slavkovich, V.; Nishino, I.; Khan, R.; Goldberg, I. J.; Graziano, J.; Manfredi, G.; Schon, E. A. *Hum. Mol. Genet.* **2010**, *19*, 170—180.
60. Zeng, L.; Miller, E. W.; Pralle, A.; Isacoff, E. Y.; Chang, C. J. *J. Am. Chem. Soc.* **2006**, *128*, 10—11.
61. Miller, E. W.; Zeng, L.; Domaille, D. W.; Chang, C. J. *Nat. Protocols*. **2006**, *1*, 824—827.
62. Que, E. L.; Chang, C. J. *J. Am. Chem. Soc.* **2006**, *128*, 15942—15943.
63. Domaille, D. W.; Que, E. L.; Chang, C. J. *Nat. Chem. Biol.* **2008**, *4*, 168—175.
64. Que, E. L.; Domaille, D. W.; Chang, C. J. *Chem. Rev.* **2008**, *108*, 1517—1549.
65. Que, E. L.; Chang, C. J. *Chem. Soc. Rev.* **2010**, *39*, 51—60.
66. Que, E. L.; Gianolio, E.; Barker, S. L.; Aime, S.; Chang, C. J. *Dalton Trans.* **2010**, *39*, 469—476.
67. Domaille, D. W.; Zeng, L.; Chang, C. J. *J. Am. Chem. Soc.* **2010**, *132*, 1194—1195.
68. Dodani, S. C.; Domaille, D. W.; Nam, C. I.; Miller, E. W.; Finney, L. A.; Vogt, S.; Chang, C. J. *Proc. Natl. Acad. Sci. U.S.A.* **2011**, *108*, 5980—5985.
69. Yang, L.; McRae, R.; Henary, M. M.; Patel, R.; Lai, B.; Vogt, S.; Fahrni, C. J. *Proc. Natl. Acad. Sci. U.S.A.* **2005**, *102*, 11179—11184.
70. Wegner, S. V.; Arslan, H.; Sunbul, M.; Yin, J.; He, C. *J. Am. Chem. Soc.* **2010**, *132*, 2567-2569.
71. Taki, M.; Iyoshi, S.; Ojida, A.; Hamachi, I.; Yamamoto, Y. *J. Am. Chem. Soc.* **2010**, *132*, 5938—5939.
72. Merchant, S. S.; Allen, M. D.; Kropat, J.; Moseley, J. L.; Long, J. C.; Tottey, S.; Terauchi, A. M. *Biochim. Biophys. Acta*. **2006**, *1763*, 578—594.
73. Robinson, K. M.; Janes, M. S.; Pehar, M.; Monette, J. S.; Ross, M. F.; Hagen, T. M.; Murphy, M. P.; Beckman, J. S. *Proc. Natl. Acad. Sci. U.S.A.* **2006**, *103*, 15038—15043.
74. Murphy, M. P.; Smith, R. A. J. *Annu. Rev. Pharmacol. Toxicol.* **2007**, *47*, 629—656.
75. Ross, M. F.; Prime, T. A.; Abakumova, I.; James, A. M.; Porteous, C. M.; Smith, R. A. J.; Murphy, M. P. *Biochem. J.* **2008**, *411*, 633—645.
76. Porteous, C. M.; Logan, A.; Evans, C.; Ledgerwood, E. C.; Menon, D. K.; Aigbirhio, F.; Smith, R. A. J.; Murphy, M. P. *Biochim. Biophys. Acta*. **2010**, *1800*, 1009—1017.
77. Dickinson, B. C.; Chang, C. J. *J. Am. Chem. Soc.* **2008**, *130*, 9638—9639.
78. Dickinson, B. C.; Srikun, D.; Chang, C. J. *Curr. Opin. Chem. Biol.* **2010**, *14*, 50—56.
79. Hardy, M.; Chalier, F.; Ouari, O.; Finet, J.; Rockenbauer, A.; Kalyanaraman, B.; Tordo, P. *Chem. Commun.* **2007**, 1083—1085.
80. Hoye, A. T.; Davoren, J. E.; Wipf, M. P.; Kagan, V. E. *Acc. Chem. Res.* **2008**, *41*, 87—97.
81. Biasutto, L.; Matarei, A.; Marotta, E.; Bradaschia, A.; Sassi, N.; Garbisa, S.; Zoratti, M.; Paradisi, C. *Bioorg. Med. Chem. Lett.* **2008**, *18*, 5594—5597.
82. Ripke J.; Zarse, K.; Ristow, M.; Birringer, M. *ChemBioChem*. **2009**, *10*, 1689—1696.
83. Abu-Gosh, S. E.; Kolvazon, N.; Tirosh, B.; Ringel, I.; Yavin, E. *Mol. Pharmaceutics*. **2009**, *6*, 1138—1144.
84. Yousif, L. F.; Stewart, K. M.; Kelley, S. O. *ChemBioChem*. **2009**, *10*, 1939—1950.
85. Loudet, A.; Burgess, K. *Chem. Rev.* **2007**, *107*, 4891—4932.
86. Ulrich, G.; Ziessel, R.; Harriman, A. *Agnew. Chem. Int. Ed.* **2008**, *47*, 1184—1201.
87. Hamza, I.; Prohaska, J.; Gitlin, J. D. *Proc. Natl. Acad. Sci. U.S.A*. **2003**, *100*, 1215—1220.
88. Chen, L. B. *Ann. Rev. Cell Biol*. **1988**, *4*, 155—81.
89. Johnson, L. V.; Walsh, M. L.; Chen, L. B. *Proc. Natl. Acad. Sci. U.S.A.*, **1980**, *77*, 990—994.

90. Bellingham, S. A.; Lahiri, D. K.; Maloney, B.; Fontaine, S. L.; Multhaup, G.; Camakaris, J. *J. Biol. Chem.* **2004**, *279*, 20378—20386.
91. Kaler, S. G. *Nat. Rev. Neurol.* **2011**, *7*, 15—29.
92. Yamada, K.; Toyota, T.; Takakura, K.; Ishimaru, M.; Sugawara, T. *New J. Chem.* **2001**, *25*, 667—669.
93. Maryanoff B. E.; Reitz, A. B.; Duhl-Emswiler, B. A. *J. Am. Chem. Soc.* **1985**, *107*, 217—226.
94. Ross, J. A.; Ross, B. P.; Rubinsztein-Dunlop, H.; McGeary, R. P. *Synth. Commun*. **2006**, *36*, 1745—1750.
95. Karstens, T.; Kobs, K. *J. Phys. Chem.* **1980**, *84*, 1871—1872.
96. Martell, A. E.; Smith, R. M. *Critical Stability Constants*, Plenum Press: New York, 1989.
97. Finney, L.; Mandava, S.; Ursos, L.; Zhang, W. et al. *Proc. Natl. Acad. Sci. USA*. **2007** *104*, 2247—2252.
98. Capaldi, R. A.; Marusich, M. F.; Taanman, J. W. *Methods Enzymol.* **1995**, *260*, 117—132.
99. Bradford, M. M. *Anal. Biochem.* **1976**, *72*, 248—254.

Chapter 4:
Endogenous Copper Modulates Spontaneous Activity of Neural Circuits

Abstract

We have used calcium imaging to demonstrate a novel role for endogenous copper in the regulation of spontaneous activity in developing hippocampal and retinal neural circuits. Interception of extracellular copper cycling through acute chelation increases the cell participation and frequency of calcium transients. Likewise, genetic manipulation of CTR1 synchronizes the spontaneous network activity. Finally, pharmacological blocking of the excitatory NMDA receptor negates the effects of copper chelation suggesting that endogenous copper is needed to tune excitation and inhibition in neural development.

Introduction

The foundation of cellular signal transduction relies on a rapid relay of information mediated by intricate messenger systems that rely on the spatial and temporal positioning of small organic molecules, gaseous species, or metal cations.[1-3] Specifically, the mobilization of alkali and alkaline earth metal ions including sodium, potassium, and calcium have been well characterized in a variety of cellular processes.[1,2] These metal ion fluxes are tightly gated by ion channels and transporters. Likewise, cells have evolved intricate machinery to acquire and efflux transition metal ions like iron, zinc, and copper.[4,5] In particular, a portion of cellular copper is cycled at cell surface as it taken up by copper transporter 1 (CTR1) and pumped out of the cell by ATP7A. Further, owing to its tight regulation and redox-active nature, we hypothesize that cells, in particular in the brain, can strategically utilize copper to control cellular signaling mechanisms.

In this regard, the brain is a large processing unit composed of networks of cells that acquire, process, and transmit signals in a dynamic fashion. Specifically, information is spatially propagated across these large connective spaces in the form spontaneous chemical and electrical bursts or depolarizations that are thought to be essential for the organization and maturation of neural circuits during development.[6-8] This spontaneous activity is mediated through excitatory and inhibitory receptors and can be registered through calcium waves.[8] Here, we present our results on how endogenous copper modulates the spontaneous network activity of the developing hippocampus and retina.

Results and Discussion

Modulation of spontaneous activity with copper chelation in dissociated hippocampal neurons. In the first part of this study, we have explored the spontaneous activity of a random network of dissociated hippocampal neurons. Cultures of embryonic neurons (DIV 12-15) were stained with the commercially available Ca^{2+} indicator Oregon Green BAPTA-1 AM (OGB) followed by time-lapse imaging. Basal level calcium transients were recorded for up to 10 min. Representative traces from four individual cells in the field of imaging are shown in Figure 4-1a. These calcium transients or waves have a rapid rise time and short duration, which results from membrane depolarization as opposed to calcium release from internal stores. The entire network is represented in a raster format where the x-axis represents the duration of the experiment and individual cells that participate in the calcium transient are shown as white tick marks along the y-axis (Figure 4-1b). This data shows that dissociated hippocampal cultures, which consist of neurons and glia, have random basal calcium transients. Next, we used a selective, extracellular

copper chelator, bathocuproine disulfonate (BCS), to bind or intercept labile copper. BCS forms a complex with Cu^{+} and Cu^{2+}, and it is important to note that the imaging media did not contain copper.[9] The chelator (200 μM) was acutely bath applied to the same field of cells followed by time-lapse calcium imaging. BCS increases the frequency of the calcium transients resulting in greater cell participation or a more synchronized network (4-1c, 4-1d). We speculate that BCS can chelate copper from or form a ternary complex with a cell surface copper binding protein/peptide or intercept basal levels of extracellular copper cycling, which would propagate a cascade of signals leading to more frequent calcium transients.

Spontaneous activity in CTR1$^{-/-}$ hippocampal neurons. Altering the expression of CTR1, which is a selective transporter that gates copper entry into the cell, can mimic pharmacological copper chelation. We used a pan-neuronal CTR1 knockout mouse generated by Professor Dennis Thiele's lab to investigate the role of CTR1 in spontaneous activity. Calcium transients were recorded from OGB stained wildtype (WT) and CTR1$^{-/-}$ hippocampal neurons (Figure 4-2). Similar to the effects seen with BCS, CTR1$^{-/-}$ neurons have more frequent and synchronized wave patterns. These data suggest that extracellular copper cycling and intracellular copper stores controlled by CTR1 can perturb cellular calcium signal transduction. Moreover, the effects of BCS arise from selective copper binding potentially from CTR1 or another extracellular copper bound protein.

Pharmacological manipulation of copper cycling in the retinal network. As mentioned above, dissociation of neurons followed by development *in vitro* results in formation of random connections that produce basal levels of spontaneous activity.[6] In order to rule out the potential artifacts that can arise from a random network, we have studied the effects of copper chelation in the intact retinal circuit. The retina is a well-studied model for spontaneous activity during development; however, copper dynamics and machinery have not been examined during the time of wave propagation.[7] Prior to retinal calcium imaging, we established the expression of CTR1 during retinal development by western blot analysis (Figure 4-3). Preliminary findings show that CTR1 is expressed as the retina develops from postnatal (P) days 4 to 20. Currently, methods are being developed to use new copper sensors to study labile Cu^{+} and measure total copper by inductively coupled plasma mass spectrometry during retinal development.

Structurally, the retina is a stratified tissue consisting of rods, cones, horizontal cells, bipolar cells, amacrine cells, Müller glia, and ganglion cells.[7,10] To investigate the effects of copper chelation on retinal waves, we have used two-photon calcium imaging to record from the ganglion cell layer (GCL), which receives the sum of the inputs from the distal cell populations. Retinas were acutely isolated from P10-P13 mice and bolus loaded with the OGB as previously described.[10] Representative spontaneous wave propagation from the GCL is shown in a time lapse circle cell plot (Figure 4-4a), and traces from four different cells are shown in Figure 4-4b. The rapid rise and decline time for the retinal calcium transients is indicative of membrane depolarization similar to that seen with the hippocampal network. Acute bath application of 200 μM BCS increases the frequency of correlated waves and we find that multiple waves are clustered together (Figure 4-4b, 4-4c). The increase in the number of calcium transients is translated into the duration between waves or the wave interval. The average interwave interval decreases for BCS treated retina (median, upper/lower quartile; control: 100 sec, 60/130; BCS: 29 sec, 17/58 sec). We also quantified the percentage of cells in the field of view that participate in each wave with and without BCS treatment (Figure 4-4e). There is an increase in the proportion of GCL neurons that have an increase in intracellular calcium upon BCS treatment

(median, upper/lower quartile; control: 26%, 8.9/34; BCS: 75%, 56/78). Interestingly, acute treatment with BCS is reversible upon perfusion with fresh imaging medium (median, upper/lower quartile; wash wave interval: 100 sec, 60/130; wash cell participation: 12%, 1/20), which suggests that BCS can not chelate copper from a cell surface protein but is likely forming a ternary complex or is briefly altering copper cycling at the cell surface. Taken together, these results suggest that the excitability of the retinal tissue increases upon addition of BCS as more ganglion cells participate in each wave event.

Spontaneous activity in CTR1$^{+/-}$ retinal tissue. In order study the effects of copper cycling in the retina through a genetic approach we adopted two different methods: a heterozygous CTR1 mouse model (CTR1$^{+/-}$) and a short hairpin RNAi (shRNA) knockdown of CTR1 (Figure 4-5). The CTR1$^{+/-}$ mouse model generated by Professor Dennis Thiele's laboratory has been previously characterized.[11] Total metal content in the brain of CTR1$^{+/-}$ mice is reduced by 50% relative to the CTR1 WT mouse.[11] The retina is part of the central nervous system, so it is possible that total or labile copper could change in this tissue in the CTR$^{+/-}$ system. Encouraged by this fact and that the heterozygous model could be readily maintained and genotyped compared to the pan-neuronal CTR1$^{-/-}$ mouse used above, we recorded calcium transients in CTR1$^{+/-}$ derived retina. CTR1 expression is not significantly different in CTR1$^{+/-}$ retina versus the WT retina (Figure 4-6a), but we are currently developing methods to verify if labile copper dynamics or total copper content is altered in CTR1$^{+/-}$ retina. For calcium imaging, retinal tissues from P10 and P12 CTR$^{+/-}$ mice have been isolated and bolus loaded with OGB. The interwave interval is shorter (median, upper/lower quartile; control: 100 sec, 60/130; CTR1$^{+/-}$: 76 sec, 54/91) and the proportion of cells participating in a wave increases (median, upper/lower quartile; control: 26%, 8.9/34; CTR1$^{+/-}$: 40%, 15/58) for the CTR1$^{+/-}$ retina as compared to age matched WT counterparts. CTR1$^{+/-}$ retina treated with 200 μM BCS are more excitable as seen with WT retina (median, upper/lower quartile; CTR1$^{+/-}$ wave interval: 76 sec, 54/91; BCS wave interval: 52 sec, 37/69 sec; CTR1$^{+/-}$ cell participation: 40%, 15/58; BCS cell participation: 73%, 52/77). We see the BCS can affect the CTR1$^{+/-}$ retina since the model is not a knockout, but we can knockout CTR1 in the retina with adeno-associated virus and methods for this experiment are currently being developed. With this preliminary data, we have shown that copper is necessary for spontaneous activity through the functions of CTR1 and although the CTR1$^{+/-}$ model is an artificial system, brain copper deficiency derived from Menkes disease could have implications in retinal development.[12]

Pharmacological manipulation of excitatory receptors in the retina. We next used pharmacological manipulation to understand the balance of excitation and inhibition in the retina upon extracellular copper chelation. Recent evidence suggests that endogenous and exogenous copper alters the sensitization of the *N*-methyl-*D*-aspartate (NMDA) ionotropic receptor, which can contribute to the overall excitability of the retinal tissue.[13,14] As such, we postulated that chelation with BCS at the level of CTR1 could depolarize the membrane of the retinal circuit and then modulate the downstream activation of the NDMA receptor. Calcium transients were first recorded in OGB stained control retina and then from BCS treated retina (Figure 4-6a, 4-6b). We then bath applied BCS with AP5, a well-established drug that blocks the NMDA receptor. Co-treatment with BCS and AP5 does not abolish retinal waves, which means that the retinal tissue is intact and viable for wave propagation. Representative traces show that treatment with AP5 abolishes the clustered calcium transients seen with BCS treatment (Figure 4-6a, 4-6b). Moreover, the interwave interval increases back to control levels (median, upper/lower quartile; control: 92 sec, 59/95; BCS: 141 sec, 50/199; BCS+AP5: 96 sec, 9/108) and the percentage of

waving cells returns to control levels (median, upper/lower quartile; control: 36%, 23/51; BCS: 82%, 81/93; BCS+AP5 20%, 3.6/62) (Figure 4-6c, 4-6d). BCS could form a ternary complex with copper bound on the surface of the NMDA receptor; however, there is no biochemical evidence of this binding. Of note is that the inputs into the GCL are a summation of excitation and inhibition from the other cell types found in the tissue so it is plausible that the effects of BCS on the circuit are not exclusive to the NMDA receptor, but rather could be derived from a combination of its perturbations on both excitatory and inhibitory receptors and/or directly at the level of CTR1. All of these factors could modulate calcium uptake. Pharmacological manipulation of inhibitory receptors in the retina results in greater excitability and if combined with BCS the effects on calcium transients would be additive. Hence this approach would not provide useful mechanistic insight into the effects of BCS. Alternatively, electrophysiological measurements of overexpressed neuronal receptors in an orthologous system such as HEK 293T cells or oocytes would be useful to identify potential molecular target(s) of BCS.

Concluding Remarks

In this work, we utilize calcium imaging to demonstrate a novel role for copper in the regulation of spontaneous activity. We have shown that acute extracellular copper chelation in dissociated culture and intact retinal tissues, increases the cell participation and frequency of calcium transients during network maturation. Moreover, modulation of cellular copper status through genetic knockdown or mutation of CTR1 in both systems enhances the excitability of the neural network. Finally, pharmacological inhibition of the NMDA receptor negates the effects of copper chelation providing evidence for NMDAR or it effectors as a molecular target of copper binding. Taken together our findings suggest that endogenous copper is used to tune inhibitory and excitatory inputs during circuit development through the dynamic functions of CTR1 which include: regulation of intracellular copper concentrations, cell surface copper recycling, and/or loading of copper onto extracellular membrane receptors involved in calcium uptake.

Experimental Section

Neuronal cell culture. Primary hippocampal cultures were prepared using the method described by Goslin and Banker.[15] Neuronal cultures were prepared from the brains of WT and CTR1 pan-neuronal knockout rats/mice at embryonic days 18-21, plated on 12 mm poly-L-lysine coated coverslips in serum-based medium with B27 supplement (Life Technologies), and then replaced and maintained in neurobasal media. All animal care and experimental protocols were approved by the Animal Care and Use Committees at the University of California, Berkeley and Duke University.

Dissociated hippocampal neuron imaging.[16] For calcium imaging analysis, fields of cells were chosen randomly from four or more independent batches of cultures. DIV 12-15 cultured hippocampal neurons were incubated and stained with 5 μM Ca^{2+}-sensitive dye, Oregon Green BAPTA-1 AM (OGB) (Life Technologies) for 30 min in HEPES buffered saline (HBS; in mM: 5 glucose, 120 NaCl, 10 HEPES, 2 $CaCl_2$, 2.5 KCl, 2 $MgCl_2$), washed with HBS for 10 min, and then subjected to time-lapse imaging. Images were acquired on a Leica confocal imaging system (CS SP) equipped with an argon gas ion laser and a Leica inverted microscope (DM IRBE) fitted

with a Leica 63x objective (HCX PL Apo; NA, 1.32). OGB was excited at 488 nm, and the fluorescence signal was collected at 500-540 nm. Images were acquired every 1.45 s at 512 x 512 pixels. Bathocuproine disulfonate disodium salt (BCS, Sigma) was bath applied on-stage. Images were corrected for motion artifacts using the Turboreg ImageJ plugin. 5x5 pixel regions of interest were manually selected within all cells in the field of view using custom MATLAB algorithms. Fluorescence signals were averaged within these regions over time. Cell events were identified when the change in fluorescence exceeded 10% of the cell's baseline fluorescence.

Retinal preparation. All experiments were preformed on acutely isolated mouse retinas. Male and female C57BL/6 mice obtained from Harlan were used for WT recordings and CTR1 heterozygous mice were maintained and genotyped according to published procedures.[10] All procedures were approved by the Institutional Animal Care and Use Committee at the University of California, Berkeley. P10-P13 C57BL/6 mice of either sex were deeply anesthetized with isoflurane and decapitated. Eyes were removed, and retinas were isolated in oxygenated artificial cerebrospinal fluid (ACSF; in mM: 119 NaCl, 26.2 $NaHCO_3$, 11 glucose, 2.5 KCl, 1 K_2HPO_4, 2.5 $CaCl_2$, 1.3 $MgCl_2$).

Preparation of retinal extracts and immunoblotting. A representative protocol is as follows: retina were isolated as described above and one pair of retina for each sample were homogenized for 15 sec and vortexed for 15 sec three times in 40 µL of radioimmunoprecipitation (RIPA) buffer (50 mM Tris, pH 7.4, 150 mM NaCl, 1% Triton X-100, 0.5% sodium deoxycholate, and 0.1% SDS) supplemented with protease inhibitors (Roche Complete MiniTab) and phosphatase inhibitors (Thermo Scientific Halt Phosphatase Inhibitor Cocktail), lysed for 30 min on ice, and cleared by centrifugation at 13.2 x 10^3 rpm for 10 min at 4 °C. Protein concentration was determined by bicinchoninic acid (BCA) assay (Pierce), 5 µL of 4x Laemmli buffer (0.25 mM Tris, 2% SDS, 40% glycerol, 20% beta-mercaptoethanol, 0.04% bromophenol blue) was added, the samples denatured at 37 °C for 10 min, and 5 or 10 µg of total protein were loaded and separated on a 4-12% Bis-tris gel (NuPAGE Novex, Invitrogen). Proteins were transferred to PVDF membranes (Immobilon, Millipore) with a semi-dry transfer system (Biorad) at constant voltage (15 V) for 35 min for CTR1. The blots were blocked for 1 h in 5% nonfat dry milk in wash buffer (10 mM Tris, pH 7.5, 100 mM NaCl, 0.1% Tween-20), and incubated overnight at 4 °C in anti-CTR1 1:1000, which was kindly provided by Dennis Thiele. Membranes were washed 5 times for 5 min in wash buffer, incubated at room temperature with 1:2000 secondary antibody, washed 5 times for 5 min in wash buffer, and then visualized using enhanced chemiluminescence (Luminata Classico Western HRP Substrate, Millipore) recorded on a BioRad GelDoc imaging station. The blot was stripped using Restore Plus stripping buffer (Thermo Scientific) according to manufacturer's instructions. The blot was then washed 5 times for 5 min in wash buffer, and then probed for anti-actin 1:2000 (Millipore) and developed as described above.

Retinal calcium imaging. Retinas were loaded with Oregon Green 488 BAPTA-1 AM using the multicell bolus loading technique.[10] Two-photon calcium imaging of neurons in the GCL was preformed using a custom-modified two-photon microscope (Fluoview 300, Olympus America Inc.). XYZ scans were used to localize neurons in the GCL. Time series images were acquired at 1 Hz using a 60x objective (Olympus LUMPlanFI/IR 60x/0.90W) with the excitation laser tuned to 790 nm. ACSF containing BCS and/or D-(-)-2-amino-5-phosphonopentanoic acid were bath applied on stage. Images were corrected for motion artifacts using the Turboreg ImageJ plugin. 10x10 pixel regions of interest were manually selected within all cells in the field of view using

custom MATLAB algorithms. Fluorescence signals were averaged within these regions over time. Cell events were identified when the change in fluorescence exceeded 15% of the cell's baseline fluorescence within 1 second. Cells were categorized as participating in a retinal wave if cell events correlated with neighboring cells.

Preparation of CTR1 adeno-associated virus (AAV) plasmids. Two CTR1 29-mer shRNA sequences and one 29mer scrambled sequence were excised from the Origene retroviral RFP vector pRFP-C-RS and inserted into pAAV-BASIC-tdTomato by Vector Biolabs. The shRNA sequences are shown below.

CTR1 tube ID FI337329: 5' GTTAACTTCAGCCAGGATTGATGGCAGCT 3'

CTR1 tube ID FI337330: 5' CAAGTCAGCATTCGCTACAATTCCATGCC 3'

Scramble catalog ID TR30015: 5' GCACTACCAGAGCTAACTCAGATAGTACT 3'

The AAV plasmids (50 ng of DNA) were transformed into SURE 2 Super competent cells (Agilent Technologies) according to manufacturer's instructions on Luria broth agar plates with 50 μg/mL carbenicillin. Twenty clones were selected and grown in 3 mL of Luria broth (LB) with 50 μg/mL carbenicillin for 7 to 8 hr followed by a portion (1.8 mL) harvested for mini prep (Qiagen) and a second portion was stored as a glycerol stock (0.9 mL of culture with 0.3 mL of 50% glycerol). Plasmid DNA concentration was determined by a NanoDrop Spectrophotomer (Thermo Scientific). The plasmid DNA for each clone was subjected to two different restriction endonuclease digests with Sma1 and Pst1 (New England Biolabs). A typical protocol: 0.5 μg to 1 μg of DNA, 1 μL of enzyme, 2.5 μL buffer, 0.25 μL of BSA were diluted into 20.25 μL of Milli-q water and the duration and temperature of the digest was followed as described by the manufacturer. The restriction endonuclease digest (8 μL to 12 μL) was resolved on a 1.5% agarose gel containing ethidium bromide electrophoresis with tris-acetate buffer at 85V (Biorad) and then recorded on a BioRad GelDoc imaging station. One clone for each plasmid was selected for maxi prep (Qiagen). The glycerol stock for each clone was thawed and 2 x 125 μL of this stock was diluted into 2 x 125 mL of LB broth with 50 μg/ml carbenicillin. The cultures were grown for 7 to 8 hr and then harvested for maxi prep (Qiagen). The plasmid DNA was quantified, subjected to two different restriction endonuclease digests with Sma1 and Pst1, resolved, and visualized as described above. Quintara Biosciences sequenced the shRNA loop in the scramble AAV plasmid and the UC Berkeley DNA Sequencing Facility sequenced the shRNA loop in the CTR1 AAV plasmids with a U6 forward primer synthesized by Integrated DNA Technologies. The shRNA sequences of the AAV plasmids are shown below. The plasmids were given to Dr. Mei Li at the UC Berkeley Vision Science Core in the Gene Delivery Module for the preparation of the CTR1 and scramble AAV serotype 9.

U6 Primer: 5' GGACTATCATATGCTTACCG 3'

CTR1 AAV FI337329: 5' GTTAACTTCAGCCAGGATTGATGGCANCT 3'

CTR1 AAV FI337330: 5' CAAGTCAGCATTCGCTACAATTCCATGCC 3'

Scramble AAV TR30015: GCACTACCAGAGCTAACTCAGATAGTACT 3'

Figures

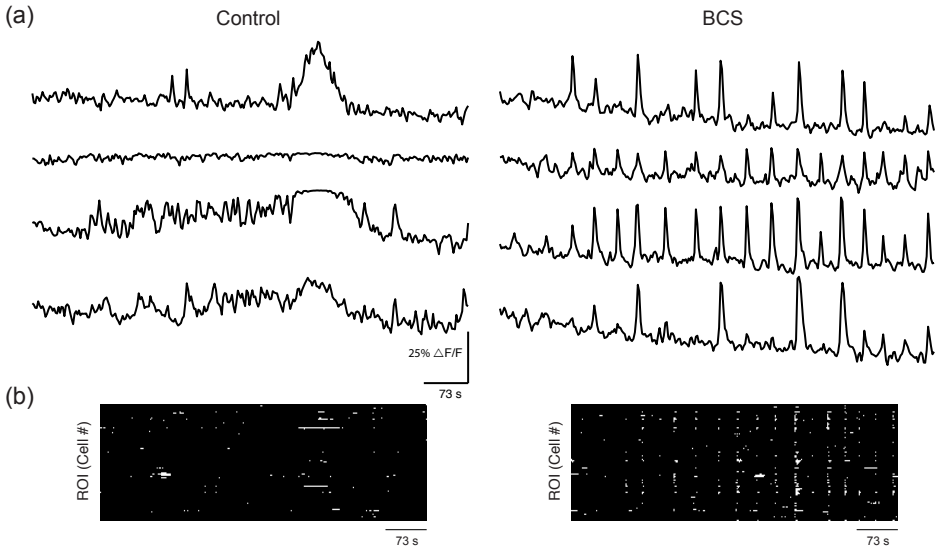

Figure 4-1. Spontaneous activity increases in the presence of BCS in dissociated hippocampal culture. (a) Sample ΔF/F traces from averaged regions within control and 200 μM BCS treated dissociated rat hippocampal neurons stained with Oregon Green BAPTA-1 AM (OGB). Each trace represents a different cell. (b) Raster plots of neuronal calcium transients greater than 10% ΔF/F for all cells in the field of view. Total imaging duration is 7.25 minutes. This data is representative of at least three independent hippocampal cultures.

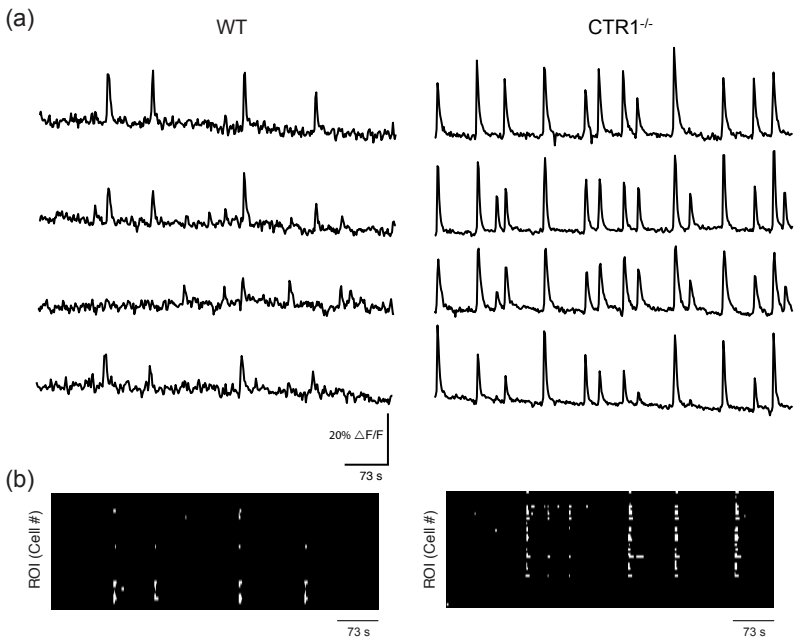

Figure 4-2. Spontaneous activity of CTR1$^{-/-}$ mimics the effects of BCS in dissociated hippocampal culture.(a) Sample ΔF/F traces from averaged regions within WT and CTR1$^{-/-}$ dissociated mouse hippocampal neurons stained with OGB. Each trace represents a different cell. (b) Raster plots of neuronal calcium transients greater than 10% ΔF/F for all cells in the field of view. Total imaging duration is 7.25 minutes. This data is representative of at least three independent hippocampal cultures.

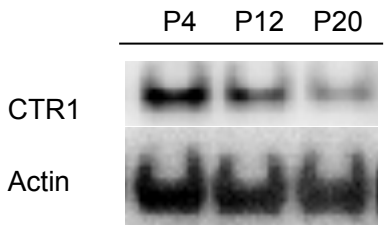

Figure 4-3. Representative western blot of CTR1 and actin expression in WT retina at P4, P12, and P20.

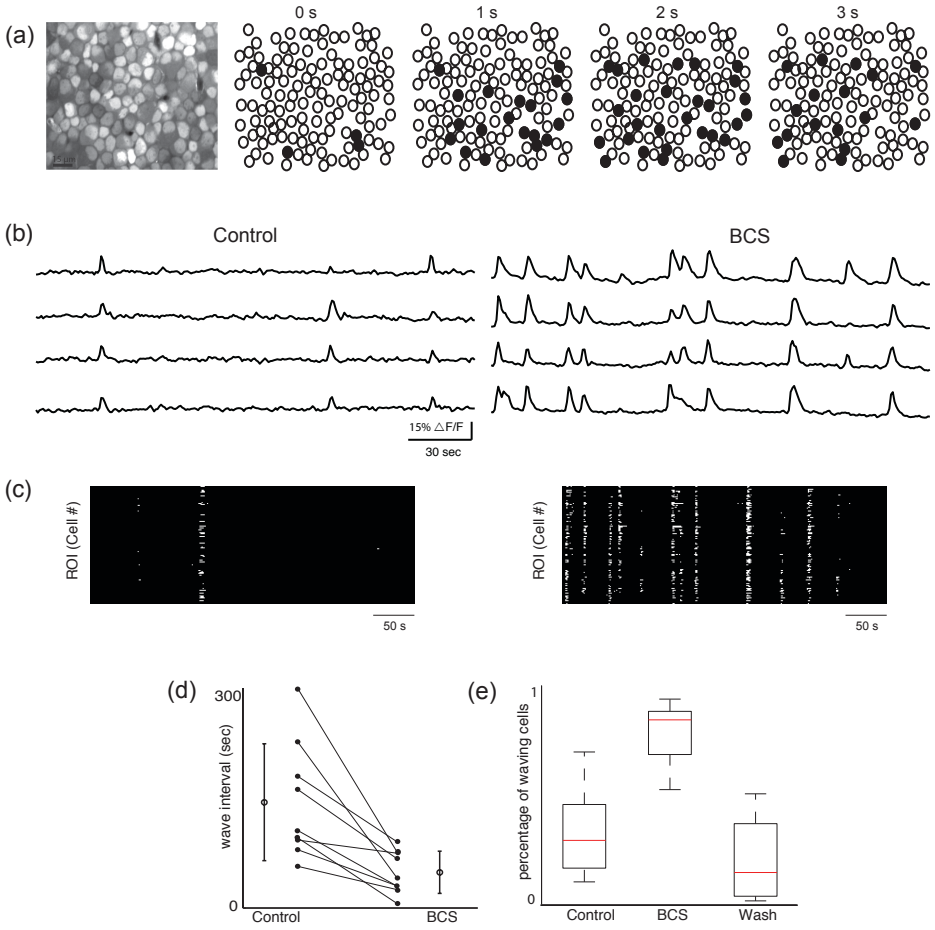

Figure 4-4. BCS increases wave frequency and cell participation in retina spontaneous activity. (a) Example of wave propagation in the ganglion cell layer (GCL) observed with two-photon calcium imaging at a frame rat of 1 Hz. Leftmost image is in the retinal sample loaded with OGB. Circles are identified cells; black indicates cells with ΔF/F of > 15% in that frame. (b) Sample ΔF/F traces from averaged regions within control and 200 μM BCS treated. Each trace represents a different cell. (c) Raster plots of neuronal calcium transients greater than 15% ΔF/F for all cells in the field of view. Total imaging duration is 5 minutes. (d) Summary of effects of BCS on interwave interval. (e) Summary of effects of BCS on proportion of waving cells pooled across retinas (N=9 retinas, $p<0.001$, paired two-tailed *t*-test). The red line is the median of the distributions, the edges of the box are the lower and upper quartiles, with whiskers extending to the most extreme values that are still considered not to be outliers.

(a)

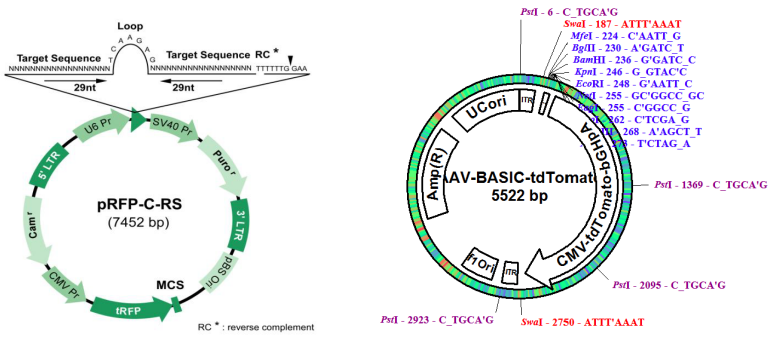

(b)

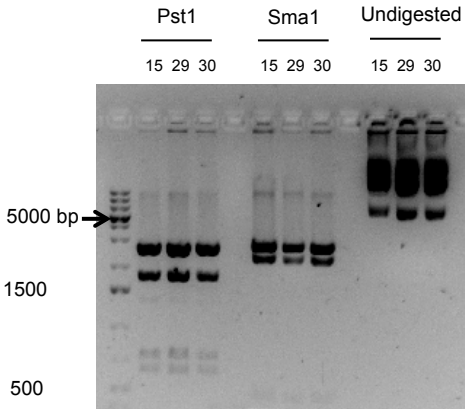

Figure 4-5. (a) Plasmid maps of pRFP-C-RS and pAAV-BASIC-tdTomato vectors. (b) Sma1 and Pst1 digests of scramble (15) and CTR1 (29, 30) AAV plasmids confirm integrity of the ITRs.

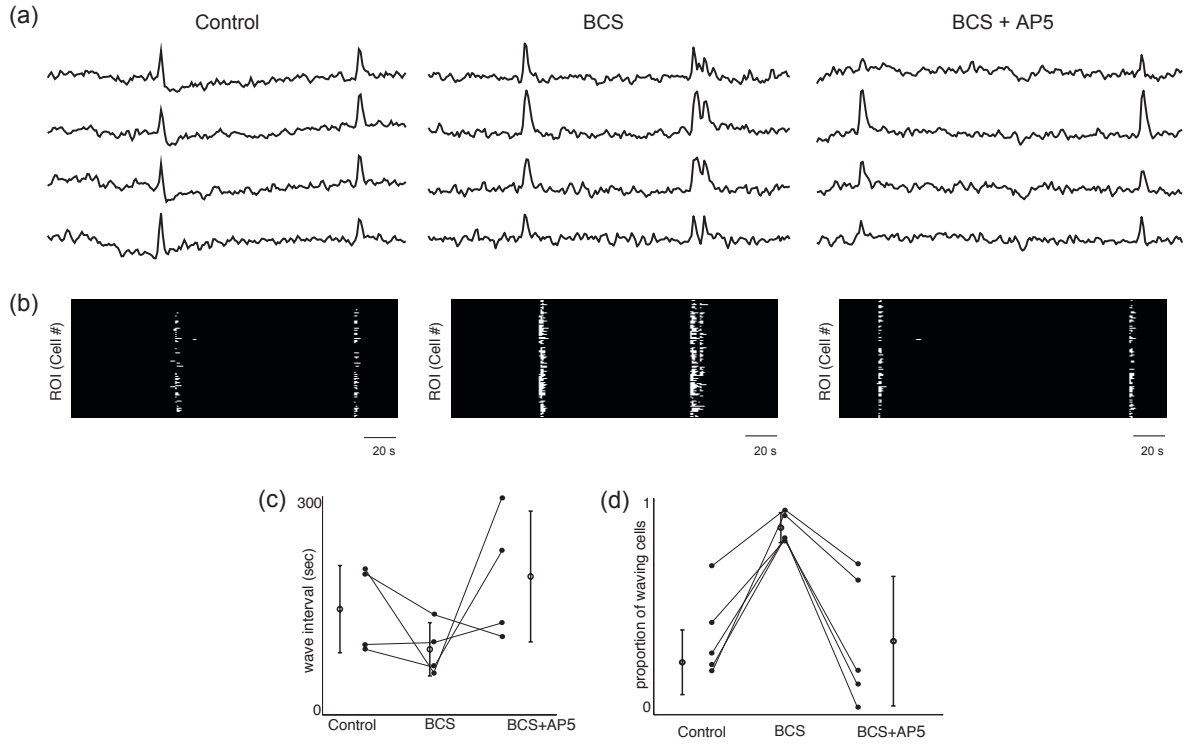

Figure 4-6. NMDAR inhibitor AP5 negates the effect of BCS on spontaneous activity in the retina. (a) Sample ΔF/F traces from averaged regions within control, 200 μM BCS, and 200 μM and 50 μM AP5 treated retina. Each trace represents a different cell. (b) Raster plots of neuronal calcium transients greater than 15% ΔF/F for all cells in the field of view. Total imaging duration is 5 minutes. (c) Summary of effects of BCS and AP5 on interwave interval (N = 5 retinas). Lines connect values of interwave interval per retina in control versus BCS (left) and BCS+AP5 (right). Open circles are group means and SD. (d) Summary of the effects of BCS and BCS+AP5 on the average proportion of cells that participated per wave. Lines connect values of average cell participation per retina in control versus BCS and BCS+AP5. Open circles are group means and SD.

References

1. Alberts, B.; Johnson, A.; Lewis, J.; Raff, M.; Roberts, K.; Walter, P. *Molecular Biology of the Cell, 4th ed.*; Taylor & Francis Group: New York, **2002**.
2. Clapham, D. E. *Cell*. **2007**, *131*, 1047—1058.
3. Kajimura, M.; Fukda, R.; Bateman, R. M.; Yamamoto, T.; Suematsu, M. *Antioxid. Redox Signal*. **2010**, *13*, 157—192.
4. Que, E. L.; Domaille, D. W.; Chang, C. J. *Chem. Rev.* **2008**, *108*, 1517—1549.
5. Nevitt, T.; Ohrvik, H.; Thiele, D. J. *Biochim. Biophys. Acta.* **2012**, *1823*, 1580—1593.
6. Mazzoni, A.; Brocacard, F. D.; Garcia-Perez, E.; Bonifazi, P.; Ruaro, M. E.; Torre, V. *PLoS ONE*. **2007**, *2*, e439.
7. Blankenship, A. G.; Feller, M. B. *Nat. Rev. Neurosci*. **2010**, *11*, 18—29.
8. Ackman, J. B.; Burbridge, T. J.; Crair, M. C. *Nature*. **2012**, *490*, 219—225.
9. Cherny, R. A.; Barnham, K. J.; Lynch, T.; Volitakis, I.; Li, Q. et al. *J. Struct. Biol.* **2000**, *130*, 209—216.
10. Firl, A.; Sack, G. S.; Newman, Z. L.; Tani, H.; Feller, M. B. **2013**, *109*, 1969—1978.
11. Lee, J.; Prohaska, J. R.; Thiele, D. J. *Proc. Natl. Acad. Sci. U.S.A.* **2001**, *98*, 6842—6847.
12. Kaler, S. G. *Nat. Rev. Neurol*. **2011**, *7*, 15—29.
13. You, H. Tsutshi, S.; Hameed, S.; Kannanayakal, T. J.; Chen, L. et al. *Proc. Natl. Acad. Sci. U.S.A.* **2012**, *109*, 1737—1742.
14. Trombley, P. Q.; Shepherd, G. M.; *J. Neurophysiol.* **1996**, *76*, 2536—2546.
15. Goslin, K.; Asmussen, H.; Banker, G. *Culturing Nerve Cells, 2nd ed.*; MIT Press: Massachusetts, **1998**.
16. Zhang, X.; Poo, M. M. *Neuron*. **2002**, *36*, 675—688.

Chapter 5:
Identification of Kinases for ATP7A with High-Throughput Screening

Abstract

We have combined high-throughput RNAi screening with immunofluorescence methods to understand how the kinome regulates the copper mediated mobilization of ATP7A in mammalian cells. In our first kinase screen with RAW 264.7 macrophages, we identified three kinases that partially prevent the translocation of ATP7A in the presence of copper: Pfkfb1, Prkd3, and Trpm7. However, the small dynamic range of the assay, population heterogeneity, and low transfection efficiency limited the interpretation of our results. Next, we optimized an ATP7A immunofluorescence protocol in the easy to transfect HeLa cell line. We find ATP7A disappears from the Golgi apparatus and appears in the nucleus with acute copper treatment. This readout will significantly enhance our dynamic range and increase the probability for the successful identification of kinases that phosphorylate ATP7A.

Introduction

The mammalian cell is a complex reaction vessel equipped with small organic building blocks and metal ions to carry out an array of overlapping reactions cascades necessary for cellular homeostasis. In these canonical signaling pathways sodium, potassium, and calcium are mobilized for the rapid relay of cellular information, whereas transition metal ions like iron, copper and zinc are typically positioned in the active sites of enzymes to carry out organic transformations.[1] However, we hypothesize that copper in particular is poised to be involved in canonical signal transduction pathways since it is redox active, has a unique coordination sphere, and is tightly regulated in the cell.

In an effort to elucidate new roles of copper in cellular signaling pathways, we have utilized a high-throughput RNAi screening approach where subsets of the entire mammalian genome can be assayed for a loss of function based on a silencing of a gene but this method requires a robust readout of cellular copper.[2] In order to this, we monitored the trafficking of the copper efflux pump ATP7A via immunofluorescence. Under basal conditions, ATP7A metallates different cuproenzymes at the trans-Golgi network and recycles between the trans-Golgi network to the plasma membrane and under conditions of excess copper this translocation is enhanced as ATP7A effluxes copper out of the cell (Figure 5-1a).[3] ATP7A is phosphorylated at resting conditions and treatment with exogenous copper increases this level of phosphorylation.[4] Recently, serine/threonine phosphorylation sites in human and hamster ATP7A have been identified and eight phosphosites increase upon copper treatment, but the kinases involved in regulating the localization and trafficking of ATP7A have yet to be identified (Figure 5-1b).[4]

With this information in hand, we became interested in how the kinome and cellular copper machinery intersect with ATP7A as the readout. We will be able to identify kinases involved in the regulation of ATP7A under resting, copper deficient, or copper supplemented conditions. Additionally, the kinase screen will provide insight into how kinome alters copper entry through CTR1 and distribution to ATP7A via its chaperone ATOX1. This experiment can be divided into two parts: optimization and screening (Figure 5-2). In the optimization phase, methods for both the immunofluorescence assay and transfection need to be developed and the variables are outlined in Table 5-1. Here, we present optimization methods and preliminary results for how the kinome can regulate the copper mediated mobilization of ATP7A in RAW 264.7 macrophages and HeLa cells.

Results and Discussion

Optimization of a high-throughput kinase screen in RAW 264.7 macrophages. ATP7A is known change in expression and localization in response to copper and proinflammatory agents including lipopolysaccharides (LPS) and interferon-gamma (IFN-γ) in murine RAW 264.7 macrophages.[5] Motivated by the rich copper biology in this immune cell, we started to investigate how the kinome and copper machinery intersect with high-throughput screening. Immunostaining of ATP7A has been previously reported in mouse cell lines with an antibody raised against C-terminus of ATP7A, however, these methods required further optimization to be used in a screening format.[5]

The kinase library contains 762 genes distributed in 3-384 well plates, so we used automated liquid handling systems to generate reproducible results. We first plated different densities of cells on different black/clear bottom 384-well plates for 48 h, and then fixed the cells with microscopy grade paraformaldehyde (PFA, 4% in PBS for 10 min) and washed the cells with PBS. For a screen, the cells must attach to the plate and maintain their adherence and morphology post fixation. Additionally, the RAW 264.7 macrophages are immune cells so they can become activated, which could alter how the intracellular kinase machinery modifies ATP7A. We found that 4000 cells/well plated for 48 h on a Corning 384-well TC treated black/clear bottom plate was suitable. In the next part of the assay development we used a robust primary antibody against ATP7A developed by Betty Eipper and commercialized by Hycult Biotech for immunostaining.[6] Typically, ATP7A immunofluorescence assays are done with cells plated on glass coverslips where all of the manipulations are done by hand and the cells are imaged with a confocal microscope, but this protocol had to be translated into a 384-well format with automated liquid handling and imaging on a high-throughput epifluorescence microscope. We first defined methods on the Velocity 11 liquid handling system followed by testing different parameters in the immunofluorescence protocol (Figure 5-3). An ideal immunostaining protocol maintains the integrity of the intracellular antigen and subcellular structure, and to this end we found that the permeabilization step was critical for ATP7A. If the cells are under permeabilized the antibody cannot get to the antigen and harsh permeabilization can be disruptive. We screened different concentrations and incubation times of Triton X-100 and saponin as these two surfactants represent the extremes of permeabilization reagents. Triton X-100 can displace both proteins and lipids whereas saponin is milder and can selectively displace cholesterol from membranes.[7] Immunostaining of ATP7A was optimal with 0.1% saponin combined with 5% donkey serum block for 1 h. We also varied the concentration of primary ATP7A and secondary antibody to provide the largest signal to noise on the ImageXpress Micro epifluorescence system. The ATP7A signal was co-localized with GM130, a cis-Golgi protein (Figure 5-4). In this cell type the Golgi is compact the so cis-Golgi marker is usable as opposed to a trans-Golgi maker, and similar results have been previously reported.[5] With these variables optimized, we altered cellular copper status by treating the cells with a selective, extracellular copper chelator, bathocuproine disulfonate (BCS), to bind or intercept labile copper and with copper chloride ($CuCl_2$) for 1-3 hr. Consistent with other studies, we find that ATP7A retracts and resides in the Golgi with BCS treatment, and acute copper supplementation results in a mobilization of ATP7A into the cytosol (Figure 5-2).[3] On the confocal system, we find that ATP7A resides at the plasma membrane, but we could not acquire that level of resolution on the epifluorescence system. With the immunostaining protocol optimized, we next established methods for automated data analysis. We used a translocation-enhanced module on the imaging system to define the size and location of the Golgi with the GM130 marker. Then we quantified the ATP7A signal in the

presence of BCS or $CuCl_2$ for 2 h and found that copper treated cells have about 75% less ATP7A in the Golgi. Given this 3-fold dynamic range we were encouraged to continue to optimize the transfection protocol.

An optimization procedure for siRNA screening in RAW 264.7 macrophages has been previously reported, so we used this as a starting point.[8] It is important to note that this cell line is difficult to transfect, but the reverse transfection method is quite effective. In this method the siRNA is seeded in the well and combined with a lipid-based transfection reagent followed by plating of the cells. As the cells adhere to the plate they come into direct contact with the complex forcing a more effective uptake of the siRNA. For a transfection to be efficient a high percentage of cells need to take up the siRNA and the gene of interest must be silenced with limited toxicity and off-tangent effects. We first evaluated siRNA uptake by transfecting cells with fluorescein isothiocyanate (FITC) labeled siRNA combined with three different lipid-based transfection reagents at different volumes for 48 and 72 h. The cells were fixed, stained with Hoescht 33342 to mark the nuclei, and imaged on the ImageXpress Micro system. Representative images are shown in Figure 5-5a, where DharmaFECT 3, DharmaFECT 4, Lipofectamine LTX show uptake of the fluorescently labeled siRNA at 48 h relative to the background fluorescence in the control sample. At 72 h, there was less intracellular fluorescence as it is likely that at that time point that the cells start to degrade the siRNA. All three of the transfection reagents showed efficient uptake of the labeled siRNA at all transfection volumes used. From here, cells were transfected with a siRNA against ERK2 as a model kinase gene, with all three transfection reagents for 48 h and 72 h. Western blot analysis of the transfected cells for ERK2 shows that transfection with DharmaFECT 4 at two different siRNA concentrations and transfection volumes shows sufficient knockdown of ERK2 at 48 h (Figure 5-5b). Finally, we used a WST-1 cell proliferation assay to assess the toxicity of DharmaFECT 4 in cells transfected with 25 nM FITC siRNA at different transfection reagent volumes. As can be seen in Figure 5-5c, there is no significant change in cell growth of transfected cells when compared to the control.

High-throughput kinase screen in RAW 264.7 macrophages. With the optimization described above (Table 5-2), we completed a kinase screen in RAW 264.7 macrophages transfected with 20 nM siRNA and DharmaFECT4 (0.12 μL/384 well) for 48 h. The cells were treated with BCS and $CuCl_2$ for 1 h to avoid any transcriptional effects followed by processing for immunofluorescence. All six plates were imaged on the ImageXpress Micro system followed by automated analysis with the translocation-enhanced module. If a kinase phosphorylated ATP7A and prompted its translocation in the presence of copper, we would anticipate that a greater percentage of ATP7A would reside in the Golgi in the absence of that kinase. As such, we quantified the fluorescence intensity of ATP7A in the Golgi compartment as defined by the GM130 marker in both BCS and $CuCl_2$ treated cells and found that there was a 40-50% less ATP7A in copper treated transfected with control siRNAs. If the knockdown of kinase altered the shape of the Golgi it would be reflected in the GM130 marker. The mean fluorescence intensity for nine sites in each well was recorded and subjected to an outlier test defined in Microsoft Excel. Then the average of all of the sites was calculated and two different approaches for mining the dataset were used. An ideal case would be where knockdown of a kinase prevented the translocation of ATP7A from the Golgi in the presence of copper so when compared to its BCS treated counterpart there would be no change in the ATP7A immunofluorescence signal. First we calculated the ratio of the ATP7A fluorescence intensity in the $CuCl_2$ treated wells relative to the BCS treated wells for each gene. The ratio of the ATP7A

fluorescence intensity in the $CuCl_2$ treated well compared to the BCS treated well would be 1 if ATP7A did not translocate when a kinase was silenced. Wells transfected with negative or GFP control siRNAs were the baseline for comparison. With this analysis, most of the genes were considered to be a positive hit regardless of the threshold that we set. In our second approach, we sorted the ATP7A fluorescence intensity in the Golgi compartment from highest to lowest for both treatments. A higher ATP7A fluorescence signal in the copper treated cells would mean that the kinase is involved in the copper mediated translocation of the protein, and with this analysis we significantly refined the dataset to a few potential hits for each kinase plate. For these potential kinases, we plotted the distribution of the fluorescence intensity for all of the cells in the well compared to one of the negative or GFP control transfected wells. One example histogram is shown in Figure 5-6a; however, an important consideration is that the expression of ATP7A could change when a kinase is silenced so the BCS treated cells serve as a control for this variable. The potential hits were further refined and one kinase from each plate was selected: 6-phosphofructo-2-kinase/fructose-2,6-biphosphatase 1 (Pfkfb1), protein kinase D3 (Prkd3), and transient receptor potential cation channel, subfamily M, member 7 (Trpm7). Each plate had at least four wells that were transfected with the negative and GFP control siRNAs, and the average ATP7A fluorescence intensity for each control and the top three genes are shown in Figure 5-6b. If the expression of ATP7A does not change when a kinase is knocked down then the fluorescence intensity for the negative and GFP control versus the gene of interest should not be significantly different with BCS treatment. There is variability between the two control siRNAs, but when the gene of interest is compared to the negative control there is not a significant change in the expression of ATP7A. When the average ATP7A fluorescence intensity of these three genes treated with $CuCl_2$ is compared to the negative and GFP controls, there is an increase in the ATP7A fluorescence intensity suggesting that these kinases could be involved in the copper mediated trafficking of ATP7A. Of note is that the distribution in the example histogram is quite broad and only a small change is observed when the entire well is plotted which is further evident in visual inspection of the images. This variability is likely attributed to cell aggregates that were apparent during image acquisition and low transfection efficiency. These factors combined with the heterogeneity in the wells transfected with the control siRNAs were limiting factors in this initial screen, but nonetheless these three initial hits are promising. Prkd3 is part of the protein kinase C family of serine and threonine-specific kinases, and recently it has been shown that protein kinase D is involved in the expression and trafficking of the copper transporter ATP7B so it is likely that this kinase could also phosphorylate ATP7A since ATP7B is not expressed in the RAW 264.7 macrophages.[9] Pfkfb1 regulates the levels of fructose-2,6-biphosphate which reflects changes in the energy status of the cell through AMP activated protein kinase (AMPK). In this context, cellular copper levels can alter the activation of AMPK and trafficking of ATP7A could signal a shift in cellular metabolism.[10] Finally, Trpm7 is a non-selective ion channel and kinase so it could gate copper entry into the cell or another metal that indirectly alters ATP7A trafficking.[11] Given these initial results, we wanted to increase our dynamic range and transfection efficiency so we decided to use a simple model cell line like HEK 293T or HeLa cells for our next kinase screen.

Optimization of a high-throughput kinase screen in HeLa cells. Both HEK 293T and HeLa cells express ATP7A and are more commonly used in siRNA based screening assays as they are not specialized cells like the RAW 264.7 macrophages. We used two different approaches to identify kinases involved in copper mediated trafficking of ATP7A in these human cell lines. First, in an effort to increase our dynamic range we attempted to generate a stable cell that would

express a functional, fluorescently tagged Venus-ATP7A;[12] however, during the selection process cells only expressed the fluorescent protein and not the ATP7A component of the plasmid. Additionally, many of the colonies only incorporated the antibiotic resistance part of the plasmid. These results are likely due to the large size and toxic nature of the Venus-ATP7A plasmid. With these limitations, we tried to clone the Venus-ATP7A into a plasmid with an internal ribosome entry site so that the genes for the labeled ATP7A and the antibiotic resistance marker would be expressed on the same mRNA, but cloning of the plasmid was not successful.

Next, we tried to optimize a protocol for ATP7A immunostaining in human cell lines (Table 5-2). The method described above for the RAW 264.7 macrophages was used for ATP7A immunostaining in both HEK 293T and HeLa cells plated on glass coverslips with several different anti-ATP7A antibodies, but similar results were not obtained. Contrary to published results, ATP7A localized to the nucleus instead of the trans-Golgi in both cell types under control and copper supplemented conditions.[13] The Triton-X 100 and saponin permeabilization was too harsh since the antibody accumulated in the nucleus. Owing to the poor membrane integrity of these cell types, we screened permeabilization conditions with the milder surfactant Tween-20. ATP7A localized to the Golgi and responded to copper treatment in cells permeabilized with Tween-20, followed by blocking, and addition of the antibody raised against the C-terminus. From here, the same immunofluorescence method was applied with the automation setup where the Velocity 11 was used for all liquid handling. The cells were plated on poly-D-lysine coated 384 well plates, and treated with BCS and $CuCl_2$, and after 2 h, half of the media (26 µL) was removed with the Velocity 11 followed by the addition of 8% PFA supplemented with 8% sucrose in HBSS (26 µL) for 15 min. Sucrose was added to the fixative to maintain cell morphology. Both cell types were adherent post-fixation and washing with the Velocity 11, but during the reminder of the protocol the cells started to peel off the plate. With these results, we used the Velocity 11 for dispensing non-bulk liquids like the permeablization, block, and antibodies but we optimized cell washing with the ELx405 select deep well microplate washer. The HEK 293T cells did not adhere to the plate with the gentler washing, so the remainder of the protocol was tested with the HeLa cell line. The washer was set to leave a cushion volume (12.5 µL) in each well such that the impact of liquid addition with the Velocity 11 would be reduced, but the residual volume from each wash step resulted in a higher background fluorescence compared to complete aspiration that is done with glass coverslips. In order to reduce the background, we screened agents to increase the immunofluorescence signal including ammonium chloride, fish skin gelatin, and Image-iT FX Signal Enhancer and varied the composition of the block solutions to include bovine serum albumin (BSA) and goat serum. Treating the fixed and permeabilized (0.625% Tween 20, 30 min) samples with the Image-iT FX Signal Enhancer followed by blocking with 12.5% goat serum/1.25% BSA and addition of the Hycult primary antibody and secondary antibodies was most effective. The immunofluorescence shows that ATP7A resides in the Golgi with 500 µM BCS treatment, and upon supplementation with 200 µM $CuCl_2$ the ATP7A signal is more diffuse (Figure 5-7a). Encouraged by these results, we used an antibody from Abcam that is raised against the N-terminus of ATP7A. Consistent with previous reports, we find that ATP7A localizes to the nucleus with copper treatment (Figure 5-7b).[14] With this antibody we can look for the disappearance of signal from the Golgi when compared to the GM130 marker and appearance of signal in the nucleus when compared to the Hoescht 33342 stain, so from a data analysis point of view one can get more information. In order to assess the dynamic range with the Abcam antibody we are designing a mini-screen with siRNAs against the model kinase ERK2 and

copper genes, ATOX1 and ATP7A. In the absence of ATOX1, the cell should make more ATP7A so there should be more immunofluorescence signal, but the protein will not translocate in the presence of copper since ATOX1 cannot deliver copper to ATP7A. Silencing of ATP7A should represent the lower end of the immunofluorescence signal. With these two genes we will be able to define a dynamic range and calculate the Z'-factor, which is typically used to define the robustness of a screen.[15]

For the mini-screen, we next optimized methods for reverse transfection in the HeLa cells. Unlike the RAW 264.7 macrophages, HeLa cells are more commonly used in RNAi screens and easier to transfect. HeLa cells were transfected with a 25 and 50 nM ERK2 siRNA with Lipofectamine 2000 or DharmaFECT 4. ERK2 is silenced at both concentrations of siRNA and with both transfection reagents; however, bright field imaging of the wells prior to lysis showed that Lipofectamine 2000 was more toxic than DharmaFECT 4 (Figure 5-6a). Next, cells were transfected with 4 different siRNAs against ATP7A and ATOX1 with DharmaFECT4 and both genes are effectively silenced (Figure 5-6b, c). Finally, WST-1 assay shows that DharmaFECT 4 combined with varying concentrations of negative control siRNA is not toxic.

Concluding Remarks

In this study, we have used high throughput screening methods to understand how RNAi knockdown against the kinome alters the intracellular copper status through ATP7A trafficking. It is known that the phosphorylation of ATP7A causes it to shuttle copper from the trans-Golgi network to the plasma membrane; however, the kinases that mediate this have yet to be identified. In our first kinase screen RAW 264.7 macrophages, we have identified a handful of kinases that partially prevent the translocation of ATP7A in the presence of copper, but it is possible that the cellular machinery can alter the expression of ATP7A upon the knockdown of a kinase. Although we have not pursued follow-up studies with the kinases involved in regulating ATP7A expression, these genes can potentially be powerful to elucidate transcriptional regulation of cellular copper machinery. Moreover, in an effort to control for changes in protein expression and increase the signal to noise ratio, methods have been developed and optimized to do an automated ATP7A immunofluorescence assay in HeLa cells. This optimization study demonstrates the potential utility of high throughput RNAi screening in the discovery of new roles of copper in mammalian cell biology either through ATP7A trafficking or even monitoring labile Cu^{+} pools with newly developed fluorescent copper reporters.

Experimental Section

Optimization of immunostaining in RAW 264.7 macrophages. All of the instrumentation used for high throughput liquid handling was completed at the UC Berkeley Screening Center with assistance from Trish Birk. Ann Fischer at the UC Berkeley Tissue Culture Facility cultured the cells used below. RAW 264.7 macrophages cells were plated in 10-cm plates and for trypsinization the media was removed, the cells were washed once with PBS, then the PBS was removed, and 0.25% trypsin-EDTA (Invitrogen) was added for at least 5 min at 37 °C, 5% CO_2. Phenol red free DMEM with high glucose, non-essential amino acids 10% fetal bovine serum (FBS), sodium pyruvate (complete media) was then added to the plates and the cells were scraped followed by centrifugation at 1200 rpm for 5 min. The supernatant was removed and the cell pellet was re-suspended in complete media (5 mL) from which a portion (50 μL) was diluted

into PBS (950 µL) followed by counting with the Scepter (Millipore). RAW 264.7 macrophages (4000 cells/well) in complete media (50 µL/well) were added to each well with Multidrop Combi reagent dispenser (Thermo Scientific). All of liquid handling described below was completed with the Velocity 11 (Agilent) using 70 µL Axygen automation tips. After 48 hours, solutions of bathocuproine disulfonate (BCS, Sigma) and copper chloride dihydrate ($CuCl_2$, Sigma) in 137 mM saline was added (1 µL) with the Multidrop Combi reagent dispenser to a final concentration of 200 µM. The cells were incubated 37 °C, 5% CO_2 for 2 h. Then media was removed and the cells were fixed with 4% PFA (16% aqueous stock solution, Electron Microscopy Sciences) in PBS for 10 min. The cells were then washed 3 x 50 µL with PBS for 5 min each. The cells were blocked and permeabilized for 1 h with 0.1% saponin (Sigma) and 5% donkey serum (Jackson ImmunoResearch) in PBS. The block was removed and the antibody was added in 0.1% saponin/5% donkey serum with ATP7A at 1:100 (Hycult Biotech, Catalog #HP8040) and GM130 1:400 (BD Biosciences, Catalog #558712) at 4 °C overnight. The next day, the primary antibodies were removed and the cells were washed with PBS (2 x 50 µL) for 10 min, and washed PBS (1 x 50 µL) for 30 min. Then the secondary antibodies (1:125, Alexa Fluor 488 donkey anti-rabbit IgG, Alexa Fluor 594 donkey anti-mouse IgG, Invitrogen) and nuclear stain (Hoescht 33342, 2 µM final concentration) were added for 2 h at room temperature. The cells were washed with PBS as described above for the primary, and then fresh PBS (50 µL) was added prior to imaging. Images were acquired on the ImageXpress Micro system (Molecular Devices) with a 20x ELWD objective at the UC Berkeley Screening Center or Stem Cell Center with assistance from Mary West.

Uptake of FITC labeled siRNA in RAW 264.7 macrophages. For uptake of siRNA, RAW 264.7 macrophages were transfected with 100 nM fluorescein isothiocyanate (FITC) labeled siRNA (Qiagen). The siRNA in OptiMEM (Invitrogen) was first seeded (5 µL) into a 384-well Greiner TC treated black/clear bottom plate, with the Velocity 11. Then three different transfection reagents (DharamaFECT 3, DharamaFECT 4, and Lipofectamine LTX, 0.07 µL/well) in OptiMEM were added (10 µL). The siRNA-transfection reagent complex was allowed to form for 30 min. RAW 264.7 macrophages cells were plated in six-well plates and prepared for plating as described above. For siRNA uptake, RAW 264.7 macrophages (5000 cells/well) in complete media (30 µL/well) were added to each well. After 48 h, media was removed, the cells fixed with 4% PFA in PBS, washed with PBS, PBS with 2 µM Hoescht 33342 was added, washed and imaged in fresh PBS. All liquid handling was completed on the Velocity 11. Images were acquired as described above.

Transfection and immunoblotting of ERK2 in RAW 2647 macrophages. For knockdown of ERK2 in RAW 264.7 macrophages, siRNA against ERK2 (Qiagen) was diluted into OptiMEM to give 225 nM and 450 nM stock solutions. The siRNA solutions were allowed to equilibrate for 5 min at room temperature and then 100 µL of each stock solution was seeded into a Corning Costar 24-well cell culture plate without coating to give a final concentration of 25 nM and 50 nM after the addition of transfection reagent and cells. DharmaFECT3, DharmaFECT 4, and Lipofectamine LTX (2.8 or 4.2 µL/well) were diluted into OptiMEM (200 µL) and allowed to equilibrate for 5 min at room temperature and then added to the siRNA. The complex was allowed to form for at least 30 min. RAW 264.7 macrophages cells (P10) were plated in 10-cm plates and and prepared for plating as described above. For the ERK2 knockdown, RAW 264.7 macrophages (100,000 cells/well) in complete media (600 µL/well) were added to each well. After 48 h, the media was removed, the cells were washed 2x with cold PBS, and then lysed in radioimmunoprecipitation (RIPA) buffer (50 mM Tris, pH 7.4, 150 mM NaCl, 1% Triton X-

100, 0.5% sodium deoxycholate, and 0.1% SDS) supplemented with protease inhibitors (Roche Complete MiniTab) and phosphatase inhibitors (Thermo Scientific Halt Phosphatase Inhibitor Cocktail), lysed for 30 min on ice, and cleared by centrifugation at 13.2 x 10^3 rpm for 10 min at 4 °C. Protein concentration was determined by bicinchoninic acid (BCA) assay (Pierce). Equal amounts of protein were combined with 5 µL of 4x Laemmli buffer (0.25 mM Tris, 2% SDS, 40% glycerol, 20% beta-mercaptoethanol, 0.04% bromophenol blue), the samples denatured at 95 °C for 5 min, and were loaded and separated on a 4-12% Bis-tris gel (NuPAGE Novex, Invitrogen). Proteins were transferred to PVDF membranes (Immobilon, Millipore) with a semi-dry transfer system (Biorad) at constant voltage (15 V) for 35 min. The blots were blocked for 1 h in 5% nonfat dry milk in wash buffer (10 mM Tris, pH 7.5, 100 mM NaCl, 0.1% Tween-20), and incubated overnight at 4 °C with anti-ERK at 1:1000 (Cell Signaling, Catalog# 4695). Membranes were washed 5 times for 5 min in wash buffer, incubated at room temperature with 1:2000 secondary antibody, washed 5 times for 5 min in wash buffer, and then visualized using enhanced chemiluminescence (Western Lightning Plus ECL, PerkinElmer) recorded on a BioRad GelDoc imaging station. Equal sample loading was confirmed by Ponceau staining.

WST-1 assay of RAW 264.7 macrophages. FITC labeled siRNA (Qiagen) was prepared in Opti-MEM (Invitrogen) for a final concentration of 25 nM. The siRNA solution was allowed to equilibrate at room temperature for 5 min prior to seeding 5 µL into the wells of a Corning 384-well TC treated black/clear bottom plate (Catalog# 3712). Stock solutions of DharmaFECT 4 (0.05, 0.1, 0.14, and 0.18 µL/well) (Thermo Scientific) were prepared in Opti-MEM and allowed to equilibrate at room temperature for 5 min followed by seeding 10 µL of this stock solution into each well. The siRNA and transfection reagent were allowed to complex for at least 30 min. For control cells without siRNA and transfection reagent 15 µL of Opti-MEM was seeded in the wells. RAW 264.7 macrophages (P2) were plated 10-cm plates and prepared for plating as described above. For the WST-1 assay, RAW 264.7 macrophages (5000 cells/well) in complete media (35 µL) were added to each well. After 48 h, the WST-1 reagent (5 µL) was added directly into the wells. For the baseline reading media with WST-1 was used. The absorbance at 440 nm and 600 nm was recorded on the SpectraMax M2 (BioTek) every 30 min for up to 2 h.

Kinase screen for RAW 264.7 macrophages. The Qiagen mouse kinome library was purchased through the UC Berkeley Screening Center and contains 762 genes in three plates (4 siRNAs/well). The siRNAs on the edges were removed and re-arrayed by hand onto the available re-arrayed by hand into empty wells. The siRNAs (2 µL, 20 nM final concentration) were daughtered into six Corning 384 well TC treated black/clear bottom plates (Catalog #3712) with 10 µL Axygen automation tips on the Velocity 11. A stock solution of the DharmaFECT4 transfection reagent (0.12 µL/well) in OptiMEM (10 µL/well) was added with the Multidrop Combi reagent and the resulting complex was allowed to form for at least 30 min. RAW 264.7 macrophages (P4) were plated in complete media as described above (4000 cells/well plated in 35 µL). After 48 h, saline solutions of BCS (200 µM final concentration) were added to three plates and $CuCl_2$ were added for 1 h at 37 °C, 5% CO_2. The cells were processed for immunofluorescence and imaged as described above. Data analysis was completed using the translocation-enhanced module on the ImageXpress Micro system. The Golgi compartment was defined by GM130, and the mean fluorescence intensity of ATP7A that overlapped with the Golgi was quantified from nine sites per well. From here, the outlier test defined in Microsoft Excel was used to refine the data from the nine sites and the mean fluorescence intensity of the entire well was used for further analysis.

Optimization of immunostaining in HeLa cells. OptiMEM (10 µL) was seeded into each well of a Greiner 384-well poly-D-lysine coated black/clear bottom plate with the Multidrop Combi reagent dispenser followed by cell plating. HeLa cells (P18) were plated one day of growth in 3 10-cm plates. For trypsinization the media was removed, the cells were washed once with PBS, then the PBS was removed, and 0.05% trypsin-EDTA (Invitrogen) was added for 5 min at 37 °C. Phenol red free, DMEM with high glucose, glutamax, sodium pyruvate, and 10% FBS (complete media) was then added to the trypsinized cells followed by centrifugation at 1200 rpm for 5 min. The supernatant was removed and the cell pellet was re-suspended in complete media (10 mL) from which a portion (50 µL) was diluted into PBS (950 µL) followed by counting with the Scepter. HeLa cells (1350 cells/well) in complete media (40 µL/well) were added to each well with the Multidrop Combi reagent dispenser. After 48, BCS (1 µL, final concentration 500 µM) and $CuCl_2$ (1 µL, final concentration 200 µM) prepared in 137 mM saline were added with the Multidrop Combi reagent dispenser for 3 h. Half of the media (25 µL) was removed with the Velocity 11, followed by the addition of 25 µL of 8% PFA/8% sucrose in HBSS (Invitrogen) with the Velocity 11. The cells were fixed for 15 min at room temperature followed by 4 x 50 µL PBS washes without final aspirate for 5 min each with a ELx405 select deep well microplate washer (Biotek). The plate was stored at 4 °C overnight. The following day, the plate was washed with a final aspirate to leave a 12.5 µL residual volume in each well and then the cells were permeabilized with 37.5 µL of 0.625% Tween-20 (Sigma) in PBS (prepared from a 10% stock solution w/v) for 30 min at room temperature. The Velocity 11 was used to add the permeabilization agent. After 30 min, the cells were washed with 2 x 50 µL PBS for 5 min. The washer was set to a double wash in each wash cycle with the first wash being set to no final aspirate and the second with final aspirate to leave a residual volume of 12.5 µL. Then 37.5 µL of Image-iT FX Signal Enhancer (Invitrogen) was added with the Velocity 11 for 30 min. The cells were then washed with 2 x 50 µL PBS for 5 min with the double wash cycle setting with a residual volume of 12.5 µL. Subsequently, the cells were blocked with 1.25% fatty acid free bovine serum albumin (BSA, Sigma) and 12.5% goat serum (Jackson ImmunoResearch) in PBS for 1 h at room temperature, followed by washing with 2 x 50 µL PBS for 5 min with the double wash cycle setting with one wash without final aspirate and the other with final aspirate leaving behind a residual volume of 12.5 µL. The BSA solution was filtered prior to use and the goat serum was cleared by centrifugation at 13.2 x 10^3 rpm at 4 °C for 10 min prior to use. Primary antibody (37.5 µL) was added with the Velocity 11 in block 4 °C overnight. The concentration of the ATP7A from both Hycult Biotech and Abcam (Catalog #ab42486) was 1:80 and the concentration of GM130 was 1:240. The next day, the cells were washed 4 x 50 µL PBS for 10 min with the double wash cycle setting. Three washes were set to no final aspirate and the last wash was set to final aspirate to leave 2 x 50 µL PBS for 5 min with the double wash cycle setting to leave a residual volume of 12.5 µL. Secondary antibodies (1:100 final concentration, Alexa Fluor 488 goat anti-rabbit IgG, Alexa Fluor 594 goat anti-mouse IgG, Invitrogen) and the nuclear stain (Hoescht 33342, 2 µM final concentration) were added with the Velocity 11 for 2 h at room temperature. The secondary antibodies were cleared at13.2 x 10^3 rpm for 10 min at 4 °C prior to use to remove aggregates. The cells were then washed 4 x 50 µL PBS for 10 min with the double wash cycle setting without final aspirate. For all liquid handing with the Velocity 11, the tips were washed with PBS after each reagent was dispensed. On the Velocity 11, all additions were done at slow speed with a small working distance relative to the sample, and all aspirations were done at high speed with a large working distance relative to the sample. Samples were imaged as described above for the RAW macrophages.

Transfection and immunoblotting of ERK2, ATP7A, and ATOX1 in HeLa cells. For knockdown of ERK2 in HeLa cells, siRNA against ERK2 (Qiagen) was diluted directly into a Corning Costar 24-well cell culture plate without coating from a 100 μM stock into 100 μL of OptiMEM to give a final concentration of 25 nM and 50 nM after the addition of transfection reagent and cells. The AllStars negative control siRNA was diluted to 25 nM and 50 nM from a 100 μM stock. The siRNA solutions were allowed to equilibrate at room temperature for 5 min. Lipofectamine 2000 or DharmaFECT 4 (1 μL/well) was diluted in OptiMEM (200 μL) and allowed to equilibrate for 5 min at room temperature and then added to the siRNA. The complex was allowed to form for at least 30 min. HeLa cells (P9) were plated in 2 10-cm plates for 3 days prepared for plating as described above. For the ERK2 knockdown, HeLa cells (32,000 cells/well) in complete media (600 μL/well) were added to each well. After 48 h, the cells were lysed and processed for western blot analysis as described above. Equal amounts of protein were combined with 5 μL of Laemmli buffer, the samples denatured at 95 °C for 5 min, the samples were loaded and separated on a 4-12% bis-tris gel. Proteins were transferred to PVDF membranes with a semi-dry transfer system at constant voltage (15 V) for 35 min. The blots were blocked for 1 h in 5% BSA in wash buffer, and incubated overnight at 4 °C in anti-ERK2 1:1000. Membranes were washed 5 times for 5 min in wash buffer, incubated at room temperature with 1:2000 secondary antibody, washed 5 times for 5 min in wash buffer, and then visualized using enhanced chemiluminescence (Western Lightning Plus ECL, PerkinElmer) recorded on a BioRad GelDoc imaging station. Equal sample loading was confirmed by Ponceau staining. For knockdown of ATP7A in HeLa cells, siRNAS against ATP7A (Qiagen) were diluted directly into a Corning Costar 24-well cell culture plate without coating from a 50 μM stock into 100 μL of OptiMEM to give a final concentration of 50 nM and 100 nM after the addition of transfection reagent and cells. The AllStars negative control siRNA was diluted to 50 nM and 100 nM from a 100 μM stock. The siRNA solutions were allowed to equilibrate at room temperature for 5 min. DharmaFECT 4 (1 μL/well) was diluted in OptiMEM (200 μL) and allowed to equilibrate for 5 min at room temperature and then added to the siRNA. The complex was allowed to form for at least 30 min. HeLa cells (P14) were plated for 1 day in 3 10-cm plates and prepared for plating as described above. For the ATP7A knockdown, HeLa cells (32,000 cells/well) in complete media (600 μL/well) were added to each well. After 48 h, the cells were lysed and processed for western blot analysis as described above. Equal amounts of protein were combined with 5 μL of Laemmli buffer, the samples denatured at 37 °C for 10 min, the samples were loaded and separated on a 4-12% bis-tris gel. Proteins were transferred to PVDF membranes with the semi-dry transfer system at constant voltage (15 V) for 40 min. The blots were blocked for 1 h in 5% BSA in wash buffer, and incubated overnight at 4 °C in anti-ATP7A 1:1000 (Hycult Biotech). Membranes were washed 5 times for 5 min in wash buffer, incubated at room temperature with 1:2000 secondary antibody, washed 5 times for 5 min in wash buffer, and then visualized using enhanced chemiluminescence (Western Lightning Plus ECL, PerkinElmer) recorded on a BioRad GelDoc imaging station. Equal sample loading was confirmed by Ponceau staining. For knockdown of ATOX1 in HeLa cells, siRNAs against ATOX1 (Qiagen) were diluted directly into a Corning Costar 12-well cell culture plate without coating from a 50 μM stock into 200 μL of Opti-MEM (Invitrogen) to give a final concentration of 50 nM after the addition of transfection reagent and cells. The AllStars negative control siRNA was diluted directly into the well in 200 μL of Opti-MEM from a 100 μM stock to give a final concentration of 50 nM after the addition of transfection reagent and cells. The solutions of the siRNA were allowed to equilibrate for 5 min at room temperature. DharmaFECT 4 (2 μL/well) was diluted in

OptiMEM and allowed to equilibrate for 5 min and then added (400 µL) to the siRNA. The siRNA and tranfection reagent were allowed to equilibrate for at least 30 min. HeLa cells (P20) were plated for 2 days in 4 10-cm plates and prepared for plating as described above. For the ATOX1 knockdown, HeLa cells (64,000 cells/well) in complete media (1200 µL/well) were added to each well. After 48 h, the cells were lysed and processed for western blot analysis as described above. Equal amounts of protein were combined with Novex tricine SDS sample buffer (12.5 µL) (Invitrogen) and NuPAGE reducing agent (2.5 µL) (Invitrogen) and heated at 85 °C for 2 min. The samples were resolved on a Novex 10-20% tricine gel (Invitrogen) and proteins were transferred to a PVDF membrane with the semi-dry transfer system at constant voltage (15 V) for 30 min. The blots were blocked for 1 h in 5% BSA in wash buffer (10 mM Tris, pH 7.5, 100 mM NaCl, 0.1% Tween-20), and incubated overnight at 4 °C in anti-ATOX1 1:500 (Abcam, Catalog #ab54865). Membranes were washed 5 times for 5 min in wash buffer, incubated at room temperature with 1:2000 secondary antibody, washed 5 times for 5 min in wash buffer, and then visualized using enhanced chemiluminescence (Luminata Classico Western HRP Substrate, Millipore) recorded on a BioRad GelDoc imaging station. The blot was stripped using Restore Plus stripping buffer (Thermo Scientific) according to manufacturer's instructions. The blot was then washed 5 times for 5 min in wash buffer, and then probed for anti-actin 1:2000 (Millipore) and developed as described above.

WST-1 assay of HeLa cells. Stock solutions of AllStars negative control siRNA (Qiagen) were prepared in Opti-MEM (Invitrogen) at 1 µM, 500 nM, 250 nM, and 125 nM and allowed to equilibrate at room temperature for 5 min prior to seeding 15 µL of each solution into 4 different wells of a Greiner 96-well poly-L-lysine coated black/clear bottom plate. Opti-MEM alone was seeded in wells without siRNA. A stock solution of DharmaFECT 4 (0.15 µL/well) (Thermo Scientific) was prepared in Opti-MEM and allowed to equilibrate at room temperature for 5 min followed by seeding 30 µL of this stock solution into each well. Opti-MEM alone was seeded in wells without transfection reagent. The siRNA and transfection reagent were allowed to complex for at least 30 min. For control cells without siRNA or transfection reagent 45 µL of Opti-MEM was seeded in the wells. HeLa cells (P20) were plated in 4 10-cm plates and prepared for plating as described above. For the WST-1 assay, HeLa cells (4500 cells/well) in complete media (105 µL) were added to each well. After 48 h, the WST-1 reagent (15 µL) was added directly into the wells. For the baseline reading media with WST-1 was used. The absorbance at 440 nm and 600 nm was recorded on the SpectraMax M2 every 30 min for upto 2 h.

Tables and Figures

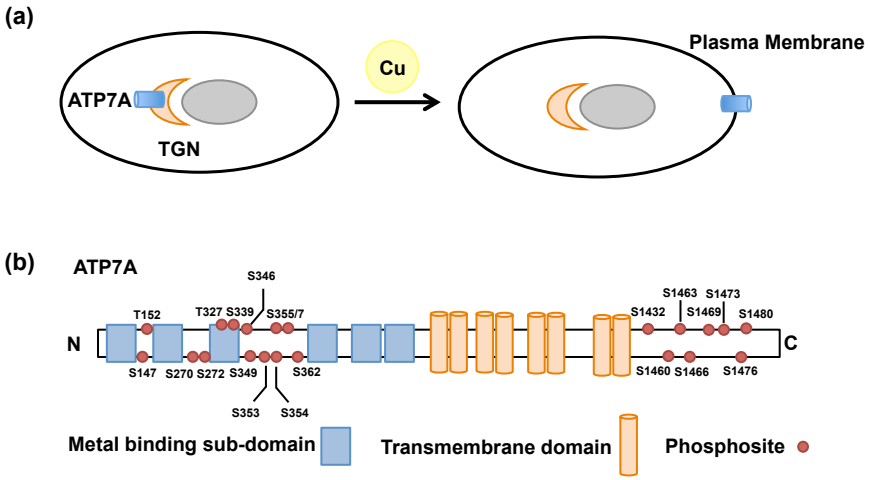

Figure 5-1. (a) Schematic for the copper mediated trafficking of ATP7A from the trans-Golgi network to the plasma membrane. (b) Schematic of the phosphorylation sites identified for human and hamster ATP7A found in Reference 4.

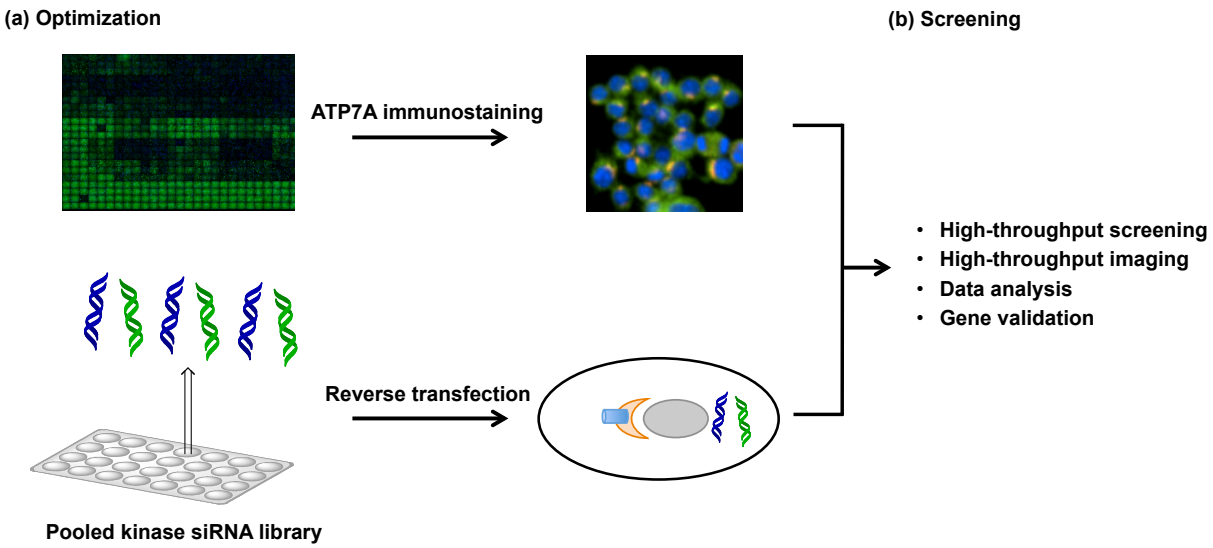

Figure 5-2. Schematic of a high-throughput screen to discover kinases involved in the copper mediated trafficking of ATP7A. (a) Conditions for ATP7A immunostaining and reverse transfection must be optimized in the first phase. (b) In the next phase, screening is followed by imaging, data analysis, and gene validation.

Immunostaining	Transfection
Fixation	Cell type
Permeabilization	Plate coating
Block	Cell density
Primary antibody	Cell passage
Secondary antibody	Transfection reagent
Localization marker	Transfection toxcity
Liquid handling	Transfection efficiency
Image acquisition	Knockdown efficiency

Table 5-1. In the development phase of the assay variables for both immunostaining and transfection must be optimized.

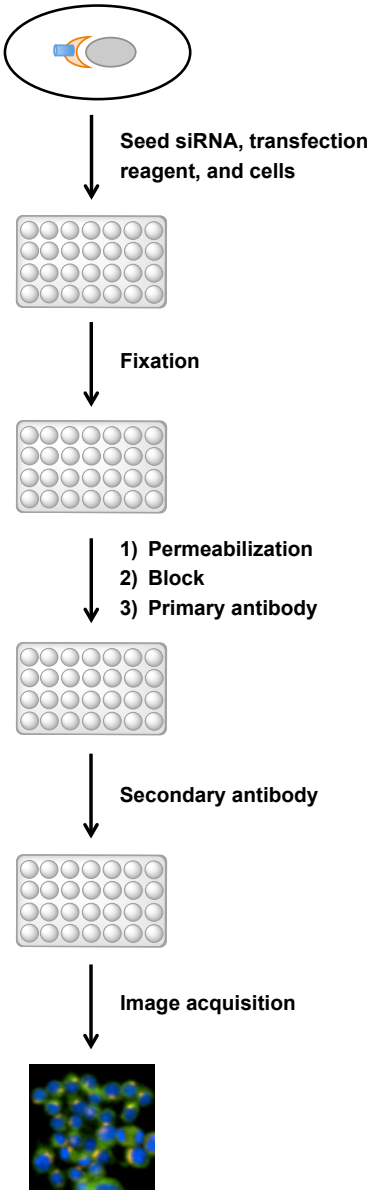

Figure 5-3. Typical steps in an immunofluorescence protocol. Wash steps have been excluded in the schematic.

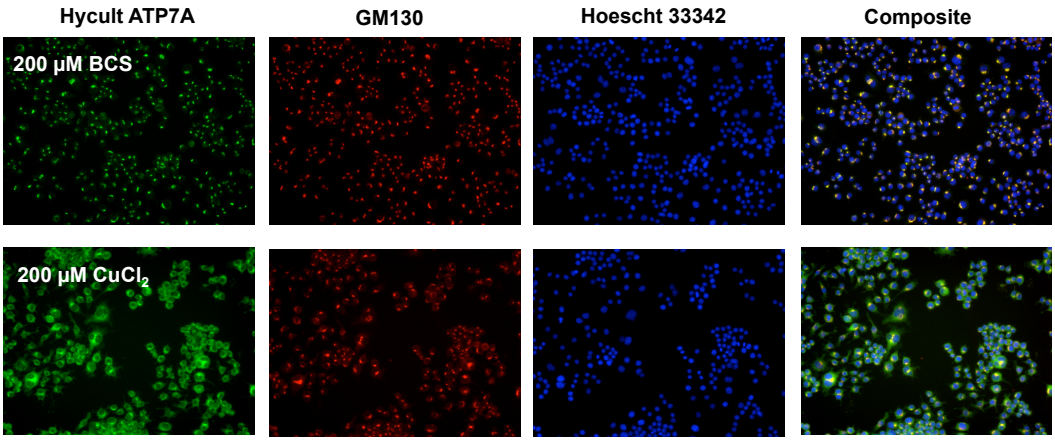

Figure 5-4. Representative immunofluorescence images of ATP7A, GM130 (cis-Golgi marker), and Hoescht 33342 (nuclear marker) in RAW 264.7 macrophages treated with 200 µM BCS and 200 µM $CuCl_2$ for 2 h.

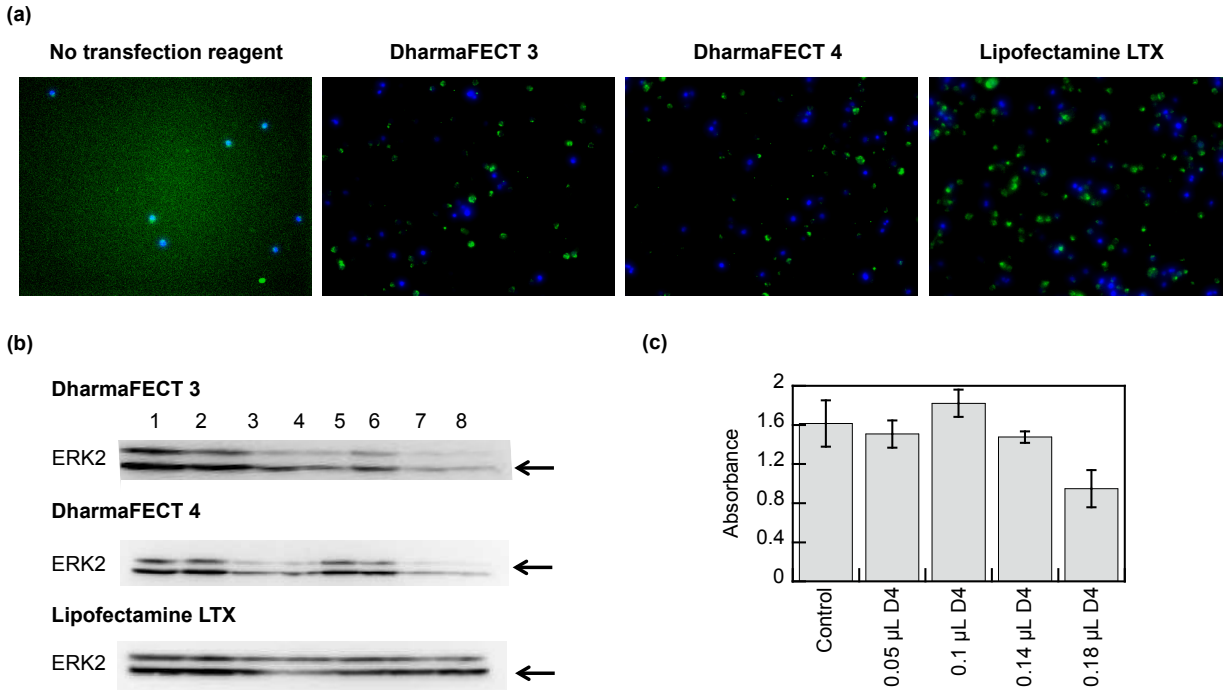

Figure 5-5. (a) Representative images of RAW 264.7 macrophages transfected with 100 nM FITC-labeled siRNA combined with DharmaFECT 3, DharmaFECT 4, or Lipofectamine LTX transfection reagent for 48 h. Nuclei were stained with Hoescht 33342 and are shown in blue. (b) Representative western blot showing ERK2 knockdown in RAW 264.7 macrophages transfected with ERK2 siRNA combined with DharmaFECT 3, DharmaFECT 4, or Lipofectamine LTX transfection reagent in a 24-well plate for 48 h. Each lane is defined as follows: lane number (transfection reagent volume in µL, amount of siRNA in nM). Lane 1 (0, 0), 2 (2.8, 0), 3 (2.8, 25), 4 (2.8, 50), 5 (4.2, 0), 6 (4.2, 25), 7 (4.2, 50). The band that corresponds to ERK2 is marked with an arrow. Equal sample loading was confirmed by Ponceau staining. (c) WST-1 cell viability assay of RAW 264.7 macrophages after transfection for 48 h with 25 nM FITC-labeled siRNA combined with varying amounts of DharmaFECT 4. Control treatment had no siRNA or transfection reagent. The volumes listed correspond to a 384 well plate. The average of at least four wells for each transfection is shown and the error bars represent standard deviation.

(a)

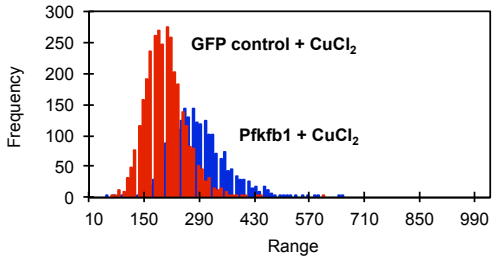

(b)

	Mean Fluorescence Intensity	
Gene	**BCS**	**Cu**
Negative control	555	222
GFP control	484	203
Pfkfb1	545	263
Negative control	585	252
GFP control	476	216
Prkd3	586	299
Negative control	568	257
GFP control	548	265
Trpm7	579	303

Figure 5-6. Summary of kinases that could be involved in the copper mediated trafficking of ATP7A. (a) Representative histogram for the fluorescence intensity of ATP7A in the Golgi compartment of RAW 264.7 macrophages transfected with siRNAs against GFP and Pfkfb1 for 48 h and treated with 200 μM $CuCl_2$ for 1 h. (b) Table of mean fluorescence intensities of ATP7A in the Golgi compartment of RAW 264.7 macrophages transfected with siRNAs for the negative control, GFP, or gene of interest for 48 h with 200 μM BCS or 200 μM $CuCl_2$ for 1 h.

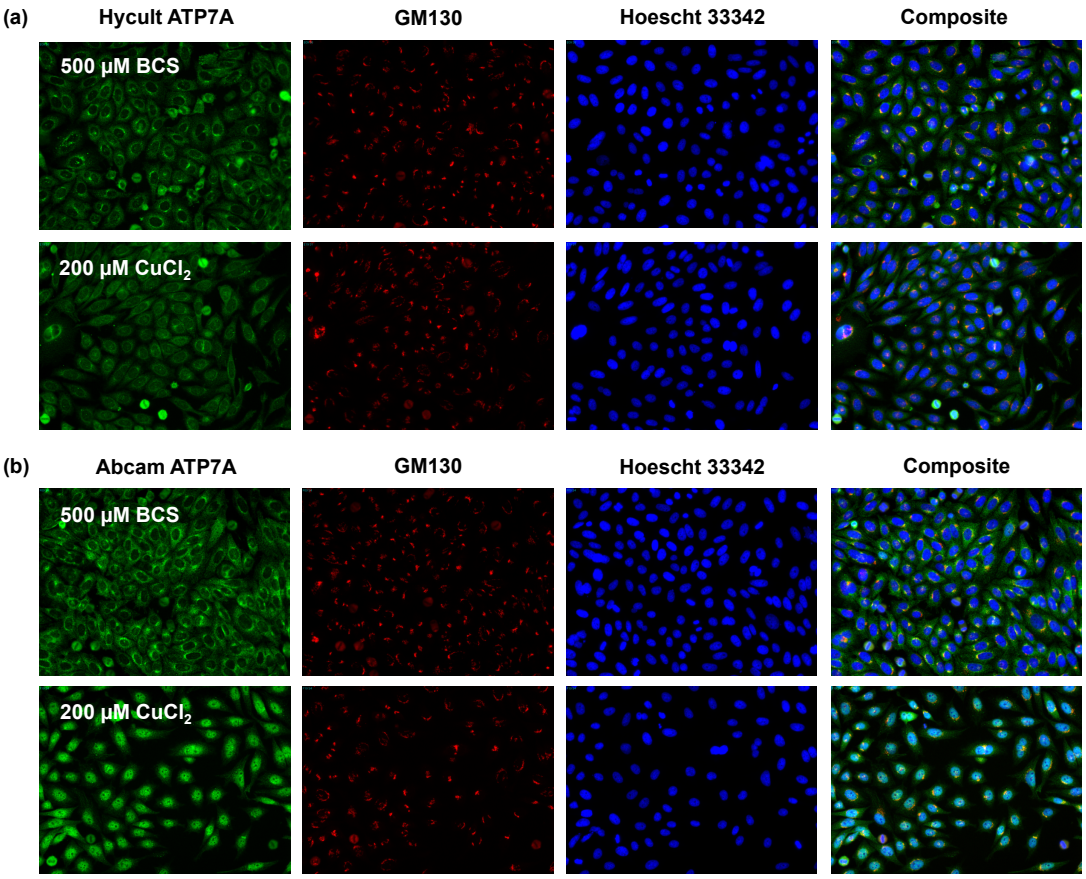

Figure 5-7. Representative immunofluorescence images of ATP7A, GM130 (cis-Golgi marker), and Hoescht 33342 (nuclear marker) in HeLa cells treated with 500 μM BCS or 200 μM $CuCl_2$ for 3 h with two different antibodies against ATP7A: (a) anti-ATP7A from Hycult Biotech and (b) anti- ATP7A from Abcam.

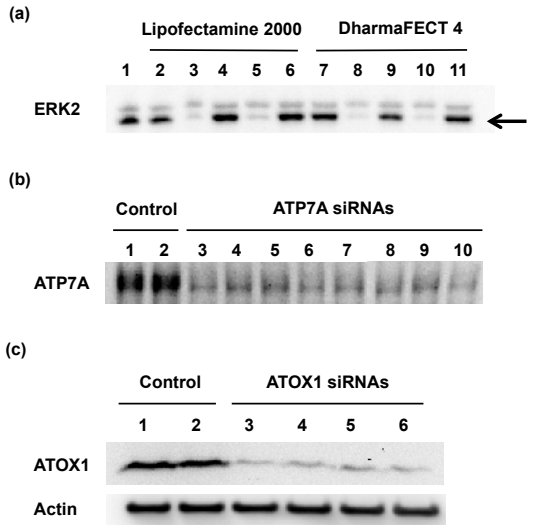

Figure 5-8. (a) Representative western blot showing ERK2 knockdown in HeLa cells transfected with negative control or ERK2 siRNA combined with Lipofectamine 2000 (L2000) or DharmaFECT 4 (D4) transfection reagent in a 24-well plate for 48 h. Each lane is defined as follows: lane number (name of transfection reagent, name of siRNA, amount of siRNA in nM). Lane 1 (none, none, 0), 2 (L2000, none, 0), 3 (L2000, ERK2, 25), 4 (L2000, negative, 25), 5 (L2000, ERK2, 50), 6 (L2000, negative, 50), 7 (D4, none, 0), 8 (D4, ERK2, 25), 9 (D4, negative, 25), 10 (D4, ERK2, 50), 11 (D4, negative, 50). The band that corresponds to ERK2 is marked with an arrow. Equal sample loading was confirmed by Ponceau staining. (b) Representative western blot showing ATP7A knockdown in HeLa cells transfected with negative control siRNA or 4 different siRNAs against ATP7A combined with DharmaFECT 4 in a 24-well plate for 48 h. Each lane is defined as follows: lane number (name of siRNA, amount of siRNA in nM). Lane 1 (negative, 50), 2 (negative, 100), 3 (ATP7A 1, 50), 4 (ATP7A 4, 50), 5 (ATP7A 5, 50), 6 (ATP7A 6, 50), 7 (ATP7A 1, 100), 8 (ATP7A 4, 100), 9 (ATP7A 5, 100), 10 (ATP7A 6, 100). Equal sample loading was confirmed by Ponceau staining. (c) Representative western blot showing ATOX1 knockdown in HeLa cells transfected with 50 nM negative control siRNA or 4 different siRNAs against ATOX1 with DharmaFECT 4 in a 24-well plate for 48 h. Each lane is defined as follows: lane number (name of siRNA). Lane 1 (none), 2 (negative), 3 (ATOX1 2), 4 (ATOX 1 5), 5 (ATOX 1 6), 6 (ATOX1 7). Equal sample loading was confirmed by re-probing the blot for actin.

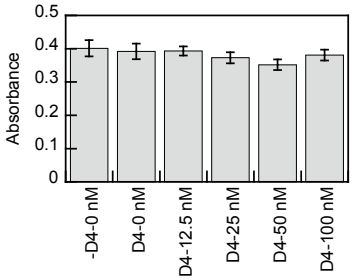

Figure 5-9. WST-1 cell viability assay of HeLa cells after transfection for 48 h with varying amounts of negative control siRNA combined with a fixed volume of DharmaFECT 4 (D4). The average of at least four for each transfection is shown and the error bars represent standard deviation. WST-1 reading shown was completed 1 h after the reagent was added.

Fixation	RAW 264.7	HeLa
4% PFA in PBS	✓	✗
4% PFA in HBSS	N/A	✗
4% PFA/4% sucrose in HBSS	N/A	✓
Permeabilization		
0.1% Saponin in block 1 h	✓	✗
0.1% Triton-X 100 in block 1 h	N/A	✗
0.25% Triton-X 100 in block 1 h	N/A	✗
0.5% Triton-X 100 in block 1 h	N/A	✗
0.2% Triton-X 100 5 min	N/A	✗
0.25% Tween-20 30 min	N/A	✓
0.5% Tween-20 30 min	N/A	✓
Background reducers		
100 mM ammonium chloride	N/A	✗
Image-iT Signal enahncer	N/A	✓
Block		
5% Donkey serum	✓	N/A
5% Goat serum, 1% BSA	N/A	✗
5% Goat serum, 1% FSG	N/A	✗
1% BSA, 1% FSG	N/A	✗
10% Goat serum, 1% BSA	N/A	✓
anti-ATP7A antibody		
Hycult Biotech C-terminus	✓	✓
Betty Eipper C-terminus	✓	✓
Steve Kaler C-terminus	N/A	✗
Neuromab N-terminus	N/A	✗
Sigma C-terminus, chicken	N/A	✗
Abcam N-terminus	N/A	✓
Liquid handling		
Velocity 11	✓	✗
Velocity 11 + ELx405 washer	N/A	✓
Plate coating		
TC treated	✓	✗
Poly-D-lysine	N/A	✓
Cell Density		
Cell density in 384 well	4000	1500
siRNA		
nM of siRNA	20	25
Transfection reagent		
Dharmafect 3	✓	N/A
Dharmafect 4	✓	✓
Lipofectamine LTX	✗	N/A
Lipofectamine 2000	N/A	✓

Table 5-2. Variables that were screened and optimized for ATP7A immunofluorescence in RAW 264.7 macrophages and HeLa cells. Abbrreviations: PFA (paraformaldehyde), FSG (fish skin gelatin), BSA (bovine serum albumin), ✗ means that the condition did not work and ✓ means that the condition did work.

References

1. Que, E. L.; Domaille, D. W.; Chang, C. J. *Chem. Rev.* **2008**, *108*, 1517—1549.
2. Moffat, J.; Sabatini, D. M.; *Nat. Rev. Mol. Cell Bol*. **2007**, *7*, 177—187.
3. Lutsenko, S.; Barnes, N. L.; Bartee, M. Y.; Dmitriev, O. Y. *Physiol. Rev.* **2007**, *87*, 1011—1046.
4. Veldhuis, N. A.; Valova, V. A.; Gaeth, A. P.; Palstra, N.; Hannan, K. M. et al. *Int. J. Biochem. Cell Biol.* **2009**, *41*, 2043—2412.
5. White, C.; Lee, J.; Kambe, T.; Fritsche, K.; Petris, M. J. *J. Biol. Chem.* **2009**, *284*, 33949—33956.
6. Steveson, T. C.; Ciccotosto, G. D.; Ma, X. M.; Mueller, G. P.; Mains, R. E.; Eipper, B. A. *Endocrinology*. **2003**, *144*, 188—200.
7. Jamur, M. C.; Oliver, C. *Methods Mol. Biol.* **2010**, *588*, 63—66.
8. Carralot, J. P.; Kim, T. K.; Lenseigne, B.; Boese, A. S.; Sommer, P. et al. *J. Biomol. Screen.* **2009**, *14*, 151—160.
9. Pilankatta, R.; Lewis, D.; Inesi, G.; *J. Biol. Chem.* **2011**, *286*, 7389—7396.
10. Gybina, A. A; Prohaska, J. R. *Exp. Biol. Med.* **2008**, *233*, 1262—1270.
11. Monteilh-Zoller, M. K.; Hermosura, M. C.; Nadler, M. J. S.; Scharenberg, A. M.; Penner, R.; Fleig, A. *J. Gen. Physiol.* **2003**, *121*, 49—60.
12. Yi, L.; Donsante, A.; Kennerson, M. L.; Mercer, J. F.; Garbern, J. Y.; Kaler, S. G. *Hum. Mol. Genet.* **2012**, *21*, 1794—1807.
13. Holloway, Z. G.; Grabski, R.; Szul, T.; Styers, M. L.; Coventry, J. A.; Monaco, A. P.; Sztul, E. *Am. J. Physiol. Cell Phsyiol.* **2007**, *293*, C1753—C1767.
14. Collins, J. F.; Hua, P.; Lu, Y.; Ranganathan, P. N. *Am. J. Physiol. Gastrointest. Liver Phsyiol.* **2009**, *297*, G695—G707.
15. Malo, N.; Hanley, J. A.; Cerquozzi, S.; Pelletier, J.; Nadon, R. *Nat. Biotech.* **2006**, *24*, 167—175.

Appendix 1:
Aza BODIPY Based Near Infrared Copper Sensors

Introduction

Bioavailable Cu^+ in our lab has been visualized in cellular systems with dyes that consist of a BODIPY fluorophore and a soft thioether rich receptor suitable for the binding of soft Cu^+.[1-5] These Cu^+-specific probes emit in the visible region (ca. 550 nm) and are suitable for thin samples such as cell monolayers, but thicker samples (e.g. tissue slices) require fluorescent probes that absorb and emit at longer wavelengths to minimize interference from native biological components. Near-infrared (NIR) fluorescent scaffolds satisfy this demand. With absorption and emission characteristics in the "therapeutic window" (650 – 900 nm), NIR-based fluorescent probes allow for deep tissue imaging in living organisms, and provide a technique to investigate biological processes in consideration of integrated biological systems.[6]

NIR imaging scaffolds include the cyanines, naphthoquinones, oxazines, squarines, and a more recent platform is the aza-dipyrromethene boron difluoride (aza-BODIPY) scaffold.[6] This scaffold's properties include long wavelength excitation and emission (650 nm-850 nm in H2O/Cremphor EL), high extinction coefficients, quantum yields, biocompatibility, and a modular synthesis.[7-12] We have explored the aza-BODIPY framework as a fluorescent reporting unit for our target NIR Cu^+-responsive probe by attaching the receptor to the core through a phenyl or benzyl linker. This appendix describes the synthesis and characterization of two aza-BODIPY based near-infrared copper sensors, NCS1 and NCS2.

Results and Discussion

Synthesis of Near-Infrared Copper Sensors. Schemes A1-1 and A1-2 outline the synthetic route to the near-IR Cu^+ responsive indicator N-CS1, where the receptor is introduced directly into the π-system of the fluorophore. The synthesis of N-CS1 begins with the construction of a pyrrole containing the open chain tetrathiaaza receptor. Commercially available *N*-phenyl diethanolamine is first tosylated to give **1**.[13] Then ethyl 2-hydroxyethyl sulfide is converted to thiol **2** with thiourea and HBr.[1] Coupling of **1** and **2** in DMF in the presence of Cs_2CO_3 affords **3** in 42% yield. Vilsmeier formylation of **3** with $POCl_3$ in DMF followed by basic workup generates aldehyde **4** in 92% yield and condensation with acetophenone furnishes chalcone **5** in 49% yield. The subsequent Michael addition of CH_3NO_2 to **5** provides nitro adduct **6** in 80% yield. Sequential Nef reaction and condensation with NH_4OAc delivers pyrrole **7** in 12% yield. The requisite nitrosopyrrole is constructed in an analogous manner,[14] with an additional step to install the nitroso pyrrole in the α-position of the diarylpyrrole (**10**). The cross condensation of **7** and **10** in $AcOH/Ac_2O$ provides azadipyrrin **11** in 18% yield as a dark blue oil. Conversion of the azadipyrrin into the corresponding BF_2-chelate is achieved via treatment of **11** with $BF_3{\bullet}OEt_2$ and DIEA in CH_2Cl_2 to give the target compound N-CS1 (**12**) in 55% yield as a dark green oil.

Schemes A1-3 and A1-4 outline the synthetic scheme for N-CS2, which incorporates a benzyl linked receptor. The synthesis of N-CS2 begins with construction of the pyrrole unit with a benzyl alcohol. Commercially available terephthaldehyde mono-diethylacetal is first reduced with $NaBH_4$ to give alcohol **13**,[15] and the acetal is removed with *p*-TsOH to provide aldehyde **14** in 97% yield. Aldol condensation with acetophenone affords chalcone **15** in 26% yield, and installation of the nitromethyl group provides **16** in 88% yield. Standard Nef reaction conditions followed by condensation with NH_4OAc furnishes pyrrole **17** in 23% yield. Cross condensation of **10** and **17** provides the acetylated azadipyrrin **18** in 78% yield as a dark blue solid, which is

then treated with NaOH to deliver **19** in 96% yield. Several attempts to activate the benzyl alcohol for displacement were explored including mesylation, bromination, and tosylation in a variety of chlorinated solvents; however, poor solubility and degradation of **19** limited the efficient conversion of **19** to **20.** The most effective method was the chlorination of **19** in the presence of DMAP, TEA and TsCl in CH_2Cl_2 to give **20** in 29% yield. Nucleophilic displacement with the tetrathiaza receptor **21**[1] provides **22** in 17% yield. Conversion of **22** into the corresponding BF_2-chelate is achieved with BF_3•OEt_2 and DIEA in CH_2Cl_2 to give the target compound N-CS2 (**23**) in 52% yield as a dark green solid.

Spectroscopic Properties of N-CS1 and N-CS2.

Spectroscopic evaluation of the N-CS dyes shows characteristic aza-BODIPY absorption and emission elements.[12,16] Table A1-1 provides a summary of properties in MeOH, including the driving forces accessed by N-CS1 and N-CS2. The spectroscopic properties of the N-CS dyes were first evaluated in several different solvents, including: 20 mM HEPES (pH 7), 1:1 MeOH and HEPES, MeOH, 1% Triton X-100 in HEPES, and dye formulation in Cremophor-EL (Cr-EL). Initially, we examined the formulation of N-CS1 in Cr-EL, which is a common emulsifying agent. This technique has been used previously for the spectroscopic evaluation of aza-BODIPY dyes.[17] N-CS1 (5 μM dye formulated in Cr-EL) in phosphate buffered saline (PBS) shows two major absorptions at 618 nm and 743 nm and weak fluorescence at 813 nm. Upon addition of Cu^+, the absorption bands shift to 662 nm and 708 nm; however, there is no change in the fluorescence intensity at 813 nm. From here, we chose to examine the behavior of N-CS1 in a more organic environment. In MeOH, the apo N-CS1 dye (10 μM) exhibits two major absorption peaks at 610 nm and 735 nm ($\varepsilon = 2.0 \times 10^4$ $M^{-1}cm^{-1}$, $\varepsilon = 1.6 \times 10^4$ $M^{-1}cm^{-1}$) with a fluorescence emission band centered at 826 nm ($\Phi = 0.0013$) (Figures A1-2, A1-3). Upon addition of Cu^+, the absorption bands at 610 nm and 735 nm decrease in intensity and a single band appears at 665 nm ($\varepsilon = 5.4 \times 10^4$ $M^{-1}cm^{-1}$). There is a fluorescence intensity increase of ca. 10.6-fold with a slight blue shift in the emission maximum to 812 nm ($\Phi = 0.011$).

Spectral properties of N-CS2 (10 μM), a benzyl amine analog of N-CS1, were initially examined in 20 mM HEPES, pH 7. N-CS2 shows one major absorption band at 675 nm with a weak fluorescence emission band at 711 nm, and upon addition of Cu^+, the absorption band and emission band remain unchanged with no increase in fluorescence intensity. The next aqueous formulation was with 1% Triton X-100 in HEPES. Triton X-100 is a non-ionic surfactant that consists of polyethylene glycol chains. In this formulation, N-CS2 (10 μM) exhibits a single absorption at 685 nm with weak fluorescence emission at 678 nm. Upon addition of Cu^+, the absorption shifts to 665 nm with no change in the emission maximum. The increase in fluorescence intensity was not determined because it exhibited an irreproducible time dependent turn-on response. In a 1:1 mixture of MeOH and HEPES, N-CS2 (10 μM) shows one absorption at 715 nm with a fluorescence emission band at 671 nm. Addition of one equivalent of Cu^+ induces a shift in the absorption to 665 nm with a 4.4-fold increase in fluorescence intensity at 678 nm. Spectroscopic evaluation of N-CS2 was also performed in MeOH. In MeOH, N-CS2 (2 μM) shows a prominent absorption at 650 nm ($\varepsilon = 8.9 \times 10^4$ $M^{-1}cm^{-1}$) with emission ($\Phi = 0.017$) centered at 670 nm (Figures A1-3, A1-4). Upon addition of Cu^+, the absorption band maintains its position at 650 nm ($\varepsilon = 9.0 \times 10^4$ $M^{-1}cm^{-1}$) with a modest fluorescence intensity increase ($\Phi =$ 0.037) of ca. 2.3-fold at 670 nm. As indicated by the quantum yields of both the apo and bound probes, N-CS1 is dimmer than N-CS2 (Table A1-1). This difference can be rationalized in consideration of a Rehm-Weller analysis. The calculated ΔG_{PET} values for N-CS1 and N-CS2 are

-1.29 eV and -1.18 eV, respectively (Table A1-1). This indicates that there is a greater driving force for electron transfer in N-CS1, which makes PET quenching more effective. As a result the quantum yield of N-CS1 is lower than N-CS2 in the unbound state. Although N-CS2 has a smaller turn-on response, it is a more suitable design because it is a brighter dye scaffold.

Binding analysis using the method of continuous variations (Job's plot) indicates that 1:1 Cu^{+}:dye complexes are responsible for the enhanced fluorescence responses observed for the N-CS dyes (Figures A1-5, A1-6). Apparent dissociation constant values (K_d) for N-CS1 and N-CS2 are 40 pM and 2 pM, respectively (Figures A1-7, A1-8). The difference in K_d values can be rationalized with respect to the basicity of the receptor nitrogen. N-CS1 has an aniline-type receptor, whereas N-CS2 has more basic alkyl amine in the receptor framework. The stronger Lewis base in the N-CS2 receptor allows for tighter binding of Cu^{+} ions and provides a more thermodynamically stable complex. The N-CS fluorophores are selective for Cu^{+} over other biologically relevant metal ions (Figures A1-9 and A1-10), including millimolar concentrations of Mg^{2+} and Ca^{2+}. The N-CS dyes are also selective for Cu^{+} over an excess of the first row transition metal ions: Mn^{2+}, Fe^{2+}, Co^{2+}, Ni^{2+}, and Cu^{2+}. Finally the emission profiles of the apo or the Cu^{+}-bound N-CS probes or their turn-on responses to Cu^{+} are unaffected by millimolar concentrations of Zn^{2+}, indicating the selectivity for d^{10} Cu^{+} over d^{10} Zn^{2+}.

Fluorescence Detection of Cu^{+} in Living Cells Using Confocal Microscopy

We next sought to apply the N-CS2 probe for visualizing labile copper levels in living cells where the ability of the N-CS2 indicator to reversibly respond to changes in labile Cu^{+} concentrations within living mammalian cells in culture was tested. Live human embryonic kidney cells (HEK 293T) incubated with 10 μM N-CS2 for 3 h at 37 ºC exhibit intracellular fluorescence as determined by confocal microscopy (Figure A1-11a) and, cells grown with 200 μM $CuCl_2$ supplemented in the growth medium overnight show an increase in intracellular fluorescence upon staining with N-CS2 (Figure A1-11b). Subsequent treatment with a cell-permeable, copper-specific chelator affords a decrease in the fluorescence levels, indicating that there are fluorescence enhancements due to the increased concentration of intracellular copper (Figure A1-11c). Quantification of this experiment is shown in Figure A1-11d. N-CS2 can recognize and respond reversibly to changes in labile copper levels within live-cell samples.

Conclusion and Future Work

We have investigated the aza-BODIPY scaffold as a potential scaffold for the development of NIR Cu^{+} sensors. Even though the N-CS1 design affords a larger turn-on response to Cu^{+}, N-CS2 serves as better starting point since overall the dye is brighter. Although N-CS2 did not demonstrate a response to Cu^{+} cell culture, the viability of HEK 293T cells upon incubation with N-CS2 demonstrates the non-toxic nature of this dye scaffold. Future efforts can enhance the solubility and turn-on response of the N-CS dyes to make them suitable for cellular imaging experiments.

Experimental Section

Synthetic Materials and Methods. All reactions were carried out under a dry N_2 atmosphere and stirred magnetically unless stated otherwise. Silica gel P60 (SiliCycle) and activated basic aluminum oxide (Brockmann) were used for column chromatography. Preparative thin layer

chromatography was performed using SiliCycle 60 F254 silica gel (precoated sheets, 1 mm thick). Analytical thin layer chromatography was performed using SiliCycle 60 F254 silica gel (precoated sheets, 0.25 mm thick) and EMD Chemicals 60 F254 basic aluminum oxide. Compounds **1**,[13] **2**,[1] **8**,[14] **9**,[14] **10**,[14] **13**,[15] **21**,[1] and **24**,[18] were synthesized according to literature procedures. Compounds **8** was kindly provided by Aaron Albers. Compounds **21** and [tris(ethylthio)ethyl)amine] (TEMEA)[19] were kindly provided by Dylan Domaille. Unless otherwise noted, all chemicals were used as received. ^{1}H and ^{13}C NMR spectra were collected in $CDCl_3$ or $(CD_3)_2CO$ (Cambridge Isotope Laboratories, Cambridge, MA) at 25 °C on a Bruker AV-300 or Bruker AVQ-400 spectrometer at the College of Chemistry NMR Facility at the University of California, Berkeley. All chemical shifts are reported in the standard notation of parts per million using the peak of residual proton or carbon signals of $CDCl_3$ or $(CD_3)_2CO$ as an internal reference. Mass spectral analyses were carried out at the College of Chemistry Mass Spectrometry Facility at the University of California, Berkeley.

Synthesis.

***N*,*N*-Bis(2-(2-(ethylthio)ethylthio)ethyl)aniline (3). 3** was synthesized according to a modified literature procedure.[20] A solution of **1** (7.81 g, 16.0 mmol) and **2** (3.90 g, 31.9 mmol) in DMF (230 mL) was heated at 60 °C for 3 d under a nitrogen atmosphere. The DMF was removed by vacuum distillation, and the resulting residue was dissolved in CH_2Cl_2 (200 mL) and filtered to remove any salts. The filtrate was washed with water (2 x 100 mL) and the combined organics were dried over Na_2SO_4, concentrated to dryness, and purified by column chromatography (silica gel, hexanes/CH_2Cl_2 60/40 to 0/100) to yield a colorless, pungent oil (2.63 g, 42%). ^{1}H NMR (400 MHz, $CDCl_3$): δ 2.56 (q, 4H, J = 7.2 Hz), 2.71-2.81 (m, 12H), 3.55 (t, 4H, J = 7.6 Hz), 6.66 (d, 2H, J = 8 Hz), 6.72 (t, 1H, J = 7.2 Hz), 7.22-7.26 (m, 2H). ^{13}C NMR (100 MHz, $CDCl_3$): δ 14.9, 26.2, 29.5, 32.0, 32.6, 51.7, 112.0, 116.9, 129.7, 146.6. HRFAB-MS calculated for [MH^+] 390.14176, found 390.14107.

4-(Bis(2-(2-(ethylthio)ethylthio)ethyl)amino)benzaldehyde (4). 4 was synthesized according to a modified literature procedure.[21,22] $POCl_3$ (0.96 mL, 11 mmol) was added dropwise to a stirring solution of **3** (1.86 g, 4.77 mmol) in anhydrous DMF (8 mL). The reaction mixture was stirred overnight at room temperature. The crude mustard yellow reaction mixture was poured into H_2O (75 mL), and the pH was adjusted to pH 9 with solid K_2CO_3. The reaction mixture was extracted with CH_2Cl_2 (2 x 100 mL), the organics were combined, dried over Na_2SO_4, and concentrated to dryness to provide **4** as a yellow oil (1.84 g, 92%). ^{1}H NMR (400 MHz, $CDCl_3$): δ 1.23 (t, 6H, J = 7.4 Hz), 2.53 (q, 4H, J = 7.6 Hz), 2.69-2.79 (m, 12H), 3.63 (t, 4H, J = 7.6 Hz), 6.67 (d, 2H, J = 8.8 Hz), 7.71 (d, 2H, J = 8.8 Hz), 9.71 (s, 1H). ^{13}C NMR (100 MHz, $CDCl_3$): δ 14.8, 26.1, 29.3, 29.7, 31.8, 32.6, 51.5, 111.0, 125.9, 132.4, 151.4, 190.1. HRFAB-MS calculated for [MLi^+] 424.14485, found 424.14519.

(*E*)-3-(4-(Bis(2-(2-(ethylthio)ethylthio)ethyl)amino)phenyl)-1-phenylprop-2-en-1-one (5). A solution of acetophenone (1.00 g, 8.32 mmol) and NaOH (1.00 g, 25.0 mmol) in EtOH/H_2O (85:15 v/v, 50 mL) was added dropwise to a stirring suspension of **4** (1.84 g, 4.40 mmol) in EtOH/H_2O (85:15 v/v, 20 mL) at 0 °C. After 30 min THF (20 mL) was added to enhance the solubility of **4**. The reaction mixture continued to stir at room temperature overnight. Ice (50 mL) was added, and the mixture was neutralized with aqueous 1 M HCl and extracted with EtOAc (2 x 75 mL). The combined organics were dried over Na_2SO_4, concentrated to dryness, and purified by column chromatography (silica gel, CH_2Cl_2) to afford **5** as a yellow oil (1.12 g, 49%). ^{1}H

NMR (400 MHz, $CDCl_3$): δ 1.26 (t, 6H, *J* = 7.4 Hz), 2.56 (q, 4H, *J* = 7.2 Hz), 2.71-2.80 (m, 12H), 3.62 (t, 4H, *J* = 7.4 Hz), 6.66 (d, 2H, *J* = 8.8 Hz), 7.34 (d, 2H, *J* = 15.6 Hz), 7.47-9.56 (m, 5H) 7.76 (d, 1H, *J* = 7.6 Hz), 8.00 (d, 2H, *J* = 7.2 Hz). ^{13}C NMR (100 MHz, $CDCl_3$): δ 14.9, 26.2, 29.5, 29.8, 31.9, 32.6, 51.1, 111.7, 117.6, 123.5, 128.4, 128.6, 130.9, 132.4, 139.0, 145.3, 148.7, 190.7. HRFAB-MS calculated for [M^+] 519.17580, found 519.17459.

3-(4-(Bis(2-(2-(ethylthio)ethylthio)ethyl)amino)phenyl)-4-nitro-1-phenylbutan-1-one (6). **5** (1.12 g, 2.15 mmol), CH_3NO_2 (1.2 mL, 22 mmol), and Et_2NH (2.2 mL, 21 mmol) were dissolved in anhydrous methanol (20 mL) and heated to reflux at 70 °C for 2 d. The reaction was cooled and a saturated aqueous solution of NH_4Cl (20 mL) was added. The reaction mixture was extracted with CH_2Cl_2 (3 x 30 mL), the organics were combined, dried over Na_2SO_4, concentrated to dryness, and purified by column chromatography (silica gel, CH_2Cl_2) to afford **6** as a yellow oil (1.00 g, 80%). ^{1}H NMR (400 MHz, $CDCl_3$): δ 1.26 (t, 6H, *J* = 7.4 Hz), 2.57 (q, 4H, *J* = 7.4 Hz), 2.70-2.79 (m, 12H), 3.34-3.53 (m, 6H), 4.11 (t, 1H, *J* = 7.0 Hz), 4.63 (dd, 1H, *J* = 8 Hz, *J* = 12 Hz), 4.78 (dd, 1H, *J* = 5.2 Hz, *J* = 8.8 Hz), 6.58 (d, 3H, *J* = 8.4 Hz), 7.13 (d, 2H, *J* = 8.8 Hz) 7.46 (t, 2H, *J* = 7.6 Hz), 7.57 (t, 1H, *J* = 7.2 Hz), 7.92 (d, 2H, *J* = 7.6 Hz). ^{13}C NMR (100 MHz, $CDCl_3$): δ 14.9, 26.2, 29.5, 31.9, 32.6, 38.5, 41.8, 51.6, 80.0, 112.2, 126.9, 128.1, 128.7, 128.8, 133.6, 136.5, 146.2, 197.2. HRFAB-MS calculated for [MH^+] 581.2000, found 581.1987.

***N*,*N*-Bis(2-(2-(ethylthio)ethylthio)ethyl)-4-(5-phenyl-1*H*-pyrrol-3-yl)aniline (7)**. A stirred solution of **6** (1.00 g, 1.72 mmol) in MeOH (8 mL) and THF (8 mL) at room temperature was treated with finely crushed KOH (504 mg, 8.98 mmol). After 1 h, the mixture was added dropwise to a solution of H_2SO_4 (4 mL) in anhydrous MeOH (16 mL) at 0 °C over 20 min, and warmed to room temperature for 1 h. Ice (50 mL) and H_2O (50 mL) were added, and the mixture was neutralized with 5 M NaOH, and extracted with CH_2Cl_2 (4 x 40 mL). The organics were combined and washed with H_2O (100 mL), dried over Na_2SO_4, and concentrated to dryness to give a golden brown oil, which was carried into the next stage without further purification. The oil was treated with AcOH (20 mL) and NH_4OAc (1.34 g, 17.4 mmol) and the resulting solution was heated to 100 °C for 1 h. The reaction was cooled to room temperature, ice was added (50 mL), the mixture was neutralized with 5 M NaOH, and extracted with CH_2Cl_2 (3 x 50 mL). The organics were combined, dried over Na_2SO_4, concentrated to dryness, and purified by column chromatography (alumina, 10% EtOAc in CH_2Cl_2) to afford **7** as a crude brown oil, which was carried to the next stage without further purification (108 mg, 12%). ^{1}H NMR (400 MHz, $CDCl_3$): δ 1.26 (s, 6H), 2.56-2.76 (m, 16H), 3.57 (br s, 4H), 6.49-6.74 (m, 3H), 7.00 (br s, 1H), 7.16-7.49 (m, 7H), NH not observed. HRFAB-MS calculated for [M^+] 530.19178, found 530.19276.

(*Z*)-*N*-(3-(4-(Bis(2-(2-(ethylthio)ethylthio)ethyl)amino)phenyl)-5-phenyl-2*H*-pyrrol-2-ylidene)-3,5-diphenyl-1*H*-pyrrol-2-amine (11). **7** (108 mg, 0.203 mmol) and **10** (52 mg, 0.21 mmol) were dissolved in AcOH (1 mL) and Ac_2O (0.3 mL) and heated to 100 °C for 2 h. During the course of the reaction, an intense blue color formed. The reaction was then cooled to room temperature, ice (25 mL) and 5 M NaOH (5 mL) was added and the mixture was stirred for 1 hr. The solution was extracted with CH_2Cl_2 (2 x 25 mL). The combined organics were dried over Na_2SO_4, concentrated to dryness, and purified by column chromatography (alumina, CH_2Cl_2) to furnish **11** as a dark blue oil (27 mg, 18%). ^{1}H NMR (400 MHz, $CDCl_3$): δ 1.25 (t, 6H, *J* = 7.0 Hz), 2.56 (d, 4H, *J* = 7.2 Hz), 2.78-2.83 (m, 12H), 3.65 (br s, 4H), 6.70 (d, 2H, *J* = 8 Hz), 7.11

(d, 2H, J = 7.6 Hz), 7.43-7.54 (m, 9H), 7.89 (d, 2H, J = 7.6 Hz), 7.99-8.05 (m, 6H). HRFAB-MS calculated for [M^+] 760.27618, found 760.27629.

1-(4-(Bis(2-(2-(ethylthio)ethylthio)ethyl)amino)phenyl)-5,5-difluoro-3,7,9-triphenyl-5*H*-dipyrrolo[1,2-*c*:1',2'-*f*][1,3,5,2]triazaborinin-4-ium-5-uide (NIR-Coppersensor-1, N-CS1, 12). **11** (27 mg, 0.035 mmol) was dissolved in dry CH_2Cl_2 (3 mL), treated with DIEA (0.200 mL, 1.15 mmol) and the resulting mixture was stirred for 15 minutes at room temperature. BF_3•OEt_2 (0.200 mL, 1.58 mmol) was then added, and the reaction mixture was stirred at room temperature overnight. The mixture was diluted with CH_2Cl_2 (15 mL) and washed with H_2O (10 mL). The organic phase was dried over Na_2SO_4, concentrated to dryness, and purified by column chromatography (silica, CH_2Cl_2) to provide **12** as a dark green oil (16 mg, 55%). ^{1}H NMR (400 MHz, $CDCl_3$): δ 1.26 (t, 6H, J = 7.2 Hz), 2.57 (q, 4H, J = 7.6 Hz), 2.74-2.85 (m, 12H), 3.67 (t, 4H, J = 7.4 Hz), 6.74 (d, 2H, J = 8.4 Hz), 6.86 (s, 1H), 6.98 (s, 1H), 7.43-7.49 (m, 9H), 8.01-8.06 (m, 6H), 8.10 (d, 2H, J = 9.2 Hz). ^{13}C NMR (100 MHz, $CDCl_3$): δ 15.0, 26.3, 29.6, 32.0, 32.8, 52.0, 112.4, 116.2, 118.4, 128.6, 128.6, 128.7, 128.9, 129.2, 129.5, 129.5, 129.7, 120.8, 131.0, 131.7, 131.8, 132.2, 133.1. HRESI-MS calculated for [MH^+] 809.2823, found 809.2832.

4-(Hydroxymethyl)benzaldehyde (14). **14** was synthesized according to a modified literature procedure.[23] Compound **13** (6.30 g, 30.0 mmol) and *p*-TsOH (2.92 g, 15.4 mmol) were dissolved in THF (45 mL) and water (9 mL) and were heated to reflux at 70 °C for 8 h. The reaction was cooled to room temperature, diluted with water (100 mL), and extracted with CH_2Cl_2 (2 x 100 mL). The combined organics were dried over Na_2SO_4 and concentrated to dryness to afford **15** as a white crystalline solid (3.95 g, 97%). ^{1}H NMR characterization was consistent with that previously reported in the literature.[24]

(*E*)-3-(4-(Hydroxymethyl)phenyl)-1-phenylprop-2-en-1-one (15). A solution of acetophenone (3.50 g, 29.1 mmol) in EtOH/H_2O (85:15 v/v, 34 mL) at 0 °C was treated with a NaOH (1.46 g, 36.5 mmol) in EtOH/H_2O (85:15 v/v, 40 mL), followed by a dropwise addition of **15** (3.95 g, 29.0 mmol) and NaOH (1.46 g, 36.5 mmol) in EtOH/H_2O (85:15 v/v, 88 mL). Once the addition was complete, the reaction mixture was stirred at room temperature for 60 h. Ice (50 mL) and H_2O (50 mL) were added, the pH was adjusted to pH 1-2 with 1 M HCl, and extracted with CH_2Cl_2 (4 x 100 mL). The combined organics were dried over Na_2SO_4 and concentrated to dryness to afford a crude yellow solid. A minimal amount Et_2O was added to the crude yellow solid and the mixture was placed in the refrigerator overnight. The resulting precipitate was filtered and washed with cold Et_2O. The filtrate was concentrated to dryness, washed with Et_2O, and the resulting precipitate was collected by filtration again to furnish **16** as a light yellow solid (1.77 g, 26%). ^{1}H NMR (100 MHz, $CDCl_3$): δ 4.73 (s, 2H), 7.40 (d, 2H, J = 8 Hz), 7.50 (t, 3H, J = 8 Hz), 7.57-7.62 (m, 3H), 7.77 (d, 1H, J = 15.6), 8.00 (d, 2H, J = 6.8 Hz). ^{13}C NMR (100 MHz, $CDCl_3$): δ 64.8, 121.9, 127.4, 128.6, 128.7, 128.8, 133.0, 134.2, 138.2, 143.7, 144.8, 192.3. HRFAB-MS calculated for [MH^+] 239.10720, found 239.10738.

3-(4-(Hydroxymethyl)phenyl)-4-nitro-1-phenylbutan-1-one (16). **15** (1.77 g, 7.43 mmol), CH_3NO_2 (4.00 mL, 74.4 mmol), and Et_2NH (7.70 mL, 74.8 mmol) were dissolved in anhydrous MeOH (50 mL) and heated to reflux overnight. Ice (50 mL) and H_2O (50 mL) were added, and the pH was adjusted to pH 8-9 with 1 M HCl. The reaction was diluted with 100 mL of H_2O and extracted with CH_2Cl_2 (2 x 50 mL). The organics were combined, dried over Na_2SO_4, concentrated to dryness and diluted with EtOAc (75 mL) and washed with H_2O (100 mL) and

brine (100 mL). The organic phase was dried over Na_2SO_4, concentrated to dryness yield a thick, golden brown oil, which was carried onto the next stage without further purification (1.95 g, 88%). ^{1}H NMR (400 MHz, $CDCl_3$): δ 3.42 (t, 2H J = 7.6 Hz), 4.20 (p, 1H, J = 7.2 Hz, J = 14.2 Hz), 4.67-7.58 (m, 2H), 4.83 (dd, 1H, J = 6.6 Hz, J = 12.6 Hz), 7.27 (q, 4H, J = 8 Hz), 7.44 (t, 2H, J = 7.6 Hz), 7.56 (t, 1H, J = 7.4 Hz), 7.89 (d, 2H, J = 8 Hz). ^{13}C NMR (100 MHz, $CDCl_3$): δ 39.0, 41.5, 64.7, 79.6, 128.8, 128.6, 128.1, 128.0, 133.71, 136.3, 138.4, 140.7, 197.1.

(4-(5-Phenyl-1*H*-pyrrol-3-yl)phenyl)methanol (17). A stirred solution of **16** (1.95 g, 6.51 mmol) in anhydrous MeOH (20 mL) and anhydrous THF (40 mL) at room temperature was treated with finely crushed KOH (1.92 g, 34.2 mmol). After 1 h, the mixture was added dropwise to a solution of H_2SO_4 (13 mL) in anhydrous MeOH (65 mL) at 0 °C over 30 min. The solution warmed to room temperature and was stirred for 1 h. Ice (50 mL) and H_2O (50 mL) were added, and the pH was adjusted to pH 10-11 with 4 M NaOH and extracted with CH_2Cl_2 (2 x 100 mL). The combined organics were washed with brine (1 x 100 mL), and the organic phase dried over Na_2SO_4, and concentrated to dryness to yield a crude brown oil, which was carried into the next stage without further purification. The oil was treated with AcOH (33 mL) and NH_4OAc (2.50 g, 32.4 mmol) and heated to 100 °C for 1 h. The reaction mixture was cooled to room temperature, ice (50 mL) and H_2O (100 mL) were added, and the mixture was neutralized with 4 M NaOH. The solution was extracted with CH_2Cl_2 (2 x 100 mL), washed with H_2O (2 x 100 mL) and brine (1 x 100 mL). The organics were combined, dried over Na_2SO_4, and concentrated to dryness to afford a crude purple solid. A minimal amount of CH_2Cl_2 was added to the crude solid and this mixture was placed in the refrigerator for 8 h. The resulting precipitate was filtered and washed with cold CH_2Cl_2 to give **18** as a light blue solid (380 mg, 23%). ^{1}H NMR (400 MHz, $(CD_3)_2CO$): δ 4.15 (s, 1H), 4.61 (s, 2H), 6.96 (s, 1H), 7.19 (t, 1H, J = 7.4 Hz), 7.29-7.29 (m, 5H), 7.59 (d, 2H, J = 8 Hz), 7.70 (d, 2H, J = 8 Hz). ^{13}C NMR (100 MHz, $(CD_3)_2CO$): δ 64.7, 104.3, 116.9, 124.4, 125.3, 126.6, 126.7, 127.9, 129.6, 133.6, 134.0, 135.7, 140.2. HRFAB-MS calculated for [M^+] 249.11536, found 249.11458.

(*Z*)-4-(2-(3,5-Diphenyl-1*H*-pyrrol-2-ylimino)-5-phenyl-2*H*-pyrrol-3-yl)benzyl acetate (18). **10** (109 mg, 0.437 mmol) and **17** (109 mg, 0.439 mmol) were dissolved in AcOH (4.3 mL) and Ac_2O (0.9 mL) and heated to 100 °C overnight. During the course of the reaction an intense blue color formed. The mixture was concentrated to dryness, and purified by column chromatography (alumina, CH_2Cl_2) to furnish **18** as a dark blue solid (194 mg, 78%). ^{1}H NMR (400 MHz, $CDCl_3$): δ 2.13 (s, 3H), 5.17 (s, 2H), 7.17 (s, 1H), 7.19 (s, 1H), 7.36-7.54 (m, 11H), 7.91-7.95 (m, 4H), 8.016-8.06 (m, 4H). ^{13}C NMR (100 MHz, $CDCl_3$): δ 21.23, 66.4, 114.5, 115.2 126.5, 126.6, 128.0, 128.3, 129.1, 129.2, 129.9, 130.1, 132.0, 132.1, 133.7, 133.8, 135.3, 141.3, 142.8, 149.2, 150.1, 154.2, 155.7, 171.1. HRESI-MS calculated for [MH^+] 522.2182, found 522.2178.

(*Z*)-(4-(2-(3,5-Diphenyl-1*H*-pyrrol-2-ylimino)-5-phenyl-2*H*-pyrrol-3-yl)phenyl)methanol (19). A rapidly stirring solution of **18** (194 mg, 0.372 mmol) in MeOH (3 mL) and THF (6 mL) at 0 °C was treated with a dropwise addition of 5 M NaOH (5 mL). The reaction mixture was stirred at room temperature for 3 h, whereupon the reaction mixture was diluted with EtOAc (75 mL). The organic layers were separated and the organic phase was washed with H_2O (2 x 20 mL). The organic phase was dried over Na_2SO_4, concentrated to dryness, and purified by column chromatography (alumina, 0.6% MeOH in CH_2Cl_2) to yield **19** as a dark blue solid (156 mg, 96%). ^{1}H NMR (400 MHz, $CDCl_3$): δ 4.71 (s, 2H), 7.18 (s, 2H), 7.40-7.51 (m, 11H), 7.92 (br s, 4H), 8.03 (br s, 4H). HRESI-MS calculated for [MH^+] 480.2076, found 480.2075.

(*Z*)-*N*-(3-(4-(Chloromethyl)phenyl)-5-phenyl-2*H*-pyrrol-2-ylidene)-3,5-diphenyl-1*H*-pyrrol-2-amine (20). A solution of **19** (89 mg, 0.19 mmol), TEA (32 mg, 0.32 mmol), CH_2Cl_2 (2 mL), and THF (0.5 mL) cooled to 0 °C was treated with a dropwise addition of TsCl (67 mg, 0.35 mmol) in a solution of TEA (32 mg, 0.32 mmol), CH_2Cl_2 (2 mL) and DMAP (30 mg, 0.25 mmol). The reaction mixture warmed to room temperature and stirring continued for 18 h. The reaction mixture was diluted with CH_2Cl_2 (20 mL) and washed with dilute HCl (20 mL). The organic phase was dried over Na_2SO_4, concentrated to dryness, and the residue was purified by column chromatography (alumina, CH_2Cl_2) to furnish **20** as a dark blue solid (27 mg, 29%) ^{1}H NMR (400 MHz, $CDCl_3$): δ 4.65 (s, 2H), 7.12 (s, 1H), 7.15 (s, 1H), 7.38-7.50 (m, 11H), 7.85-7.91 (m, 4H), 7.98-8.03 (m, 4H). HRESI-MS calculated for [M^+] 497.16588, found 497.16595.

(*Z*)-*N*-(3-(4-((Bis(2-(2-(ethylthio)ethylthio)ethyl)amino)methyl)phenyl)-5-phenyl-2*H*-pyrrol-2-ylidene)-3,5-diphenyl-1*H*-pyrrol-2-amine (22) 20 (27 mg, 0.054 mmol), **21** (35 mg, 0.11 mmol), KI (50 mg, 0.30 mmol), K_2CO_3 (45 mg, 0.33 mmol) were dissolved in anhydrous CH_3CN (2 mL) and heated to 40 °C for 2 h under a nitrogen atmosphere. The reaction mixture was diluted with CH_2Cl_2 (10 mL) and washed with H_2O (10 mL). The organic phase was dried over Na_2SO_4, concentrated to dryness, and purified by column chromatography (alumina, 10% hexanes in CH_2Cl_2) to provide **22** as a dark blue solid (7 mg, 17%). ^{1}H NMR (400 MHz, $CDCl_3$): δ 1.22 (t, 6H, J = 7.4 Hz), 2.53 (q, 4H, J = 7.6 Hz), 2.70 (br s, 12H), 2.77-2.79 (m, 4H), 3.72 (s, 2H), 7.21 (s, 2H), 7.39-7.56 (m, 11H), 7.97 (d, 2H, J = 7.6), 8.05 (t, 4H, J = 8.6 Hz). HRESI-MS calculated for [MH^+] 775.2997, found 775.2993.

1-(4-((Bis(2-(2-(ethylthio)ethylthio)ethyl)amino)methyl)phenyl)-5,5-difluoro-3,7,9-triphenyl-5*H*-dipyrrolo[1,2-*c*:1',2'-*f*][1,3,5,2]triazaborinin-4-ium-5-uide (NIR-Coppersensor-2, N-CS2, 23) 22 (7 mg, 0.009 mmol) was dissolved in dry CH_2Cl_2 (2 mL), treated with DIEA (0.150 mL, 0.861 mmol) and the resulting mixture was stirred for 15 min at room temperature. BF_3•OEt_2 (0.150 mL, 1.18 mmol) was then added, and the reaction mixture was stirred at room temperature overnight. The mixture was washed with H_2O (2 x 25 mL), the organic phase was dried over Na_2SO_4, concentrated to dryness and purified by column chromatography (alumina, CH_2Cl_2) to provide **23** as a dark green solid (4 mg, 52%). ^{1}H NMR (400 MHz, $CDCl_3$): δ 1.23 (t, 6H, J = 7.4 Hz), 2.53 (q, 4H, J = 7.3 Hz), 2.70-2.71 (br m, 12H), 2.77-2.80 (m, 4H), 3.73 (s, 2H), 7.04 (s, 2H), 7.44-7.50 (m, 11H), 8.04-8.08 (m, 8H). ^{13}C NMR (100 MHz, $CDCl_3$): δ 14.9, 26.2, 30.3, 31.9, 32.6, 54.2, 58.6, 119.1, 119.3, 128.8, 128.8, 129.1, 129.5, 129.6, 131.1, 131.4, 131.6, 131.7, 132.5, 141.2, 144.2, 145.6, 159.9. HRESI-MS calculated for [MH^+] 823.29794, found 823.29501.

Calculation of ΔG_{PET} value. DG_{PET} values were calculated from the $\Delta G_{PET} = E_{1/2}(D^+/D) - E_{1/2}(A/A^-) - \Delta E_{00} - C$, where $E_{1/2}(D^+/D)$ represents the ground state oxidation potential of the amine donor, $E_{1/2}(A/A^-)$ is the ground state reduction potential of the fluorophore, ΔE_{00} corresponds to the energy of emission, and C represents an electrostatic term for the charge separation state. The oxidation potential of *N*, *N*-dimethylaniline was used as an approximation for $E_{1/2}(D^+/D)$ for N-CS1 and the oxidation potential of triethylamine was used as an approximation for $E_{1/2}(D^+/D)$ for N-CS1. $E_{1/2}(A/A^-)$ was determined by cyclic voltammetry of the tetraphenyl-substituted boratriazaindacence core. ΔE_{00} was determined by fluorescence spectroscopy.

Cyclic voltammetry. Electrochemical experiments were conducted using a BAS CV-50W Voltammetric Analyzer (Bioanalytical Systems, Inc.) using a three electrode system made up of a glassy carbon working electrode, a Ag/AgCl reference electrode, and a platinum wire auxiliary

electrode. Cyclic voltammetry was performed in anhydrous acetonitrile containing 0.11 M electrochemical grade tetrabutylammonium hexafluorphosphate ($TBAPF_6$) and 3.1 x 10^{-3} M of compound **37**. Solutions were purged with nitrogen for 2 min prior to each experiment and run under an inert atmosphere. The scan rate was 0.1 V s^{-1}. Obtained potentials (vs. Ag/AgCl) were converted to those vs. a saturated calomel electrode (SCE) by adding 0.25 V.

Spectroscopic Materials and Methods. Millipore water was used to prepare all aqueous solutions. All final spectroscopic measurements were performed in MeOH for the N-CS dyes. Absorption spectra were recorded using a Varian Cary 50 spectrophotometer (Walnut Creek, CA) and fluorescence spectra were recorded using a Photon Technology International Quanta Master 4 L-format scan spectrofluorometer (Lawrenceville, NJ) equipped with an LPS-220B 75-W xenon lamp and power supply, A-1010B lamp housing with integrated igniter, switchable 814 photocounting/analog photomultiplier detection unit, and MD5020 motor driver. Samples for absorption and emission measurements were contained in 1-cm quartz cuvettes (1.4-mL volume, Starna, Atascadero, CA). Fluorescence quantum yields were determined by reference to 3, 3'-diethylthiacarbocyanine iodide in methanol ($\Phi = 0.36$)[25] for N-CS1 and N-CS2. The binding affinities of Cu^+ to the NCS dyes were measured using thiourea as a competitive ligand to provide buffered Cu^+ solutions. Stability constants for thiourea binding were taken from the literature: $\beta_{12} = 2.0 \times 10^{12}$, $\beta_{13} = 2.0 \times 10^{14}$, $\beta_{14} = 3.4 \times 10^{15}$.[26] Cu^+ was delivered in the form of $[Cu(MeCN)_4][PF_6]$ from an acetonitrile stock solution (1 mM, 2 mM, 5 mM). Measurements were carried out in MeOH. Excitation was provided at 665 nm and collected emission was integrated from 675-900 nm for N-CS1. For N-CS2 excitation was provided at 650 nm and collected emission was integrated from 660-900 nm. The apparent dissociation constants (K_d) were determined using the following equation: $(F - F_{min})/(F_{max} - F_{min}) = [Cu^+]/(K_d + [Cu^+])$, where F is the observed fluorescence, F_{max} is the fluorescence for the Cu^+:NCS complex, and F_{min} is the fluorescence for the free N-CS dye.

Cell Culture. HEK 293T cells were cultured in Dulbecco's Modified Eagle Medium (DMEM, Invitrogen, Carlsbad, CA) supplemented with 10% Fetal Bovine Serum (FBS, Invitrogen), glutamine (2mM) and penicillin/streptomycin (50 mg/mL, Invitrogen). One day before imaging, cells were passed and plated on 18-mm glass coverslips coated with poly-L-lysine (50 mg/mL, Sigma, St. Louis, MO). Immediately before the experiments, cells were washed with PBS buffer and imaged. Experiments to assess copper uptake were performed in the same media supplemented with the additives at the indicated concentrations.

Live-Cell Imaging. Confocal fluorescence imaging was performed with a Zeiss LSM 510 NLO Axiovert 200 laser-scanning microscope and a 40x water-immersion objective lens. Excitation of N-CS2 loaded cells at 633 nm was carried out with a HeNe laser, and emission was collected using a 634-733 nm Meta detector. N-CS2 (10 μM) was incubated with live cells samples for 3 h at 37 °C. Additions of the intracellular copper chelator TEMEA were performed directly on the microscope stage by bath application to the media.

Schemes, Figures, and Tables

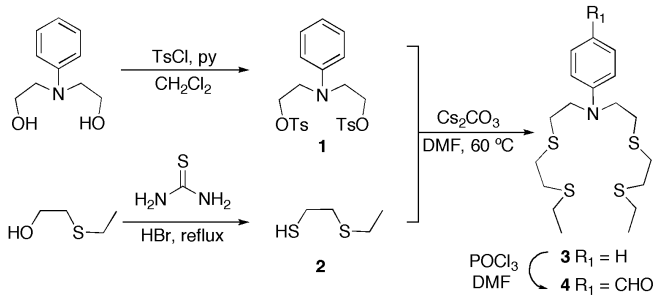

Scheme A1-1. Synthesis of compounds **1-4**.

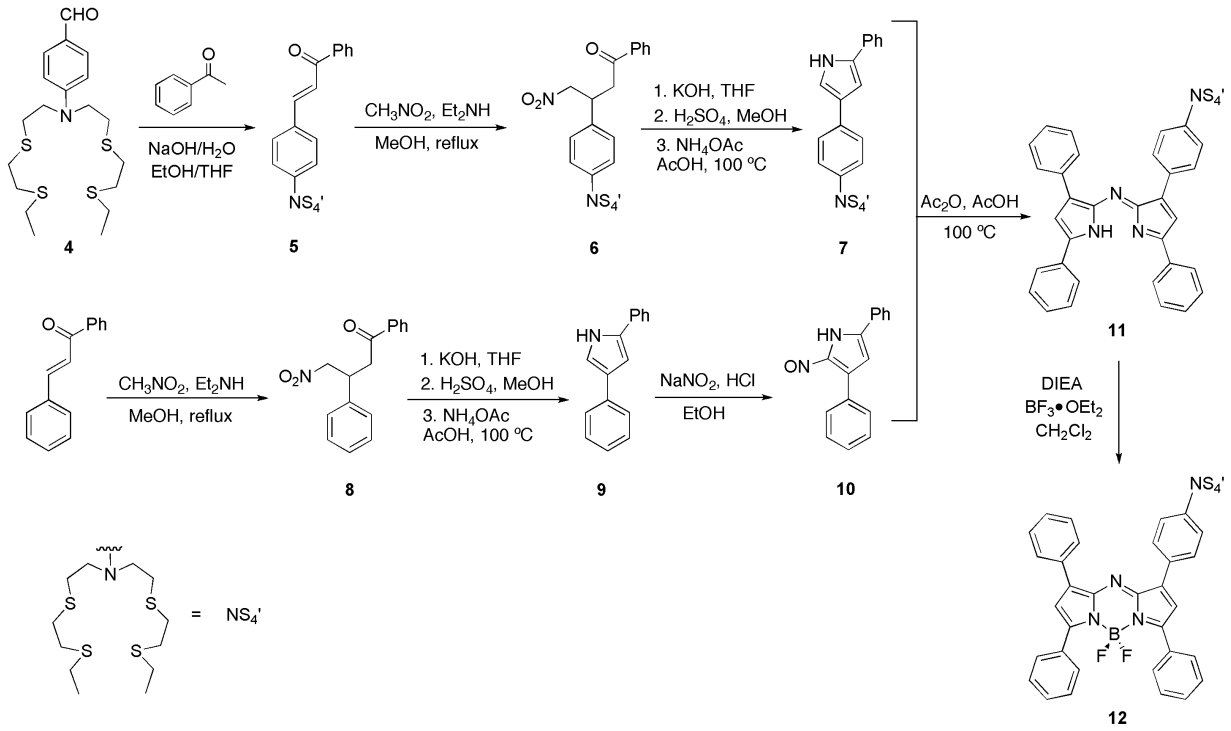

Scheme A1-2. Synthesis of compound **5-12**.

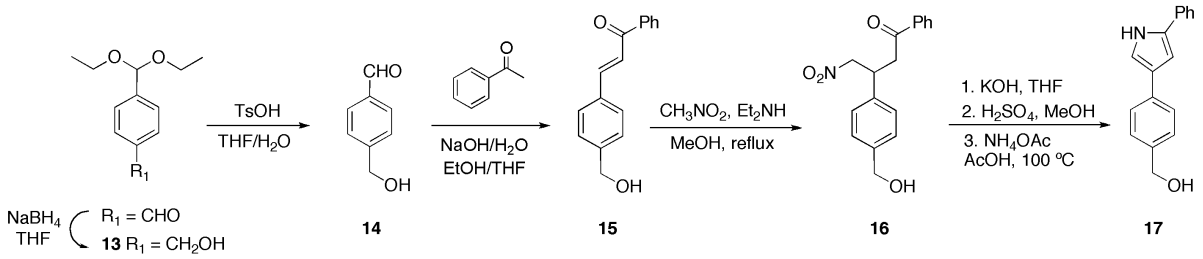

Scheme A1-3. Synthesis of compound **13-17**.

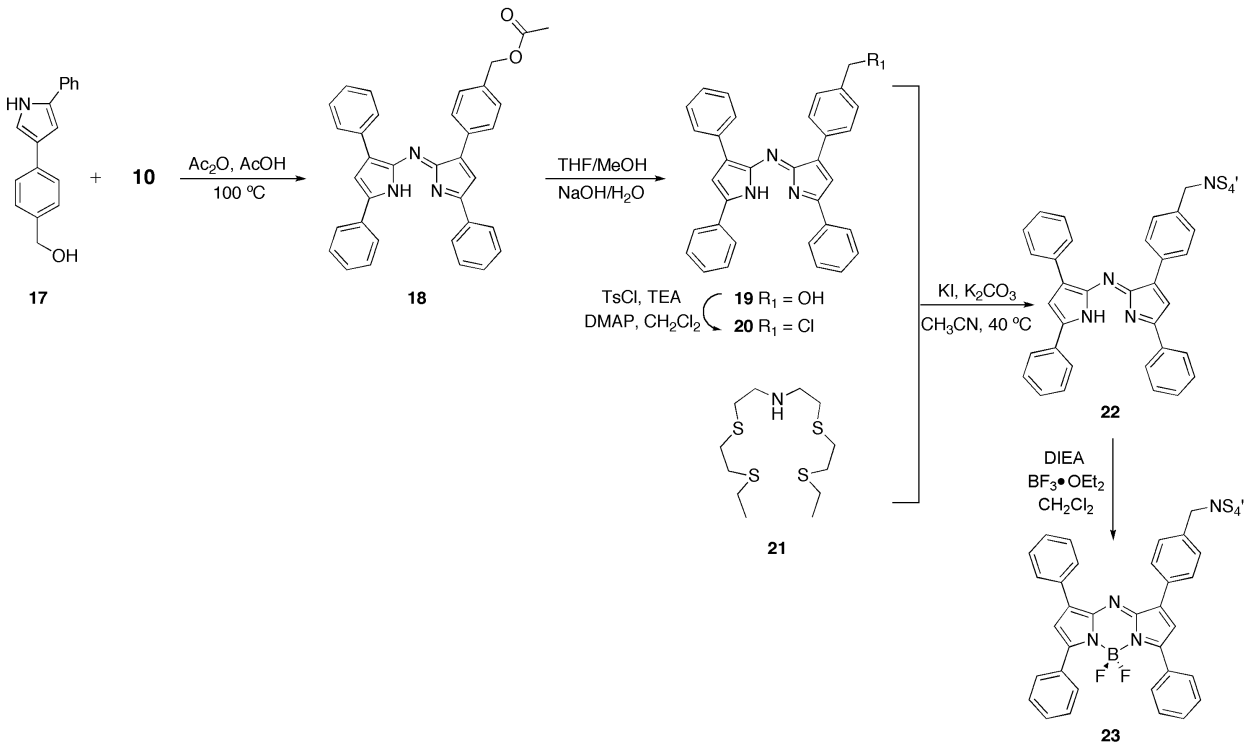

Scheme A1-4. Synthesis of compound **18-23**.

	Excitation (λ/ nm, e/ x 10^4 $M^{-1}cm^{-1}$)		Emission (λ/ nm, Φ) [b]		K_d	$E_{1/2}(A/A^-)$ [c]	ΔG_{PET} [d]
	Apo dye	Cu^+-bound	Apo dye	Cu^+-bound	(M)	(V)	(eV)
N-CS1	610, 2.0	665, 5.4	826,	812,	3.9(7) x 10^{-11}	-0.335	-1.29
(**12**)	735, 1.6		0.0013	0.011			
N-CS2	650, 8.9	650, 9.0	670,	670,	1.7(1) x 10^{-12}	-0.335	-1.18
(**23**)			0.017	0.037			

Table A1-1. Spectroscopic and thermodynamic data for N-CS chemosensors.[a]
[a]All spectroscopic measurements were performed in MeOH. [b]Quantum yields are based on a 3, 3'-diethylthiacarbocyanine iodide standard (Φ = 0.36 in MeOH).[25] [c]Values are derived from the reduction potential of the tetraphenyl-substituted boratriazaindacence core[7] (vs. SCE). [d]Oxidation potential of *N*, *N*-dimethylaniline was used for N-CS1 and the oxidation potential of triethylamine was used for N-CS2.[27]

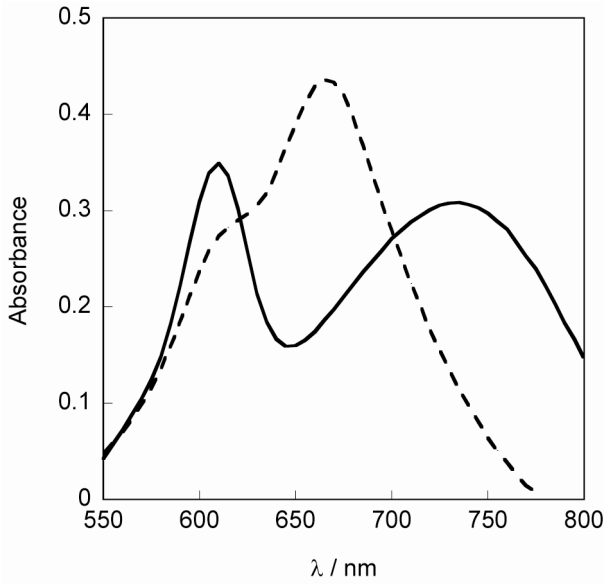

Figure A1-1. UV-visible spectra of 10 μM N-CS1 (solid line) (λ_{max} = 610 nm, 735 nm) and 10 μM N-CS1 with 10 mM Cu^{+} (dotted line) (λ_{max} = 665 nm). Spectra were acquired in MeOH.

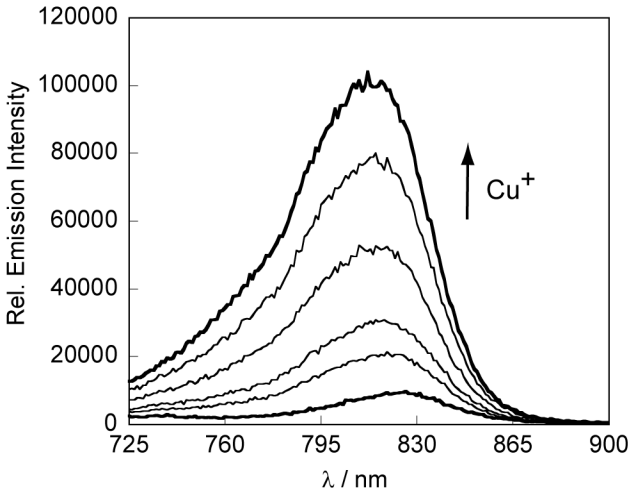

Figure A1-2. Fluorescence responses of 10 μm N-CS1 to Cu^{+}. Spectra shown are for buffered [Cu^{+}] of 0, 1.0, 2.0, 4.0, 6.0, and 8.0 μM. Spectra were acquired in MeOH, with excitation at 665 nm.

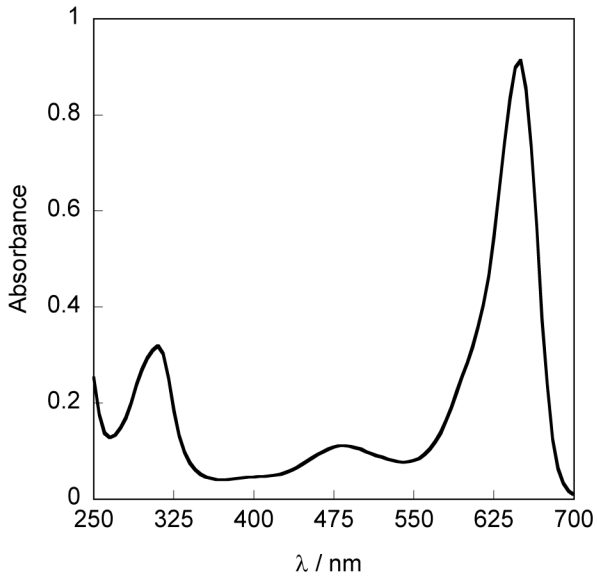

Figure A1-3. UV-visible spectrum of 10 μM N-CS2 (λ_{max} = 650 nm). No change was observed with the addition of Cu^{+} (λ_{max} = 650 nm). Spectrum was acquired in MeOH.

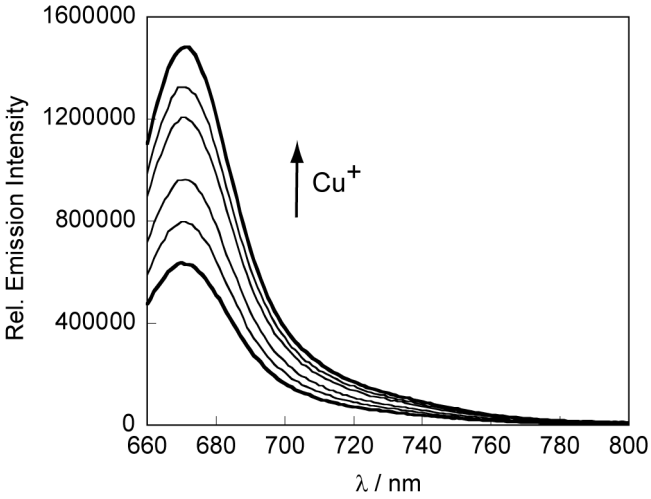

Figure A1-4. Fluorescence responses of 2 μm N-CS2 to Cu^{+}. Spectra shown are for buffered [Cu^{+}] of 0, 0.4, 0.8, 1.2, 1.6, 2.0 μM. Spectra were acquired in MeOH, with excitation at 650 nm.

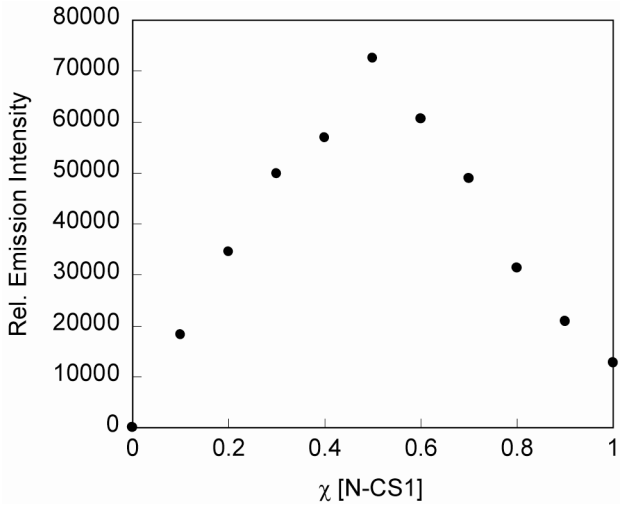

Figure A1-5. Job's plot of N-CS1 and Cu^{+}. The total concentration of N-CS1 and Cu^{+} was kept constant at 10 μM. Excitation was provided at 665 nm and the maximum emission intensity was measured. Spectra were acquired in MeOH. The maximum fluorescence response at 0.5 mol fraction of N-CS1 is consistent with the formation of a 1:1 Cu^{+}:N-CS1 complex.

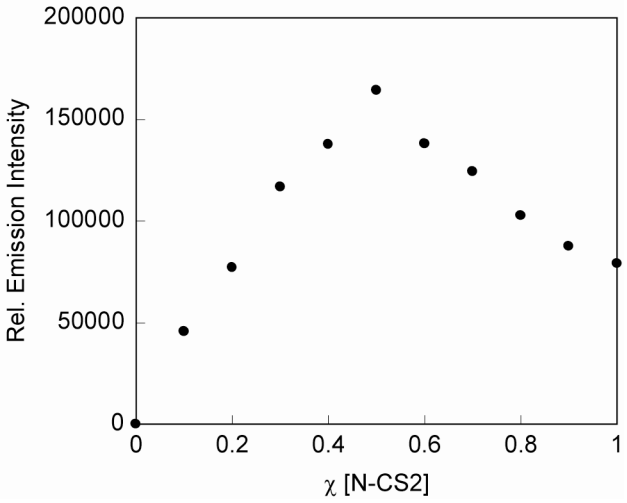

Figure A1-6. Job's plot of N-CS2 and Cu^{+}. The total concentration of N-CS2 and Cu^{+} was kept constant at 10 mM. Excitation was provided at 650 nm and the emission intensity was measured at 670 nm. Spectra were acquired in MeOH. The maximum fluorescence response at 0.5 mol fraction of N-CS2 is consistent with the formation of a 1:1 Cu^{+}:N-CS2 complex.

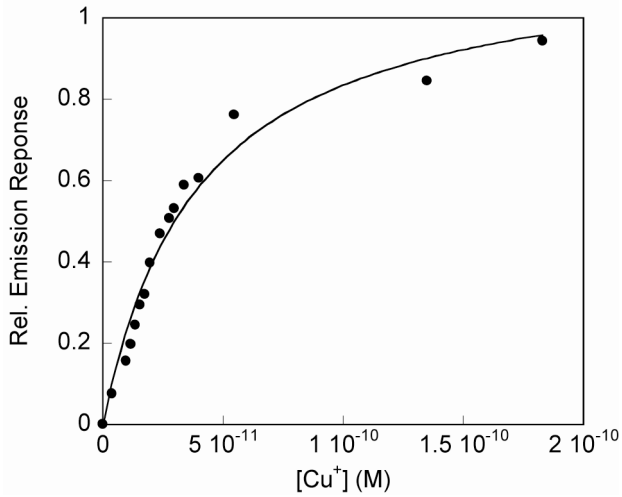

Figure A1-7. Normalized fluorescence response of 10 μM N-CS1 to thiourea buffered Cu^{+} solutions for K_d value determination. Excitation was provided at 665 nm and the collection emission was integrated from 675 to 900 nm. Spectra were acquired in MeOH. The points shown are for free Cu^{+} buffered at 3.83, 9.64, 11.6, 13.6, 15.6, 17.6, 19.723.8, 27.8, 29.8, 34, 40, 54.8, 183, and 135 pM, respectively. The observed K_d value is 4.0(5) x 10^{-11} M.

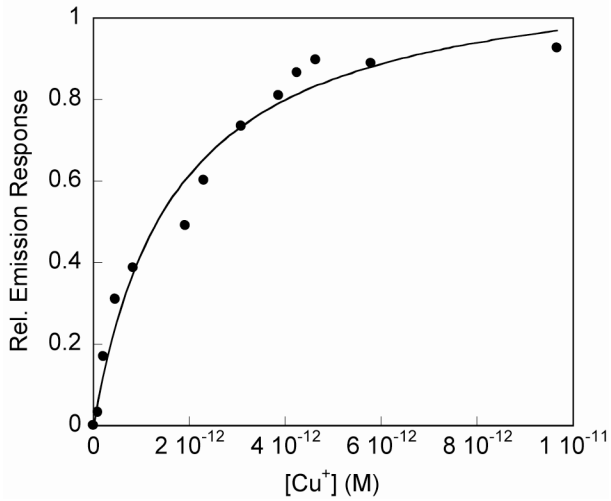

Figure A1-8. Normalized fluorescence response of 2 μM N-CS2 to thiourea buffered Cu^{+} solutions for K_d value determination. Excitation was provided at 650 nm and the collection emission was integrated from 660 to 900 nm. Spectra were acquired in MeOH. The points shown are for free Cu^{+} buffered at 95.2, 207, 455, 830, 1920, 2310, 3080, 3860, 4250, 4640, 5800, and 9670 fM, respectively. The observed K_d value is 1.7(3) x 10^{-12} M.

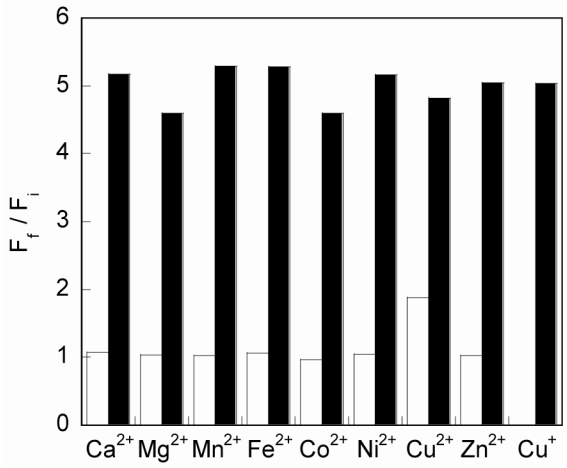

Figure A1-9. Fluorescence response of N-CS1 to various metal ions. Bars represent the final integrated fluorescence response (F_f) over the initial integrated emission (F_i). Spectra were acquired in MeOH. White bars represent the addition of an excess of the appropriate metal ion (2 mM Ca^{2+}, Mg^{2+}, and Zn^{2+}, 50 μM for all other cations) to a 10 μM solution of N-CS1. Black bars represent the subsequent addition of 10 μM Cu^{+} to the solution. Excitation was provided at 665 nm, and the collected emission was integrated over 675-900 nm.

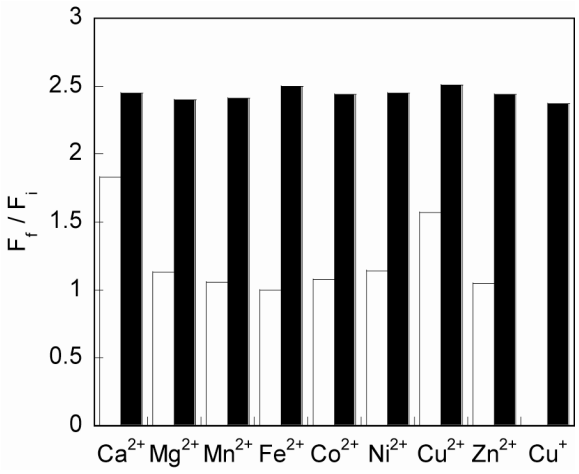

Figure A1-10. Fluorescence response of N-CS2 to various metal ions. Bars represent the final integrated fluorescence response (F_f) over the initial integrated emission (F_i). Spectra were acquired in MeOH. White bars represent the addition of an excess of the appropriate metal ion (2 mM Ca^{2+}, Mg^{2+}, and Zn^{2+}, 50 μM for all other cations) to a 2 μM solution of N-CS2. Black bars represent the subsequent addition of 2 μM Cu^{+} to the solution. Excitation was provided at 650 nm, and the collected emission was integrated over 660-900 nm.

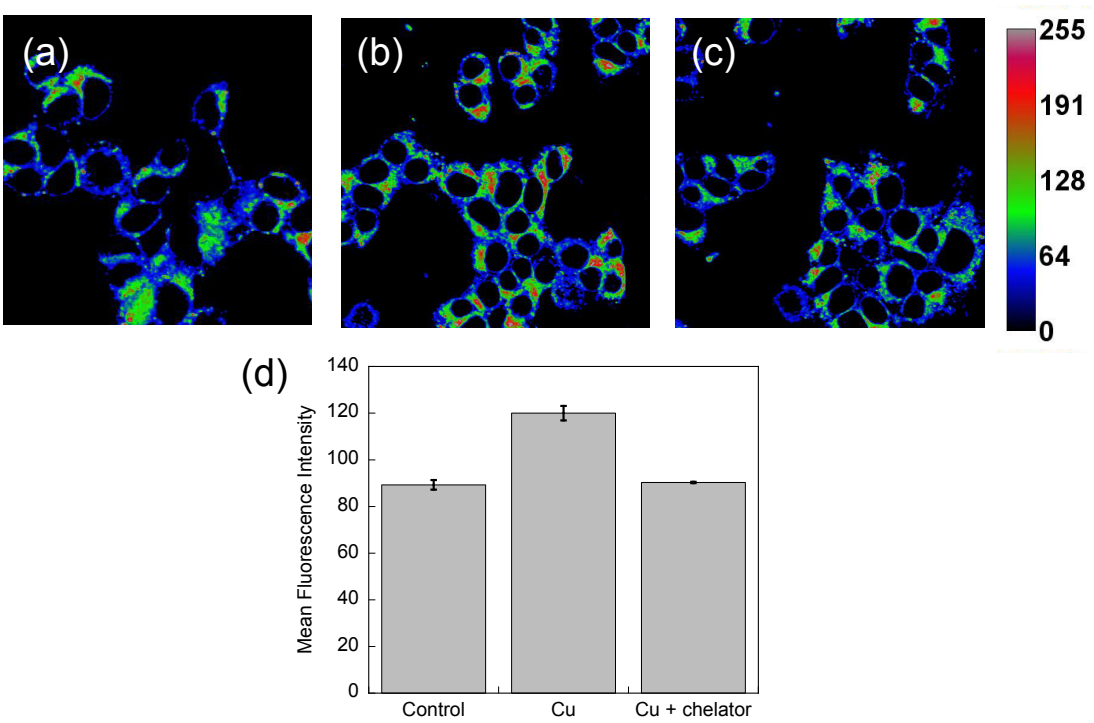

Figure A1-11. Imaging uptake of exogenously applied copper. (a) Live HEK 293T cells stained with 10 μM N-CS2 for 3 hr at 37 ºC show basal levels of copper. (b) HEK 293T cells supplemented with 200 μM $CuCl_2$ overnight at 37 ºC and then stained with 10 μM N-CS2 for 3 hr at 37 ºC. (c) Cells from (b) treated with 500 μM of the intracellular copper chelator [tris(ethylthio)ethyl)amine] (TEMEA) for 5 min at 24 ºC. (d) Quantification of change in fluorescence intensity relative to cells treated only with N-CS2. Values represent the average intensity of three randomly selected fields and error bars represent standard error measurement.

References

1. Zeng, L.; Miller, E. W.; Pralle, A.; Isacoff, E. Y.; Chang, C. J. *J. Am. Chem. Soc.* **2006**, *128*, 10—11.
2. Miller, E. W.; Zeng, L.; Domaille, D. W.; Chang, C. J. *Nat. Protocols*. **2006**, *1*, 824—827.
3. Domaille, D. W.; Zeng, L.; Chang, C. J. *J. Am. Chem. Soc.* **2010**, *132*, 1194—1195.
4. Dodani, S. C.; Domaille, D. W.; Nam, C. I.; Miller, E. W.; Finney, L. A.; Vogt, S.; Chang, C. J. *Proc. Natl. Acad. Sci. U.S.A.* **2011**, *108*, 5980—5985.
5. Dodani, S. C.; Leary, S. C.; Cobine, P. A.; Winge, D. R.; Chang, C. J. *J. Am. Chem. Soc.* **2011**, *133*, 8606—8616.
6. Frangioni, J. V. *Curr. Opin. Chem. Biol.* **2003**, *7*, 626—634.
7. Gorman, A.; Killoran, J.; O'Shea, C.; Kenna, T.; Gallagher, W. M.; O'Shea, D. F. *J. Am. Chem. Soc.* **2004**, *126*, 10619—10631.
8. Loudet, A.; Bandichhor, R.; Wu, L.; Burgess, K. *Tetrahedron* **2008**, *64*, 3642—3654.
9. Zhao, W.; Carreira, E. M. *Chem. Eur. J.* **2006**, *12*, 7254—7263.
10. Killoran, J.; McDonnell, S. O.; Gallagher, J. F.; O'Shea, D. F. *New J. Chem.* **2008**, *32*, 483—489.
11. McDonnell, S. O.; O'Shea, D. F. *Org. Lett.* **2006**, *8*, 3493—3496.
12. Killoran, J.; O'Shea, D. F. *Chem. Comm.* **2006**, 1503—1505.
13. Lee, S. J.; Jung, J. H.; Seo, J.; Yoon, I.; Park, K. M.; Lindoy, L. F.; Lee, S. S. *Org. Lett.* **2006**, *8*, 1641—1643.
14. Hall, M. J.; McDonnell, S. O.; Killoran, J.; O'Shea, D. F. *J. Org. Chem.* **2005**, *70*, 5571—5578.
15. Sarri, P.; Venturi, F.; Cuda, F.; Roelens, S. *J. Org. Chem.* **2004**, *69*, 3654—3661.
16. Gawley, R. E.; Mao, H.; Haque, M. M.; Thorne, J. B.; Pharr, J. S. *J. Org. Chem.* **2007**, *72*, 2187—2191.
17. Hall, M. J.; Allen, L. T.; O'Shea, D. F. *Org. Biomol. Chem.* **2006**, *4*, 776—780.
18. Gopalan, P.; Katz, H. E.; McGee, D. J.; Erben, C.; Zielinski, T.; Bousquet, D.; Muller, D.; Grazul, J.; Olsson, Y. *J. Am. Chem. Soc.* **2004**, *126*, 1741—1747.
19. Cooper, T. H.; Mayer, M. J.; Leung, K. H.; Ochrymowycz, L. A.; Rorabacher, D. B. *Inorg. Chem.* **1992**, *31*, 3796—3804.
20. Ishikawa, J.; Sakamoto, H.; Mizuno, T.; Otomo, M. *Bull. Chem. Soc. Jpn.* **1995**, *68*, 3071—3076.
21. Coskun, A.; Akkaya, E. U. *J. Am. Chem. Soc.* **2005**, *127*, 10464—10465.
22. Sakamoto, H.; Ishkawa, J.; Mizuno, T.; Doi, K.; Otomo, M. *Chem. Lett.* **1993**, *22*, 609—612.
23. Douty, B. D.; Salvino, J. M.; Seoane, P. R.; Dolle, R. E. *Bioorg. Med. Chem. Lett.* **1995**, *5*, 363—366.
24. Mak, C. C.; Bampos, N.; Darling, S. L.; Montalti, M.; Prodi, L.; Sanders, J. K. M. *J. Org. Chem.* **2001**, *66*, 4476—4486.
25. Bilmes, G. M.; Tocho, J. O.; Braslavsky, S. E. *J. Phys. Chem.* **1989**, *93*, 6696—6699.
26. Martell, A. E.; Smith, R. M. *Critical Stability Constants*; Plenum Press: New York, 1989.
27. Jacques, P.; Burget, D.; Allonas, X. *New J. Chem.* **1996**, *20*, 933—937.

Appendix 2:
Copper in Neural Stem Cell Differentiation

Synopsis

This appendix summarizes preliminary results and methods to study copper homeostasis in neural stem cell proliferation and differentiation by X-ray fluorescence microscopy (XRFM) and western blot analysis. Recently, several studies in hematopoietic and embryonic stem cells have examined how stem cell machinery and transition metal ion homeostasis intersect.[1—4] Owing to the fact that the adult brain is highly redox active and is a large reservoir of redox-active metal ions including copper, we became interested in how neural stem cells utilize copper to maintain a pluripotent state and for lineage determination.[5]

Results and Discussion

XRFM of Neural Stem Cells. We first used XRFM to map copper and zinc in mouse neural stem cells grown in fibroblast growth factor (FGF) and then differentiated with retinoic acid and fetal bovine serum (RA/FBS) for 2 days at sector 2ID-E at the Argonne National Laboratory.[6] Neural stem cells are maintained in a proliferative state in FGF and RA/FBS differentiation of neural stem cells results in a population of glial cells and neurons.[6] XRFM images were acquired a 1 sec dwell time at 1 micron (low-resolution) and 0.5 micron (high-resolution) step size with the 20 cm zone plate. Representative images are shown in Figure 2A-1. The high-resolution acquisition provides more spatial information as these cells are small. The phosphorus channel defines the cell body, and the zinc channel marks the nucleus. Interestingly we find that the copper is highly enriched in the cytoplasm of the undifferentiated neural stem cell, and upon differentiation the copper signal becomes more diffuse. It is important that we cannot identify the differentiated cell as a glial cell or a neuron based on the white light image. Quantification of the high-resolution images shows that total copper and not zinc decreases upon differentiation of neural progenitor cells and quantification of the low-resolution XRFM images shows a similar trend (Figure 2A-2). Unlike the proliferative stem cell state, differentiated cells are not circular in shape but spread out and have projections. As such, total metal content should be quantified in the MAPS XRF software since this measurement does not normalize by the area of the region of interest.

Western Blot Analysis of Copper Proteins in Neural Stem Cell Differentiation. We wanted to further investigate the decrease in cellular copper as seen by XRFM with western blot analysis of copper proteins during neural stem cell differentiation. First we confirmed the changes seen with canonical markers of pluripotent and differentiated cells. Neural stem cells express SOX2 and upon differentiation with RA/FBS the neural stem cells are committed down a lineage of glia and neurons. We checked the expression of three well-established neuronal proteins NeuN and βIII tubulin, and glial marker GFAP. As expected, stem cells maintained in a pluripotent state with FGF express SOX2. Upon differentiation, SOX2 decreases and the neuronal and glia proteins increase in expression (Figure 2-3a).[6] Cellular copper uptake is controlled by CTR1 and export by ATP7A and as can be seen in Figure 2-3b both of these proteins increase in expression, which provides a rationale for the change in total copper as seen by XRFM. With this data in hand, we started using CS3 presented in Chapter 2 of this dissertation to image labile copper in undifferentiated and differentiated neural stem cells; however, as noted above the cells change shape and size upon treatment with RA/FBS. As such, we were unable to see a difference in the labile copper pool upon differentiation since the dye uptake changes as well. This project has been continued by Bryan Dickinson and Lakshmi Krishnamoorthy where they have altered

cellular copper status with copper chelators and genetic methods to knockdown CTR1 and ATP7A in neural progenitor cells and have proceeded to see how the ratio of glial cells and neurons changed upon differentiation with immunofluorescence.

Experimental

Preparation of XRFM Samples. Neural stem cells were cultured and differentiated on silicon nitride windows (2 × 2 mm; 250 nm or 500 nm thickness) manufactured by Silson by Bryan C. Dickinson as described previously.[6,7] For all of the samples, the media was aspirated, the cells were washed with PBS, followed by fixation in 4% paraformaldehyde (PFA) in PBS for 10 min, and subsequently washed with PBS. Residual PBS was removed by several washes with 20 mM PIPES, pH 7.2⁄200 mM sucrose followed by air-drying. Individual cells with beads were selected on a Lecia fluorescent microscope and X-ray fluorescence imaging was carried out with the scanning X-ray microprobe at beamline 2-ID-E at the Advanced Photon Source (Argonne National Laboratory) using a 20 cm zone plate with 0.5 and 1.0 micron step size and 1 sec dwell time as previously described.[8]

Western Blot Analysis of Neuronal and Copper Proteins. Cellular lysates were isolated and processed as described previously.[6] Representative sample preparation is as follows: 5 μL of 4x Laemmli buffer (0.25 mM Tris, 2% SDS, 40% glycerol, 20% beta-mercaptoethanol, 0.04% bromophenol blue) was combined with 5—30 μg of protein, and denatured and separated on SDS page gels. Samples for were denatured as follows: SOX2, NeuN, βIII tubulin, and GFAP at 90 °C for 5 min, CTR1 at 37 °C for 10 min, and ATP7A at 37 °C for 10 min. The percentage of SDS page gels used were as follows: 12% for SOX2, NeuN, βIII tubulin, GFAP, 15% for CTR1, and 8% for ATP7A. Proteins were transferred to PVDF membranes (Immobilon, Millipore) with a semi-dry transfer system (Biorad) at constant voltage (15 V) for 30 min for proteins smaller than 100 kDa and 40 min for proteins larger than 100 kDa. The blots incubated overnight at 4 °C in 5% nonfat dry milk in wash buffer (10 mM Tris, pH 7.5, 100 mM NaCl, 0.1% Tween-20) with primary antibodies: anti-SOX2 (1:1000, Santa Cruz, Catalog# SC17320), anti-NeuN (1:1000, Millipore, Catalog# MAB377), anti-βIII tubulin (1:1000, Sigma, Catalog# T8660), anti-GFAP (1:1000, Abcam, Catalog# Ab7260), and anti-GAPDH (1:1000, Abcam, Catalog# Ab9485). Anti-CTR1 (1:1000) was kindly provided by Dennis Thiele and Anti-ATP7A (1:1000) was kindly provided by Betty Eipper. Membranes were further processed as described previously.[7]

Figures

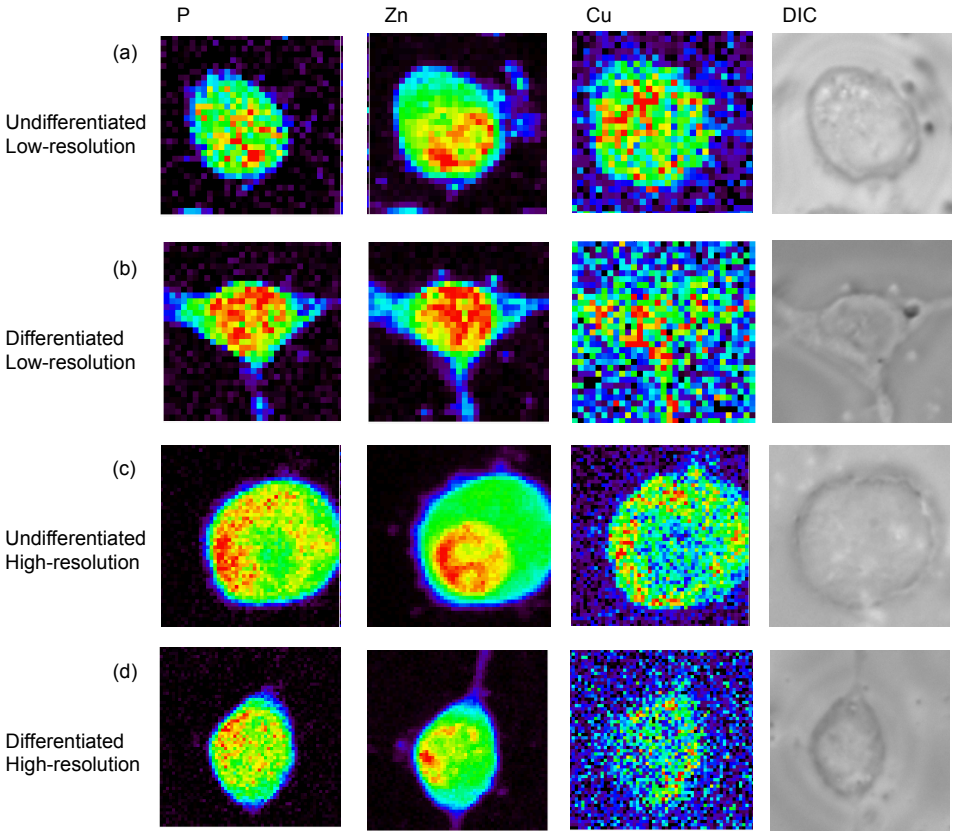

Figure 2A-1. Molecular imaging of P, Zn, and Cu distributions in undifferentiated and differentiated neural stem cells. Representative images are shown for (a) and (c) undifferentiated neural stem cells grown in FGF for 4 days and (b) and (d) neural stem cells grown in FGF for 2 days and differentiated with RA/FBS for 2 days followed by fixation and imaging by XRFM.

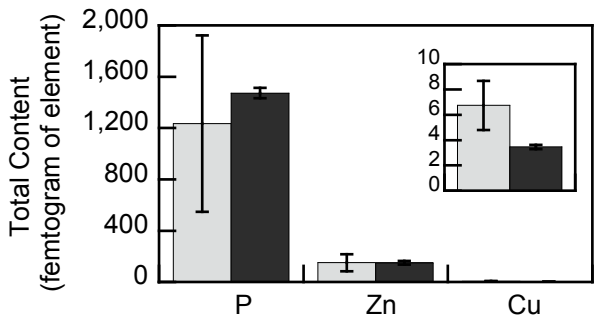

Figure 2A-2. Quantification of high-resolution XRFM images for total P, Zn, and Cu in undifferentiated (n = 4 cells) and differentiated neural stem cells (n = 3 cells). The bar graph represents the average of total content for each element and the error bars are ± s.e.m.

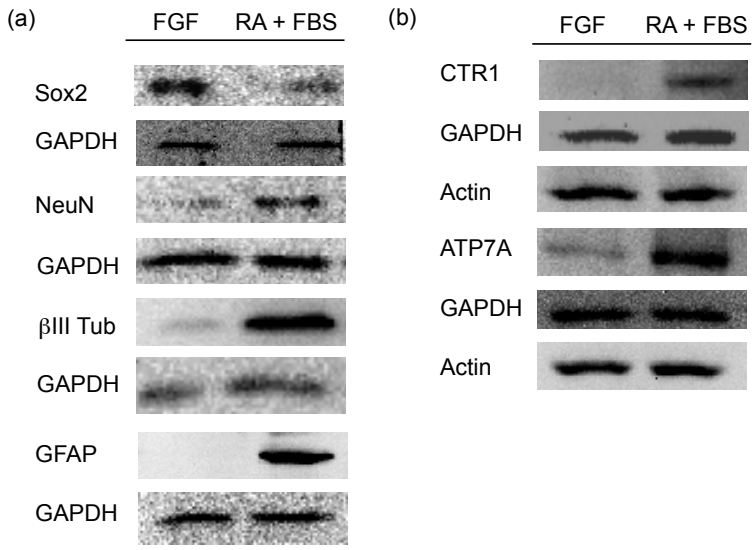

Figure 2A-3. Representative western blot analysis of neural stem cells maintained in a pluripotent state for 2—3 days with FGF followed by differentiation with RA/FBS for 4—6 days for (a) pluripotent, glia, and neuronal markers and (b) copper import and export proteins.

References

1. Huang, X.; Pierce, L. J.; Cobine, P. A.; Winge, D. R.; Spangrude, G. J. *Cell Transplant.* **2009**, *18*, 887—897.
2. Peled, T.; Glukhman, E.; Hasson, N.; Adi, S. et al. *Exp. Hematol*. **2005**, *33*, 1092—1100.
3. Zaker, F.; Nasiri, N.; Oodi, A.; Amirizadeh, N. *Hematology*. **2013**, *18*, 39—45.
4. Wolford, J. L.; Chishti, Y.; Jin, Q.; Chen, L.; Vogt, S.; Finney, L. PLoS One. 2010, *5*, e12308.
5. Que, E. L.; Domaille, D. W.; Chang, C. J. *Chem. Rev.* **2008**, *108*, 1517—1549.
6. Peltier, J.; Agrawal, S.; Robertson, M. J.; Scahaffer, D. V. *Methods Mol. Biol.* **2010**, *621*, 65—87.
7. Dickinson, B. C.; Peltier, J.; Stone, D.; Schaffer, D. V.; Chang C. J. *Nat. Chem. Biol*. **2011**, *7*, 106—112.
8. Finney, L.; Mandava, S.; Ursos, L.; Zhang, W. et al. *Proc. Natl. Acad. Sci. USA*. **2007** *104*, 2247—2252.

Appendix 3:

Molecular Imaging Approaches to Study Copper Dynamics in RAW 264.7 Macrophages

Synopsis

This appendix summarizes preliminary results and methods to study copper mobilization in RAW 264.7 macrophages by molecular imaging and X-ray fluorescence microscopy (XRFM). It has been established that proinflammatory agents including lipopolysaccharides (LPS) and interferon-gamma (IFN-γ) increase the expression and alter the localization of the copper import protein CTR1 and export protein ATP7A in RAW 264.7 macrophages.[1] Furthermore, studies in our lab have revealed hydrogen peroxide bursts in phagosomes upon acute treatment with phorbol 12-myristate 13-acetate (PMA).[2] With this information in hand our goal was to understand real-time copper dynamics in PMA, LPS, and IFN-γ stimulated RAW 264.7 macrophages.

Results and Discussion

XRFM of RAW 264.7 Macrophages. We first used XRFM to map copper in macrophages treated with LPS and IFN-γ overnight and PMA for 30 min at sector 2ID-E at the Argonne National Laboratory. In control macrophages copper is localized to the Golgi as expected (Figure 3A-1a). Phagosomes of activated cells were labeled live with latex beads followed by fixation and processing for XRFM. ATP7A has ben shown to line the phagosomal membrane in activated macrophages, so if copper is trafficked to the phagosome, we would expect to see a ring of copper around the bead.[1] It is important to note that labeling with 3 μM latex beads results in black holes within the cell that can be seen in the XRFM image (Figure 3A-1b). Phagosomes were also labeled with 1.1 μM fluorescent latex beads to mark smaller regions of interest. The phagosomal space is effectively where the bead is and several radii around the bead. However, in both LPS and IFN-γ treated macrophages there is not a large portion of cellular copper trafficked to the phagosome, but interestingly in some cases there are sulfur rings around the beads (Figure 3A-1b). Duration of stimulation, population heterogeneity, and poor resolution due to the optics are variables that need to be considered in this experiment. For the short-term stimulation with PMA for 30 min we find that there is a spatial redistribution of copper from the Golgi to the cytosol (Figure 3A-1d). For all three treatments more replicates over multiple synchrotron visits are necessary for reliable quantification of XRFM images. Additionally, owing to the small size of macrophages, XRFM images should be acquired on the 20 cm zone plate with 0.6 μM step size, 2 sec dwell time if the beam can be focused to that spot size instead of on the 10 cm zone plate with 0.6 μM step size, 2 sec dwell time since the ion current going through the sample is significantly reduced. The phagosomes should not be marked with a latex bead as these objects interfere with the assignment of the region of interest and subsequent quantification output from the MAPS software. Alternatives to the latex beads include fluorescently labeled dextran or bacteria but they must be visible in the brightfield image or by fluorescence on the Lecia fluorescent microscope at sector 2-IDE. It is also important to note that as the cell shape changes, the total content of the element should be evaluated as this measurement is independent of the area of the region of interest unlike the mean or median generated from the MAPS XRF analysis software.

Imaging Labile Copper with CS3 in RAW 264.7 Macrophages. We next used CS3 presented in Chapter 2 of this dissertation to study changes in the labile copper pool with stimulated macrophages. Overnight treatment with LPS followed by staining with CS3 shows accumulation of the dye in vesicles (Figure 3A-2). Further co-localization experiments with Cascade Blue

labeled dextran reveals that our BODIPY based copper sensors do not accumulate in phagosomes (Figure 3A-3). In order to evaluate the remodeling of copper in this process a more sensitive and hydrophilic probe that provides uniform staining will be useful as the bright puncta are an artifact of poor cell health do not convey any measure of labile copper. To continue, we find that macrophages co-treated with PMA and CS3 for 15 min show a decrease in fluorescence intensity (Figure 3A-4). As a positive control we co-treated macrophages with 4-alpha PMA an epimer of PMA, which does not bind the diacyl glycerol site of protein kinase C (PKC) like PMA, however, we see similar decrease in fluorescence intensity as determined by flow cytometry (data not shown). We had to temporarily resort to using flow cytometry as cell culturing conditions resulted in a significant portion of activated cells in the of the control population, but gating of populations of the macrophages was challenging as sample preparation by scraping the cells results in activation as well. With these initial results in hand, we have synthesized more photostable copper sensors, and current collaborative efforts with Dr. Jefferson Chan are focused on understanding the effects of PMA in real-time as it relates to the oxidation state of glutathione and ATP7A trafficking with new molecular imaging tools and biochemical assays.

Experimental

Preparation of X-ray fluorescence microscopy (XRFM) samples. RAW 264.7 macrophages were plated on poly-L-lysine coated silicon nitride windows (2 × 2 mm; 250 nm or 500 nm thickness) manufactured by Silson in a six-well plate (3 mL of media/well). The macrophages were grown for two days prior to stimulation. All stimuli described below were preared according to manufacturer's instructions. Macrophages were treated with 25 ng/μL IFN-γ from a 25 μg/mL stock solution (BD Biosceinces, Catalog# 554587) for 21 h and then 500 μL of the media was removed and mixed with 9 μL of 3 μM latex beads (Sigma, Catalog# LB30) or 2.2 μL of 1.1 μM green fluorescent latex beads (Sigma, Catalog# L4655) and added back to the well for 90 min. LPS (100 μg/mL, 100 mg/mL stock solution) stimulation and bead treatment was carried out as described above. For PMA treatment (4 μg/mL from a 1 mg/mL stock, Sigma, Catalog# P8139-1MG), macrophages were co-incubated with PMA and 6 μL 1.1 μM green fluorescent latex beads for 30 min. For all of the samples, the media was aspirated, the cells were washed with PBS, followed by fixation in 4% paraformaldehyde (PFA) in PBS for 10 min, and subsequently washed with PBS. The fixed samples were then imaged to check for sample integrity and bead uptake in PBS on a Zeiss LSM510 META/NLO Axioplan 2 laser-scanning microscope and a 40x water-immersion objective lens at the Molecular Imaging Center at the University of California, Berkeley. Then the PBS was removed and residual PBS was removed by several washes with 20 mM PIPES, pH 7.2/200 mM sucrose followed by air-drying. Individual cells with beads were selected on a Lecia fluorescent microscope and X-ray fluorescence imaging was carried out with the scanning X-ray microprobe at beamline 2-ID-E at the Advanced Photon Source (Argonne National Laboratory) using a 10 cm zone plate with 0.6-micron step size and 2 sec dwell time as previously described.[3]

Molecular imaging with copper sensors and labeling phagosomes in RAW 264.7 macrophages. The macrophages were maintained at the University of California, Berkeley Tissue Culture Facility by Ann Fischer and were plated to reach 60-70% confluence in two days on poly-L-lysine coated coverslips or chamber slides. Imaging experiments were performed with a Zeiss LSM510 META NLO Axioplan 2 laser-scanning microscope, a Zeiss 510NL META

AxioIMAGER laser-scanning microscope, and a Zeiss LSM 710 laser-scanning microscope with a 40x or 63x water-immersion objective lens. Excitation of Mito-CS1 or CS3 loaded cells at 543 nm was carried out with a HeNe laser, and emission was collected using a META detector between 554—650 nm and excitation of Cascade Blue labeled dextran was carried out with 405 nm diode laser and emission was collected between 469—522 nm. It was best to use the macrophages from P1 to P12 as they were more difficult to activate at older passages. The cells should be brought from the tissue culture facility in an insulated container as environmental perturbations can activate the cells, which result in flattening of the cells with spindles/processes and in the formation of phagosomes. Macrophages were stimulated for imaging as described above. A general protocol for staining macrophages that was developed is as follows: remove media with stimulant if added overnight, add the copper sensor (2—5 μM) in DMEM or DPBS for 15 to 30 min with PMA if it is being used, followed by washing out the sensor and imaging in fresh DMEM or DPBS. It is important to note that if DMEM is used for imaging then 5% CO_2 atmosphere at 37 °C must be used, but if imaging is carried out in DPBS then imaging at 37 °C is sufficient for short term assays. Phagosomes can be labeled as described above with latex beads, however, using fluorescently labeled dextran was found to be better suited for live-cell imaging as the dye does not stick to the dextran. Cascade Blue labeled 10,000 MW dextran (Life Technologies, Catalog# D-1976) was prepared in DPBS at 1.25 mg/mL or 5 mg/mL. In one well of a four well chamber slide macrophages were treated with 50 μL of the dextran solution and 150 μL of DPBS or DMEM with or without a copper sensor for 15 min. The cells were then washed for 5 min with DPBS or DMEM and subsequently imaged in fresh DPBS or DMEM. Imaging analysis was completed as described in Chapter 3.

Figures

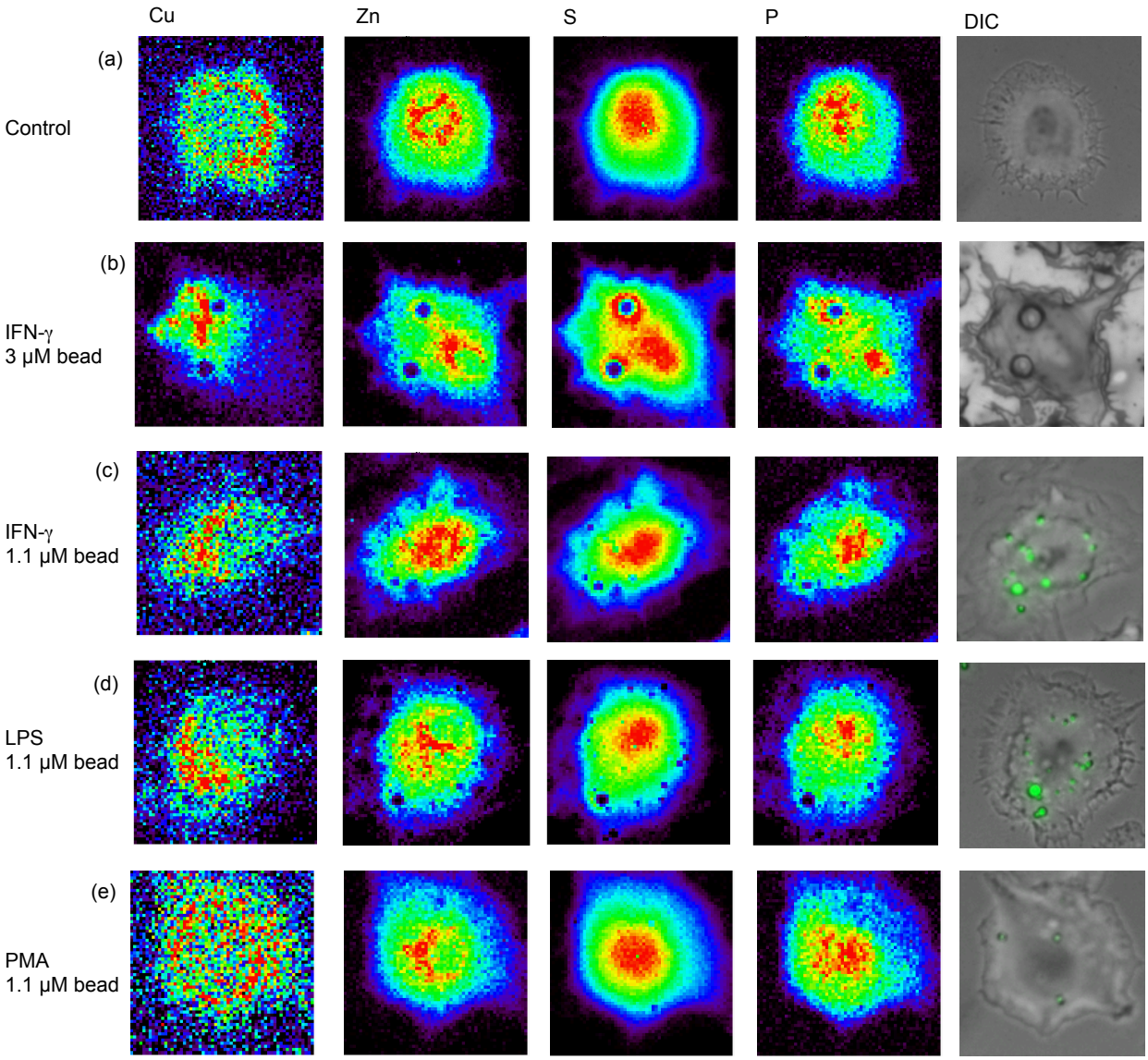

Figure 3A-1. Molecular imaging of Cu, Zn, S and P distributions in control and stimulated RAW 264.7 macrophages. Representative images are shown for (a) Control macrophages (n = 5 cells), (b) macrophages treated with 25 ng/mL IFN-γ overnight and treated with 3 μM latex beads for 90 min (n = 5 cells), (c) macrophages treated with 25 ng/mL IFN-γ overnight and treated with 1.1 μM green fluorescent latex beads for 90 min (n = 5 cells), (d) macrophages treated with 100 ng/mL LPS overnight and treated with 1.1 μM green fluorescent latex beads for 90 min (n = 5 cells), and (e) macrophages treated with 4 μg/mL PMA and 1.1 μM green fluorescent latex beads for 30 min (n = 5 cells) followed by fixation and imaging by XRFM.

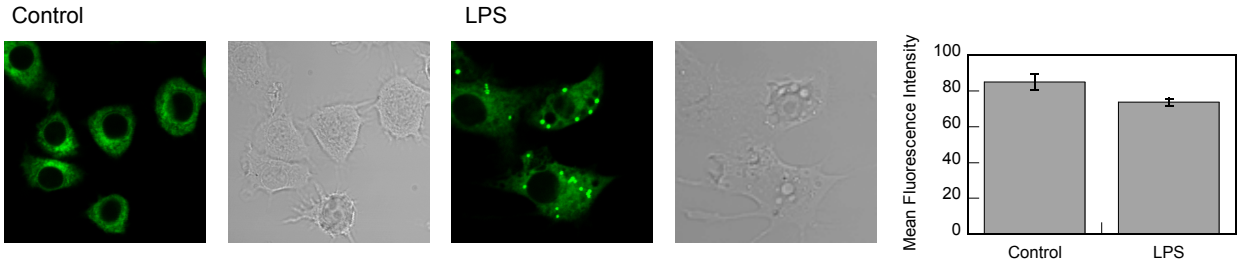

Figure 3A-2. Stimulation with LPS results in a spatial re-distribution of the dye and a slight decrease in the labile Cu^{+} pool. Representative images and quantification of RAW 264.7 macrophages incubated with and without 50 ng/mL LPS overnight followed by staining with 2 μM CS3 in DMEM for 15 min and imaging in fresh DPBS. The bar graph represents the average of at least three fields of cells and the error bars are ± s.e.m.

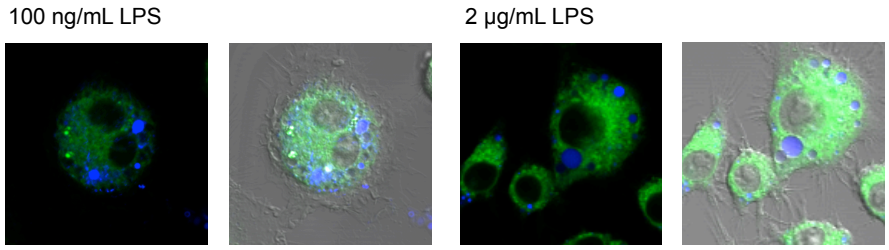

Figure 3A-1C. Representative images from RAW 264.7 macrophages treated with 100 ng/mL LPS overnight and 2 µg/mL LPS for 8 h followed by staining with 5 µM RCS4 and Cascade Blue dextran in DMEM for 15 min, washing for 5 min in DMEM, and imaging in fresh DMEM, 5% CO_2 at 37 ° C.

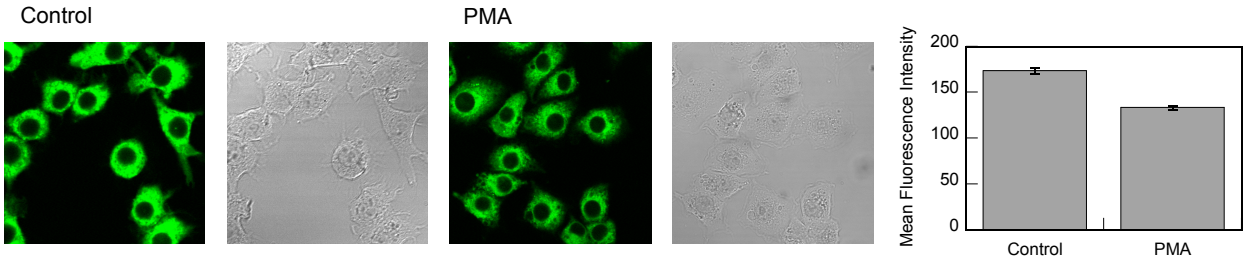

Figure 3A-4. Stimulation with PMA results in a decrease in the labile Cu^{+} pool. Representative images and quantification of RAW 264.7 macrophages stained with 2 μM CS3 or co-treated with 2 μM CS3 and 4 μg/mL 20 min in DMEM followed by imaging in fresh DPBS. The bar graph represents the average of at least three fields of cells and the error bars are ± s.e.m.

References

1. White, C.; Lee, J.; Kambe, T.; Fritsche, K.; Petris, M. J. *J. Biol. Chem.* **2009**, *284*, 33949—33956.
2. Srikun, D.; Albers, A. E.; Chang, C. J. *Chem. Sci.* **2011**, *2*, 1156—1165.
3. Finney L, Mandava S, Ursos L, Zhang W, et al. *Proc. Natl. Acad. Sci. USA*. **2007** *104*, 2247—2252.

Appendix 4:

Protocol for Characterizing a Fluorescent Metal Ion Sensor

Synopsis

This appendix describes the procedure to characterize the photophysical properties of a fluorescent metal ion sensor.

Preparing Aliquots of Dye

1. Weigh out the dye in a clean vial.
2. Calculate the volume of solvent that needs to be added to make a 20 mM stock. Use a pipet to dissolve the dye in chloroform, ethyl acetate, methanol, or acetone. It is important to pipet accurately and it can be difficult with organic solvents. Solvent can be passed through the tip prior to pipetting.
3. Make 10 μL aliquots of the dye solution into PCR tubes that are lined up in an empty pipet tip tray. Tips can be changed between each aliquot for better accuracy. Addition of 200 μL of DMSO the 10 μL aliquot will give a 1 mM stock.
4. Evaporate the solvent by placing the PCR tubes in a dessicator attached to the vacuum line.
5. Aliquots can then be stored over Drierite and stored at -80 °C.

Initial Screening of a Metal Ion Fluorescence Sensor

A few variables need to be tested out before a fluorescent sensor can be fully characterized.

1. The dye should be dissolved in DMSO and kept in the dark during the duration of the experiment. The concentration of dye should be between 500 nM and 10 μM depending on the optical brightness of the fluorophores and the slit widths for both excitation and emission. Too much dye can result in self-quenching so recording the ultra-violet visible spectrum (UV-Vis) is helpful. The buffered dye solution should not have more than 0.6 absorbance units.
2. Pipet the dye into 1 mL of buffer in the cuvette. The volume of the cuvette cannot change more than 1%. A variety of buffers should be screened including HEPES, PBS, methanol, or a combination. If a dye does not work in buffer in might work in another.
3. Mix the dye well with a transfer pipet and acquire an absorbance spectrum and an excitation/emission spectrum with and without the metal. The emission collection should begin 10 nm red shifted from the excitation wavelength. It is important to test different excitation wavelengths to see the largest dynamic emission range.
4. Metal ion solutions derived from the chloride salts are prepared in Mili-q water at the desired concentration with the exception of Cu^{+} and Fe^{2+}, and Fe^{3+}. Copper (Cu^{+}) is derived from the tetrakis(acetonitrile)copper(I) hexafluorophosphate salt and is dissolved in acetonitrile at a maximum concentration of 5 mM. Iron (Fe^{2+}) is prepared from the ferrous ammonium sulfate in degassed water. The water must be degassed for 10 min prior to dissolving the salt and then for the fluorescence measurement the buffer should be degassed and a screw cap cuvette should be used. For Fe^{3+} salts can be dissolved in water, 0.1 M HCl, or acetonitrile depending on the counterion. Do not use metal spatulas to weigh out the metal salts.

5. Pipet the metal solution into the dye solution and mix well with a transfer pipet. If an absorbance or fluorescence change is not noted then a higher concentration of the metal salt can be added or one can wait for the solution to equilibrate. If the probe is being screened for its response against a panel of ions, a variety of concentrations of metal ion should be used depending on the binding constant.

Characterization of a Metal Fluorescent Sensor

Once the initial screening of the fluorescent sensor is complete the probe needs to be thoroughly characterized. These experiments include a titration curve, dissociation constant (K_d), Job's plot or Hill plot, metal ion selectivity, molar extinction coefficient, and quantum yield. Below is an overview of how to set up these experiments and analyze the data.

Titration and Saturation Curve

For the titration curve one aliquot of the dye is needed and a metal stock solution(s). The metal of interest can be added from one stock solution or serially diluted stock solutions can be used. It is important to note that the 1 mL volume of the cuvette should not be changed by more than 10 μL. The absorption and emission profiles of the apo probe should not be altered with the maximum volume of the solvent that the metal salt is dissolved in so this should be checked. First collect an absorption and emission spectrum of the apo dye. The excitation should be selected based on the emission maxima with the largest dynamic emission range and typically this is seen with the bound probe. From here the metal ion of interest should be added. If the probe is a weak binder (more than one equivalent is needed to see maximum fluorescence intensity) as determined in the initial screening then equivalents should be added in larger increments. However, if the probe is a tight binder (one equivalent is needed to see maximum fluorescence intensity) then the metal ion of interest should be added in sub-stoichiometric increments. For example, for 2 μM dye the metal ion solution can be added 10 equivalents at a time to the desired emission maximum intensity if the probe has a weak affinity. If the probe has a strong affinity for the metal ion of interest then 0.25 equivalents at a time can be added to see maximum fluorescence turn-on at 1.0 equivalent, but the titration should be continued to 2.0 equivalents to show that the probe is saturated. Depending on the photostability of the probe and stability of probe-metal complex, a new measurement can be taken for each addition of metal or the metal can be titrated from apo to bound in one measurement. The one technical aspect of this to note is that is if small volumes are being added then the titration with increasing number of equivalents could not be accurate and this can be determined by plotting a saturation curve. The titration curve is a graph of the emission spectra with wavelength on the x-axis and emission intensity on the y-axis. For the saturation curve the number of equivalents added should be on the x-axis and the y-axis can be fluorescence intensity at the emission maximum or integrated fluorescence intensity depending if the shape of the emission spectrum changes from apo to bound. If the saturation curve shows that the fluorescence intensity is not increasing in appropriate increments as the metal is titrated into the solution then perhaps different equivalents can be added or a larger solution can be prepared in Falcon tube and then 1 mL can be transferred to the cuvette.

Dissociation Constant

For the dissociation constant one aliquot of the dye, metal stock solution(s), and a stock solution of competing ligand. The binding affinity (β values) of the competing ligand for the metal interest of should be reported in the literature and here methods for measuring the binding constant of a copper sensor with the competing ligand thiourea will be described. The Excel template created by Dylan W. Domaille for recording measurements used for calculating the K_d can be found in the electronic folders for this dissertation. The apparent dissociation constant (Kd) is determined using the following equation: (F - Fmin)/(Fmax - Fmin) =[M+]/(Kd + [M+]), where F is the observed fluorescence, F_{max} is the fluorescence for the M+:Probe complex, F_{min} is the fluorescence for free Probe, and [M+] is the "free" M+ available for complexation.

1. Record the molarity of the dye in the K_d template.
2. Acquire the fluorescence spectrum for the apo and fully bound probe.
3. Record the maximum emission or the integrated fluorescence intensity in the K_d template.
4. The β values for thiourea should be recorded in the K_d template.
5. Mix the probe with an aqueous solution of thiourea in buffer, then add 1 equivalent of Cu^+, allow the solution to equilibrate for 1 min (optional), and record the fluorescence spectrum.
6. Record the concentration of thiourea, Cu^+, and maximum emission or the integrated fluorescence intensity in the K_d template.
7. Then vary the amount of thiourea keeping the concentration of dye and Cu^+ constant and repeat steps 5 and 6 with a new sample. The amount of thiourea that is used depends on the binding affinity of the fluorescent sensors. Typically concentrations range from 1 μM to 500 μM of thiourea.
8. The goal is to acquire as many data points in the linear portion of the K_d curve so it is important to plot the data as it is acquired. The K_d curve should extend to a saturation range. On the x-axis plot free Cu^+ concentrations and on the y-axis plot the % max value. Then the data points can be fitted to y = m2 * M0/ (m1 + M0) where m1 = X e^{-Y} and m2 =1 in KaleidaGraph. X is an arbitrary number and the exponent Y can be varied from 12 to 15. The m1 value needs to be tighter than the determined K_d.

Job's plot

For the Job's one aliquot of the dye and metal stock solutions are needed. This plot indicates if the probe binds with the metal ion in a 1:1 binding stoichiometry and is typically used for sensors that show maximum emission with one equivalent of metal ion as can be determined by the saturation curve. These probes typically have nanomolar or tighter binding affinity.

1. Determine the total probe concentration that will be used. If 2 μM is used, record the fluorescence spectrum of 2 μM dye without any metal ion.
2. The next fluorescence spectrum should be recorded for 1.75 μM sensor and 0.25 μM metal ion. It is important to note that the total concentration is 2 μM.
3. The next fluorescence spectrum should be recorded for 1.5 μM sensor and 0.5 μM metal ion. The remaining spectra will be acquired in a similar fashion with varying concentrations of sensor and metal ion while keeping the total concentration constant

until 0 μM sensor and 2 μM metal ion. The maximum fluorescence will be recorded at 1 μM sensor and 1 μM metal ion, which indicates a 1:1 binding stoichiometry .

4. The mole fraction of the sensor is plotted on the x-axis and the maximum fluorescence intensity is recorded on the y-axis.

Hill plot

For probes that do not saturate with one equivalent or that bind weakly, the binding stoichiometry is determined by calculating the slope of a Hill plot. The slope determines if the binding is cooperative. If the binding of the metal ion to the probe is not cooperative then the slope is 1. The fluorescence titration curve data is used for the Hill plot, where the Hill coefficient is determined from the slope of the linear least squares fit of $\log[(F_{min}-F_1)/(F_1-F_{max})]$ on the y-axis versus $\log[M^+]$ on the x-axis. F_{min} is the integrated emission intensity for the apo probe and F_{max} is the maximum integrated emission intensity recorded in the presence of a metal ion. F_1 is the integrated emission intensity for the data points recorded between the F_{min} and F_{max}.

Metal ion selectivity

For the metal ion selectivity, one aliquot of the dye, stock solution of the metal interest, and stock solutions of competing metal ions should be prepared. Alkali and alkaline metal ions are used at 2 mM, Zn^{2+} is used at 500 μM to 2 mM, and other bio-relevant metal ions are used at 50 μM.

1. Record a fluorescence spectrum for apo probe and then the fully bound probe with the metal ion of interest.
2. Record a fluorescence spectrum of the apo probe with a competing metal ion followed by the addition of the metal ion of interest. Allow this solution to equilibrate for 1 min (optional) and then record the fluorescence spectrum. Repeat this for all of the competing metal ions.
3. Integrate the emission intensity of the apo probe with the competing metal ion (F_i) and then integrate the emission intensity upon the addition of the metal ion of interest (F_f). For the metal ion selectivity plot the metal ion of interest is recorded on the x-axis and the y-axis is ratio of F_f/F_i for each competing metal ion.

Molar extinction coefficient

For the molar extinction coefficient one aliquot of the probe and metal stock solution is needed. Record the UV-Vis spectrum for varying concentrations of the probe with and without the metal. Then record the absorption maxima for all of the concentrations and determine the extinction coefficient by using Beer's law.

Quantum yield

For the quantum yield one aliquot of the probe, metal stock solution, and a fluorophore that has similar excitation maximum as the probe and a known quantum yield.

1. Record a UV-vis spectrum for a concentration of probe and the standard fluorophore. The absorbance value should match for the probe and the standard.
2. Record fluorescence spectra for both the probe and the standard at the isosbestic point determined by the UV-vis spectrum. This is the point where both the probe and the standard will absorb the same amount of light. For example: the isosbestic point is 490 nm and the emission spectra were collected from 500 to 700 nm.

3. Record fluorescence spectra for both the probe and the standard at bluer excitation so that the entire spectrum is recorded. For example: excitation at 440 nm and the fluorescence spectra are recorded from 450 to 700 nm.
4. Integrate the fluorescence spectra and extrapolate what the integrated emission intensity would be for the spectra recorded at 490 nm if the entire spectrum was recorded (450 to 700 nm) for the probe and the standard. This value needs to be extrapolated because the probe and the standard absorb the same amount of light at 490 nm.
5. The quantum yield of the probe = (Extrapolated integrated emission intensity for the probe x quantum yield of the standard) / extrapolated integrated emission intensity for the standard.
6. Steps 1 to 5 can be repeated for the metal bound probe.

Appendix 5:
Protocol for Molecular Imaging with Copper Sensors

Synopsis

This appendix describes a general protocol for molecular imaging with fluorescent copper sensors.

Protocol

1. **Plating of cells.** For an upright microscope cells should be plated on glass coverslips and for an inverted microscope cells should be plated on glass bottomed chamber slides or dishes. Coating of the plate should be optimized based on the cell type being used.
2. **Treatment of cells.** The cells should be adherent prior to treatment with copper chloride, copper chelator, or any other pharmacological agent. Copper chloride (100 μM to 200 μM) can be added overnight directly into serum containing media, however, if the media does not contain serum low micromolar to nanomolar amounts of copper chloride should be added. There are a variety of chelators that can be used overnight including: bathocuproine disulfonate, tetraethylenepentamine, ammonium tetrathiomolybdate, and the more bioavailable bis(choline)tetrathiomolybdate. Dosages for these must be optimized depending on the cell type. Additionally, these reagents can be added for a shorter period of time (1-8 h), but ICP-MS and molecular imaging must be used to confirm that the total and labile pool are altered, respectively. For all treatments solutions should be sterile filtered and vehicle controls should be added to cells that are not treated.
3. **Dye preparation.** On the day of imaging, the dye should be dissolved in DMSO at a concentration of 1 to 5 mM and DPBS (with Mg^{2+} and Ca^{2+}) or DMEM should be warmed to 37 °C. It is important to note that DMEM is buffered by CO_2 so if it is used in the duration of the imaging the CO_2 control should be used. The dye can then be dissolved in DPBS or DMEM at a final concentration of 500 nM to 10 μM. If serum containing media is used, the dye should be used at higher concentrations 10 to 20 μM as the dye can interact with the serum proteins and bind any copper in the media.
4. **Cell staining.** The media is removed, cells are washed with DPBS or DMEM (optional), and the dye solution in DPBS or DMEM is added against the wall as to not disrupt the cells. Depending on the dye the cells are stained for 15 to 30 min at 37 °C, 5% CO_2. After staining the cell are washed with DPBS or DMEM and then imaged in fresh DPBS or DMEM.
5. **Imaging.** Typically, cells are imaged on a 40x or 63x objective. If the duration of the imaging is less than 15 min then DPBS is sufficient without temperature or CO_2 control, however, for longer imaging experiments DMEM with temperature and CO_2 control should be used. The laser power and gain settings should be kept the same between treatments. For each treatment, at least four fields of cells should be acquired.
6. **Data analysis.** ImageJ from the National Institutes of Health is used for analysis of the images. Specifically, the threshold for a field of cells is adjusted to select the pixels and is kept consistent in a given experiment. The selected pixels are analyzed for the median value. The mean of the median value for n fields of cells with standard error is reported, and statistical analyses are performed with a two-tailed Student's t-test in Microsoft Excel.

Appendix 6:
Protocols for X-ray Fluorescence Microscopy

Synopsis

This appendix summarizes methods for X-ray fluorescence microscopy (XRFM) sample preparation and data analysis. Procedures for organizing a beamrun and additional sample preparation guidelines at the beamline can be found in Appendix D of Dylan W. Domaille's dissertation.

Protocol for XRF sample preparation and data acquisition

1. Cells should be plated on silicon nitride membrane windows purchased from Silson, Catalog# SiRN-5.0-200-2.0-500 in a six-well plate. Depending on the cell type that window should be coated.
2. A XRF sample preparation protocol for cells that are genetically modified or treated pharmacologically is as follows: treat the cells, aspirate the media, wash the cells with PBS, fix the cells in 4% paraformaldehyde (PFA) in PBS for 10 min, was the cell with PBS, and remove residual PBS by several washes with 20 mM PIPES, pH 7.2⁄200 mM sucrose followed by air-drying. In all of these washes it is important the window remains under the liquid as bubbles can get trapped under the window. The frame of the sample is taped on a glass slide with reversible tape, and then the glass slide is taped into an empty pipet tip box. This procedure was used for the sample preparation of the neural stem cells described in Appendix 2 and the RAW 264.7 macrophages described in Appendix 3.
3. Detailed procedures for XRF sample preparation for correlating live-cell copper sensor imaging with XRFM were developed by Dylan W. Domaille and can be found in Appendix D of his dissertation. These methods were used in Chapter 3 for XRFM of the fibroblasts.
4. Cellular compartments can be marked with fluorescent dyes and then correlated with the metal maps acquired with XRFM. If the fluorescent dye is optically bright then it can be imaged on the Lecia epifluorescence microscope at the beamline; however some dyes are not optically bright or well retained after washing with the PIPES/sucrose preservative, so the cells can be stained live/post fixation, imaged by confocal microscopy post fixation, and then processed for XRFM. A protocol for staining the lipid droplets of 3T3L-1 adipocytes with Nile Red has been developed. 3T3L-1 adipocytes were plated on silicon nitride windows, and maintained in normal serum, high glucose DMEM prior to staining. Ten days post induction of differentiation, the cells were stained with 2 μM Nile Red (1 mM stock in DMSO) in DPBS for 15 min at 37 ºC. The staining media was removed and the cells were fixed with 4% PFA for 10 min at room temperature. The PFA was aspirated and the cells were washed with PBS followed by imaging in fresh PBS. After imaging the PBS was removed and the XRF window was washed with 20 mM PIPES, pH 7.2/200 mM sucrose followed by air-drying. The confocal microscopy images were correlated with bright field microscopy at beamline followed by XRFM (Figure AX-1)
5. Once the samples are prepared and transported to Argonne National Labs, the windows are mounted on a custom stick and cells are found with brightfield imaging. These procedures are described in Appendix D of Dylan W. Domaille's dissertation and can be further clarified by the staff scientists at the beamline.

6. There are a few variables that need to be determined prior to acquiring the XRF image including: step size, zone plate, and dwell time. Step size (0.6 to 1 micron) can enhance the resolution of the image but is limited by the optical setup on the beamline and should be clarified by the staff scientists. The zone plate (10 or 20 cm) focuses the X-ray beam onto the sample. The amount of X-ray is greater with the 20 cm zone plate and should be used for detecting copper. Finally, the dwell time is how long the detector sits on one pixel. The longer the dwell time, the greater the signal that will be acquired for a given element, and this can be evaluated by the fluorescence readout in the coarse scans. In general, a high-resolution image can be acquired on the 20 cm zone plate with a 0.6 micron step size with a 1 or 2 second dwell time. Procedures for using the microprobe will be provided by the beamline staff scientists.

Protocol for downloading XRF software and data analysis

1. Download and unzip the XRF data into a new folder in C:\XRFdata
2. Create an IDL account (http://www.exelisvis.com/ProductsServices/IDL.aspx) and login
3. Go to downloads
4. Select product as IDL, platform as windows, download type as product download, and check show previous versions
5. Click on IDL 8.1 to download the file. Please note that MAPS v 1.7.2.01 does not work well with IDL 8.2. Older data sets require MAPS v 1.6.3.1. The ordering computer in 401 Latimer has IDL 8.1 and MAPS 1.7.2.01 on the C drive. The microscope computer in 549 Latimer has IDL 7.0 and MAPS v. 1.6.3.1 on the D:/Dylan drive.
6. Download runtime_maps.zip file (http://www.stefan.vogt.net/downloads.html)
7. Unzip the IDL 8.1 file into the C:\Program Files\ITT
8. Unzip the runtime_maps.zip file into C:\XRFdata. There will be four files from this.
9. The following files need to be moved into C:\Program Files\ITT\IDL\IDL81\lib from the unzipped files in step 7: xrf_library.csv, henke.xdr, compound.dat
10. Click on maps.sav in C:\XRFdata folder to open the MAPS program
11. Click on the box that says press to change parent dir
12. Select the folder the XRF data was saved to in step 1 and click okay
13. Go to file → Open XRF Image (HDF5-avg or single element only) → img.dat. For data sets acquired prior to 2012 Go to file → img.dat.
14. Select all of the files by highlighting the first file and pressing shift and highlighting the last file
15. On the second toolbar fitted DS-IC should be shown. Note: this is important since you want to analyze the refined dataset.
16. Click options on the top toolbar and click Load Colortable and select Rainbow.
17. Then click on viewing on the top toolbar and click multi element view (M). From here a new window will open. On the right hand panel, select filter for autoscale. Then click select elements/detectors and make your selection. Underneath that change the autoscale to center 2/3.
18. On the second toolbar the 2xfm_000X.h5 where X corresponds to the MDA file number recorded during the beamrun can be selected.
19. Then go to tools on the top toolbar and select ROI analysis and a new window called ROI concentrations will open.
20. Then in the MAPS: multi element window (M) (updating) on the right panel change the mouse mode to ROI

21. Then in the ROI concentrations window click on draw ROI and select the ROI by clicking and then right click. The ROI will then be highlighted in red.
22. In the ROI concentrations window select output single and print ROI statistics. The output can then be copied and pasted into Microsoft excel. For cells that do not change in size or shape the mean and median should be analyzed; however, if the cell does change in shape or size the total content should be analyzed.

Figures

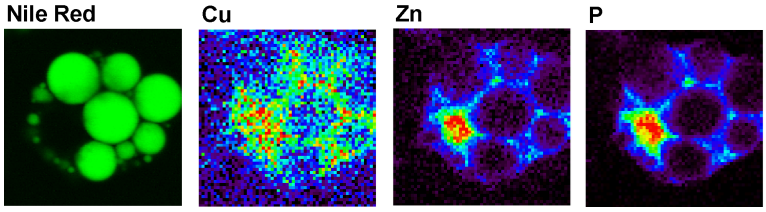

Figure A6-1. Fluorescence imaging of lipid droplets in fixed 3T3L-1 adipocytes with Nile Red and X-ray fluorescence imaging of Cu, Zn, and P distributions at 1 second pixel dwell time and 0.6 μM step-size in fixed 3T3L-1 adipocytes grown normal serum media.